Efficient Spectral and Spectral-Element Methods for Transformation Electromagnetics

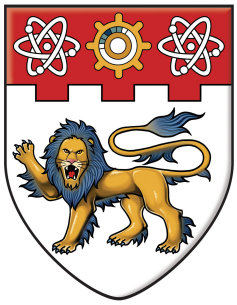

NANYANG TECHNOLOGICAL UNIVERSITY

School of Physical and Mathematical Sciences

Yang Zhiguo

School of Physical and Mathematical Sciences

A thesis submitted to the Nanyang Technological University
in fulfilment of the requirement for the degree of
Doctor of Philosophy

2017

Acknowledgement

First and foremost, I would like to thank my supervisor Prof. Li-Lian Wang for the guidance and providing me the privilege of working in this interesting research area. Without his invaluable supervision, encouragement, and wisdom over these years, this thesis could not have reached its present form.

I am grateful to Nanyang Technological University for awarding me the Research Scholarship. I am also benefited from the young, energetic and productive environment of the new School of Physical and Mathematical Sciences. In particular, I appreciate the management and leadership of Prof. San Ling, Prof. Yeow Meng Chee, Prof. Bernhard Schmidt, Prof. Huaxiong Wang and Prof. Chaoping Xing. I am appreciative of the help from the IT and Admin. staff.

I would like to express my appreciation to Prof. Guohua Wu, Prof. Liming Xiang and Prof. Viet Ha Hoang for the stimulating lectures and seminar courses. I am also indebted to the former and current members in our group including Jing Zhang, Ying Gu, Xiaodan Zhao, Michael Daniel Samson, Yang Gao, Hengfei Cui, Tiep Chu Wan for their friendship and help.

I appreciate Prof. Jie Shen of Purdue University, Prof. Zhijian Rong of Xiamen University, Prof. Bo Wang of Hunan Normal University and Dr. Lina Ma of Pennsylvania State University for many discussions and fruitful collaborations. I am also grateful to Prof. Baile Zhang and his Ph.D. student Xihang Shi and Fei Gao of Nanyang Technological University for fruitful interdisciplinary discussions.

Last but not least, I wish to thank my parents and my wife Mengjiao for their love and support.

Contents

List of Figures

Abstract

This thesis is devoted to the computation and analysis of electromagnetic wave scattering problems, with particular applications in accurate simulation of invisibility cloaks arisen from the field of transformation electromagnetics (TE). An efficient spectral-element method (SEM) is proposed for solving general two-dimensional Helmholtz equations in anisotropic media. In practice, we adopt a transparent boundary condition (TBC) characterized by the Dirichlet-to-Neumann (DtN) map to reduce wave propagation in an unbounded domain to a bounded domain. We then introduce a semi-analytic technique to integrate the global TBC with local curvilinear elements seamlessly, which is accomplished by using a novel elemental mapping and analytic formulas for evaluating global Fourier coefficients on spectral-element grids exactly.

From the perspective of TE, an invisibility cloak is devised by a singular coordinate transformation of Maxwell's equations that leads to anisotropic materials coating the cloaked region to render any object inside invisible to observers outside. An important issue resides in the imposition of appropriate boundary conditions, i.e., cloaking boundary conditions (CBCs), in order to achieve perfect invisibility. Based upon the principle that a well-behaved electromagnetic field in the original space must be well-behaved in the transformed space as well, we propose new CBCs for circular, elliptic and polygonal invisibility cloaks from the essential "pole" conditions related to singular transformations. We emphasize that our proposal of CBCs is different from any existing ones.

Last but not the least, this thesis is devoted to wavenumber explicit analysis

of three-dimensional time-harmonic Maxwell's equations in an exterior domain. The infinite domain is first reduced to a finite domain by using an exact spherical TBC involving the capacity operator. Remarkably, when the scatterer is a sphere, by using divergence-free vector spherical harmonic expansions of the fields, one can preserve divergence-free property of the electric and magnetic fields, and reduce the Maxwell's system to two sequences of decoupled one-dimensional Helmholtz problems (in the radial direction) in a similar setting. This reduction not only leads to more efficient spectral-Galerkin algorithms, but also allows us to carry out, for the first time, wavenumber explicit analysis for 3-D time-harmonic Maxwell's equations with exact transparent boundary conditions. We then use the transformed field expansion to deal with more general scatterers, and derive rigorous error estimates for the whole algorithm.

Notation

Common Notation

$\mathbb{C}$	Set of all complex numbers
$\mathbb{R}$	Set of all real numbers
$\mathbb{N}$	Set of all nonnegative integers, i.e., $\{0, 1, 2, \ldots\}$
$\mathbb{P}_N$	Set of all algebraic polynomials of degree $\leq N$
i	Complex unit, i.e., $\mathrm{i} = \sqrt{-1}$

Spaces, Inner Products and Norms

$H^s_\omega(\Lambda)$	Weighted Sobolev space $H^s_\omega(\Lambda)$ with $s \geq 0$ defined in [1]
$L^p(I)$	L^p-space on I with $1 \leq p \leq \infty$
$(\cdot, \cdot)_\omega$	Inner product of $L^2_\omega(I)$
$(\cdot, \cdot)$	Inner product of $L^2(I)$
$\|\cdot\|_\omega$	Norm of $L^2_\omega(I)$
$\|\cdot\|$	Norm of $L^2(I)$
$\|\cdot\|_\infty$	Norm of $L^\infty(I)$

Bessel, Hankel and Airy Functions

J_ν	Bessel function of the first kind of order ν
Y_ν	Bessel function of the second kind of order ν
$H^{(1)}_\nu$	Hankel function of the first kind of order ν
$h^{(1)}_\nu$	Spherical Hankel function of the first kind of order ν
Ai	Airy function of the first kind
Bi	Airy function of the second kind

Mathieu Functions

$\{\mathrm{ce}_m;\, \mathrm{se}_m\}$	Angular Mathieu functions as defined in [2]
$\{\mathrm{Mc}_m^{(1)};\, \mathrm{Ms}_m^{(1)}\}$	Radial Mathieu functions of the first kind
$\{\mathrm{Mc}_m^{(3)};\, \mathrm{Ms}_m^{(3)}\}$	Mathieu-Hankel functions

Spherical Harmonics and Vector Spherical Harmonics

Y_l^m	Spherical harmonics as normalized in [3]
$\{\boldsymbol{e}_r, \boldsymbol{e}_\theta, \boldsymbol{e}_\varphi\}$	Moving (right-handed) orthonormal coordinate basis
∇_S	Tangent gradient operator on the unit spherical surface S
$\{Y_l^m \boldsymbol{e}_r, \nabla_S Y_l^m, \nabla_S Y_l^m \times \boldsymbol{e}_r\}$	Vector spherical harmonics (VSH) defined in Morse and Feshbach [4]

Chapter 1

Introduction

In this chapter, we elaborate on motivations and background of the topics to be studied in this thesis, and highlight the main contributions.

1.1 Basics of transformation electromagnetics

Since the groundbreaking works of Pendry, Schurig and Smith [5], and Leonhardt [6], the transformation electromagnetics (TE) has emerged as a very useful tool to design a wide variety of new devices and materials with novel and unusual physical properties (see, e.g., [7, 8, 9, 10, 11, 12] and [13] for many original references therein).

The fundamental principle of TE is based on the form invariance of Maxwell's equations under any coordinate transformation (cf. [14]). More precisely, we consider the time-harmonic Maxwell's system:

$$\breve{\nabla}_{\breve{\boldsymbol{x}}} \times \breve{\boldsymbol{E}} - \mathrm{i}\omega\mu_0 \breve{\boldsymbol{H}} = \boldsymbol{0}, \quad \nabla_{\breve{\boldsymbol{x}}} \times \breve{\boldsymbol{H}} + \mathrm{i}\omega\epsilon_0 \breve{\boldsymbol{E}} = \boldsymbol{0}, \tag{1.1}$$

in the Cartesian coordinates $\breve{\boldsymbol{x}} = (\breve{x}, \breve{y}, \breve{z}) \in \mathbb{R}^3$ of the "virtual space". Here, $\mathrm{i} = \sqrt{-1}$ is the complex unit, and the electric permittivity ϵ_0, the magnetic permeability μ_0, and the angular frequency ω are positive constants. Note that $e^{-\mathrm{i}\omega t}$ time-dependence is assumed for the electric field $\breve{\boldsymbol{E}}$ and magnetic field $\breve{\boldsymbol{H}}$.

Let $\boldsymbol{x} = (x, y, z) = \boldsymbol{x}(\breve{\boldsymbol{x}})$ be a given coordinate transformation. Then the transformed Maxwell's system reads (cf. [14])

$$\nabla \times \boldsymbol{E} - \mathrm{i}\omega\mu_0\boldsymbol{\mu}\,\boldsymbol{H} = \boldsymbol{0}, \quad \nabla \times \boldsymbol{H} + \mathrm{i}\omega\epsilon_0\boldsymbol{\epsilon}\,\boldsymbol{E} = \boldsymbol{0}, \tag{1.2}$$

where "$\nabla\times$" is the curl operator in the new coordinates of the "physical space", and

$$\boldsymbol{E}(\boldsymbol{r}) = (\boldsymbol{J}^t)^{-1}\breve{\boldsymbol{E}}(\breve{\boldsymbol{r}}), \quad \boldsymbol{H}(\boldsymbol{r}) = (\boldsymbol{J}^t)^{-1}\breve{\boldsymbol{H}}(\breve{\boldsymbol{r}}), \quad \boldsymbol{\mu} = \boldsymbol{\epsilon} = \boldsymbol{J}\boldsymbol{J}^t/\det(\boldsymbol{J}). \tag{1.3}$$

with the Jacobian matrix given by $\boldsymbol{J} = \partial\boldsymbol{x}/\partial\breve{\boldsymbol{x}}$.

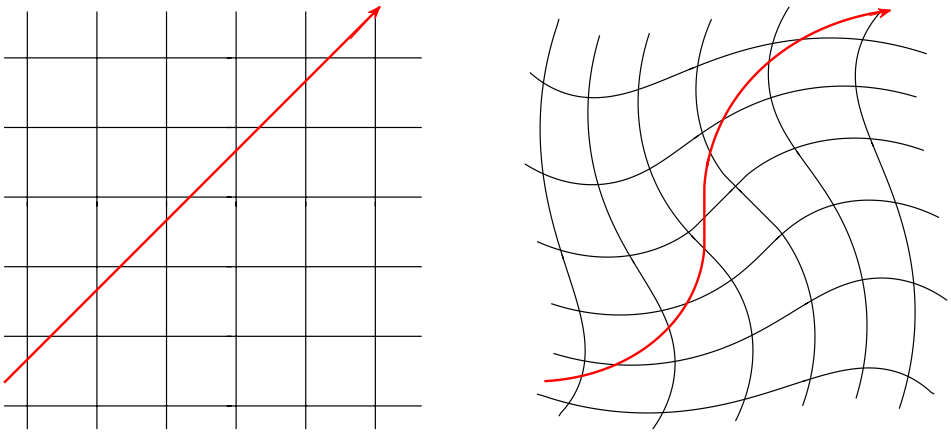

(a) Virtual space (b) Physical space

Figure 1.1: Schematic illustration of a coordinate transformation from the virtual space $\breve{\boldsymbol{x}} = (\breve{x}, \breve{y}, \breve{z})$ to the physical space $\boldsymbol{x} = (x, y, z)$.

By eliminating the magnetic field $\boldsymbol{H}$, we can obtain from (1.2) the curl-curl formulation of the time-harmonic Maxwell's equations

$$\nabla \times \left(\boldsymbol{\mu}^{-1}\nabla \times \boldsymbol{E}\right) - k^2\boldsymbol{\epsilon}\boldsymbol{E} = \boldsymbol{0}\,, \tag{1.4}$$

where $k = \omega\sqrt{\epsilon_0\mu_0}$.

In many applications, we are concerned with electromagnetic wave propagation in media with in-plane anisotropy. For example, we are interested in the situation when the components of $\boldsymbol{\epsilon}$ and $\boldsymbol{\mu}$ in (1.2) are z-invariant. Thus, under the

transverse-electric polarisation, we have $\boldsymbol{E} = (0, 0, u(x, y))^t$ and $\boldsymbol{H} = (H_1, H_2, 0)^t$. Accordingly, the material parameters in (1.3) are reduced to

$$\boldsymbol{\mu} = \boldsymbol{\epsilon} = \begin{bmatrix} \boldsymbol{C} & \boldsymbol{0}^t \\ \boldsymbol{0} & n \end{bmatrix} = \begin{bmatrix} C_{11} & C_{12} & 0 \\ C_{12} & C_{22} & 0 \\ 0 & 0 & n \end{bmatrix}, \tag{1.5}$$

where

$$\boldsymbol{C} = \frac{\boldsymbol{J}_{\rm cn}\,\boldsymbol{J}_{\rm cn}^t}{\det(\boldsymbol{J}_{\rm cn})}, \quad n = \frac{1}{\det(\boldsymbol{J}_{\rm cn})} \quad \text{with} \quad \boldsymbol{J}_{\rm cn} := \frac{\partial(x, y)}{\partial(\breve{x}, \breve{y})} = \begin{bmatrix} \partial_{\breve{x}} x & \partial_{\breve{y}} x \\ \partial_{\breve{x}} y & \partial_{\breve{y}} y \end{bmatrix}. \tag{1.6}$$

Note that $\det(\boldsymbol{C}) = 1$, and we have

$$\boldsymbol{\mu}^{-1} = \boldsymbol{\epsilon}^{-1} = \begin{bmatrix} C_{22} & -C_{12} & 0 \\ -C_{12} & C_{11} & 0 \\ 0 & 0 & n^{-1} \end{bmatrix}. \tag{1.7}$$

Then we derive from the first equation of (1.2) and (1.7) that

$$\begin{aligned} \boldsymbol{H} &= \frac{\boldsymbol{\mu}^{-1}}{\mathrm{i}\omega\mu_0} \nabla \times \boldsymbol{E} = \frac{\boldsymbol{\mu}^{-1}}{\mathrm{i}\omega\mu_0} \big(u_y, -u_x, 0\big)^t \\ &= \frac{1}{\mathrm{i}\omega\mu_0} \big(C_{12}u_x + C_{22}u_y, -C_{11}u_x - C_{12}u_y, 0\big)^t. \end{aligned} \tag{1.8}$$

Inserting it into the second equation of (1.2), we obtain the two-dimensional Helmholtz equation:

$$\nabla \cdot (\boldsymbol{C}(\boldsymbol{r})\ \nabla u(\boldsymbol{r})) + k^2 n(\boldsymbol{r})\, u(\boldsymbol{r}) = 0. \tag{1.9}$$

Thus, a coordinate transformation operating on Maxwell's equations leads to new material parameters $\boldsymbol{\epsilon}$ and $\boldsymbol{\mu}$, which enable us to design novel electromagnetic devices to steer waves almost at will. We refer to [15, 16] for more details.

One of the most appealing examples of the TE technique is the electromagnetic invisibility cloak [5, 6, 17, 18, 19, 20, 21, 22, 23, 24, 25, 26, 27]. Following the approach in [5], cloaking a central cylindrical region of radius R_1 by a concentric cylindrical shell of radius R_2 requires the coordinate transformation as follows:

$$r = \frac{R_2 - R_1}{R_2}\breve{r} + R_1, \quad \theta = \breve{\theta}, \quad z = \breve{z}, \tag{1.10}$$

where $\breve{\boldsymbol{r}} = (\breve{r}, \breve{\theta}, \breve{z})$ is the cylindrical coordinates in the virtual space, and $\boldsymbol{r} = (r, \theta, z)$ is the cylindrical coordinates in the physical space.

The origin in Figure 1.2 is mapped to the circle $r = R_1$ that produces an "empty" space: $0 \le r < R_1$, forming the "cloaked region" to conceal any object inside. The annulus $R_1 < r < R_2$ constitutes the "cloak", where the material parameters are obtained by applying the transformation (1.10) to the Maxwell's equations. The material parameters in the exterior region $r > R_2$ are positive constants.

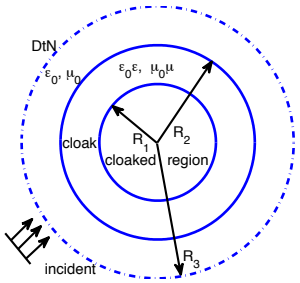

Figure 1.2: Schematic illustration of a circular cloak

Next, we derive in detail the material parameters for the circular cylindrical cloak. Since the transformation (1.10) is z-invariant, we adopt (1.6) to simplify the calculation. By the chain rule, $\boldsymbol{J}_{\rm cn}$ in (1.6) can be computed by

$$\boldsymbol{J}_{\rm cn} = \frac{\partial(x,y)}{\partial(\breve{x},\breve{y})} = \frac{\partial(x,y)}{\partial(r,\theta)}\frac{\partial(r,\theta)}{\partial(\breve{r},\breve{\theta})}\frac{\partial(\breve{r},\breve{\theta})}{\partial(\breve{x},\breve{y})}. \tag{1.11}$$

Let $\boldsymbol{T}_\theta$ be defined as

$$\boldsymbol{T}_\theta = \begin{bmatrix} \cos\theta & -\sin\theta \\ \sin\theta & \cos\theta \end{bmatrix} \tag{1.12}$$

and note that $\theta = \breve{\theta}$. We therefore have

$$\frac{\partial(x,y)}{\partial(r,\theta)} = \boldsymbol{T}_\theta \,\mathrm{diag}\big(1, r\big), \quad \frac{\partial(\breve{r},\breve{\theta})}{\partial(\breve{x},\breve{y})} = \mathrm{diag}\big(1, \breve{r}^{-1}\big)\,\boldsymbol{T}_\theta^t$$

and

$$\frac{\partial(r,\theta)}{\partial(\breve{r},\breve{\theta})} = \mathrm{diag}\big(\partial_{\breve{r}} r, 1\big).$$

Thus, from (1.11) and the above, we obtain

$$\boldsymbol{J}_{\rm cn} = \boldsymbol{T}_\theta \boldsymbol{J}_1 \boldsymbol{T}_\theta^t, \ \text{ where } \ \boldsymbol{J}_1 = \mathrm{diag}(\partial_{\breve{r}} r, r/\breve{r}). \tag{1.13}$$

Using (1.6) and the property $\boldsymbol{T}_\theta^t \boldsymbol{T}_\theta = \boldsymbol{I}_2$, leads to $\boldsymbol{C}$ and n in the new Cartesian coordinates:

$$\boldsymbol{C} = \boldsymbol{T}_\theta \boldsymbol{J}_1 \boldsymbol{J}_1^t \boldsymbol{T}_\theta^t / \det(\boldsymbol{J}_1) = \boldsymbol{T}_\theta \,\mathrm{diag}(\epsilon_r, \epsilon_\theta)\, \boldsymbol{T}_\theta^t, \quad n = 1/\det(\boldsymbol{J}_1) = \epsilon_z, \tag{1.14}$$

where

$$\epsilon_r = \frac{r - R_1}{r}, \quad \epsilon_\theta = \frac{r}{r - R_1}, \quad \epsilon_z = \Big(\frac{R_2}{R_2 - R_1}\Big)^2 \frac{r - R_1}{r}. \tag{1.15}$$

Accordingly, the material parameters $\boldsymbol{\epsilon}$ and $\boldsymbol{\mu}$ in the polar cylindrical coordinates are rewritten as (see [15])

$$\boldsymbol{\epsilon} = \boldsymbol{\mu} = \mathrm{diag}(\epsilon_r, \epsilon_\theta, \epsilon_z). \tag{1.16}$$

It is expected that electromagnetic waves propagating into the above media will bend smoothly around the cloaked region and propagate out without inducing any scattering.

In practice, the requirement for fabricating the material parameters (1.15) is quite stringent, thus it is also necessary to study imperfect cases. In order to investigate the imperfection caused by frequency dispersions, the permittivity and permeability of the cloak are mapped to the Drude or Lorentz models (cf. [28]). We postpone the modelling of dispersive cloaks using the Drude model in Section 1.4.

1.2 Some existing numerical methods

Thanks to the fascinating applications of TE technique such as invisibility cloaks, numerical simulation plays an important role in modelling of the electromagnetic wave interaction with these devices since it serves as a reliable tool to the justification of expensive physical experiments and validation of theoretical predictions.

The numerical simulation and analysis of the Maxwell's and Helmholtz problems have been investigated by various computational methods. Among them, finite difference method (cf. [29, 30]) is popular because of its simplicity and easy implementation. Zhao et al. proposed a finite difference time-domain (FDTD) method in [31] to simulate the 2-D cloaking structures with Drude model. Liang et al [32] proposed an interesting energy conserved splitting FDTD scheme for solving Maxwell's equations in metamaterials. However, this method is most applicable to problems with regular domains and homogeneous media. Since the

shape of the domain prescribed with metamaterial maybe complex, it is preferable to use finite element method [33, 34, 35, 36] to discretise the domain. The finite-element-based COMSOL Multiphysics package has been extensively used in the simulation of different cloaks (see [37, 38]). Li and his collaborators developed a finite element time-domain (FETD) method for the simulations of circular, elliptic and carpet cloaks in a series of papers [39, 40, 41]. However, it is known that when the wavenumber becomes large, the mesh size should be adapted otherwise large error may occur to deteriorate the approximation. It has been shown, at least for some simple cases, that errors of pth order numerical methods for the Helmholtz equation behave like $O(k^{p+1}h^p)$, (see [42, 43, 44]). Hence, high-order methods are particularly preferable for this type of problem over low-order methods. The spectral method (see, e.g., [45, 46, 47]) is a method of choice for wave simulation due to its high order accuracy and free of dispersive error. Nevertheless, The disadvantage of lacking the flexibility for dealing with complex domain limits its usage in complicated situations. Spectral-element method (SEM) (see, e.g., [48, 49, 50]) combines the advantage of both methods and is more desirable for simulation of wave propagations in complex geometry. It is worthwhile to note that the development of spectral and spectral-element solvers for the Helmholtz equation and Maxwell's equations is of fundamental importance for these highly oscillatory problems.

1.3 Frequency-domain simulations

In this thesis, we focus on the frequency-domain simulations, which often involve the time-harmonic Maxwell's equations and Helmholtz equation.

Assume the anisotropic media induced by coordinate transformations and all the other inhomogeneities are enclosed in a finite volume (in three dimensions) or cross section (in two dimensions). By (1.4) and (1.9), the problems of interest

are summarised as follows:

$$\nabla \times \left(\boldsymbol{\mu}^{-1}\nabla \times \boldsymbol{E}\right) - k^2\boldsymbol{\epsilon}\boldsymbol{E} = \boldsymbol{F} \quad \text{in } \mathbb{R}^3, \tag{1.17a}$$

$$(\nabla \times \boldsymbol{E}^{\text{sc}}) \times \hat{\boldsymbol{x}} - \mathrm{i}k\boldsymbol{E}_T^{\text{sc}} = o(r^{-1}) \quad \text{as } r \to \infty, \tag{1.17b}$$

and

$$\nabla \cdot \left(\boldsymbol{C}\,\nabla u\right) + k^2 n\, u = f \quad \text{in } \mathbb{R}^2, \tag{1.18a}$$

$$\partial_r u_{\text{sc}} - \mathrm{i}k\, u_{\text{sc}} = o(r^{-1/2}) \quad \text{as } r \to \infty. \tag{1.18b}$$

Here, we list below the notation and setting.

- The inhomogeneity of $\boldsymbol{\epsilon}$, $\boldsymbol{\mu}$, and $\boldsymbol{F}$ (resp. $\boldsymbol{C}$, n and f) are supported in a ball (resp. a cylinder) B_R of radius $r = R$. Note that for $r > R$, we have $\boldsymbol{\epsilon} = \boldsymbol{\mu} = \boldsymbol{I}_3$ and $\boldsymbol{F} = \boldsymbol{0}$ (resp. $\boldsymbol{C} = \boldsymbol{I}_2, n = 1$ and $f = 0$), where $\boldsymbol{I}_3$ is the 3×3 identity matrix (resp. $\boldsymbol{I}_2$ is the 2×2 identity matrix).

- The far-field condition (1.17b) is known as the Silver-Müller radiation condition (cf. [3]) to select the outgoing fields. Here, $\boldsymbol{E}^{\text{sc}} := \boldsymbol{E} - \boldsymbol{E}^{\text{in}}$ is the scattering wave (where $\boldsymbol{E}^{\text{in}}$ is a given incident wave) and the tangential field $\boldsymbol{E}_T^{\text{sc}} = -\boldsymbol{E}^{\text{sc}} \times \hat{\boldsymbol{x}} \times \hat{\boldsymbol{x}}$. Here, $\hat{\boldsymbol{x}} = \boldsymbol{x}/r$ is the unit out normal. Likewise, (1.18b) is known as Sommerfeld radiation boundary condition (cf. [3]) upon the scattering wave: $u_{\text{sc}} := u - u_{\text{in}}$ (where u_{in} is a given incident wave).

The challenges of (1.17) and (1.18) are at least threefold:

(1) unboundedness of the computational domain with highly oscillatory solution decaying slowly when $k \gg 1$;

(2) the coefficients $\boldsymbol{\epsilon}$ and $\boldsymbol{\mu}$ (resp. $\boldsymbol{C}(\boldsymbol{r})$ and $n(\boldsymbol{r})$) might be singular due to singular coordinate transformation (see (1.15)-(1.16));

(3) indefiniteness of the variational formulation.

In what follows, we briefly review some relevant techniques and outline our approaches to overcome these obstacles.

Reduction of unbounded domain

The methods of choice to deal with the first issue typically include the perfectly matched layer (PML) technique [51], boundary integral method [52, 53], and the artificial boundary condition [3, 54, 55, 56]. The latter is known as the absorbing boundary condition (ABC), if it leads to a well-posed initial-boundary value problem (IBVP) and some "energy" can be absorbed at the boundary. In particular, if the solution of the reduced problem coincides with that of the original problem, then the related ABC is dubbed as a transparent (or nonreflecting) boundary condition (TBC) (or NRBC).

The use of TBCs is desirable and beneficial (cf. the review paper [54] and the references therein) due to (i) the exterior problem in unbounded domain reduces to an equivalent boundary value problem (BVP), so one can place the DtN boundary as close as possible to the scatterer that can significantly reduce the computational cost; (ii) it is essential for accurate and stable simulations especially when the wavenumber is large.

Despite its advantages of TBCs, it poses a great challenge since such a boundary condition is global, as it involves the Fourier/Mathieu/spherical harmonic/vector spherical harmonic expressions in space. One main issue lies in *how to integrate the global TBC with the interior solver for the reduced problem by local spectral elements*? In Chapter 2, the nonlocality of the TBC in space is efficiently handled by Fourier/Mathieu expansions since the scatterer is a disk or an ellipse.

As for general bounded scatterers, we propose an algorithm in Chapter 3 to seamlessly integrate the exact circular Dirichlet-to-Neumann (DtN) TBC with local spectral elements. The key idea is to construct a new elemental mapping between the curvilinear elements along the DtN boundary and the reference square, which leads to exact evaluation of the Fourier integrals. It is noteworthy that Fournier [57] proposed a method for calculating global Fourier coefficients for given nodal values on non-conforming spectral elements, where a similar semi-analytic approach was essential for the success of the method therein. We also

remark that the recent work [58] addressed the integration of one-dimensional DtN TBC imposed on a line segment with standard rectangular elements along the boundary. Different from these works, our "local-to-global" method is built upon the use of curvilinear elements seamlessly fitting the circular boundary, and the design of a new elemental mapping leading to exact calculation of the involved Fourier integrals (see Subsection 3.1.3). We highlight that this notion can be extended to the computation of three-dimensional Maxwell's equations, though it has not been investigated before as far as we know.

Treatment of singularity of material parameters

In Chapter 2, we are concerned with mathematical and numerical study of the circular cylindrical cloak induced by the transformation (1.10) and its important variant, i.e., the elliptic cylindrical cloak [19, 59]. As addressed in Section 1.1, the coordinate transformation (1.10) suppresses a disk into an annulus so that the interior "empty" space constitutes the cloaked region Ω_0 (see Figure 1.2). Such a "point-to-circle" blowup leads to new electric permittivity and magnetic permeability parameters, which are singular at the *inner boundary* $\partial\Omega_0$ (denoted by $r = R_1$) of the cloak. Accordingly, the coefficients of the governing equation are highly singular. The presence of singularities poses significant challenges for simulation, realization and analysis as well. A critical issue resides in *how to impose suitable cloaking boundary conditions at the inner boundary, i.e., CBCs, to achieve perfect concealment of waves?* We highlight below some relevant studies and attempts, which are by no means comprehensive, given a large volume of existing literature.

- Ruan et al. [60] first analytically studied the sensitivity of the ideal cloak [5] to a small δ-perturbation of the inner boundary (i.e., from R_1 to $R_1 + \delta$, while the material parameters remained unchanged) under the transverse-electric (TE) polarization. Their findings are (i) the ideal cloak in [5] is sensitive to a tiny perturbation of the boundary; (ii) the electric field is

discontinuous across the inner boundary; and (iii) the perturbed cloak is nearly ideal in the sense that the magnitude of the fields penetrated into the cloaked region is small.

- Zhang et al. [61] provided deep insights into the physical effects, and found that the singular transformation gave rise to electromagnetic surface currents along the inner interface of the ideal cloak (also see [62]).

- To shield the incoming waves, the perfect magnetic conductor (PMC) condition (i.e., the tangential component of the magnetic field vanishes) was imposed at $r = R_1$ in finite-element simulations (see, e.g., [37, 59, 63]). Indeed, such a condition can be naturally implemented by using Nédélec edge-elements [64] in the Cartesian coordinates (see, e.g., [35, 36]). However, in the polar coordinates, the PMC condition is automatically satisfied, so it does not lead to an independent condition (see Remark 2.2).

- Weder [65] proposed CBCs for general point transformed cloaks from the perspective of energy conservation. Its implication to the three-dimensional ideal spherical cloak by Pendry et al. [5] is that the tangential components of the electric and magnetic fields have to vanish at the spherical cloaked boundary $\partial\Omega_0^+$, and that the normal components of the curl of both fields have to vanish at the inner spherical surface $\partial\Omega_0^-$. Under this set of CBCs, the interior fields (i.e., in Ω_0) are decoupled from the exterior fields. However, CBCs in [65] are not applicable to the ideal circular cloak, as the tangent component of the electric field does not vanish at $r = R_1^+$ (cf. [60, 61]).

- Lassas and Zhou [66, 67] proposed some non-local pseudo-differential CBCs from a limiting process of non-singular approximate two-dimensional Helmholtz cloaking. Their findings also indicate that CBCs for two dimensions and three dimensions take different forms, and their physical effects on the cloak interface are very different as well.

Based upon the principle that a well-behaved electromagnetic field in the original space must be well-behaved in the transformed space as well, we obtained in Chapter 2 the CBCs for circular and elliptic cloaks that intrinsically relate to the essential "pole" conditions of a singular transformation. In Chapter 3, we extend the principle to the investigation of polygonal invisibility cloaks and propose new CBCs under a "local" coordinate system (see Proposition 3.3). Given the new CBCs, the governing equation in the cloaked region is decoupled from the exterior region. Accordingly, no wave can propagate into the cloaked region, and vice versa. We emphasise that the new CBCs are indispensable for spectrally accurate simulations. We also show that the proposed spectral-element solver provides a reliable tool to study how the defects affect the perfectness of an ideal cloak (see Subsection 3.2.5).

1.4 Time-domain simulations

Due to its capability of capturing wide-band signals and modelling more general material inhomogeneities and nonlinearities, time-domain simulation [29, 49, 68, 69] is also very important in the study of wave interaction with electromagnetic devices, especially in the investigation of dispersive properties of metamaterials and invisibility cloaks. In what follows, we briefly outline the procedures to obtain the governing equations for time-domain circular invisibility cloaks coupled with Drude model. Recall that in (1.16), the values of ϵ_r and ϵ_z are less than one for some $r \in (R_1, R_2)$. Based on the principle in [70, 71], we map ϵ_r and ϵ_z to $\tilde{\epsilon}_r(r,\omega)$ and $\tilde{\epsilon}_z(r,\omega)$ using Drude model (taking ϵ_r as an example)

$$\tilde{\epsilon}_r := \tilde{\epsilon}_r(r,\omega) = 1 - \frac{\omega_p^2}{\omega(\omega + \mathrm{i}\gamma)}, \quad \text{with} \quad \omega_p^2 := \omega_c(\omega_c + \mathrm{i}\gamma)(1 - \epsilon_r), \tag{1.19}$$

where ω_c is the operating frequency, γ is the given collision frequency, and ω_p is known as the plasma frequency. Thus, the material parameters in (1.16) become

$$\tilde{\boldsymbol{\epsilon}}(\omega) = \tilde{\boldsymbol{\mu}}(\omega) = \mathrm{diag}\big(\tilde{\epsilon}_r(r,\omega),\ \epsilon_\theta,\ \tilde{\epsilon}_z(r,\omega)\big). \tag{1.20}$$

Using an inverse Fourier transform and the rules $\mathrm{i}\omega \to \partial_t$, $\omega^2 \to -\partial_t^2$ to (1.2) and the constitutive relation

$$\boldsymbol{D} = \epsilon_0 \tilde{\boldsymbol{\epsilon}}(\omega)\boldsymbol{E}, \quad \boldsymbol{B} = \mu_0 \tilde{\boldsymbol{\mu}}(\omega)\boldsymbol{H}, \tag{1.21}$$

we obtain the time-dependent Maxwell's equations

$$\frac{\partial \boldsymbol{B}}{\partial t} = -\nabla \times \boldsymbol{E}, \quad \frac{\partial \boldsymbol{D}}{\partial t} = \nabla \times \boldsymbol{H}, \tag{1.22}$$

and the time-domain constitutive relation for the first equation in (1.21) (detailed derivation and the time-domain formulation for the second equation see [31])

$$\begin{aligned}\epsilon_0\epsilon_\theta\Big(\frac{\partial^2}{\partial t^2} + \gamma\frac{\partial}{\partial t} + \omega_p^2\Big)E_x = &\Big[\Big(\frac{\partial^2}{\partial t^2} + \gamma\frac{\partial}{\partial t} + \omega_p^2\Big)\sin^2\theta + \epsilon_\theta\Big(\frac{\partial^2}{\partial t^2} + \gamma\frac{\partial}{\partial t}\Big)\cos^2\theta\Big]D_x \\ &+ \Big[\epsilon_\theta\Big(\frac{\partial^2}{\partial t^2} + \gamma\frac{\partial}{\partial t}\Big) - \Big(\frac{\partial^2}{\partial t^2} + \gamma\frac{\partial}{\partial t} + \omega_p^2\Big)\Big]\sin\theta\cos\theta D_y\,.\end{aligned}$$

It seems that there is no existing work on time-domain spectral-element method developed for cloak simulation yet. We address in Section 5.2 some ideas for the time-domain computation to be explored in the future.

1.5 Wavenumber explicit analysis for Maxwell's equations

There has been a longstanding research interest in wavenumber explicit estimates for the Helmholtz and Maxwell's problems. In particular, much effort has been devoted to the Helmholtz equations (see, e.g., [42, 43, 44, 72, 73, 74, 75, 76, 77, 78, 79, 80] as a partial list of literature). Most of the analysis is essentially based on the Rellich identities [76, 81] (also see, e.g., [78, 79, 80]), which applies only to star-shaped domains (or the bounded scatterer is of star-shape, see [79]). Moreover, most of the results were established only for the Helmholtz equation with an approximate boundary condition: $\partial_r u - \mathrm{i}ku = 0$ instead of the exact DtN boundary condition. For the Maxwell's equations, Hiptmair et al. [82]

(and independently by [83]) derived for the first time the wavenumber explicit estimates for the time-harmonic Maxwell's equations but with an approximate boundary condition: $(\nabla \times \boldsymbol{E}) \times \boldsymbol{e}_r - \mathrm{i}k\boldsymbol{E}_T = \boldsymbol{h}$.

The analysis can not be applied to scattering problems with TBC at an artificial boundary, a situation considered in Chapter 4. Indeed, as shown in [77, 79], the presence of the exact DtN boundary condition brought about significant challenges even for the Helmholtz equation due to the Hankel functions involved in the DtN condition.

The main purposes of Chapter 4 are to extend the analysis in [77] to the Maxwell's equations, and in the meantime, provide an essential improvement, which is critical to obtaining the desired estimate for the Maxwell's equations, to an estimate for the Helmholtz equation in [77]. We demonstrate that the spectral algorithm and analysis for the Maxwell's equations in the spherical domain are the major component for dealing with general scatterers using the transformed field expansion (TFE) approach [84].

1.6 Main contributions and outline

The main contents and contributions of this dissertation are highlighted as follows.

- In Chapter 2, we conduct a mathematical study and numerical experiments of the ideal circular cylindrical cloak using the approach in Pendry et al. [5] and its important variant, i.e., the elliptic cylindrical cloak [19, 59]. We propose CBCs based on the principle that *a smooth electromagnetic field in the original coordinates must be regular near the cloaking boundary in transformed domain*. This situation is reminiscent to the imposition of "pole" conditions associated with the polar transformation (see, e.g., [45, 85, 86]). We also find that for the elliptic cylindrical cloak,

the CBCs should be imposed differently for the cosine-elliptic and sine-elliptic components of the decomposed fields. With these at our disposal, we can rigorously show that the governing equation in the cloaked layer can be decoupled from the exterior region, and the total fields in the cloaked region vanish under mild conditions. We emphasize that our proposal of CBCs is different from any existing ones. Using the exact circular (resp., elliptic) DtN non-reflecting boundary conditions to reduce the unbounded domain to a bounded domain, we introduce an accurate and efficient Fourier-Legendre spectral-element method (FLSEM) (resp., Mathieu-Legendre spectral-element method (MLSEM)) to simulate the circular cylindrical cloak (resp., elliptic cylindrical cloak). We provide ample numerical results to demonstrate that the perfect concealment of waves can be achieved for the ideal circular/elliptic cylindrical cloaks under our proposed CBCs and accurate numerical solvers.

- In Chapter 3, we present an efficient spectral-element method (SEM) for solving general two-dimensional Helmholtz equations in anisotropic media, with particular applications in accurate simulation of polygonal invisibility cloaks, concentrators and circular rotators arisen from the field of transformation electromagnetics. Once again, we adopt an exact circular DtN TBC to reduce wave propagation in an unbounded domain to a bounded domain. We then introduce a semi-analytic technique to integrate the global TBC with local curvilinear elements seamlessly, which is accomplished by using a novel elemental mapping and analytic formulas for evaluating global Fourier coefficients on spectral-element grids exactly. We also propose new CBCs for polygonal invisibility cloaks from the essential "pole" conditions related to singular transformations. This allows for the decoupling of the governing equations of inside and outside the cloaked regions. With this efficient spectral-element solver at our disposal, we can study the interesting phenomena when some defects and lossy or dispersive media are placed in the

cloaking layer of an ideal polygonal cloak.

- In Chapter 4, we are concerned with wavenumber explicit analysis of three-dimensional time-harmonic Maxwell's equations in an exterior domain. The infinite domain is first reduced to a finite domain by using an exact spherical TBC involving the capacity operator. Remarkably, when the scatterer is a sphere, by using divergence-free vector spherical harmonic expansions of the fields, one can preserve divergence-free property of the electric and magnetic fields, and reduce the Maxwell's system to two sequences of decoupled one-dimensional Helmholtz problems (in the radial direction) in a similar setting. This reduction not only leads to more efficient spectral-Galerkin algorithms, but also allows us to carry out, for the first time, wavenumber explicit analysis for three-dimensional time-harmonic Maxwell's equations with exact TBCs. We then use the transformed field expansion to deal with more general scatterers, and derive rigorous error estimates for the whole algorithm.

- The last chapter is for some concluding remarks and future works.

Chapter 2

Circular and Elliptic Cylindrical Invisibility Cloaks

As already described in Section 1.3, the main purposes of this chapter are devoted to mathematical study and numerical simulation of the ideal circular and elliptic cylindrical cloaks. We proposed the new CBCs (see Subsection 2.1.3 and Subsection 2.2.2) for ideal circular and elliptic cloaks, which together with a fast spectral-element solver, demonstrated that the cloaks can achieve perfect concealment of incoming incident waves with very mild conditions on the incident frequency.

This chapter is organised as follows. In Section 2.1, we study the ideal circular cylindrical cloak. We start with formulating the governing equation including CBCs and DtN non-reflecting boundary conditions, and then show that the field in the cloaked region vanishes. Finally, we describe the FLSEM for numerical simulations. In Section 2.2, we focus on the mathematical and numerical study of the elliptic cylindrical cloak. In Section 2.3, we provide numerous simulation results to demonstrate the perfectness of the ideal cloaks based on our proposed CBCs and numerical solvers.

2.1 Circular cylindrical cloaks

In this section, we formulate the problem that models the ideal circular cylindrical cloak and describe the FLSEM for its numerical simulation. We put the emphasis on the imposition of CBCs.

2.1.1 Governing equation

Recall that the material parameters of the circular cloak associated with the coordinate transformation (1.10) is given in (1.16). It is free to set any values for the permeability and permittivity in the cloaked region: $r < R_1$. Without loss of generality (cf. [5]), we set $\boldsymbol{\epsilon} = \boldsymbol{\mu} = \boldsymbol{I}_3$ for $r < R_1$.

In what follows, we consider the transverse-electric polarised electromagnetic field, that is, the electrical field only exists in the z direction: $\boldsymbol{E} = (0, 0, u)^t$. Then by the first equation of (1.2), we have

$$\boldsymbol{H} = \frac{1}{\mathrm{i}\omega\mu_0} \begin{cases} \Big(\dfrac{1}{r - R_1}\dfrac{\partial u}{\partial \theta}, -\dfrac{r - R_1}{r}\dfrac{\partial u}{\partial r}, 0\Big)^t, & \text{if} \quad R_1 < r < R_2, \\ \Big(\dfrac{1}{r}\dfrac{\partial u}{\partial \theta}, -\dfrac{\partial u}{\partial r}, 0\Big)^t, & \text{if} \quad r < R_1 \quad \text{or} \quad r > R_2. \end{cases} \tag{2.1}$$

Eliminating $\boldsymbol{H}$ from the Maxwell's equations (1.2), we obtain the two-dimensional Helmholtz equations in polar coordinates:

$$\mathcal{L}_0[u] := \frac{1}{r}\frac{\partial}{\partial r}\Big(r\frac{\partial u}{\partial r}\Big) + \frac{1}{r^2}\frac{\partial^2 u}{\partial \theta^2} + k^2 u = 0, \qquad \text{if} \quad r < R_1 \quad \text{or} \quad r > R_2; \tag{2.2}$$

$$\mathcal{L}_1[u] = 0, \quad \text{if} \quad R_1 < r < R_2, \tag{2.3}$$

for all $\theta \in [0, 2\pi)$, where $b = R_2/(R_2 - R_1)$ and

$$\mathcal{L}_1[u] := \frac{1}{r - R_1}\frac{\partial}{\partial r}\Big((r - R_1)\frac{\partial u}{\partial r}\Big) + \frac{1}{(r - R_1)^2}\frac{\partial^2 u}{\partial \theta^2} + k^2 b^2 u. \tag{2.4}$$

The Sommerfeld radiation boundary condition (1.18b) is imposed for the scattering wave u_{sc} (see Figure 1.2).

2.1.2 Exact DtN boundary condition

We now consider the boundary and transmission conditions to achieve perfect cloaking.

Starting with the outmost, we adopt the domain truncation by imposing an artificial boundary condition at $r = R_3 > R_2$ using the exact Dirichlet-to-Neumann (DtN) technique (see, e.g., [56, 3]):

$$\partial_r u_{\rm sc} - T_{R_3} u_{\rm sc} = 0 \quad \text{at} \quad r = R_3, \tag{2.5}$$

where the DtN map T_{R_3} is defined as

$$T_{R_3}[\psi] = \sum_{|m|=0}^{\infty} \mathcal{T}_m \hat{\psi}_m e^{{\rm i}m\theta}, \quad \text{with} \tag{2.6}$$

$$\hat{\psi}_m = \frac{1}{2\pi}\int_0^{2\pi} \psi(R_3,\theta) e^{-{\rm i}m\theta}{\rm d}\theta, \quad \mathcal{T}_m := \frac{kH_m^{(1)\prime}(kR_3)}{H_m^{(1)}(kR_3)}. \tag{2.7}$$

Here, $H_m^{(1)}(z)$ is the Hankel function of the first kind (cf. [87]). This yields the exact artificial boundary conditions of the total field u:

$$\partial_r u - T_{R_3} u = \partial_r u_{\rm in} - T_{R_3} u_{\rm in} := h \quad \text{at} \;\; r = R_3. \tag{2.8}$$

Remark 2.1. *The exact DtN boundary condition is global in the physical space (due to the involvement of a Fourier series), but it is local in the expansion coefficient space. Given the geometry of the cloak, we can fully take this advantage in both simulation and analysis.* □

2.1.3 Transmission conditions and CBCs

For clarity of exposition, let us denote

$$R_0 = 0; \quad I_i = (R_i, R_{i+1}), \quad \Omega_i = I_i \times [0, 2\pi), \quad i = 0, 1, 2; \quad \Omega = \bigcup_{i=0}^{2} \Omega_i. \tag{2.9}$$

Correspondingly, we define

$$\boldsymbol{H}^i = \boldsymbol{H}|_{\Omega_i}, \quad \boldsymbol{E}^i = \boldsymbol{E}|_{\Omega_i}, \quad u^i = u|_{I_i}, \quad i = 0, 1, 2. \tag{2.10}$$

The conditions at the material interface $r = R_2$ are the standard transmission conditions, that is, the tangential components of $\boldsymbol{E}$ and $\boldsymbol{H}$ are continuous across the interface (see, e.g., [28, Sec. 1.5] and [35]):

$$\boldsymbol{n} \times (\boldsymbol{E}^1 - \boldsymbol{E}^2) = \boldsymbol{0}, \quad \boldsymbol{n} \times (\boldsymbol{H}^1 - \boldsymbol{H}^2) = \boldsymbol{0} \quad \text{at} \quad r = R_2, \tag{2.11}$$

where $\boldsymbol{n}$ is the unit out normal vector. A direct calculation from (2.1), leads to

$$u^1 - u^2 = 0, \quad b^{-1}\partial_r u^1 - \partial_r u^2 = 0 \quad \text{at} \quad r = R_2. \tag{2.12}$$

As mentioned in Section 1.3, how to impose suitable conditions so that there is no wave propagating into the cloaked region, appears unsettled. The analysis in Ruan et al. [60] implies that

$$\boldsymbol{E}^1 \neq \boldsymbol{0}, \quad \boldsymbol{n} \times (\boldsymbol{E}^0 - \boldsymbol{E}^1) \neq \boldsymbol{0} \quad \text{at} \quad r = R_1, \tag{2.13}$$

while the tangential component is continuous across the inner boundary, namely,

$$\boldsymbol{n} \times (\boldsymbol{H}^0 - \boldsymbol{H}^1) = \boldsymbol{0} \quad \text{at} \quad r = R_1. \tag{2.14}$$

Zhang et al. [61] demonstrates that the exotic physical effect (2.13) is attributed to the surface current induced by the singular transformation.

We find from (2.1) and (2.14) that

$$\lim_{r \to R_1} \Big(\partial_r u^0 - \frac{r - R_1}{r} \partial_r u^1 \Big) = 0, \tag{2.15}$$

which implies

$$\partial_r u^0(R_1, \theta) = 0, \quad \partial_r u^1(R_1, \theta) \ \text{ is finite.} \tag{2.16}$$

Remark 2.2. *To shield the wave from propagating into the cloaked region, the PMC condition (i.e.,* $\boldsymbol{n} \times \boldsymbol{H}^1 = \boldsymbol{0}$*), is imposed in many simulations in Cartesian coordinates (see, e.g., [37, 61, 63]). Unfortunately, we infer from* (2.16) *that in the polar coordinates, the* PMC *condition (equivalent to* $\partial_r u^1(R_1, \theta)$ *being finite) does not lead to an independent condition.* □

At this point, one condition is lacking at the inner boundary. Our viewpoint is that the electromagnetic fields in the original coordinates must still be finite after the coordinate transformation. Therefore, letting $r \to R_1^+$ in (2.1) yields

$$\frac{\partial u^1}{\partial \theta}(R_1, \theta) = 0, \quad \theta \in [0, 2\pi). \tag{2.17}$$

Alternatively, it can be derived from the transformed gradient:

$$\nabla u = \frac{1}{b}\Big(\frac{\partial u^1}{\partial r}, \frac{1}{r - R_1}\frac{\partial u^1}{\partial \theta}\Big)^t, \quad R_1 < r < R_2. \tag{2.18}$$

We reiterate that (2.17) is intimately related to the essential "pole condition" (EPC), associated with the polar transformation (singular at the origin). It is imposed based on the principle that the solution in the polar coordinates should have desired regularity, when it is transformed back to Cartesian coordinates (see, e.g., [45, 86]). As shown in [85, 47], the condition: $\partial_\theta u(0, \theta) = 0$ is *essential* for spectrally accurate computations. Indeed, such a notion can be extended to other singular transformations (see e.g., [88]). In this context, the transformation (1.10) spans the origin to the circle $r = R_1$, so the essential "pole" condition is transplanted to $r = R_1^+$.

The problem of interest is summarised as follows:

$$\mathcal{L}_0[u^0] = 0 \quad \text{in} \quad \Omega_0; \quad \partial_\theta u^0(0, \theta) = \partial_r u^0(R_1, \theta) = 0; \tag{2.19}$$

$$\mathcal{L}_1[u^1] = 0 \quad \text{in} \quad \Omega_1; \quad \partial_\theta u^1(R_1, \theta) = 0; \tag{2.20}$$

$$u^1 = u^2, \quad b^{-1}\partial_r u^1 = \partial_r u^2 \quad \text{at} \quad r = R_2, \tag{2.21}$$

$$\mathcal{L}_0[u^2] = 0 \quad \text{in} \quad \Omega_2; \quad \partial_r u^2 - T_{R_3} u^2 = g \quad \text{at} \quad r = R_3; \tag{2.22}$$

for all $\theta \in [0, 2\pi)$. Note that (i) the operators $\mathcal{L}_0$ and $\mathcal{L}_1$ are defined in (2.2)-(2.4); (ii) the EPC: $\partial_\theta u^0(0, \theta) = 0$ is imposed at the origin due to the singular polar transformation; and (iii) the source of the system is the incident wave in the data g (cf. (2.8)).

Remarkably, under the condition (2.15), the subproblem (2.19) is decoupled from (2.20)-(2.22). Moreover, we can show that $u^0 \equiv 0$ is the unique solution, if

the wave number k is not an eigenvalue of the Bessel operator with the boundary conditions in (2.23). Indeed, we write $u^0(r,\theta) = \sum_{|m|=0}^{\infty} \hat{u}_m^0(r)e^{\mathrm{i}m\theta}$. Then (2.19) is reduced to

$$\begin{aligned} &\frac{1}{r}\frac{d}{dr}\Big(r\frac{d\hat{u}_m^0}{dr}\Big) - \frac{m^2}{r^2}\hat{u}_m^0 + k^2\hat{u}_m^0 = 0, \quad 0 < r < R_1; \\ &\hat{u}_m^0(0) = 0, \quad \text{if} \quad m \neq 0; \quad \frac{d}{dr}\hat{u}_m^0(R_1) = 0, \quad m = 0, \pm 1, \cdots . \end{aligned} \tag{2.23}$$

We claim from the Sturm-Liouville theory of the Bessel operator (see, e.g., [89, 90]) the following conclusion.

Proposition 2.1. *If k is not an eigenvalue of the Bessel problem* (2.23)*, or equivalently, $J_m'(kR_1) \neq 0$ for any model m, then we have $\hat{u}_m^0 \equiv 0$ for every m, so the solution of* (2.19) *$u^0 \equiv 0$.*

We see that with a reasonable assumption on the frequency of the incident wave, the cloak can perfectly shield the waves from penetrating into the cloaked region.

2.1.4 Fourier-Legendre-spectral-element method

We next present an accurate and efficient numerical method for solving (2.20)-(2.22). Observe from (2.8) that the DtN boundary condition in (2.22) is global in the physical space, but it is local in the frequency space of Fourier expansion. It is therefore advantageous to use Fourier spectral approximation in θ-direction, and Legendre spectral-element method in r-direction.

We expand the solution and given data in Fourier series:

$$\big\{u^j(r,\theta), g(\theta)\big\} = \sum_{|m|=0}^{\infty} \big\{\hat{u}_m^j(r), \hat{g}_m\big\}e^{\mathrm{i}m\theta}, \quad j = 1, 2. \tag{2.24}$$

Then (2.20)-(2.22) reduce to a sequence of one-dimensional equations:

$$\frac{1}{r-R_1}\frac{d}{dr}\Big((r-R_1)\frac{d\hat{u}_m^1}{dr}\Big)-\frac{m^2}{(r-R_1)^2}\hat{u}_m^1+k^2b^2\hat{u}_m^1=0,\quad R_1<r<R_2; \tag{2.25}$$

$$\hat{u}_m^1(R_1)=0,\ \text{if } m\neq 0;\ \ \hat{u}_m^1(R_2)=\hat{u}_m^2(R_2),\ \ b^{-1}\frac{d}{dr}\hat{u}_m^1(R_2)=\frac{d}{dr}\hat{u}_m^2(R_2); \tag{2.26}$$

$$\frac{1}{r}\frac{d}{dr}\Big(r\frac{d\hat{u}_m^2}{dr}\Big)-\frac{m^2}{r^2}\hat{u}_m^2+k^2\hat{u}_m^2=0,\quad R_2<r<R_3; \tag{2.27}$$

$$\Big(\frac{d}{dr}-\mathcal{T}_{m,k}\Big)\hat{u}_m^2(R_3)=\hat{g}_m,\quad \text{where}\ \ \mathcal{T}_{m,k}:=\frac{kH_m^{(1)'}(kR_3)}{H_m^{(1)}(kR_3)}. \tag{2.28}$$

Note that the global DtN boundary condition is decoupled for each mode m, and by the property of the Hankel function, we have $\mathcal{T}_{-m,k}=\mathcal{T}_{m,k}$ (see [77, (2.32)]).

Hereafter, let $\Lambda=(a,b)$ and $\varpi(x)>0$ be a generic weight function on Λ, which is absolutely integrable. Let $H^s_\varpi(\Lambda)$ be the weighted Sobolev space as defined in Admas [1]. In particular, $L^2_\varpi(\Lambda)=H^0_\varpi(\Lambda)$ with the inner product $(\cdot,\cdot)_\varpi$ and norm $\|\cdot\|_\varpi$. We drop the weight function, whenever $\varpi=1$.

Let $I_1=(R_1,R_2)$ and $I_2=(R_2,R_3)$ as before, and let $I=(R_1,R_3)$. Define the weight function ω and the piecewise constant function ρ:

$$\omega(r)=\begin{cases} r-R_1, & \text{if}\ \ r\in I_1,\\ r, & \text{if}\ \ r\in I_2,\end{cases}\qquad \rho=\begin{cases} b^2, & \text{if}\ \ r\in I_1,\\ 1, & \text{if}\ \ r\in I_2.\end{cases} \tag{2.29}$$

Recall that $b=R_2/(R_2-R_1)$ as defined in (2.4). Introduce the space

$$Y_m(I):=\big\{u\in H^1_\omega(I)\cap L^2_{\omega^{-1}}(I)\ :\ u(R_1)=0\big\},\ \text{if } m\neq 0;\ \ Y_0(I)=H^1_\omega(I). \tag{2.30}$$

Note that the functions in $Y_m(I)$ are continuous, while the weight function ω is not continuous, across the material interface $r=R_2$. The weak form of (2.25)-(2.28) is to find $\hat{u}_m\in Y_m(I)$ for each mode m, such that

$$\begin{aligned}\mathcal{B}_m(\hat{u}_m,v):=&(\hat{u}_m',v')_\omega+m^2(\hat{u}_m,v)_{\omega^{-1}}-k^2(\rho\hat{u}_m,v)_\omega\\ &-R_3\mathcal{T}_{m,k}\,\hat{u}_m(R_3)\bar{v}(R_3)=R_3\hat{g}_m\bar{v}(R_3),\quad \forall v\in Y_m(I),\end{aligned} \tag{2.31}$$

where $\bar{v}$ is the complex conjugate of v. We show the following proposition on the well-posedness of (2.31).

Proposition 2.2. *For each mode m, the problem* (2.31) *has a unique solution* $\hat{u}_m \in Y_m(I)$.

Proof. It is clear that by (2.31),

$$\mathrm{Re}\big\{\mathcal{B}_m(\hat{u}_m,\hat{u}_m)\big\} = \|\hat{u}_m'\|_\omega^2 + m^2\|\hat{u}_m\|_{\omega^{-1}}^2 - k^2\|\rho\hat{u}_m\|_\omega^2 - R_3\,\mathrm{Re}(\mathcal{T}_{m,k})|\hat{u}_m(R_3)|^2,$$

and

$$\mathrm{Im}\big\{\mathcal{B}_m(\hat{u}_m,\hat{u}_m)\big\} = -R_3\,\mathrm{Im}(\mathcal{T}_{m,k})|\hat{u}_m(R_3)|^2.$$

Recall that (see, e.g., [3, 77]):

$$\mathrm{Re}(\mathcal{T}_{m,k}) < 0, \quad \mathrm{Im}(\mathcal{T}_{m,k}) > 0.$$

Thus, we have

$$\mathrm{Re}\big\{\mathcal{B}_m(\hat{u}_m,\hat{u}_m)\big\} \geq \|\hat{u}_m'\|_\omega^2 + m^2\|\hat{u}_m\|_{\omega^{-1}}^2 - k^2\|\rho\hat{u}_m\|_\omega^2,$$

and $\hat{u}_m(R_3) = 0$, if $\hat{g}_m = 0$. Using the Fredholm alternative (cf. [3, Thm. 5.4.5]), we reach the conclusion. □

We now discuss the numerical solution of (2.31). Let $\mathbb{P}_N$ be the complex-valued polynomials of degree at most N, and let $\boldsymbol{N} = (N_1, N_2)$. We introduce the approximation space:

$$Y_m^{\boldsymbol{N}}(I) = \big\{u \in Y_m(I) \,:\, u|_{I_i} \in \mathbb{P}_{N_i}, \quad i = 1,2\big\}, \tag{2.32}$$

where the functions are continuous across $r = R_2$ (cf. (2.26)). Given a cut-off number $M > 0$, the FLSEM approximation to the solution of (2.20)-(2.22) is

$$u_M^{\boldsymbol{N}}(r,\theta) = \sum_{|m|=0}^{M} \hat{u}_m^{\boldsymbol{N}}(r)e^{\mathrm{i}m\theta}, \tag{2.33}$$

where $\{\hat{u}_m^{\boldsymbol{N}}\}$ are computed from the Legendre-spectral-element approximation to (2.31), that is, find $\hat{u}_m^{\boldsymbol{N}} \in Y_m^{\boldsymbol{N}}(I)$ such that

$$\mathcal{B}_m(\hat{u}_m^{\boldsymbol{N}}, v) = R_3\hat{g}_m\bar{v}(R_3), \quad \forall v \in Y_m^{\boldsymbol{N}}(I), \quad 0 \leq |m| \leq M. \tag{2.34}$$

Remark 2.3. *We can apply the same argument as for Proposition* 2.2 *to show that* (2.34) *admits a unique solution in* $Y_m^{\boldsymbol{N}}(I)$. □

For each mode m, the two-domain spectral-element scheme (2.34) can be implemented efficiently by using the modal Legendre polynomial basis and the Schur complement technique (cf. [91]). Here, we omit the details. We provide in Section 2.3 ample numerical results to demonstrate that our proposed CBCs and FLSEM leads to accurate simulations of the ideal circular cylindrical cloak.

2.2 Elliptic cylindrical cloaks

The elliptic cylindrical cloaks have been much less studied (see, e.g., [20, 21, 19]), compared with intensive investigations of the circular cylindrical cloaks. Though it is straightforward to extend the coordinate transformation in [5] to the elliptic case, the coordinate transformation possesses quite different nature of singularity. Thus, much care is needed to impose CBCs, as to be shown shortly.

2.2.1 Elliptic coordinates and Mathieu functions

To formulate the problem and algorithm, we briefly review the elliptic coordinates and the related angular and radial Mathieu functions. The elliptic coordinates (ξ, η) are related to the Cartesian coordinates $\boldsymbol{x} = (x, y)$ by

$$x = a\cosh\xi\cos\eta, \quad y = a\sinh\xi\sin\eta, \quad a > 0, \tag{2.35}$$

where $\xi \in [0, \infty)$ and $\eta \in [0, 2\pi)$. The coordinate lines are confocal ellipses (of constant ξ) and hyperbolae (of constant η) with foci fixed at $-a$ and a on the x-axis. The scale factors and the Jacobian of the elliptic coordinate system are

$$h = h_\xi = h_\eta = a\sqrt{\cosh^2\xi - \cos^2\eta}, \quad J = h_\xi h_\eta = h^2. \tag{2.36}$$

The (angular) Mathieu equation reads (cf. [87]):

$$\frac{d^2\Phi}{d\eta^2} + (\lambda - 2q\cos 2\eta)\Phi = 0 \quad \text{with} \quad q = \frac{a^2k^2}{4}, \tag{2.37}$$

where λ is the separation constant. The angular Mathieu equation (2.37) supplemented with periodic boundary conditions admits a countable set of eigen-pairs:

$$\big\{\lambda_m^{\rm c}(q),\ {\rm ce}_m(\eta;q)\big\}_{m=0}^{\infty},\quad \big\{\lambda_m^{\rm s}(q),\ {\rm se}_m(\eta;q)\big\}_{m=1}^{\infty}. \tag{2.38}$$

Note that the symbols "ce" and "se", abbreviation of "cosine-elliptic" and "sine-elliptic", were first introduced in [92]. To facilitate the analysis afterwards, let us denote

$$\tilde\lambda_m^{\rm c}(q) := \lambda_m^{\rm c}(q) + 2q,\quad \tilde\lambda_m^{\rm s}(q) := \lambda_m^{\rm s}(q) + 2q. \tag{2.39}$$

Then for any fixed $q > 0$, from the standard Sturm-Liouville theory (cf. [89]), the eigenvalues are in order of

$$0 < \tilde\lambda_0^{\rm c}(q) < \tilde\lambda_1^{\rm s}(q) < \tilde\lambda_1^{\rm c}(q) < \cdots < \tilde\lambda_m^{\rm s}(q) < \tilde\lambda_m^{\rm c}(q) < \cdots. \tag{2.40}$$

When $q = 0$, the Mathieu functions reduce to the trigonometric functions:

$${\rm ce}_0(\eta;0) = \frac{1}{\sqrt{2}};\quad {\rm ce}_m(\eta;0) = \cos(m\eta),\quad {\rm se}_m(\eta;0) = \sin(m\eta),\quad m \ge 1, \tag{2.41}$$

and correspondingly, $\lambda_m^{\rm c}(0) = \lambda_m^{\rm s}(0) = m^2$. Indeed, the angular Mathieu functions share many properties with their conterparts: cosines and sines. For example, ${\rm ce}_m(\eta;q)$ is an even function in η, and ${\rm se}_m(\eta;q)$ is odd. They are π-periodic when m is even, and 2π-periodic when m is odd. Moreover, the set of Mathieu functions $\{{\rm ce}_m, {\rm se}_{m+1}\}_{m=0}^{\infty}$ forms a complete orthogonal system in $L^2(0,2\pi)$ (cf. [93, 87]):

$$\int_0^{2\pi} {\rm ce}_m\,{\rm ce}_n\,d\eta = \int_0^{2\pi} {\rm se}_m\,{\rm se}_n\,d\eta = \pi\delta_{mn};\quad \int_0^{2\pi} {\rm ce}_m\,{\rm se}_n\,d\eta = 0. \tag{2.42}$$

The radial (or modified) Mathieu equation (cf. [87]):

$$\frac{d^2\Psi}{d\xi^2} - (\lambda - 2q\cosh 2\xi)\Psi = 0, \tag{2.43}$$

plays an analogous role as the Bessel equation in the polar coordinates. Like the Bessel functions, there are several types of radial Mathieu functions, but each type has even and odd versions, quite different notation is used to denote such functions in literature [93, 87]. Here, we adopt the notation and conventions

in [87], where $\{\mathrm{Mc}_m^{(i)}; \mathrm{Ms}_m^{(i)}\}, i = 1, 2, 3, 4$, correspond to the Bessel functions: $J_m, Y_m, H_m^{(1)}, H_m^{(2)}$ in [2], respectively. In what follows, we just use the radial Mathieu functions of the first kind $\{\mathrm{Mc}_m^{(1)}(\xi; q); \mathrm{Ms}_m^{(1)}(\xi; q)\}$, and the Mathieu-Hankel functions: $\{\mathrm{Mc}_m^{(3)}(\xi; q); \mathrm{Ms}_m^{(3)}(\xi; q)\}$. Both types satisfy (2.43) with $\lambda = \lambda_m^{\mathrm{c}}$ and $\lambda = \lambda_m^{\mathrm{s}}$ for Mc_m and Ms_m, respectively.

2.2.2 Governing equation

Following the idea of Pendry et al. [5], a coordinate transformation, which compresses the elliptic region $0 \le \zeta < \xi_2$ into the elliptic annular region $0 < \xi_1 < \xi < \xi_2$, was extended to devise an elliptic cylindrical cloak (see e.g., [59, 19]):

$$\xi = \frac{\zeta}{d} + \xi_1, \quad \eta = \eta, \quad z = z \quad \text{with} \quad d = \frac{\xi_2}{\xi_2 - \xi_1}, \tag{2.44}$$

where (ζ, η, z) is the elliptic-cylindrical coordinates in the virtual space, and (ξ, η, z) is the coordinates of the physical space. This leads to the study of the time-harmonic Maxwell's equations in the physical space with new material parameters:

$$\boldsymbol{\epsilon} = \boldsymbol{\mu} = \mathrm{diag}(\epsilon_\xi, \epsilon_\eta, \epsilon_z), \quad \text{if} \quad \xi_1 < \xi < \xi_2; \quad \boldsymbol{\epsilon} = \boldsymbol{\mu} = \boldsymbol{I}_3, \quad \text{if} \quad \xi > \xi_2, \tag{2.45}$$

with the components in the cloaking layer (cf. [59]), given by

$$\epsilon_\xi = \mu_\xi = \frac{1}{d}, \quad \epsilon_\eta = \mu_\eta = d, \quad \epsilon_z = \mu_z = d\frac{\cosh^2(d(\xi - \xi_1)) - \cos^2\eta}{\cosh^2\xi - \cos^2\eta}. \tag{2.46}$$

Like before, we assume that the material parameters in the cloaked region are constants.

As with the circular case, we consider the transverse-electric polarised electromagnetic field with $\boldsymbol{E} = (0, 0, v)^t$. We solve $\boldsymbol{H}$ from the first equation of (1.2), and eliminate $\boldsymbol{H}$. Then we obtain the following Helmholtz equations, together with the exact DtN boundary at the outer ellipse $\xi = \xi_3 (> \xi_2)$, in elliptic coordinates:

$$\big(d^{-2}\partial_\xi^2+\partial_\eta^2\big)v+k^2a^2\big(\cosh^2(d(\xi-\xi_1))-\cos^2\eta\big)v=0 \quad \text{in } \Lambda_1; \tag{2.47a}$$

$$\big(\partial_\xi^2+\partial_\eta^2\big)v+k^2a^2\big(\cosh^2\xi-\cos^2\eta\big)v=0 \quad \text{in } \Lambda_0\cup\Lambda_2; \tag{2.47b}$$

$$(\partial_\xi-\mathbb{T}_{\xi_3})v=\phi \quad \text{at } \xi=\xi_3, \tag{2.47c}$$

where

$$k=\omega\sqrt{\varepsilon_0\mu_0}; \quad \Lambda_i:=(\xi_i,\xi_{i+1})\times[0,2\pi), \quad i=0,1,2 \quad \text{with} \quad \xi_0:=0,$$

and $\mathbb{T}_{\xi_3}$ is the DtN map (cf. [56, 94]), given by

$$\begin{aligned}\mathbb{T}_{\xi_3}v=&\sum_{m=0}^{\infty}\frac{\partial_\xi \mathrm{Mc}_m^{(3)}(\xi_3;q)}{\mathrm{Mc}_m^{(3)}(\xi_3;q)}\hat{v}_m^{\mathrm{c}}(\xi_3)\,\mathrm{ce}_m(\eta;q)\\&+\sum_{m=1}^{\infty}\frac{\partial_\xi \mathrm{Ms}_m^{(3)}(\xi_3;q)}{\mathrm{Ms}_m^{(3)}(\xi_3;q)}\hat{v}_m^{\mathrm{s}}(\xi_3)\,\mathrm{se}_m(\eta;q),\end{aligned} \tag{2.48}$$

with

$$\hat{v}_m^{\mathrm{c}}(\xi_3)=\frac{1}{\pi}\int_0^{2\pi}v(\xi_3,\eta)\,\mathrm{ce}_m(\eta;q)\,d\eta, \quad \hat{v}_m^{\mathrm{s}}(\xi_3)=\frac{1}{\pi}\int_0^{2\pi}v(\xi_3,\eta)\,\mathrm{se}_m(\eta;q)\,d\eta.$$

Note that in (2.47c), ϕ is induced by the incident wave, i.e., $\phi=(\partial_\xi-\mathbb{T}_{\xi_3})v_{\mathrm{in}}$.

Naturally, we impose continuity of the tangential components of $\boldsymbol{E}$ and $\boldsymbol{H}$ across the elliptic interface $\xi=\xi_2$, leading to the transmission conditions as with (2.12):

$$v^1=v^2, \quad d^{-1}\partial_\xi v^1=\partial_\xi v^2, \quad \text{at } \xi=\xi_2, \tag{2.49}$$

where for clarity, we denote $v^i=v|_{\Lambda_i}$ for $i=0,1,2$.

The critical issue is the imposition of CBCs at the inner boundary $\xi=\xi_1$. To tackle this, we decompose the solution and data into ce- and se-components as follows:

$$\begin{aligned}\big\{v;\,\phi\big\}&=\sum_{m=0}^{\infty}\big\{\hat{v}_m^{\mathrm{c}}(\xi);\,\hat{\phi}_m^{\mathrm{c}}\big\}\mathrm{ce}_m(\eta;q)+\sum_{m=1}^{\infty}\big\{\hat{v}_m^{\mathrm{s}}(\xi);\,\hat{\phi}_m^{\mathrm{s}}\big\}\mathrm{se}_m(\eta;q)\\&:=\big\{v_{\mathrm{ce}};\,\phi_{\mathrm{ce}}\big\}+\big\{v_{\mathrm{se}};\,\phi_{\mathrm{se}}\big\}.\end{aligned} \tag{2.50}$$

Correspondingly, the polarized $\boldsymbol{E}$ and $\boldsymbol{H}$ fields are split into two components: $\boldsymbol{E} = \boldsymbol{E}_{\rm ce} + \boldsymbol{E}_{\rm se}$ and $\boldsymbol{H} = \boldsymbol{H}_{\rm ce} + \boldsymbol{H}_{\rm se}$. Following the analytic study in [19] and the δ-perturbation analysis in [60], it is necessary to require the tangential component of $\boldsymbol{H}_{\rm ce}$ and $\boldsymbol{E}_{\rm se}$ continuous across the inner boundary $\xi = \xi_1$, leading to

$$v^0_{\rm se} = v^1_{\rm se}, \quad d^{-1}\partial_\xi v^0_{\rm ce} = \partial_\xi v^1_{\rm ce} \quad \text{at} \ \ \xi = \xi_1. \tag{2.51}$$

Nevertheless, we are short of one condition for each component. Similar to (2.18), we have

$$\nabla v = \frac{1}{a\sqrt{\cosh^2(d(\xi-\xi_1)) - \cos^2\eta}}\Big(\frac{1}{d}\frac{\partial v^1}{\partial \xi}, \frac{\partial v^1}{\partial \eta}\Big)^t, \quad \xi_1 < \xi < \xi_2. \tag{2.52}$$

We see that the singularity of the transformation (2.44) only occurs at two points $(\xi_1, 0)$ and (ξ_1, π). Thus, taking the limit $\xi \to \xi_1^+$, leads to the analogue of the essential "pole" conditions in elliptic coordinates:

$$\partial_\xi v^1(\xi_1, 0) = \partial_\xi v^1(\xi_1, \pi) = 0, \quad \partial_\eta v^1(\xi_1, 0) = \partial_\eta v^1(\xi_1, \pi) = 0. \tag{2.53}$$

Using the property (cf. [87]):

$$\mathrm{ce}'_m(0; q) = \mathrm{ce}'_m(\pi; q) = 0, \quad \mathrm{se}_m(0; q) = \mathrm{se}_m(\pi; q) = 0, \tag{2.54}$$

we find from (2.50) that (2.53) is equivalent to

$$\partial_\xi v^1_{\rm ce}(\xi_1, 0) = 0, \quad v^1_{\rm se}(\xi_1, 0) = 0. \tag{2.55}$$

We summarize the problem that models the ideal elliptic cylindrical cloak: given $\phi = \phi_{\rm ce} + \phi_{\rm se}$, find

$$v = v_{\rm ce} + v_{\rm se} \ \ \text{with} \ \ v^i = v^i_{\rm ce} + v^i_{\rm se} = (v_{\rm ce} + v_{\rm se})|_{\Lambda_i}, \quad i = 0, 1, 2, \tag{2.56}$$

satisfying the following systems.

(i) For the ce-component in the cloaked region Λ_0:

$$\big(\partial^2_\xi + \partial^2_\eta\big)v^0_{\rm ce} + k^2a^2\big(\cosh^2\xi - \cos^2\eta\big)v^0_{\rm ce} = 0, \quad 0 < \xi < \xi_1; \tag{2.57}$$

$$\partial_\xi v^0_{\rm ce}(0, 0) = \partial_\xi v^0_{\rm ce}(\xi_1, 0) = 0. \tag{2.58}$$

Note that the essential pole condition at the origin is necessary, while $\partial_\xi v^0_{\rm ce}(\xi_1, 0) = 0$ is derived from the second condition in (2.51) and (2.55).

(ii) For the ce-component in $\Lambda_1 \cup \Lambda_2$:

$$\big(d^{-2}\partial_\xi^2 + \partial_\eta^2\big)v_{\rm ce}^1 + k^2a^2\big(\cosh^2(d(\xi-\xi_1)) - \cos^2\eta\big)v_{\rm ce}^1 = 0 \ \text{ in } \Lambda_1; \quad (2.59a)$$

$$\partial_\xi v_{\rm ce}^1(\xi_1, 0) = 0; \qquad v_{\rm ce}^1 = v_{\rm ce}^2, \quad d^{-1}\partial_\xi v_{\rm ce}^1 = \partial_\xi v_{\rm ce}^2 \qquad \text{at} \quad \xi = \xi_2; \quad (2.59b)$$

$$\big(\partial_\xi^2 + \partial_\eta^2\big)v_{\rm ce}^2 + k^2a^2\big(\cosh^2\xi - \cos^2\eta\big)v_{\rm ce}^2 = 0 \qquad \text{in} \quad \Lambda_2, \quad (2.59c)$$

$$(\partial_\xi - \mathbb{T}_{\xi_3})v_{\rm ce}^2 = \phi_{\rm ce} \qquad \text{at} \quad \xi = \xi_3. \quad (2.59d)$$

(iii) The se-component $v_{\rm se}$ satisfies the same equations in (i)-(ii) with $v_{\rm se}^i$ and $\phi_{\rm se}$ in place of $v_{\rm ce}^i$ and $\phi_{\rm ce}$, respectively, while (2.58) and the first condition in (2.59b) are respectively replaced by

$$v_{\rm se}^0(0,0) = v_{\rm se}^0(\xi_1, 0) = 0; \quad v_{\rm se}^1(\xi_1, 0) = 0. \quad (2.60)$$

We see that $v_{\rm ce}^0$ and $v_{\rm se}^0$ are decoupled from $v_{\rm ce}^i$ and $v_{\rm se}^i$, $i = 1, 2$. Indeed, using (2.37) and the expansion (2.50), the problem (2.57)-(2.58) reduces to

$$(\hat{v}_m^{\rm c})''(\xi) - \big(\lambda_m^{\rm c} - 2q\cosh(2\xi)\big)\,\hat{v}_m^{\rm c}(\xi) = 0, \quad 0 < \xi < \xi_1, \quad (2.61)$$

$$(\hat{v}_m^{\rm c})'(0) = (\hat{v}_m^{\rm c})'(\xi_1) = 0, \quad (2.62)$$

and similarly, we have

$$(\hat{v}_m^{\rm s})''(\xi) - \big(\lambda_m^{\rm s} - 2q\cosh(2\xi)\big)\,\hat{v}_m^{\rm s}(\xi) = 0, \quad 0 < \xi < \xi_1, \quad (2.63)$$

$$\hat{v}_m^{\rm s}(0) = \hat{v}_m^{\rm s}(\xi_1) = 0. \quad (2.64)$$

Similar to Proposition 2.1, one deduces the following conclusions from the standard theory of ordinary differential equations (cf. [89, 90]) and also from the properties of Mathieu functions (cf. [87]).

Proposition 2.3. *If k and ξ_1 are chosen such that $\mathrm{Mc}_m^{(1)\prime}(k\xi_1) \neq 0$ and $\mathrm{Ms}_m^{(1)}(k\xi_1) \neq 0$ for any mode m, then we have $\hat{v}_m^{\rm c} = \hat{v}_m^{\rm s} \equiv 0$ for every m, so both the problem (2.57)-(2.58) and the problem of* se*-component in Λ_0 with (2.60) have only trivial solutions in the cloaked region.*

2.2.3 Mathieu-Legendre-spectral-element method

In what follows, we present an accurate and efficient numerical algorithm to simulate the ideal elliptic cylindrical cloak.

Using the Mathieu expansion in η-direction (see (2.50)), we obtain the system of the ce-component in $\Lambda_1 \cup \Lambda_2$:

$$-d^{-2}(\hat{v}_m^{\rm c})''(\xi) + \big(\tilde{\lambda}_m^{\rm c} - 4q\cosh^2(d(\xi-\xi_1))\big)\hat{v}_m^{\rm c} = 0, \quad \xi_1 < \xi < \xi_2; \tag{2.65a}$$

$$(\hat{v}_m^{\rm c})'(\xi_1) = 0; \quad \hat{v}_m^{\rm c}(\xi_2^-) = \hat{v}_m^{\rm c}(\xi_2^+), \quad d^{-1}(\hat{v}_m^{\rm c})'(\xi_2^-) = (\hat{v}_m^{\rm c})'(\xi_2^+); \tag{2.65b}$$

$$-(\hat{v}_m^{\rm c})''(\xi) + \big(\tilde{\lambda}_m^{\rm c} - 4q\cosh^2(\xi)\big)\hat{v}_m^{\rm c}(\xi) = 0, \quad \xi_2 < \xi < \xi_3; \tag{2.65c}$$

$$\Big(\frac{d}{d\xi} - \mathcal{D}_m^{\rm c}\Big)\hat{v}_m^{\rm c}(\xi_3) = \hat{\phi}_m^{\rm c}, \quad \text{where} \;\; \mathcal{D}_m^{\rm c} := \frac{{\rm Mc}_m^{(3)\prime}(\xi_3;q)}{{\rm Mc}_m^{(3)}(\xi_3;q)}. \tag{2.65d}$$

Recall that $\tilde{\lambda}_m^{\rm c} := \lambda_m^{\rm c} + 2q > 0$ (see (2.39)). The se-component satisfies the same system with $\hat{v}_m^{\rm s}$, $\hat{\phi}_m^{\rm s}$ and $\tilde{\lambda}_m^{\rm s}$ in place of $\hat{v}_m^{\rm c}$, $\hat{\phi}_m^{\rm c}$ and $\tilde{\lambda}_m^{\rm c}$ in (2.65), respectively, while the first condition in (2.65b) and $\mathcal{D}_m^{\rm c}$ in (2.65d), are respectively replaced by

$$\hat{v}_m^{\rm s}(\xi_1) = 0, \quad \mathcal{D}_m^{\rm s} := \frac{{\rm Ms}_m^{(3)\prime}(\xi_3;q)}{{\rm Ms}_m^{(3)}(\xi_3;q)}, \quad m \geq 1. \tag{2.66}$$

With a little abuse of notation, we still denote $I_1 = (\xi_1, \xi_2)$, $I_2 = (\xi_2, \xi_3)$, and $I = (\xi_1, \xi_3)$. To formulate the problem into a compact form (see (2.68) below), we introduce the piecewise functions:

$$\varpi = \begin{cases} d^{-1}, & \text{if} \;\; \xi \in I_1, \\ 1, & \text{if} \;\; \xi \in I_2, \end{cases} \qquad \chi = \begin{cases} \cosh^2(d(\xi-\xi_1)), & \text{if} \;\; \xi \in I_1, \\ \cosh^2\xi, & \text{if} \;\; \xi \in I_2. \end{cases} \tag{2.67}$$

Recall that $d = \xi_2/(\xi_2 - \xi_1)$ defined in (2.44). Apparently, these two functions are uniformly bounded.

The weak form of (2.65) is to find $\hat{v}_m^{\rm c} \in H^1(I)$ for each mode m, such that

$$\begin{aligned} \mathcal{B}_m^{\rm c}(\hat{v}_m^{\rm c}, \psi) := {} & (\varpi(\hat{v}_m^{\rm c})', \psi') + \tilde{\lambda}_m^{\rm c}(\varpi^{-1}\hat{v}_m^{\rm c}, \psi) - 4q(\varpi^{-1}\chi\hat{v}_m^{\rm c}, \psi) \\ & - \mathcal{D}_m^{\rm c}\hat{v}_m^{\rm c}(\xi_3)\bar{\psi}(\xi_3) = \hat{\phi}_m^{\rm c}\bar{\psi}(\xi_3), \quad \forall \psi \in H^1(I), \quad m = 0, 1, \cdots. \end{aligned} \tag{2.68}$$

Similarly, the weak form of the se-component is to find $\hat{v}_m^{\rm s} \in {}_0H^1(I) := \{v \in H^1(I) \,:\, v(\xi_1) = 0\}$ for each mode m, such that

$$\mathcal{B}_m^{\rm s}(\hat{v}_m^{\rm s}, \psi) = \hat{\phi}_m^{\rm s}\bar{\psi}(\xi_3), \quad \forall \psi \in {}_0H^1(I), \quad m = 1, 2, \cdots, \tag{2.69}$$

where the bilinear form $\mathcal{B}_m^{\rm s}(\cdot,\cdot)$ is defined by replacing $\tilde{\lambda}_m^{\rm c}$ and $\mathcal{D}_m^{\rm c}$ in $\mathcal{B}_m^{\rm c}(\cdot,\cdot)$ by $\tilde{\lambda}_m^{\rm s}$ and $\mathcal{D}_m^{\rm s}$, respectively.

Like Proposition 2.2, we next show the unique solvability of (2.68) and (2.69).

Proposition 2.4. *For each mode m, the problem* (2.68) (*resp.* (2.69)) *has a unique solution $\hat{v}_m^{\rm c} \in H^1(I)$ (resp. $\hat{v}_m^{\rm s} \in {}_0H^1(I)$).*

Proof. For simplicity, denote

$$\mathrm{M}_m^{(i)} = \mathrm{Mc}_m^{(i)} \ \text{ or } \ \mathrm{Ms}_m^{(i)}, \quad i = 1, 2, 3; \quad \mathcal{D}_m = \mathcal{D}_m^{\rm c} \ \text{ or } \ \mathcal{D}_m^{\rm s}.$$

Recall that (see e.g., [87])

$$\mathrm{M}_m^{(3)} := \mathrm{M}_m^{(1)} + \mathrm{i}\mathrm{M}_m^{(2)}; \quad \mathrm{M}_m^{(1)}\mathrm{M}_m^{(2)\prime} - \mathrm{M}_m^{(2)}\mathrm{M}_m^{(1)\prime} = \frac{2}{\pi}\,. \tag{2.70}$$

Then a direct calculation from (2.66) and (2.70) leads to

$$\begin{aligned} \mathrm{Im}(\mathcal{D}_m) &= \frac{\mathrm{M}_m^{(1)}(\xi_3; q)\mathrm{M}_m^{(2)\prime}(\xi_3; q) - \mathrm{M}_m^{(2)}(\xi_3; q)\mathrm{M}_m^{(1)\prime}(\xi_3; q)}{|\mathrm{M}_m^{(3)}(\xi_3; q)|^2} \\ &= \frac{2/\pi}{|\mathrm{M}_m^{(3)}(\xi_3; q)|^2} > 0. \end{aligned} \tag{2.71}$$

Moreover, by (2.65d),

$$\mathrm{Re}(\mathcal{D}_m) = \frac{\mathrm{M}_m^{(1)}(\xi_3; q)\mathrm{M}_m^{(1)\prime}(\xi_3; q) + \mathrm{M}_m^{(2)}(\xi_3; q)\mathrm{M}_m^{(2)\prime}(\xi_3; q)}{|\mathrm{M}_m^{(3)}(\xi_3; q)|^2}. \tag{2.72}$$

Note that $\{\mathrm{M}_m^{(i)}(\xi; q)\}_{i=1}^2$ can not have common zero, and are analytic for all $\xi > 0$ (see, e.g., [87]), so $|\mathrm{Re}(\mathcal{D}_m)|$ is a finite constant for fixed m, q and ξ_3. To this end, let C be a generic positive constant depending on m, q, ξ_2 and ξ_3.

We first consider (2.68) and obtain that

$$\begin{aligned} \mathrm{Re}\big\{\mathcal{B}_m^{\rm c}(\hat{v}_m^{\rm c}, \hat{v}_m^{\rm c})\big\} &= \|\varpi(\hat{v}_m^{\rm c})'\|^2 + \tilde{\lambda}_m^{\rm c}\|\varpi^{-1}\hat{v}_m^{\rm c}\|^2 \\ &\quad - 4q\|\varpi^{-1}\chi\hat{v}_m^{\rm c}\|^2 - \mathrm{Re}(\mathcal{D}_m^{\rm c})|\hat{v}_m^{\rm c}(\xi_3)|^2, \end{aligned} \tag{2.73}$$

and

$$\mathrm{Im}\big\{\mathcal{B}_m^{\mathrm{c}}(\hat{v}_m^{\mathrm{c}}, \hat{v}_m^{\mathrm{c}})\big\} = -\mathrm{Im}(\mathcal{D}_m^{\mathrm{c}})|\hat{v}_m^{\mathrm{c}}(\xi_3)|^2. \tag{2.74}$$

Let $I_2 = (\xi_2, \xi_3)$ as before. Recall the Sobolev inequality (see, e.g., [47, (B.33)]): for any $w \in H^1(I_2)$,

$$\max_{x\in\bar{I}_2} |w(x)|^2 \le \Big(\frac{1}{\xi_3 - \xi_2} + 2\Big)\|w\|_{L^2(I_2)}\|w\|_{H^1(I_2)}. \tag{2.75}$$

Therefore, we further derive from the Cauchy-Schwartz inequality that

$$\begin{aligned} |\mathrm{Re}(\mathcal{D}_m^{\mathrm{c}})||\hat{v}_m^{\mathrm{c}}(\xi_3)|^2 &\le C\big(\|\varpi(\hat{v}_m^{\mathrm{c}})'\|^2 + \|\chi\hat{v}_m^{\mathrm{c}}\|^2\big)^{1/2}\|\chi\hat{v}_m^{\mathrm{c}}\| \\ &\le C\big(\|\varpi(\hat{v}_m^{\mathrm{c}})'\|\|\chi\hat{v}_m^{\mathrm{c}}\| + \|\chi\hat{v}_m^{\mathrm{c}}\|^2\big) \le \frac{1}{2}\|\varpi(\hat{v}_m^{\mathrm{c}})'\|^2 + C\|\chi\hat{v}_m^{\mathrm{c}}\|^2. \end{aligned} \tag{2.76}$$

Therefore, by (2.73) and (2.76),

$$\mathrm{Re}\big\{\mathcal{B}_m^{\mathrm{c}}(\hat{v}_m^{\mathrm{c}}, \hat{v}_m^{\mathrm{c}})\big\} \ge \frac{1}{2}\|\varpi(\hat{v}_m^{\mathrm{c}})'\|^2 + \tilde{\lambda}_m^{\mathrm{c}}\|\varpi^{-1}\hat{v}_m^{\mathrm{c}}\|^2 - (4q + C)\|\varpi^{-1}\chi\hat{v}_m^{\mathrm{c}}\|^2. \tag{2.77}$$

Moreover, by (2.71), $\hat{v}_m^{\mathrm{c}}(\xi_3) = 0$, if $\hat{\phi}_m^{\mathrm{c}} = 0$. Using the Fredholm alternative (see, e.g., [3, Thm. 5.4.5]), we reach the conclusion.

The uniqueness of the solution for (2.69) can be shown similarly. □

We now introduce the numerical schemes. Define the approximation spaces:

$$Z_m^{\mathrm{c},\boldsymbol{N}}(I) = \big\{v \in H^1(I) : v|_{I_i} \in \mathbb{P}_{N_i},\ i = 1, 2\big\};\ Z_m^{\mathrm{s},\boldsymbol{N}}(I) = Z_m^{\mathrm{c},\boldsymbol{N}}(I)\cap H_0^1(I), \tag{2.78}$$

where $\boldsymbol{N} = (N_1, N_2)$. Given a cut-off number $M > 0$, the MLSEM approximation to the solution of (2.47) in $\Lambda_1 \cup \Lambda_2$ is

$$v_M^{\boldsymbol{N}}(\xi, \eta) = \sum_{m=0}^{M} \hat{v}_m^{\mathrm{c},\boldsymbol{N}}(\xi)\mathrm{ce}_m(\eta; q) + \sum_{m=1}^{M} \hat{v}_m^{\mathrm{s},\boldsymbol{N}}(\xi)\mathrm{se}_m(\eta; q), \tag{2.79}$$

and $\{\hat{v}_m^{\mathrm{c},\boldsymbol{N}}, \hat{v}_m^{\mathrm{s},\boldsymbol{N}}\}$ are computed from the Legendre-spectral-element schemes: find $\hat{v}_m^{\mathrm{c},\boldsymbol{N}} \in Z_m^{\mathrm{c},\boldsymbol{N}}(I)$ such that

$$\mathcal{B}_m^{\mathrm{c}}(\hat{v}_m^{\mathrm{c},\boldsymbol{N}}, \psi) = \hat{\phi}_m^{\mathrm{c}}\bar{\psi}(\xi_3), \quad \forall\psi \in Z_m^{\mathrm{c},\boldsymbol{N}}(I), \quad 0 \le m \le M, \tag{2.80}$$

and find $\hat{v}_m^{\mathrm{s},\boldsymbol{N}} \in Z_m^{\mathrm{s},\boldsymbol{N}}(I)$ such that

$$\mathcal{B}_m^{\mathrm{s}}(\hat{v}_m^{\mathrm{s},\boldsymbol{N}}, \psi) = \hat{\phi}_m^{\mathrm{s}}\bar{\psi}(\xi_3), \quad \forall\psi \in Z_m^{\mathrm{s},\boldsymbol{N}}(I), \quad 1 \le m \le M. \tag{2.81}$$

Remark 2.4. *The unique solvability of* (2.80)-(2.81) *can be shown as the continuous problems in Proposition 2.4.* □

As with the circular case, the two-domain spectral-element scheme for each mode can be implemented by using the modal Legendre polynomial basis and the Schur complement technique (cf. [91]), but it is noteworthy that the resulted linear systems are full and dense due to the involvement of the non-polynomial weight function χ in (2.67).

2.3 Numerical results

In this section, we provide ample numerical results to demonstrate that our proposed approach produces accurate simulation of the ideal circular and elliptic cylindrical cloaks.

2.3.1 Circular cylindrical cloaks

Assuming that the incident wave is a plane wave with an incident angle θ_0:

$$u_{\rm in}(r,\theta) = e^{{\rm i}kr\cos(\theta-\theta_0)} = \sum_{|m|=0}^{\infty} {\rm i}^m J_m(kr) e^{{\rm i}m(\theta-\theta_0)}, \tag{2.82}$$

we can derive from the full-wave analysis in Ruan et al. [60] that the ideal cloaking problem admits the exact solution:

$$u(r,\theta) = \begin{cases} u_{\rm in}(b(r-R_1),\theta), & \text{if } \ R_1 < r < R_2, \\ u_{\rm in}(r,\theta), & \text{if } \ r > R_2, \end{cases} \tag{2.83}$$

which vanishes in the cloaked region: $r < R_1$.

We first examine the numerical error: $E_{\boldsymbol{N}} = \max_{|m|\le M} \|\hat{u}_m - \hat{u}_m^{\boldsymbol{N}}\|_{\boldsymbol{N},\infty}$, where $\|\cdot\|_{\boldsymbol{N},\infty}$ denotes the maximum pointwise errors at the Legendre-Gauss-Lobatto points (with a linear transformation) used in each subinterval. In the computation, we take $M = 70$ (so that the truncation error in θ direction is negligible),

and choose $\theta_0 = 0$ and $(R_1, R_2, R_3) = (0.2, 0.6, 1.0)$. In Figure 2.1 (left), we plot $\log_{10}(E_{\boldsymbol{N}})$ against $\boldsymbol{N} = (N, N)$ for $k = 30, 50, 70$. Observe that the error decays exponentially, when $N > N_0(k)$. The expected transition value $N_0(k)$ can be estimated by using the notion of "number-of-points-per-wavelength" (cf. [45]). Indeed, for large k, the Bessel function behaves like (cf. [87]):

$$J_m(z) \sim \sqrt{\frac{2}{\pi z}} \cos\Big(z - \frac{m\pi}{2} - \frac{\pi}{4}\Big).$$

We infer from the approxibility of Legendre polynomial expansions to trigonometric functions (cf. [45]) that as soon as

$$N > \frac{ek}{4} \max\{R_2, R_3 - R_2\} - \frac{1}{2},$$

the error begins to decay. Approximately, we take $N_0(k)$ to be ceiling round-off of this low bound. For $k = 30, 50, 70$, we find that $N_0 = 12, 20, 29$, respectively, which agrees with the numerical results in Figure 2.1 (left). In Figure 2.1 (right), we plot the zeroth mode in the expansion (2.82) (see the solid line) versus the numerical approximation of $\hat{u}_0^{\boldsymbol{N}}(r)$ with $k = 70$ and $\boldsymbol{N} = (50, 50)$ (with marker "+"). We see that this mode is not continuous across the inner boundary $r = R_1$, which is the major reason for the surface currents (cf. [61]) and the violation of PEC condition (cf. (2.13)).

We next illustrate the electric wave propagations and profiles under different incident angles and frequencies. In Figure 2.2, we depict the electric-field distributions (real and imaginary parts in the top row) simulated by the proposed FLSEM with $\theta_0 = 0, k = 20$, $(R_1, R_2, R_3) = (0.2, 0.6, 1.0)$, $M = 25$ and $\boldsymbol{N} = (20, 20)$. We see that when a TE plane wave is incident on the circular cloak, it is completely guided and bent around the cloaked region without inducing any scattering waves. Moreover, the propagating wavefronts perfectly emerge from the other side of the cloaked region without any distortion, which are best testified to by profiles of $\mathrm{Re}\{u_M^{\boldsymbol{N}}\}$ and $\mathrm{Im}\{u_M^{\boldsymbol{N}}\}$ along x-axis (cf. (2.33)) in Figure 2.2. Once again, we observe that the real part is discontinuous across the inner

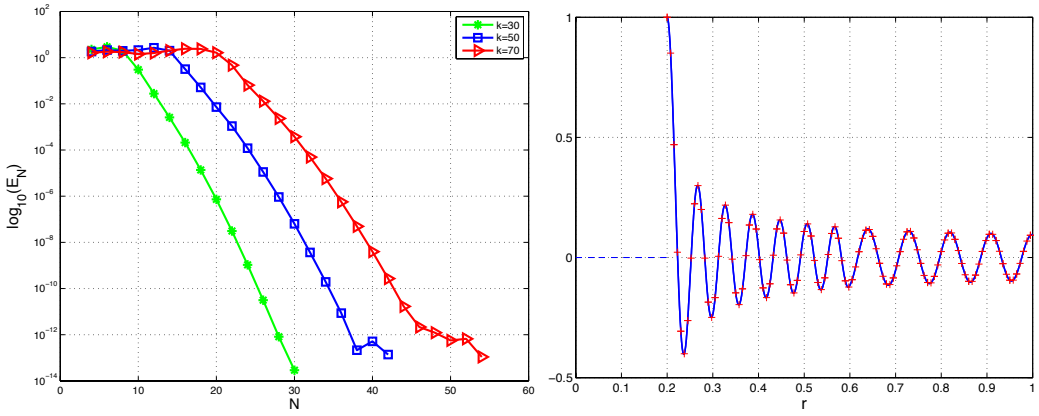

Figure 2.1: Left: errors against various N for some samples of k. Right: the zeroth mode (in solid line) versus its numerical approximation $\hat{u}_0^{\boldsymbol{N}}$ (marked by "+", with $k = 70$ and $\boldsymbol{N} = (50, 50)$).

boundary, attributed to the surface currents induced by the singular coordinate transformation (cf. [61]).

To further demonstrate the performance of the proposed approach, we set the incident angle $\theta_0 = \pi/3$, increase the incident frequency to $k = 100$ and enlarge the cloaked region by taking $(R_1, R_2, R_3) = (0.3, 0.9, 1.0)$. We depict in Figure 2.3 the same type of numerical results (obtained by the FLSEM with $M = 120$ and $\boldsymbol{N} = (100, 20)$) as in Figure 2.2. Again, the highly oscillatory oblique incident wave is perfectly steered by the cloaking layer, and completely shielded from the cloaked region. It is also worthwhile to point out that the exact boundary condition can be placed as close as possible to the cloak that can significantly reduce the number of grid points in the outermost artificial shell, especially when the incident frequency is high.

2.3.2 Wave generated by an external source

We now use an external source, compactly supported in the annulus $R_2 < r < R_3$, as the wavemaker, and turn off the incident wave. More precisely, we modify

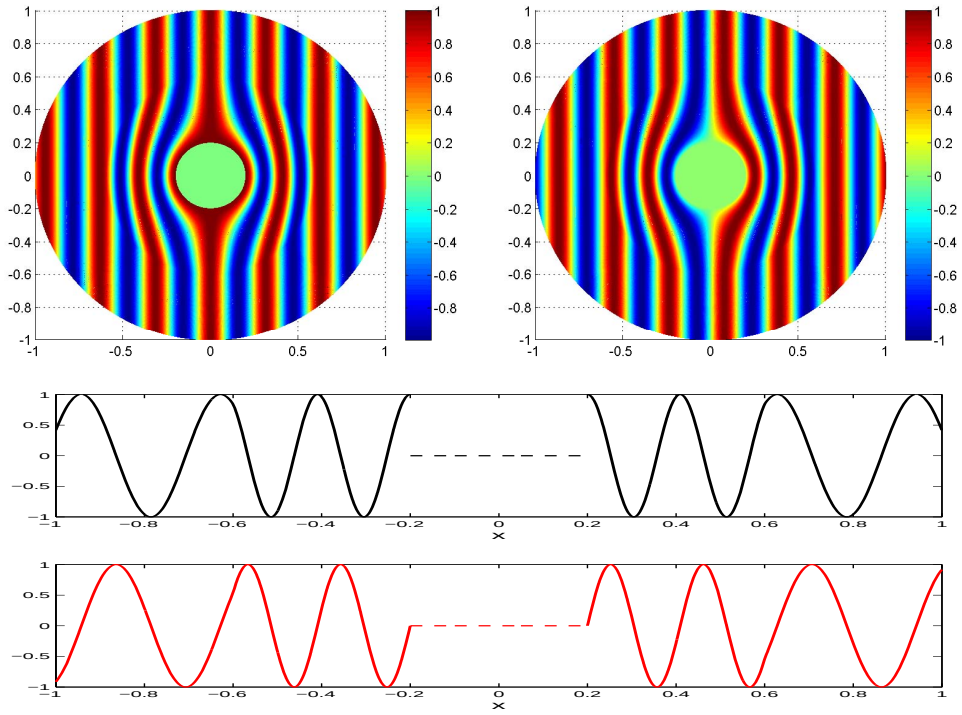

Figure 2.2: Row 1: real (left) and imaginary (right) parts of the electric-field distributions. Row 2-3: profiles of the real and imaginary parts of the electric-field along x-axis.

(2.22) as

$$\mathcal{L}_0[u^2] = f \quad \text{in} \quad \Omega_2; \quad (\partial_r - T_{R_3})u^2 = 0 \quad \text{at} \quad r = R_3. \tag{2.84}$$

In this situation, there is no closed-form exact solution. In practice, we use the Guassian function in Cartesian coordinates:

$$f(x, y) = \alpha \exp\Big(-\frac{(x-\beta)^2 + (y-\kappa)^2}{2\gamma^2}\Big), \tag{2.85}$$

where $\alpha, \beta, \kappa, \gamma$ are tuneable constants. To this end, we take $(R_1, R_2, R_3) = (0.2, 0.6, 1.0)$, $\alpha = 100$, $\beta = -0.8$, $\kappa = 0$ and $\gamma = 0.02$. The source at $r = R_3$ is nearly zero. The plots of the electric-field distributions in Figure 2.4 are computed from the FLSEM with $k = 40$, $M = 40$ and $\boldsymbol{N} = (40, 150)$. The non-plane waves generated by the source are smoothly bent and the cloak does not produce

any scattering. We also observe from Figure 2.4 that the waves seamlessly pass through the outer artificial boundary without any reflecting.

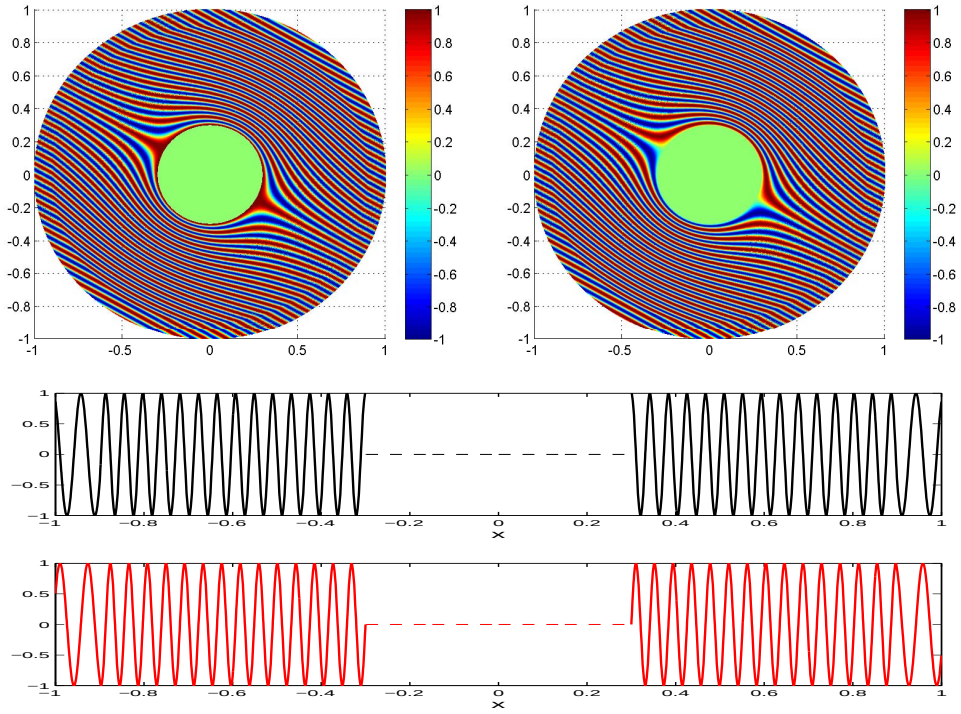

Figure 2.3: Row 1: real (left) and imaginary (right) parts of the electric-field distributions. Row 2-3: profiles of the real and imaginary parts of the electric-field along $\theta = \pi/3$.

2.3.3 Elliptic cylindrical cloaks

We first consider an incident plane wave in (2.82), which, in the elliptic coordinates (cf. (2.35)), can be expanded in terms of Mathieu functions (cf. [95, P.

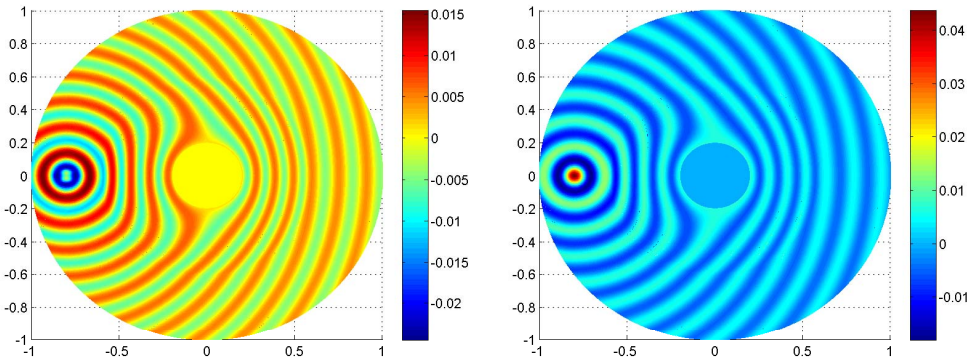

Figure 2.4: Electric-field distributions with an external source compactly supported in the outmost shell. Left: real part; right: imaginary part.

218]):

$$\begin{aligned} v_{\text{in}}(\xi,\eta) &= \exp(\mathrm{i}ka(\cosh\xi\cos\eta\cos\theta_0+\sinh\xi\sin\eta\sin\theta_0)) \\ &= \sqrt{\frac{8}{\pi}}\sum_{m=0}^{\infty}\mathrm{i}^m \mathrm{Mc}_m^{(1)}(\xi;q)\mathrm{ce}_m(\theta_0;q)\mathrm{ce}_m(\eta;q) \\ &\quad + \sqrt{\frac{8}{\pi}}\sum_{m=1}^{\infty}\mathrm{i}^m \mathrm{Ms}_m^{(1)}(\xi;q)\mathrm{se}_m(\theta_0;q)\mathrm{se}_m(\eta;q). \end{aligned} \tag{2.86}$$

Note that when $q=0$, it reduces to (2.82). Following [19], we obtain the exact solution for the ideal elliptic cloak similar to the circular case in (2.83):

$$v(\xi,\eta)=\begin{cases} v_{\text{in}}(d(\xi-\xi_1),\eta), & \text{if } \ \xi_1<\xi<\xi_2, \\ v_{\text{in}}(\xi,\eta), & \text{if } \ \xi>\xi_2, \end{cases} \tag{2.87}$$

which vanishes if $0<\xi<\xi_1$.

To illustrate the spectral accuracy of MLSEM, we tabulate in Table 2.1 the numerical errors $E_{\boldsymbol{N}}$ (defined as in the circular case) for different $\boldsymbol{N}=(N,N)$ and for several k. In the simulation, we take $a=0.6, \theta=0, (\xi_1,\xi_2,\xi_3)=(0.7,1.3,1.5)$ and $M=70$.

We next illustrate electric-field distributions. The circular cloak is perfectly symmetric, so the way of bending the waves is independent of the incident angle.

Table 2.1: Convergence of MLSEM

	$k = 30$	$k = 50$	$k = 70$
N	error	error	error
30	8.63E-07	2.75E-02	1.32
40	4.66E-12	8.42E-06	8.50E-02
50	9.03E-15	4.87E-10	3.52E-05
60	1.57E-14	2.27E-14	5.89E-09
70	1.66E-14	2.08E-14	2.73E-13

However, as pointed out in, e.g., [59], the incident wave along the major axis (i.e., $\theta_0 = 0$) leads to significantly better cloaking effect with much less scattering and bears the greatest resemblance to the circular cloak, compared with other directions. Note that in [59], PEC condition was imposed at the inner boundary $\xi = \xi_3$ in the finite-element simulation, and the electric-field distributions exhibited observable scattering waves when the incident angle $\theta_0 \neq 0$. However, using our proposed CBCs and numerical solver, the perfect cloaking effect can be achieved equally and no any scattering is induced for any incident angles. Apart from plotting the electric-field distributions, we also depict the time-averaged Poynting vector (cf. [28]):

$$\boldsymbol{S} = \mathrm{Re}\,\{\boldsymbol{E} \times \boldsymbol{H}^*\}/2, \tag{2.88}$$

which indicates the directional energy flux density. In Figures 2.5-2.7 (where $\theta_0 = 0, \pi/4, \pi$, respectively, and in all cases, $a = 0.6$, $(\xi_1, \xi_2, \xi_3) = (0.7, 1.3, 1.5)$, $k = 20$, $M = 30$ and $\boldsymbol{N} = (20, 20)$), we plot the real part of the electric-field distributions (note: the imaginary part behaves very similarly), and the corresponding Poynting vector fields. We find that the waves are again steered smoothly around the elliptic cloaked region without reflecting and scattering. We particularly look at the Poynting vectors in Figure 2.8, where the energy flux attempts to flow across

$r = \xi_1$, but it is directed by the cloak. Once again, the surface current is induced on the cloaking interface as with the circular cloak. It is noteworthy that the incident wave perpendicular to the major axis (see Figure 2.8) is of particular interest, as the shape is like a slap and the waves are difficult to steer (cf. [20]). However, using our approach, the perfect concealment of waves can be achieved as with other incident angles.

Finally, we conduct a test by adding an external source (cf. Subsection 2.3.2), and turning off the incident wave. Accordingly, we modify (2.47b) and (2.47c) as

$$\begin{aligned} &\big(\partial_\xi^2 + \partial_\eta^2\big)v + k^2a^2\big(\cosh^2\xi - \cos^2\eta\big)v = f \quad \text{in} \quad \Lambda_2; \\ &(\partial_\xi - \mathbb{T}_{\xi_3})v = 0 \quad \text{at} \quad \xi = \xi_3, \end{aligned} \tag{2.89}$$

where f is compactly supported in the elliptic layer $\xi_2 < \xi < \xi_3$. Like before, we take f to be (2.85) with $\alpha = 1000$, $\beta = 0$, $\kappa = 1.148$, $\gamma = 0.01$. Figure 2.8 is computed from MLSEM with $k = 20$, $M = 30$ and $\boldsymbol{N} = (50, 100)$ and illustrates the real (left) and imaginary (right) part of the electric-field distributions induced by external source. Once again, we see that the waves are smoothly bent without penetrating into the elliptic cloaked region. Moreover, the cloak does not induce any scattering, and indeed, we see the fields near the source totally unaffected.

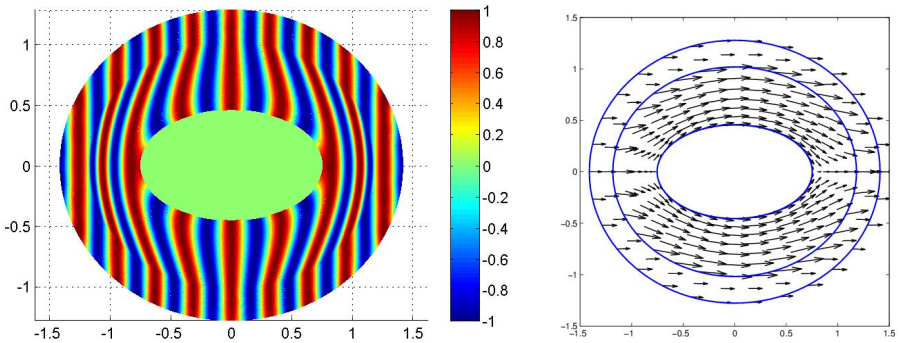

Figure 2.5: Real part of the electric-field distribution (left) and the related Poynting vector (right), where the incident angle $\theta_0 = 0$.

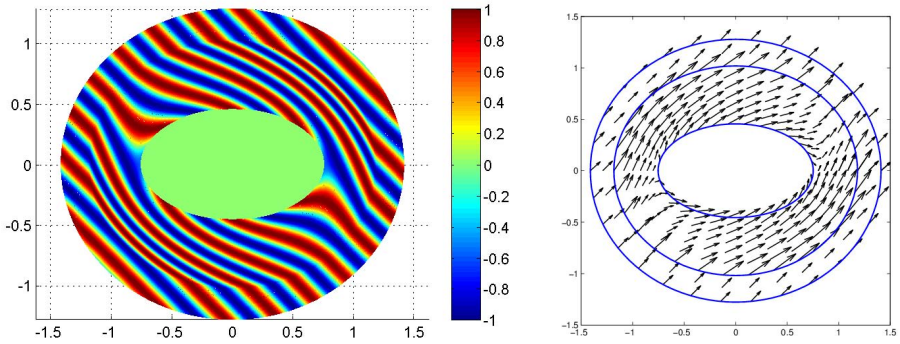

Figure 2.6: Real part of the electric-field distribution (left) and the related Poynting vector (right), where the incident angle $\theta_0 = \pi/4$.

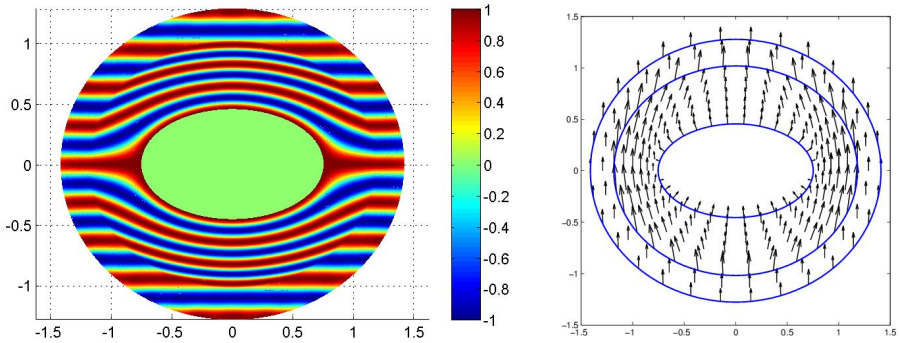

Figure 2.7: Real part of the electric-field distribution (left) and the related Poynting vector (right), where the incident angle $\theta_0 = \pi$.

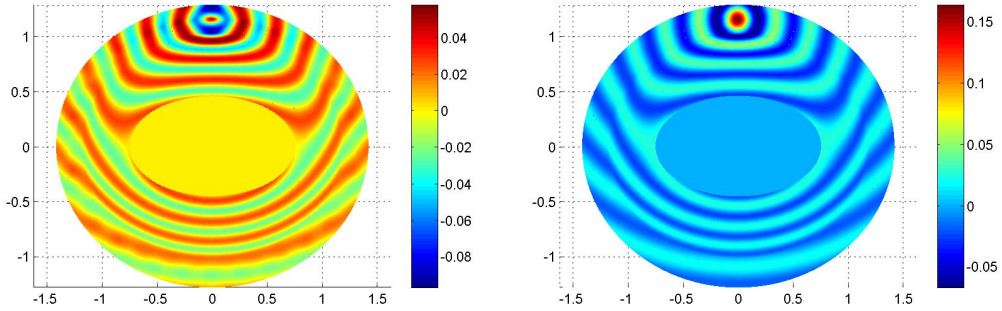

Figure 2.8: The real (left) and imaginary (right) part of electric-field distribution with different sources.

Chapter 3

Polygonal Invisibility Cloaks

In this chapter, we are mainly concerned with simulation of general two-dimensional Helmholtz equations in anisotropic media using spectral-element method (SEM), with particular applications in accurate simulation of polygonal invisibility cloaks resulting from the field of TE. As addressed in Section 1.3, the unbounded domain is truncated to a bounded one by imposing an exact circular DtN TBC. Such a boundary condition presents a great challenge to be incorporated with spectral-element solvers since it involves the Fourier expressions in space. We introduce a semi-analytic technique to integrate the global TBC with local curvilinear elements seamlessly, which is accomplished by using a novel elemental mapping and analytic formulas for evaluating global Fourier coefficients on spectral-element grids exactly.

Compared with circular and elliptic invisibility cloaks studied in Chapter 2, the polygonal cloaks enjoy more flexibility to hide objects with complex shapes, which are however much less studied. Indeed, many of the previous principles and approaches for CBCs are not extendable to the polygonal case. Following the spirit of Subsection 2.1.2, we propose new CBCs under a "local" coordinate system (see Proposition 3.3), under which the governing equation in the cloaked region is decoupled from the exterior region. Accordingly, no wave can propagate into the cloaked region, and vice versa. We emphasize that the new CBCs are

indispensable for spectrally accurate simulations. We also show that the proposed spectral-element solver provides a reliable tool to study how the defects affect the perfectness of an ideal cloak (see Subsection 3.2.5).

The rest of the chapter is organised as follows. In Section 3.1, we present the model problem of interest and introduce the technique to seamlessly integrate the global DtN BC with local spectral elements. Section 3.2 is for accurate simulation of polygonal invisibility cloak, where new CBCs are derived and efficient techniques are introduced to deal with singular material parameters. Various numerical results are provided to show the perfectness of invisibility, and the effects of defects and lossy or dispersive media. Section 3.3 concerns the extension of the spectral-element solver to the simulation of electromagnetic concentrators and rotators. The last section is for some extensions to three-dimensional setting.

3.1 Spectral-element discretisation of DtN BC

In this section, we first truncate the aforementioned Helmholtz problem in (1.18) arisen from transformation electromagnetics with DtN BC. We then discretise the model problem by spectral-element method and focus on how to seamlessly integrate the global DtN BC with local elements.

3.1.1 2-D Helmholtz equation with anisotropic coefficients

In summary, the Helmholtz problem truncated with DtN boundary condition reads

$$\nabla \cdot (\boldsymbol{C}(\boldsymbol{r})\nabla u(\boldsymbol{r})) + k^2 n(\boldsymbol{r}) u(\boldsymbol{r}) = f(\boldsymbol{r}) \quad \text{in } B_R, \tag{3.1}$$

$$[\![u]\!] = [\![\boldsymbol{C}\,\nabla u]\!] = 0 \quad \text{at } \Gamma := \partial\Omega_-, \tag{3.2}$$

$$\partial_r u - T_R[u] = h \quad \text{at } \Gamma_R, \tag{3.3}$$

where

$$[\![u]\!] := u^- - u^+, \quad [\![\boldsymbol{C}\,\nabla u]\!] := \boldsymbol{n} \cdot (\boldsymbol{C}^-\nabla u^- - \boldsymbol{C}^+\nabla u^+), \tag{3.4}$$

$u^{\pm} := u|_{\Omega_{\pm}}$, $\boldsymbol{C}^{\pm} := \boldsymbol{C}|_{\Omega_{\pm}}$ and $\boldsymbol{n}$ is the unit outer normal vector along Γ. Here, T_R is the DtN map defined in (2.6)-(2.7).

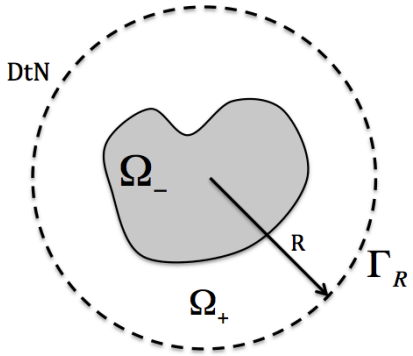

Figure 3.1: Illustration of geometry

In general, we make the following assumptions.

(i) $\boldsymbol{C}$ is assumed to be a symmetric positive definite matrix in $\mathbb{R}^{2\times 2}$, and for a given positive constant c_1 and every non-zero column vector $\boldsymbol{\xi}$,

$$0 < \boldsymbol{\xi}^t \boldsymbol{C}\, \boldsymbol{\xi} \leq c_1, \quad \forall\, \boldsymbol{\xi} \in \mathbb{R}^2, \ \text{ a.e. in } \mathbb{R}^2. \tag{3.5}$$

(ii) The coefficient is bounded below and above, and for a given positive constant n_1,

$$0 < n \leq n_1, \quad \text{a.e. in } \mathbb{R}. \tag{3.6}$$

(iii) The inhomogeneity of the medium is confined in a bounded domain Ω_- with Lipschitz boundary, and f is compactly supported in disc B_R of radius $R > 0$ (see Figure 3.1):

$$\boldsymbol{C} = \boldsymbol{I}_2, \quad n = 1 \quad \text{in} \quad \mathbb{R}^2 \setminus \bar{\Omega}_-; \quad \text{supp}(f) \subseteq B_R, \tag{3.7}$$

where $\boldsymbol{I}_2$ is the 2×2 identity matrix. In what follows, we are interested in the case where Ω_- is a penetrable scatterer.

Note that the inhomogeneity of the medium is confined in a bounded domain Ω_- with Lipschitz boundary, and f is compactly supported in disc B_R of radius $R > 0$ (see Figure 3.1):

$$\boldsymbol{C} = \boldsymbol{I}_2, \quad n = 1 \quad \text{in} \quad \mathbb{R}^2 \setminus \bar{\Omega}_-; \quad \text{supp}(f) \subseteq B_R, \tag{3.8}$$

where $\boldsymbol{I}_2$ is the 2×2 identity matrix. In what follows, we are interested in the case where Ω_- is a penetrable scatterer.

In Sections 3.2-3.3, we shall introduce the coordinate transformations for polygonal invisibility cloaks, concentrators and rotators, and compute the corresponding material parameters $\boldsymbol{C}$ and n via (1.6). It is noteworthy that in all cases, the coordinate transformations are identity in $\mathbb{R}^2 \setminus (\Omega_- \cup \Omega_+)$ (cf. Figure 3.1), so the unbounded problem can be truncated to a bounded one by the aforementioned DtN boundary condition. Moreover, we can derive (3.4) below from the standard transmission conditions (see, e.g., [28, Sec. 1.5] and [35]), that is, the continuity of the tangential components of $\boldsymbol{E}$ and $\boldsymbol{H}$ at the interface $\Gamma := \partial\Omega_-$.

3.1.2 Spectral-element scheme

Define the line integral along Γ_R

$$\langle u, v\rangle_{\Gamma_R} := \oint_{\Gamma_R} u\,\bar{v}\,\mathrm{d}\gamma. \tag{3.9}$$

A weak formulation of (3.1)-(3.3) is to find $u \in H^1(B_R)$ such that

$$\begin{aligned} \mathscr{B}(u, v) :&= (\boldsymbol{C}\,\nabla u, \nabla v)_{B_R} - k^2(nu, v)_{B_R} - \langle T_R[u], v\rangle_{\Gamma_R} \\ &= \mathscr{F}(v) := -(f, v)_{B_R} + \langle h, v\rangle_{\Gamma_R}, \quad \forall v \in H^1(B_R), \end{aligned} \tag{3.10}$$

where by (2.6)-(2.7),

$$\langle T_R[u], v\rangle_{\Gamma_R} = \frac{R}{2\pi} \sum_{|m|=0}^{\infty} \mathcal{T}_m\Big(\int_0^{2\pi} u(R,\theta) e^{-\mathrm{i}m\theta}\mathrm{d}\theta\Big)\overline{\Big(\int_0^{2\pi} v(R,\theta) e^{-\mathrm{i}m\theta}\mathrm{d}\theta\Big)}. \tag{3.11}$$

Remark 3.1. *From (see, e.g., [3, P. 87])*

$$-\frac{|m|+1}{R} \leq \mathrm{Re}(\mathcal{T}_m) \leq \frac{1}{R}, \quad 0 < \mathrm{Im}(\mathcal{T}_m) \leq k, \quad |m| = 0, 1, \cdots, \tag{3.12}$$

we obtain the well-posedness of (3.10) *from* (3.5) *and* (3.12) *(cf. [3]).* □

Remark 3.2. *In the numerical implementation, the infinite series in the DtN boundary condition* (2.6)-(2.7) *is approximated by its truncation, i.e.,* $T_R^M[u] := \sum_{|m|=0}^{M} \mathcal{T}_m \hat{u}_m e^{\mathrm{i}m\theta}$. *The issue of how to choose the cut-off number* M *has been investigated by a number of literatures. Harari et al. [96] proved that when* $M \geq kR$, *the solvability of* (3.10) *with the approximated DtN condition* $T_R^M[u]$ *can be guaranteed. The priori error estimate is otained in* L^2 *and* H^1 *norm in [97] and numerical experiments on finding the optimal choose of* M *shows that* $M \geq kR$ *is a sufficient but conservative condition. Grote and Keller [56] proposed a modified DtN boundary condition such that the well-posedness of the approximate problem is always guaranteed regardless of the choose of* M. □

For the sake of simplicity, we assume that Ω_- is a polygon or a disk. Nevertheless, our approach can be easily extended to more complex domains. The computational domain B_R is partitioned by non-overlapping quadrilateral elements $\{\Omega^e\}_{e=1}^E$ with straight or curvilinear sides. Note that the sides are specially chosen such that in the outer boundary Γ_R are aligned with them. To be more precise,

$$\Gamma_R = \bigcup_{e=1}^{E_R} \Gamma_R^e, \quad \bigcup_{e=1}^{E_R} \big[\theta_e, \theta_{e+1}\big] = [0, 2\pi], \quad r = R, \tag{3.13}$$

where $\Gamma_R^e := \Gamma_R \cap \bar{\Omega}^e \neq \emptyset$ for all $e \in \{1, \cdots, E\}$, and $\theta_1 = \theta_{E_R+1}$ (see Figure 3.2 (a)). Let $\boldsymbol{\chi}^e : Q := (-1, 1)^2 \to \Omega^e$ be a one-to-one transforamtion in each element

$$\boldsymbol{r} = \boldsymbol{x} = (x, y) = \boldsymbol{\chi}^e(\xi, \eta) := \big(\chi_1^e(\xi, \eta), \chi_2^e(\xi, \eta)\big), \quad \forall\, (\xi, \eta) \in Q. \tag{3.14}$$

Gordon and Hall [98] proposed a elemental transformation which transforms Q into any curvilinear quadrilateral, with certain parameterisation of the "edges" (see, e.g., [99, 46]). In (3.19)-(3.20) below, a special parameterisation of Gordon

and Hall transformation is used to incorporate the local spectral elements with the global DtN operators.

Denote by $\mathcal{P}_N$ the set of all polynomials with highest degree at most N in $[-1,1]$. Denote the spectral-element approximation space

$$V_N^E := \left\{ v \in C(B_R) \,:\, v(\boldsymbol{x})|_{\Omega^e} = v(\boldsymbol{\chi}^e) \in \mathcal{P}_N^2 := \mathcal{P}_N \otimes \mathcal{P}_N,\ 1 \le e \le E \right\}. \quad (3.15)$$

The corresponding spectral-element numerical scheme of (3.10) is to find $u_N^E \in V_N^E$ such that

$$\begin{aligned} \mathscr{B}_N^M(u_N^E, v_N^E) :&= (\boldsymbol{C}\,\nabla u_N^E, \nabla v_N^E)_{B_R} - k^2 (n u_N^E, v_N^E)_{B_R} \\ &\quad - \langle T_R^M[u_N^E], v_N^E \rangle_{\Gamma_R} = \mathscr{F}(v_N^E), \quad \forall\, v_N^E \in V_N^E, \end{aligned} \quad (3.16)$$

where we recall the truncated DtN operator $T_R^M[u_N^E]$ in Remark 3.2.

3.1.3 Seamless integration of SEM with global DtN TBC

The continuous inner product $(\cdot,\cdot)_\Omega$ and the trace integral $\langle h, v_N^E \rangle_{\Gamma_R}$ can be apprximated by the usual discrete inner product based on tensorial Legendre-Gauss-Lobatto (LGL) quadrature (see, e.g., [99]). However, since the DtN is a global operator and the spectral-element solution is piecewise continuous, we need to pay more attention to treat the term $\langle T_R[u_N^E], v_N^E \rangle_{\Gamma_R}$. The fast Fourier transform (FFT) can be applied here, but one more intermediate procedure is needed to interpolate from spectral-element grids to Fourier points. Note that $u_N^E|_{\Gamma_R} \in C^0$, only first-order convergence is achieved by a naive interpolation.

Next, we propose an efficient semi-analytical method to evaluate $\langle T_R[u_N^E], v_N^E \rangle_{\Gamma_R}$. Let $\{\xi_j = \eta_j\}_{j=0}^N$ be the LGL points in $[-1,1]$, and let $\{l_j\}_{j=0}^N$ be the associated Lagrange interpolating basis polynomials. The corresponding spectral-element grids and basis on $\bar{\Omega}^e$ are given by

$$\boldsymbol{x}_{ij} = \boldsymbol{\chi}^e(\xi_i, \eta_j), \quad \psi_{ij}(\boldsymbol{x}) = l_i(\xi) l_j(\eta), \quad 0 \le i, j \le N. \quad (3.17)$$

Thus, we have

$$u_N^E(x,y)\Big|_{\Omega^e} = \sum_{i,j} \tilde{u}_{ij}^e\, l_i(\xi) l_j(\eta), \quad (3.18)$$

where the unknowns $\{\tilde{u}_{ij}^e\}$ are determined by the scheme (3.16).

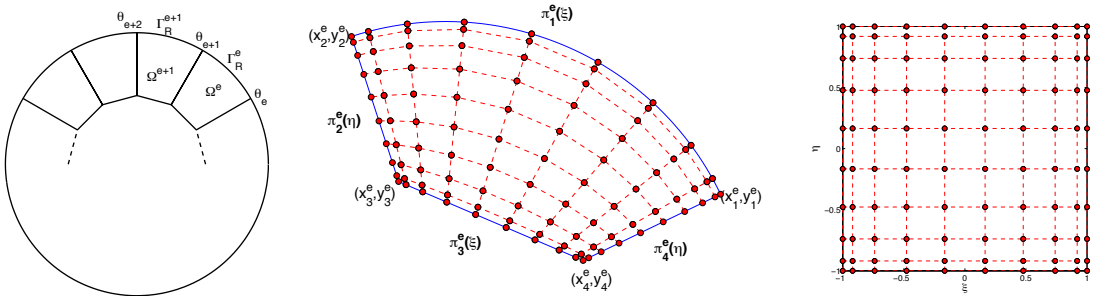

(a) Mesh (b) Mapped LGL grids on Ω^e (c) Tensorial LGL points on Q

Figure 3.2: SEM mesh along Γ_R and the mapped grids on a curvilinear element via the proposed transformation from the tensorial LGL points on a reference square .

We now particularly look at the Gordon-Hall transform for a curvilinear element Ω^e with vertices $\{(x_i^e, y_i^e)\}_{i=1}^4$ along Γ_R (with one arc-shaped side and three straight sides). Let $\{\boldsymbol{\pi}_j^e(t), t \in [-1,1]\}_{j=1}^4$ be, respectively, the parametric form of four sides such that

$$\boldsymbol{\pi}_1^e(-1) = \boldsymbol{\pi}_4^e(1), \quad \boldsymbol{\pi}_1^e(1) = \boldsymbol{\pi}_2^e(1), \quad \boldsymbol{\pi}_2^e(-1) = \boldsymbol{\pi}_3^e(1), \quad \boldsymbol{\pi}_3^e(-1) = \boldsymbol{\pi}_4^e(-1), \tag{3.19}$$

see Figure 3.2 (b). Correspondinly, the Gordon-Hall transform is given by

$$\begin{aligned} \boldsymbol{x} = \boldsymbol{\chi}^e(\xi,\eta) = \boldsymbol{\pi}_1^e(\xi)\frac{1+\eta}{2} + \boldsymbol{\pi}_3^e(\xi)\frac{1-\eta}{2} + \frac{1+\xi}{2}\boldsymbol{\pi}_2^e(\eta) + \frac{1-\xi}{2}\boldsymbol{\pi}_4^e(\eta) \\ - \left(\boldsymbol{\pi}_1^e(-1)\frac{1-\xi}{2} + \boldsymbol{\pi}_1^e(1)\frac{1+\xi}{2}\right)\frac{1+\eta}{2} \\ - \left(\boldsymbol{\pi}_3^e(-1)\frac{1-\xi}{2} + \boldsymbol{\pi}_3^e(1)\frac{1+\xi}{2}\right)\frac{1-\eta}{2}, \end{aligned} \tag{3.20}$$

where the edge $\eta = 1$ of Q is mapped to the arc $\Gamma_R^e = \{r = R,\ \theta \in (\theta_e, \theta_{e+1})\}$ of Ω_e, i.e.,

$$\Gamma_R^e : \ x = \chi_1^e(\xi,1) = \pi_{11}^e(\xi), \ \ y = \chi_2^e(\xi,1) = \pi_{12}^e(\xi), \quad \forall\, \xi \in (-1,1). \tag{3.21}$$

Therefore, the mapped grids on Γ_R^e (see Figure 3.2) satisfy

$$\cos\theta_j^e = R^{-1}\pi_{11}^e(\xi_j) \ \text{ or } \ \sin\theta_j^e = R^{-1}\pi_{12}^e(\xi_j), \quad 1 \le j \le N. \tag{3.22}$$

We now turn to $\langle T_R^M[u_N^E], v_N^E\rangle_{\Gamma_R}$ in (3.16). Thanks to (3.11) and (3.18), we need to evaluate

$$\begin{aligned}\int_0^{2\pi} u_N^E(x,y)\big|_{\Gamma_R} e^{-\mathrm{i}m\theta}\,\mathrm{d}\theta &= \sum_{e=1}^{E_R}\int_{\theta_e}^{\theta_{e+1}} u_N^E(x,y)\big|_{\Gamma_R^e} e^{-\mathrm{i}m\theta}\,\mathrm{d}\theta \\ &= \sum_{e=1}^{E_R}\sum_i \tilde{u}_{iN}^e \int_{-1}^{1} l_i(\xi) e^{-\mathrm{i}m\theta(\xi)}\frac{\mathrm{d}\theta}{\mathrm{d}\xi}\,\mathrm{d}\xi.\end{aligned} \tag{3.23}$$

Represent $\{l_i\}$ in terms of Legendre polynomials, and (3.23) suffices to compute

$$\mathbb{I}_{nm}^e := \int_{-1}^{1} P_n(\xi)\, e^{-\mathrm{i}m\theta(\xi)}\,\frac{\mathrm{d}\theta}{\mathrm{d}\xi}\,\mathrm{d}\xi, \quad \text{for } \ n \ge 0, \ \ |m| \ge 0, \tag{3.24}$$

where P_n is the Legendre polynomial of degree n, and by (3.21),

$$\frac{\mathrm{d}\theta}{\mathrm{d}\xi} = \frac{1}{R}\frac{\mathrm{d}\gamma}{\mathrm{d}\xi} = R^{-1}\sqrt{\left[\partial_\xi\pi_{11}^e(\xi)\right]^2 + \left[\partial_\xi\pi_{12}^e(\xi)\right]^2}. \tag{3.25}$$

As is shown in (3.24), due to the higly oscillatory term $e^{\mathrm{i}m\theta(\xi)}$ for large m in the integrand, it is preferable to resort to a analytic formulas in computing $\mathbb{I}_{nm}^e$ to guarantee the accuracy and efficiency. While essentially, this relies on the choice of the form for $\boldsymbol{\pi}_1(\xi)$. In what follows, we propose a parametric form that allows for exact evaluation of (3.25) by analytic formulas (see Propositions 3.1-3.2). To spawn the idea, we first show the obstacles, if one employs a commonly-used parametric form.

A commonly-used parametric form for $\boldsymbol{\pi}_1^e(\xi)$

Following the ideas of the cubed-sphere transformation (cf. [100, 101]) and the "ray" coordinates (cf. [102]), one can project the secant line: (x_1^e, y_1^e), (x_2^e, y_2^e) to the arc Γ_R^e via the "rays" from the origin. This leads to:

$$\boldsymbol{\pi}_1^e(\xi) = (\pi_{11}^e(\xi), \pi_{12}^e(\xi)) = \left(\frac{R\,d_1(\xi)}{\sqrt{d_1^2(\xi)+d_2^2(\xi)}}, \frac{R\,d_2(\xi)}{\sqrt{d_1^2(\xi)+d_2^2(\xi)}}\right), \tag{3.26}$$

where

$$d_1(\xi) = \frac{x_2^e - x_1^e}{2}\xi + \frac{x_1^e + x_2^e}{2}, \quad d_2(\xi) = \frac{y_2^e - y_1^e}{2}\xi + \frac{y_1^e + y_2^e}{2}. \tag{3.27}$$

Since $\cos\theta = R^{-1}\pi_{11}^e(\xi)$, we find

$$\theta(\xi) = \begin{cases} \alpha, & \text{if} \quad \theta \in [0, \pi), \\ 2\pi - \alpha, & \text{if} \quad \theta \in [\pi, 2\pi), \end{cases} \qquad \alpha := \cos^{-1}\left(\frac{d_1(\xi)}{\sqrt{d_1^2(\xi) + d_2^2(\xi)}}\right), \tag{3.28}$$

and (3.25) reads

$$\frac{\mathrm{d}\theta}{\mathrm{d}\xi} = \frac{|x_1^e y_2^e - x_2^e y_1^e|}{2(d_1^2(\xi) + d_2^2(\xi))}, \quad \forall\, \xi \in [-1, 1]. \tag{3.29}$$

Inserting (3.28) and (3.29) into (3.24), one immediately finds that the integrand in $\mathbb{I}_{nm}^e$ takes a complicated form and must be computed numerically. Nevertheless, due to the existence of the term $e^{\mathrm{i}m\theta(\xi)}$, the integrand is highly oscillatory, when $|m|$ is large.

A new parametric form for $\boldsymbol{\pi}_1^e(\xi)$

Here, different approach is applied to parameterise Γ_R^e. To be more precise, we look for

$$\boldsymbol{\pi}_1^e(\xi) = \big(\pi_{11}^e(\xi), \pi_{12}^e(\xi)\big) = R(\cos\theta, \sin\theta), \quad \theta \in [\theta_e, \theta_{e+1}], \;\; \xi \in [-1, 1], \tag{3.30}$$

such that $\mathrm{d}\gamma = a\,\mathrm{d}\xi$, that is, the arc length γ is linear in ξ.

Proposition 3.1. *Let Ω^e be the curvilinear element as in* Figure 3.2 (b). *Then the new elemental mapping from the reference square Q to Ω^e takes the form*

$$x = \pi_{11}^e(\xi)\frac{1+\eta}{2} + \frac{(1+\xi)(1-\eta)}{4}x_3^e + \frac{(1-\xi)(1-\eta)}{4}x_4^e, \tag{3.31}$$

$$y = \pi_{12}^e(\xi)\frac{1+\eta}{2} + \frac{(1+\xi)(1-\eta)}{4}y_3^e + \frac{(1-\xi)(1-\eta)}{4}y_4^e, \tag{3.32}$$

where

$$\boldsymbol{\pi}_1^e(\xi) = \big(\pi_{11}^e(\xi), \pi_{12}^e(\xi)\big) = R\big(\cos(\hat{\theta}_e\xi + \beta_e), \sin(\hat{\theta}_e\xi + \beta_e)\big), \tag{3.33}$$

with

$$\hat{\theta}_e = \frac{\theta_{e+1} - \theta_e}{2}, \quad \beta_e = \frac{\theta_e + \theta_{e+1}}{2}. \tag{3.34}$$

Proof. Let $\gamma = a\xi + b$. The arc length along Γ_R^e is $\gamma = R(\theta - \theta_e)$, so we have

$$a\xi + b = R(\theta - \theta_e). \tag{3.35}$$

Since $\theta = \theta_e$ (resp. $\theta = \theta_{e+1}$) is mapped to $\xi = -1$ (resp. $\xi = 1$), we find

$$a = b = \hat{\theta}_e R, \quad \theta = \hat{\theta}_e \xi + \beta_e, \quad \xi \in [-1, 1]. \tag{3.36}$$

Inserting it into (3.30) leads to the new parametric form (3.33). Together with the parameterisation for the straight sides, e.g.,

$$\boldsymbol{\pi}_4^e(\eta) = \frac{\boldsymbol{x}_1^e - \boldsymbol{x}_4^e}{2}\eta + \frac{\boldsymbol{x}_1^e + \boldsymbol{x}_4^e}{2}, \quad \eta \in [-1, 1], \tag{3.37}$$

and (3.20), we have (3.31)-(3.32). This ends the proof. □

Different from (3.28)-(3.29), the new parameterisation has a linear dependence of θ in ξ, so in (3.24),

$$\theta(\xi) = \hat{\theta}_e \xi + \beta_e, \quad \frac{\mathrm{d}\theta}{\mathrm{d}\xi} = \hat{\theta}_e. \tag{3.38}$$

This enables us to utilize the following analytic approach to compute the integrals of interest.

Proposition 3.2. *Under the new transformation in* Proposition 3.1*, the integral in* (3.24) *can be computed by*

$$\mathbb{I}_{n0}^e = 2\hat{\theta}_e \delta_{n0}; \quad \mathbb{I}_{nm}^e = \frac{2\hat{\theta}_e}{\mathrm{i}^n}\sqrt{\frac{\pi}{2m\hat{\theta}_e}} J_{n+1/2}(m\hat{\theta}_e)\, e^{-\mathrm{i}m\beta_e}, \tag{3.39}$$

and $\mathbb{I}_{n,-m}^e = (\mathbb{I}_{nm}^e)^*$ *for* $n \geq 0$ *and* $m \geq 1$*, where* $J_{n+1/2}$ *is the Bessel function of the first kind, and* $\hat{\theta}, \beta_e$ *are defined in* (3.34)*.*

Proof. By (3.24) and (3.38),

$$\mathbb{I}_{nm}^e = \int_{-1}^{1} P_n(\xi)\, e^{-\mathrm{i}m\theta(\xi)} \frac{\mathrm{d}\theta}{\mathrm{d}\xi}\, \mathrm{d}\xi = \hat{\theta}_e\, e^{-\mathrm{i}m\beta_e} \int_{-1}^{1} P_n(\xi) e^{-\mathrm{i}m\hat{\theta}_e\xi}\, \mathrm{d}\xi. \tag{3.40}$$

It is clear that for $m = 0$, we have $\mathbb{I}_{00}^e = 2\hat{\theta}_e$, and with the help of the orthogonality of Legendre polynomials, we have $\mathbb{I}_{n0}^e = 0$ when $n \geq 1$. What's more, $\mathbb{I}_{n,-m}^e =$

$(\mathbb{I}_{nm}^{e})^*$, so only the integrals with $m \geq 1$ need to be evaluated. Recall the analytic formulas (cf. [103])

$$\int_{-1}^{1} P_n(\xi)\, e^{-\mathrm{i}mx\xi}\, \mathrm{d}\xi = \frac{1}{\mathrm{i}^n}\sqrt{\frac{2\pi}{mx}} J_{n+1/2}(mx), \quad \text{for } mx > 0. \tag{3.41}$$

Thus, (3.39) follows immediately. □

3.1.4 An illustrative numerical example

It is seen that as a by-product, the new transformation provides an efficient approach to evaluate the Fourier coefficients via (3.39). In a nutshell, $[0, 2\pi]$ is partitioned into $\{[\theta_e, \theta_{e+1}]\}_{e=1}^{E_R}$, and the underlying function (3.18) on each subinterval is approximated by Legendre polynomials and the new parameterisation (3.33) is used so that the analytical formula (3.39) can be applied. Here, one example is given to illustrate this semi-analytic approach.

A plane wave with incident angle θ_0 can be expressed in terms of Fourier series as follows (cf. [87, P. 360]):

$$e^{\mathrm{i}k(x\cos\theta_0 + y\sin\theta_0)} = \sum_{|m|=0}^{\infty} \hat{g}_m e^{\mathrm{i}m\theta} \quad \text{with} \quad \hat{g}_m = \mathrm{i}^m J_m(kR) e^{-\mathrm{i}m\theta_0}. \tag{3.42}$$

Denote $\hat{g}_{m,N}^{E_R}$ be the approximation to $\hat{g}_m$, and measure the error $\max_{|m|\leq M}|\hat{g}_m - \hat{g}_{m,N}^{E_R}|$. We plot the numerical errors against N (with fixed $E_R = 4$) , and against the number of elements E_R (with fixed $N = 10$) in Figure 3.3 (right), for $R = 1$, $M = 20, k = 10, 20, 30$ and $\theta_0 = \pi/4$. Observe that in both cases the errors decay exponentially.

3.2 Accurate simulation of polygonal invisibility cloaks

In this section, the proposed spectral-element solver in Section 3.1 is applied to simulate the polygonal invisibility cloak, and the influences of defects, lossy or

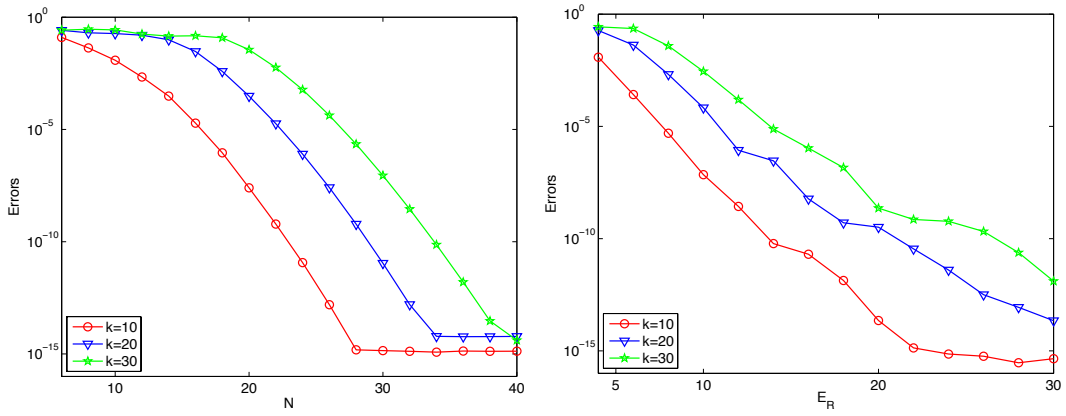

Figure 3.3: Numerical error $\max_{|m|\leq M}|\hat{g}_m - \hat{g}_{m,N}^{E_R}|$ with fixed $M = 20$, $\theta_0 = \pi/4$ and $k = 10, 20, 30$. Left: errors against N with $E_R = 4$. Right: errors against E_R with $N = 10$.

dispersive media in the cloaking layer are studied numerically. We particularly focus on two important issues as follows:

(i) How to impose appropriate boundary conditions at the inner boundary of the cloaking layer to allow for perfect concealment of the objects?

(ii) How to efficiently treat the singular material parameters (i.e., zero or infinite) at the cloaking interface in spectral-element discretisation to ensure accurate simulation?

3.2.1 Coordinate transformation and material parameters

Similar to Pendry et al. [5], the coordinate transformation for a polygonal cloak compresses the polygonal domain Ω_- (i.e., the polygon $AB\cdots F$) in the virtual $(\breve{x}, \breve{y})$-coordinates in Figure 3.4 (a) to the polygonal annulus $\Omega_-^a = \Omega_- \setminus \bar{\Omega}_-^p$ dubbed as the "cloaking layer" in the new (x, y)-coordinates in Figure 3.4 (b), with the inner polygonal domain $\Omega_-^p = A_pB_p\cdots F_p$ forming the "cloaked region". The electromagnetic waves from outside are expected to bend smoothly around the cloaked layer and goes out without distortion as if propagating in vacuum.

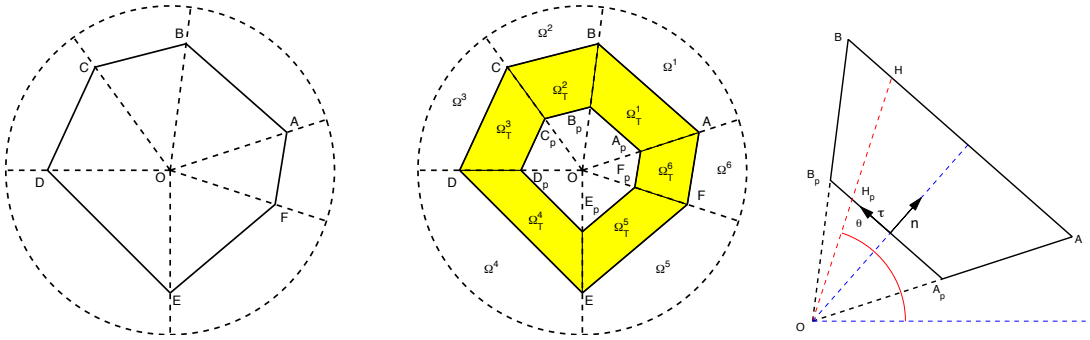

(a) $(\breve{x}, \breve{y})$-domain (b) (x, y)-domain (c) $\boldsymbol{\tau}$ and $\boldsymbol{n}$

Figure 3.4: Geometric illustration of a invisibility polygonal cloak. (a) $\Omega_- := AB \cdots F$ in the virtual coordinates $(\breve{x}, \breve{y})$. (b) $\Omega_-^p = A_pB_p \cdots F_p$. Cloaking layer (i.e., the shaded part) $\Omega_-^a = \Omega_- \setminus \bar{\Omega}_-^p$ obtained through (3.44). (c) The "local" coordinate system $(\boldsymbol{\tau}, \boldsymbol{n})$.

The underlying coordinate transformation takes simple form in two polar coordinates as shown in the diagram:

$$\boxed{\text{Virtual: } (\breve{x}, \breve{y})} \longleftrightarrow \boxed{(\breve{r}, \breve{\theta})} \xrightarrow{\text{Transform}} \boxed{(r, \theta)} \longleftrightarrow \boxed{\text{Physical: } (x, y)} \tag{3.43}$$

With this, the transformation for a polygonal invisibility cloak takes the form (see, e.g., [104]):

$$\begin{cases} r = (1 - \rho)\,\breve{r} + R_1, & \breve{r} \in [0, R_2], \quad r \in [R_1, R_2], \\ \theta = \breve{\theta}, & \breve{\theta}, \theta \in [0, 2\pi), \end{cases} \tag{3.44}$$

where

$$\rho = \frac{OA_p}{OA} = \frac{OB_p}{OB} = \cdots = \frac{OF_p}{OF}, \quad 0 < \rho < 1, \tag{3.45}$$

and $(R_1(\theta), \theta)$ (resp. $(R_2(\theta), \theta)$) is the polar parametric form of the side of the cloaked region Ω_-^p (resp. the domain Ω_-).

In order to represent R_i $(i = 1, 2)$ and discuss about the imposition of the cloaking boundary conditions hereafter, we introduce a "local" coordinate system. Consider one side of Ω_-^p, say A_pB_p in Figure 3.4 (c), with vertices (x_1, y_1) and

(x_2, y_2). Then the unit tangential and out normal vector $\boldsymbol{\tau}$ and $\boldsymbol{n}$ with respect to A_pB_p are given, respectively, by

$$\boldsymbol{\tau} = \frac{(x_2 - x_1, y_2 - y_1)}{\sqrt{(x_2 - x_1)^2 + (y_2 - y_1)^2}} := (\tau_1, \tau_2), \quad \boldsymbol{n} = (\tau_2, -\tau_1), \tag{3.46}$$

forming a "local" coordinate system. Note that for any $(x, y) \in A_pB_p$, we have $(x, y) = (R_1 \cos\theta, R_1 \sin\theta)$, which leads to $(x, y) \cdot \boldsymbol{n} = (x_2, y_2) \cdot \boldsymbol{n} = (x_1, y_1) \cdot \boldsymbol{n}$, and

$$R_1(\theta) = \frac{\tau_2 x_2 - \tau_1 y_2}{\tau_2 \cos\theta - \tau_1 \sin\theta}, \quad R_2(\theta) = \rho^{-1} R_1(\theta). \tag{3.47}$$

We next derive the material paramters $\boldsymbol{C}$ and n in the Helmholtz equation (3.1) from (1.6) and (3.44).

Lemma 3.1. *The material parameters $\boldsymbol{C}$ and n for the polygonal cloak in $B_R = \Omega_-^p \cup \bar{\Omega}_-^a \cup \Omega_+$ take different forms as follows.*

(i) *In Ω_-^a, the entries of $\boldsymbol{C}$ in (1.5)-(1.6) take the form:*

$$C_{11} = \frac{r - R_1}{r} \frac{x^2}{r^2} + \frac{1}{r(r - R_1)} \left(\frac{\mathrm{d}R_1}{\mathrm{d}\theta} \frac{x}{r} - y \right)^2, \tag{3.48}$$

$$C_{22} = \frac{r - R_1}{r} \frac{y^2}{r^2} + \frac{1}{r(r - R_1)} \left(\frac{\mathrm{d}R_1}{\mathrm{d}\theta} \frac{y}{r} + x \right)^2, \tag{3.49}$$

$$C_{12} = \frac{r - R_1}{r} \frac{xy}{r^2} + \frac{1}{r(r - R_1)} \left(\frac{\mathrm{d}R_1}{\mathrm{d}\theta} \frac{x}{r} - y \right) \left(\frac{\mathrm{d}R_1}{\mathrm{d}\theta} \frac{y}{r} + x \right), \tag{3.50}$$

and

$$n = \frac{r - R_1}{r(1 - \rho)^2}. \tag{3.51}$$

(ii) *In $\Omega_+ = B_R \setminus \bar{\Omega}_-$, we have $\boldsymbol{C} = \boldsymbol{I}_2$ and $n = 1$.*

(iii) *Following [5], we set $\boldsymbol{C} = \boldsymbol{I}_2$ and $n = 1$ in Ω_-^p.*

Remark 3.3. *It is seen from (3.47) that R_1 has a different representation in different trapezoids $\{\Omega_T^i\}_{i=1}^6$ in Figure 3.4 (b), so the entries of $\boldsymbol{C}$ and the coefficient n are piecewise functions, which might be not continuous across the sides in the radial direction, e.g., A_pA.* □

Proof. As illustrated in (3.43), the transformation is given from polar coordinates $(\breve{r},\breve{\theta})$ (of the original Cartesian coordinates $(\breve{x},\breve{y})$) to polar coordinates (r,θ) (of the new Cartesian coordinates (x,y)), so by the chain rule, the Jacobian matrix $\boldsymbol{J}_{\rm cn}$ can be computed by

$$\boldsymbol{J}_{\rm cn}=\begin{bmatrix}\partial_{\breve{x}}x & \partial_{\breve{y}}x\\ \partial_{\breve{x}}y & \partial_{\breve{y}}y\end{bmatrix}=\begin{bmatrix}\partial_r x & \partial_\theta x\\ \partial_r y & \partial_\theta y\end{bmatrix}\begin{bmatrix}\partial_{\breve{r}}r & \partial_{\breve{\theta}}r\\ \partial_{\breve{r}}\theta & \partial_{\breve{\theta}}\theta\end{bmatrix}\begin{bmatrix}\partial_{\breve{x}}\breve{r} & \partial_{\breve{y}}\breve{r}\\ \partial_{\breve{x}}\breve{\theta} & \partial_{\breve{y}}\breve{\theta}\end{bmatrix}. \tag{3.52}$$

It is clear that

$$\begin{bmatrix}\partial_r x & \partial_\theta x\\ \partial_r y & \partial_\theta y\end{bmatrix}=\begin{bmatrix}\cos\theta & -r\sin\theta\\ \sin\theta & r\cos\theta\end{bmatrix},\quad \det\Bigg(\begin{bmatrix}\partial_r x & \partial_\theta x\\ \partial_r y & \partial_\theta y\end{bmatrix}\Bigg)=r, \tag{3.53}$$

and

$$\begin{bmatrix}\partial_{\breve{x}}\breve{r} & \partial_{\breve{y}}\breve{r}\\ \partial_{\breve{x}}\breve{\theta} & \partial_{\breve{y}}\breve{\theta}\end{bmatrix}=\begin{bmatrix}\cos\breve{\theta} & \sin\breve{\theta}\\ -\sin\breve{\theta}/\breve{r} & \cos\breve{\theta}/\breve{r}\end{bmatrix},\quad \det\Bigg(\begin{bmatrix}\partial_{\breve{x}}\breve{r} & \partial_{\breve{y}}\breve{r}\\ \partial_{\breve{x}}\breve{\theta} & \partial_{\breve{y}}\breve{\theta}\end{bmatrix}\Bigg)=\frac{1}{\breve{r}}. \tag{3.54}$$

Denote

$$\tilde{\boldsymbol{J}}:=\begin{bmatrix}\partial_{\breve{r}}r & \partial_{\breve{\theta}}r\\ \partial_{\breve{r}}\theta & \partial_{\breve{\theta}}\theta\end{bmatrix}, \tag{3.55}$$

which is determined by specific coordinate transformations. With a direct calculation, we derive from (1.6) the material parameters $\boldsymbol{C}$ and n for the general transformation in (3.43):

$$C_{11}=\frac{\breve{r}}{r^3\det(\tilde{\boldsymbol{J}})}\Big(\big(x\partial_{\breve{r}}r-ry\partial_{\breve{r}}\theta\big)^2+\frac{1}{\breve{r}^2}\big(x\partial_{\breve{r}}\theta-ry\partial_{\breve{\theta}}\theta\big)^2\Big), \tag{3.56}$$

$$C_{22}=\frac{\breve{r}}{r^3\det(\tilde{\boldsymbol{J}})}\Big(\big(y\partial_{\breve{r}}r+rx\partial_{\breve{r}}\theta\big)^2+\frac{1}{\breve{r}^2}\big(y\partial_{\breve{r}}r+rx\partial_{\breve{\theta}}\theta\big)^2\Big), \tag{3.57}$$

$$\begin{aligned}C_{12}=\frac{\breve{r}}{r^3\det(\tilde{\boldsymbol{J}})}\Big(&xy\Big(\partial^2_{\breve{r}}r+\frac{1}{\breve{r}^2}\partial^2_{\breve{\theta}}r-r^2\partial^2_{\breve{r}}\theta-\frac{r^2}{\breve{r}^2}\partial^2_{\breve{\theta}}\theta\Big)\\&+\frac{(x^2-y^2)r}{\breve{r}^2}\big(\breve{r}^2\partial_{\breve{r}}r\partial_{\breve{r}}\theta+\partial_{\breve{\theta}}r\partial_{\breve{\theta}}\theta\big)\Big),\end{aligned} \tag{3.58}$$

and

$$n=\frac{1}{\det(\boldsymbol{J}_{\rm cn})}=\frac{\breve{r}}{r\det(\tilde{\boldsymbol{J}})}. \tag{3.59}$$

We derive from (3.44) that in Ω_-^a,

$$\breve{r} = \frac{1}{1-\rho}(r - R_1), \quad \breve{\theta} = \theta, \tag{3.60}$$

which leads to

$$\tilde{\boldsymbol{J}} = \begin{bmatrix} 1-\rho & \partial_\theta R_1 \\ 0 & 1 \end{bmatrix}, \quad \det(\tilde{\boldsymbol{J}}) = 1-\rho. \tag{3.61}$$

Recall that $\partial_\theta R_1$ can be worked out by (3.47). Thus, the material parameters $\boldsymbol{C}$ and n in (3.48)-(3.51) can be obtained by substituting (3.60)-(3.61) into (3.56)-(3.59). □

3.2.2 Transmission conditions and new CBCs

For clear illustration, the disk B_R is partition into a finite number of non-overlapping quadrilateral elements by the nature of material coefficients (see, Figure 3.4). Decompose

$$B_R = \Omega_-^p \cup \bar{\Omega}_-^a \cup \Omega_+, \quad \bar{\Omega}_-^a = \cup_{i=1}^6 \bar{\Omega}_T^i, \quad \bar{\Omega}_+ = \cup_{i=1}^6 \bar{\Omega}^i, \tag{3.62}$$

where $\{\Omega_T^i\}$ are trapezoidal elements. Denote by $\Gamma_\pm^p$ the "outside" and "inside" boundaries of the cloaked region Ω_-^p, respectively, aiming to distinguish that the material parameters become infinite at the outside Γ_+^p, but are positive constants at the inside Γ_-^p. we also denote by $\Gamma^a := \bar{\Omega}_+ \cap \bar{\Omega}_-^a$, i.e., the outer boundary of Ω^a.

We now discuss about the imposition of interface conditions: (i) at Γ^a and sides in the radial direction of the trapezoids $\{\Omega_T^i\}$; and (ii) at the cloaking boundary $\Gamma_\pm^p$. For case (i), we impose the standard transmission conditions, that is, the tangential components of $\boldsymbol{E}$ and $\boldsymbol{H}$ are continuous across the interface (see, e.g., [28, Sec. 1.5] and [35]). Recall that under the polarisation $\boldsymbol{E} = (0, 0, u)^t$, this leads to

$$[\![u]\!] = [\![\boldsymbol{C}\nabla u]\!] = 0 \quad \text{for case (i).} \tag{3.63}$$

In case (ii), the material parameters are singular at Γ_+^p (cf. (3.48)-(3.50)), thus (3.63) are not applicable in this case. As a matter of fact, $\boldsymbol{E}_T := \boldsymbol{n} \times \boldsymbol{E} \times \boldsymbol{n}$ is not continuous across Γ_+^p. Accordingly, the imposition of appropriate CBCs to achieve perfect cloaking effects becomes a challenging issue. Practically, the perfect conducting condition, i.e., PEC (under TM polarisation) or PMC (under TE polarisation) was enforced at Γ_+^p in simulations (see, e.g., [37] for circular cloaks, [20, 21] for elliptic cloaks, [104, 27] for polygonal cloaks, and [31, 40] for time domain cloaks). However, as commented in [37], such a condition was sufficient but not necessary. Indeed, it was shown in [105], the PEC or PMC could not lead to an independent, meaningful boundary condition for circular cylindrical cloaks in polar coordinates.

Following the idea in Subsection 2.1.2 for circular cylindrical cloaks, we propose the essential "pole" conditions at Γ_+^p dubbed as "cloaking boundary condition" (CBC), which is an essential component for accurate simulation of polygonal cloaks. This essentially relies on the use of "local" coordinate system $(\boldsymbol{\tau}, \boldsymbol{n})$ to decompose the differential operators and then carefully study the singularity.

Proposition 3.3. *Let $(\boldsymbol{\tau}, \boldsymbol{n})$ be the "local" coordinate system in* (3.46)*. The CBCs take the form*

$$\nabla_{\boldsymbol{\tau}} u^+ = \boldsymbol{\tau} \cdot \nabla u^+ = 0 \ \text{ at } \ \Gamma_+^p; \quad \nabla_{\boldsymbol{n}} u^- = \boldsymbol{n} \cdot \nabla u^- = 0 \ \text{ at } \ \Gamma_-^p, \tag{3.64}$$

where $u^+ = u|_{B \setminus \bar{\Omega}_-^p}$ and $u^- = u|_{\bar{\Omega}_-^p}$.

Proof. Similar with the principle for the derivation of CBCs for circular cylindrical cloaks, we require that the finite and well-behaved fields in $\breve{\boldsymbol{r}} = (\breve{x}, \breve{y})$ still be finite in the new coordinates $\boldsymbol{r} = (x, y)$. We therefore apply this principle to the magnetic field in the cloaking layer, and show that the essential "pole" condition of the transformation (3.44) takes the form

$$\nabla_{\boldsymbol{\tau}} u^+ = 0 \quad \text{at} \quad \Gamma_+^p. \tag{3.65}$$

By (1.3), $\boldsymbol{H}^+ = \boldsymbol{H}|_{B\setminus\bar{\Omega}^p_-}$ takes the form

$$\boldsymbol{H}^+ = (H_1^+, H_2^+, 0)^t = \frac{1}{\mathrm{i}\omega\mu_0}\big(C_{12}u_x^+ + C_{22}u_y^+, -C_{11}u_x^+ - C_{12}u_y^+, 0\big)^t. \tag{3.66}$$

Then

$$u_x^+ = \tau_1\nabla_{\boldsymbol{\tau}}u^+ - \tau_2\nabla_{\boldsymbol{n}}u^+, \quad u_y^+ = \tau_2\nabla_{\boldsymbol{\tau}}u^+ + \tau_1\nabla_{\boldsymbol{n}}u^+. \tag{3.67}$$

Substituting (3.48)-(3.50) and (3.67) into (3.66) and dividing the terms into $\nabla_{\boldsymbol{n}}u$ and $\nabla_{\boldsymbol{\tau}}u$, we obtain

$$\begin{aligned}\mathrm{i}\omega\mu_0 H_1^+ = {}& \frac{\mathrm{d}R_1}{\mathrm{d}\theta}\frac{\tau_1}{r}\nabla_{\boldsymbol{\tau}}u^+ + \frac{\tau_2}{r-R_1}\Big(r + \Big(\frac{\mathrm{d}R_1}{\mathrm{d}\theta}\Big)^2\frac{1}{r}\Big)\nabla_{\boldsymbol{\tau}}u^+ \\ & - \Big(\frac{r-R_1}{r}\tau_1 + \frac{\mathrm{d}R_1}{\mathrm{d}\theta}\frac{\tau_2}{r}\Big)\nabla_{\boldsymbol{n}}u^+\end{aligned} \tag{3.68}$$

$$\begin{aligned}\mathrm{i}\omega\mu_0 H_2^+ = {}& \frac{\mathrm{d}R_1}{\mathrm{d}\theta}\frac{\tau_2}{r}\nabla_{\boldsymbol{\tau}}u^+ - \frac{\tau_1}{r-R_1}\Big(r + \Big(\frac{\mathrm{d}R_1}{\mathrm{d}\theta}\Big)^2\frac{1}{r}\Big)\nabla_{\boldsymbol{\tau}}u^+ \\ & - \Big(\frac{r-R_1}{r}\tau_2 - \frac{\mathrm{d}R_1}{\mathrm{d}\theta}\frac{\tau_1}{r}\Big)\nabla_{\boldsymbol{n}}u^+ .\end{aligned} \tag{3.69}$$

By (3.47),

$$\frac{\mathrm{d}R_1}{\mathrm{d}\theta} = R_1\frac{\tau_1 x + \tau_2 y}{\tau_2 x - \tau_1 y}, \tag{3.70}$$

which is bounded below and above in $\bar{\Omega}^a_-$ (note: $\tau_2 x - \tau_1 y \neq 0$ since the the boundary of Γ^p_+ cannot passes through the origin). Thus, $\boldsymbol{H}^+$ is a finite field in $\bar{\Omega}^a_-$, if and only if the first condition in (3.64) holds.

Let $\boldsymbol{H}^- = \boldsymbol{H}|_{\bar{\Omega}^p_-}$. From (3.4), (3.46), (3.48)-(3.50) and (3.66), we obtain

$$\begin{aligned}\boldsymbol{n}\times\big(\boldsymbol{H}^+ - \boldsymbol{H}^-\big)\big|_{r=R_1} &= \frac{1}{\mathrm{i}\omega\mu_0}\big(0,0,[\![\boldsymbol{C}\nabla u]\!]\big)^t\big|_{r=R_1} \\ &= \frac{1}{\mathrm{i}\omega\mu_0}\big(0,0,-\boldsymbol{n}\cdot(\boldsymbol{C}\nabla u^+) + \nabla_{\boldsymbol{n}}u^-\big)^t\big|_{r=R_1} \\ &= \frac{1}{\mathrm{i}\omega\mu_0}\Big(0,0,-\frac{r-R_1}{r}\nabla_{\boldsymbol{n}}u^+ + \frac{1}{r}\frac{dR_1}{d\theta}\nabla_{\boldsymbol{\tau}}u^+ + \nabla_{\boldsymbol{n}}u^-\Big)^t\Big|_{r=R_1},\end{aligned} \tag{3.71}$$

where $|_{r=R_1}$ means that u approaches Γ^p from Γ^p_+ and Γ^p_-. Given that $\nabla_{\boldsymbol{n}}u^+$ is finite, by (3.65), we have

$$\boldsymbol{n}\times\big(\boldsymbol{H}^+ - \boldsymbol{H}^-\big)\big|_{r=R_1} = \frac{1}{\mathrm{i}\omega\mu_0}\big(0,0,\nabla_{\boldsymbol{n}}u^-\big)^t\big|_{r=R_1}. \tag{3.72}$$

Inserting the second condition in (3.64) leads to

$$\boldsymbol{H}^- \times \boldsymbol{n} = \frac{1}{\mathrm{i}\omega\mu_0}\big(\nabla \times \boldsymbol{E}^-\big) \times \boldsymbol{n} = 0 \quad \text{at } \Gamma_-^p, \tag{3.73}$$

and by (3.71), the tangential component of the magnetic field $\boldsymbol{H}$ is continuous across the cloaking boundary. □

Remark 3.4. *Weder [65] proposed CBCs for point-transformed 3D invisibility cloaks:*

$$\boldsymbol{E}^+ \times \boldsymbol{n} = \boldsymbol{H}^+ \times \boldsymbol{n} = \boldsymbol{0} \quad \text{at } \partial K_+; \tag{3.74}$$

$$(\nabla \times \boldsymbol{E}^-) \cdot \boldsymbol{n} = (\nabla \times \boldsymbol{H}^-) \cdot \boldsymbol{n} = 0 \quad \text{at } \partial K_-, \tag{3.75}$$

where K is the cloaked region. These allowed for the decoupling of the governing equations of the inside and outside, and the spherical cloak was considered as a particular application. It is important to remark that (3.74)-(3.75) *are not applicable to the 2D polygonal cloak, as*

$$\boldsymbol{E}^+ \times \boldsymbol{n} = (\tau_1, \tau_2, 0)^t\, u^+ \neq \boldsymbol{0} \quad \text{at } \Gamma_+^p.$$

Indeed, $\boldsymbol{E}^+ = (0, 0, u^+)^t$ does not vanish at the outer cloaking boundary. Moreover, the condition (3.75) *is different from* (3.73)*. Notably, the CBCs in* (3.64) *also leads to the decoupling of the inside and outside, as we will see below.* □

Given the CBCs in (3.64), the governing equations are decoupled into

$$\nabla \cdot (\boldsymbol{C}(\boldsymbol{r})\, \nabla u^+(\boldsymbol{r})) + k^2 n(\boldsymbol{r}) u^+(\boldsymbol{r}) = 0 \quad \text{in } B_R \setminus \bar{\Omega}_-^p, \tag{3.76}$$

$$\text{Interface conditions in (3.63)}; \quad \nabla_{\boldsymbol{\tau}} u^+ = 0 \quad \text{at } \Gamma_+^p, \tag{3.77}$$

$$\partial_r u^+ - T_R[u^+] = h \quad \text{at } \partial B_R, \tag{3.78}$$

and

$$\Delta u^- + k^2 u^- = 0 \quad \text{in } \Omega_-^p; \quad \nabla_{\boldsymbol{n}} u^- = 0 \quad \text{at } \Gamma_-^p. \tag{3.79}$$

Remark 3.5. *It is standard to show that* (3.79) *has a unique solution $u^-(\boldsymbol{r}) \equiv 0$, if k^2 is not an eigenvalue of $-\Delta$ in Ω_-^p with homogeneous Neumann boundary condition.* □

3.2.3 Treatment of singularities in spectral-element discretisation

In order to accurately simulate the polygonal invisibility cloaks, we face the difficulty in dealing with the singular coefficients at the cloaking interface. With the new CBCs (3.64), we seek to build $\nabla_{\boldsymbol{\tau}} u^+ = 0$ at Γ_+^a in the spectral-element approximation space. We take $\Omega_T^1 = A_pB_pBA$ as an example, where A_pB_p has vertices (x_1, y_1) and (x_2, y_2). Suppose that A_pB_p is mapped to $\eta = -1$ via (3.20), i.e.,

$$\boldsymbol{r} = \boldsymbol{\chi}^e(\xi, -1) = \Big(\frac{x_2 - x_1}{2}\xi + \frac{x_1 + x_2}{2}, \frac{y_2 - y_1}{2}\xi + \frac{y_1 + y_2}{2}\Big), \quad \xi \in [-1, 1], \tag{3.80}$$

which yields

$$\partial_x \xi = \frac{2}{x_2 - x_1}, \;\; \partial_y \xi = \frac{2}{y_2 - y_1}, \;\; \partial_x \eta = \partial_y \eta = 0. \tag{3.81}$$

One verifies readily that

$$\begin{aligned} 0 = \nabla_{\boldsymbol{\tau}} u^+\big|_{A_pB_p} &= \big(\tau_1 \partial_x \xi + \tau_2 \partial_y \xi\big)\partial_\xi u^e(\xi, -1) + \big(\tau_1 \partial_x \eta + \tau_2 \partial_y \eta\big)\partial_\eta u^e(\xi, -1) \\ &= \frac{4}{\sqrt{(x_1 - x_2)^2 + (y_1 - y_2)^2}} \partial_\xi u^e(\xi, -1), \end{aligned}$$

where $u^e = u^+(\boldsymbol{\chi}^e(\xi, -1))$. Thus in (ξ, η)-coordinates, the CBCs satisfies

$$\partial_\xi u^e(\xi, -1) = 0, \quad \xi \in [-1, 1]. \tag{3.82}$$

Thus, the approximation space in (3.15) is modified as

$$\begin{aligned} V_N^E = \big\{ v \in C(B_R \setminus \bar{\Omega}_-^p) \,:\, v(\boldsymbol{r})|_{\Omega^e} = v(\boldsymbol{\chi}^e(\xi, \eta)) \in \mathcal{P}_N^2, \; 1 \le e \le E \;\text{ and} \\ \nabla_{\boldsymbol{\tau}} v(\boldsymbol{r})|_{\Omega_T^e \cap \Gamma_+^p} = \partial_\xi v(\boldsymbol{\chi}^e(\xi, -1)) = 0, \;\; 1 \le e \le E_T \big\}, \end{aligned} \tag{3.83}$$

where $E = 12$ and $E_T = 6$ for the setting in Figure 3.4. According to (3.83), the tensorial nodal basis in (3.17) is modified as:

$$\psi_{00} = l_0(\eta), \quad \psi_{ij} = l_i(\xi) l_j(\eta), \quad 0 \le i \le N, \;\; 1 \le j \le N, \tag{3.84}$$

and note that

$$\partial_\xi \psi_{00} = 0, \quad \partial_\xi \psi_{ij}\Big|_{\eta=-1} = l_i'(\xi) l_j(-1) = 0, \quad 0 \le i \le N, \;\; 1 \le j \le N. \tag{3.85}$$

With such a modification, the singularity can be absorbed by the basis and the spectral-element scheme (3.16) can be implemented as usual.

3.2.4 Simulation results for perfect polygonal cloaks

In this part, ample numerical results are provided and we make a comparison with results generated by the finite-element-based COMSOL Multiphysics package to demonstrate that our proposed approach produces accurate simulations of the polygonal cloaks. Given an incident plane wave with an incident angle θ_0:

$$u_{\rm in}(r,\theta) = e^{{\rm i}kr\cos(\theta-\theta_0)} = \sum_{|m|=0}^{\infty} {\rm i}^m J_m(kr) e^{{\rm i}m(\theta-\theta_0)}. \tag{3.86}$$

Accordingly h in (2.8) takes the form

$$h = \partial_r u_{\rm in} - T_R[u_{\rm in}] = {\rm i}k\cos(\theta-\theta_0) u_{\rm in} - \sum_{|m|=0}^{\infty} {\rm i}^m J_m(kR) \mathcal{T}_m e^{-{\rm i}m\theta_0},$$

where we recall $\mathcal{T}_m$ given in (2.7). In what follows, we consider a pentagonal cloak with vertices $A, B, \cdots, E$ where in the polar coordinates, the radius $r = 0.7$ for all the vertices and the angle are $\theta = (\pi/5, 3\pi/7, 8\pi/9, 6\pi/5, 7\pi/4)$, respectively. We take $\rho = 0.7$ in (3.45) and $R = 1.0$, and a cut-off number $M = 60$ in (3.16) for the truncated DtN operator $T_R^M[u_N^E]$. Recall the discussion in Remark 3.2, we choose $M \ge kR$ for given k, R practically. In the following numerical studies, M is chosen relatively higher than kR due to the fact that $\boldsymbol{C}$ and n in the cloaking layer are singular and inhomogeneous (note: the results and analysis in Remark 3.2 were for Helmholtz problems with homogeneous media), and such a choice ensures the truncation error to be negligible.

We depict in Figure 3.5 the real part of electric field for $k = 40$ given by (i) SEM with 40×40-grid for each element with a total degree of freedom (DOF):

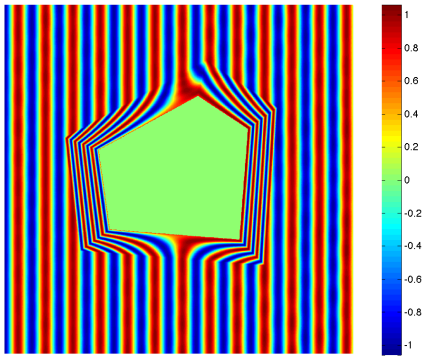

(a) Electric field (FEM)

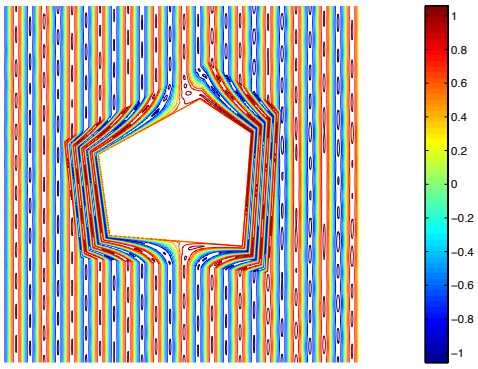

(b) Contour (FEM)

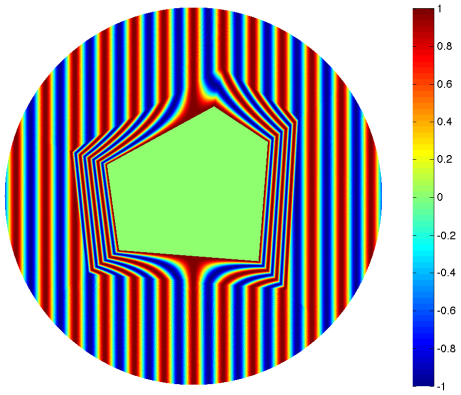

(c) Electric field (SEM)

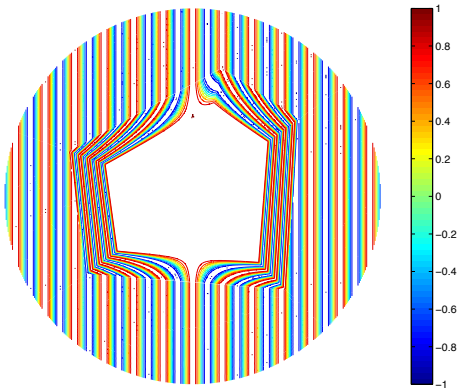

(d) Contour (SEM)

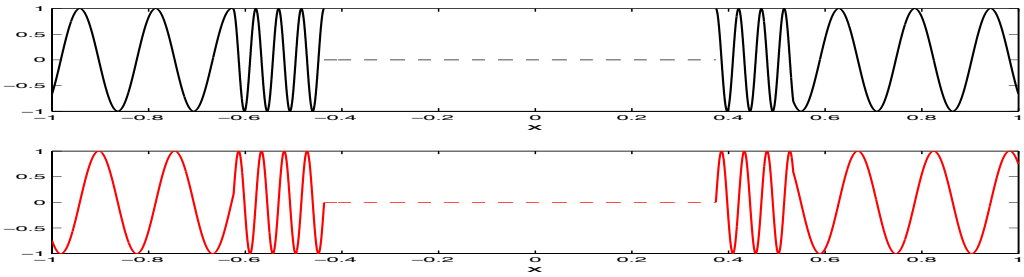

(e) Profiles of the real and imaginary parts of the electric field along $\theta = 0$ by SEM

Figure 3.5: A comparison study: SEM versus FEM, where $\theta_0 = 0$ and $k = 40$.

16,000, and (ii) FEM with piecewise quadratic finite element approximation with a total DOF: 726,933 (so as to generate reasonable results). Note that the maximum magnitude of the field should be 1. However, in Figure 3.5 (b), we observe from the colorbar that the magnitude of the field is approximately 1.05, which is caused by the numerical error and the contour between two wavefronts are slightly blended together. While the SEM result in Figure 3.5 (d) is very accurate. In fact, the proposed method to seamlessly integrating SEM with global DtN TBC and the careful treatment of the new CBCs enable us to simulate the polygonal invisibility cloaks acurately.

To further demonstrate the performance of the proposed approach, we choose an oblique incident angle $\theta_0 = \pi/4$, and increase the incident wave number to $k = 80$ (see Figure 3.6). We plot in (a) the real part of the fields with a 80×80-grid in each element with the same mesh setting in Figure 3.5 (c) and a cut-off number $M = 80$. We see that even for highly oscillatory fields, the wave is completely guided and bent around the cloaked region. Also, as is observed in the color bar, the magnitude of the field is identically 1, which implies that the wave is propagating without introducing any scattering waves. Besides, we also depict the time-averaged Poynting vector (cf. [28]): $\boldsymbol{S} = \mathrm{Re}\{\boldsymbol{E}\times\boldsymbol{H}^*\}/2$, to show the directional energy flux density. In (b), we depict the associated Poynting vector fields. We find that the energy flow vector is steered smoothly around the polygonal cloaked region without reflecting and scattering.

We now test with an external source, compactly supported in Ω_+ as the wavemaker. To be more precise, (3.76) and (3.78) are modified as

$$\begin{aligned} &\nabla\cdot(\boldsymbol{C}(\boldsymbol{r})\nabla u^+(\boldsymbol{r})) + k^2 n(\boldsymbol{r})u^+(\boldsymbol{r}) = f(\boldsymbol{r}) \ \text{ in } \ \Omega_+;\\ &\partial_r u^+ - T_R[u^+] = 0 \quad \text{at } \ \Gamma_R. \end{aligned} \tag{3.87}$$

Practically, we choose f to be a Guassian function:

$$f(\boldsymbol{r}) = \alpha\exp\Big(-\frac{(x-\beta)^2+(y-\kappa)^2}{2\gamma^2}\Big), \tag{3.88}$$

where $\alpha,\beta,\kappa,\gamma$ are tunable constants. To this end, we take $\alpha = 100$, $\beta = -0.41$, $\kappa = 0.75$ and $\gamma = 0.04$, so that f is almost zero outside B_R. In Figure 3.6 (c), we

set $k = 40$, $M = 60$ and depict the real part of the electric field obtained from SEM with 40×40-grid in each element. It is observed that the waves obtained by the external source are smoothly bent and the cloak does not produce any scattering. Also, the waves pass through the exterior boundary ∂B_R smoothly without introducing any reflection.

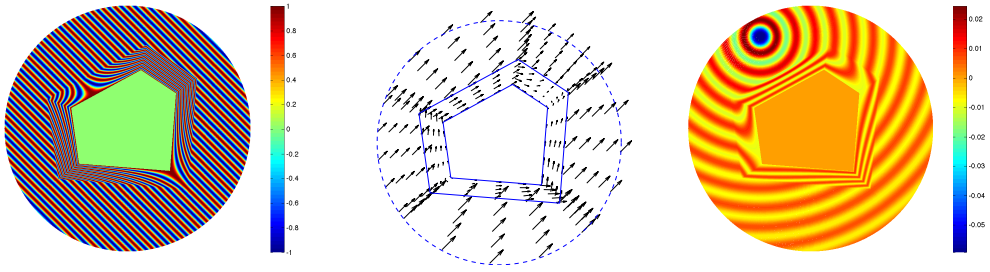

(a) Electric field (b) Poynting vector (c) External source

Figure 3.6: SEM with high frequency wave and external source.

3.2.5 Numerical study of effects of defects, lossy media and dispersive media

With the aid of the accurate SEM solver, we can further explore various situations in real applications, e.g., the effect of defects, loss and dispersion in the polygonal cloaking layer on the invisible property. Analytic investigation has been devoted to the circular and spherical cloaks (see, e.g., [37, 106, 70, 107, 71]), but the tools appear inapplicable to the polygonal cloaks.

Defects in the cloaking layer

We consider the influence of defects to the perfect polygonal cloak. As illustrated in Figure 3.7 (a)-(b), a rectangular defect with length a and width b is embedded into the cloaking layer. We set $\boldsymbol{C} = \boldsymbol{I}_2$ and $n = 1$ within the defect, so the traditional transmission condition (3.2) can be imposed at four sides, if the defect is not aligned with the cloaking boundary. In Figure 3.7 (a), we depict the electric

field distribution with defect $a = b = 0.06$ obtained by the proposed SEM with $k = 40$, $\theta_0 = 0$, $M = 60$ and $N = 40$. Observe that even with such a small defect, the electric field distribution is apparently disturbed, especially for the forward-scattering region, and the magnitude increases approximately up to 1.5 (note: it is 1 for the perfect cloak). Also notice that in the back-scattering region, the waves appear not significantly affected, so the cloaking effects seem still good. In Figure 3.7 (b), we enlarge the defect and set $a = 0.24$, $b = 0.06$. The field in both the back and forward scattering regions is deteriorated more.

Lossy media in the cloaking layer

Similar to the setting in [37, 106] for the circular and spherical cloaks, we replace the media in cloaking layer by a electric-lossy medium (cf. [28]). More precisely, the real electric permittivity $\boldsymbol{\epsilon}$ in (1.5) is replaced by a complex electric permittivity $(1 + \mathrm{i}\tan\delta)\boldsymbol{\epsilon}$, where $\tan\delta$ is a tunable constant termed as loss tangent to quantify the absorptive property of the medium. Note that this replacement only brings about the modification of the two-dimensional Helmholtz equation (1.9) as

$$\nabla \cdot (\boldsymbol{C}(\boldsymbol{r})\, \nabla u(\boldsymbol{r})) + k^2(1 + \mathrm{i}\tan\delta)n(\boldsymbol{r})\, u(\boldsymbol{r}) = 0.$$

In Figure 3.7, we depict the electric field distributions with loss tangent $\tan\delta = 0.01, 0.05$ in (c) and (d), respectively, where we take $k = 40$, $\theta_0 = 0$, $M = 60$ and $N = 40$ in each element. Observe that in the first case, the effect of the loss is almost imperceptible. As we enlarge the loss tangent to 0.05 in (d), the cloaking effect appears good in the backscattering region but is apparently deteriorated in the forward-scattering region, which is inevitable because the lossy medium absorbs the forward-travelling wave power. We point out that similar phenomena were observed for the circular and spherical cloaks in [37, 106].

Drude model and dispersive media in the cloaking layer

Based on the form-invariant coordinate transformation, the polygonal cloak can perfectly conceal arbitrary objects inside the interior polygonal domain. However, in practice, the material for manufacturing such cloaks are frequency-dependent and perfect invisibility can only be achieved for a single frequency, known as the "cloaking frequency" (cf. [5, 71, 108]). It is of much physical relevance to study the response of an ideal cloak to a non-monochromatic electromagnetic wave passing through such a dispersive cloak. The investigation along this line has been very limited to mostly analytic treatments of circular and spherical cloaks (cf. [107, 71]). We demonstrate that the proposed SEM offers an accurate means to understand some interesting phenomena of a nonmonochromatic wave interacting with a polygonal cloak.

Following the procedure in [70], we start with diagonalizing the symmetric matrices $\boldsymbol{\epsilon}$ and $\boldsymbol{\mu}$ in (1.5)-(1.6), i.e.,

$$\boldsymbol{\epsilon} = \boldsymbol{\mu} = \boldsymbol{P}\boldsymbol{\Lambda}\boldsymbol{P}^t, \quad \boldsymbol{\Lambda} = \mathrm{diag}(\lambda_1, \lambda_2, \lambda_3), \tag{3.89}$$

where $\boldsymbol{P} = (P_{ij})_{1\le i,j\le 3}$ is an orthonormal matrix (with $P_{j3} = P_{3j} = 0$ for $j = 1, 2$, and $P_{33} = 1$), and the eigenvalues are

$$\begin{aligned} \lambda_1 &= \frac{C_{11} + C_{22} + \sqrt{(C_{11} + C_{22})^2 - 4}}{2}, \\ \lambda_2 &= \frac{C_{11} + C_{22} - \sqrt{(C_{11} + C_{22})^2 - 4}}{2}, \end{aligned} \tag{3.90}$$

and $\lambda_3 = n$. From (3.48)-(3.49), we have

$$C_{11} + C_{22} = \frac{r - R_1}{r} + \frac{1}{r(r - R_1)}\Big(r^2 + \Big(\frac{dR_1}{d\theta}\Big)^2\Big) \ge \frac{r - R_1}{r} + \frac{r}{r - R_1} \ge 2, \tag{3.91}$$

which implies $\lambda_1 > 1$. However, λ_2 and λ_3 are less than 1 for some $r \in (R_1, R_2)$. Based on the principle in [70, 71], we modify λ_2 and λ_3 by using the Drude model (cf. [28]). More precisely, let $\omega_c > 0$ be the "cloaking frequency", and define

$$\tilde{\lambda}_i := \tilde{\lambda}_i(\boldsymbol{r}, \omega) = 1 - \frac{\omega_{p,i}^2}{\omega(\omega + \mathrm{i}\gamma_i)}, \quad \text{with} \quad \omega_{p,i}^2 := \omega_c(\omega_c + \mathrm{i}\gamma_i)(1 - \lambda_i), \quad i = 2, 3,$$

where $\{\gamma_i\}_{i=2}^3$ are given collision frequencies, and $\{\omega_{p,i}\}_{i=2}^3$ are known as the plasma frequencies. For notational convenience, we define

$$\beta_i := \frac{\omega_c(\omega_c + \mathrm{i}\gamma_i)}{\omega(\omega + \mathrm{i}\gamma_i)}, \quad \text{so} \quad \tilde{\lambda}_i = 1 + \beta_i(\lambda_i - 1), \quad i = 2, 3. \tag{3.92}$$

Denoting $\widetilde{\boldsymbol{\Lambda}} = \mathrm{diag}(\tilde{\lambda}_1, \tilde{\lambda}_2, \tilde{\lambda}_3)$ with $\tilde{\lambda}_1 = \lambda_1$, we then replace the material parameters $\boldsymbol{\epsilon}$ and $\boldsymbol{\mu}$ in (1.2), respectively, by

$$\tilde{\boldsymbol{\epsilon}} = \tilde{\boldsymbol{\mu}} = \boldsymbol{P}\widetilde{\boldsymbol{\Lambda}}\boldsymbol{P}^t = \begin{bmatrix} \widetilde{\boldsymbol{C}} & \mathbf{0}^t \\ \mathbf{0} & \tilde{n} \end{bmatrix}, \tag{3.93}$$

where by a direct calculation, we have

$$\widetilde{\boldsymbol{C}} = \begin{bmatrix} \widetilde{C}_{11} & \widetilde{C}_{12} \\ \widetilde{C}_{12} & \widetilde{C}_{22} \end{bmatrix} = \boldsymbol{C} + (1 - \beta_2)(1 - \lambda_2) \begin{bmatrix} P_{12}^2 & P_{12}P_{22} \\ P_{12}P_{22} & P_{22}^2 \end{bmatrix}, \tag{3.94}$$

and

$$\tilde{n} = 1 + \beta_3(\lambda_3 - 1) = \tilde{\lambda}_3. \tag{3.95}$$

One verifies readily from (3.93) that

$$\det(\tilde{\boldsymbol{\epsilon}}) = \det(\tilde{\boldsymbol{\mu}}) = \tilde{\lambda}_1\tilde{\lambda}_2\tilde{\lambda}_3 = \lambda_1\tilde{\lambda}_2\,\tilde{n} = \det(\widetilde{\boldsymbol{C}})\,\tilde{n}. \tag{3.96}$$

Thus, using the fact $\lambda_1\lambda_2 = 1$ (cf. (3.90)), we obtain from (3.92) and (3.96) that

$$\det(\widetilde{\boldsymbol{C}}) = \lambda_1\tilde{\lambda}_2 = \lambda_1(\beta_2\lambda_2 + 1 - \beta_2) = \beta_2 + (1 - \beta_2)\lambda_1. \tag{3.97}$$

Accordingly, we find that

$$\tilde{\boldsymbol{\mu}}^{-1} = \tilde{\boldsymbol{\epsilon}}^{-1} = \begin{bmatrix} \widehat{C}_{22} & -\widehat{C}_{12} & 0 \\ -\widehat{C}_{12} & \widehat{C}_{11} & 0 \\ 0 & 0 & \tilde{n}^{-1} \end{bmatrix}, \quad \text{where} \quad \widehat{C}_{ij} = \frac{\widetilde{C}_{ij}}{\beta_2 + (1 - \beta_2)\lambda_1}, \tag{3.98}$$

for $i, j = 1, 2$. Using (3.66) with $\widehat{C}_{ij}$ and $\tilde{n}$ in place of C_{ij} and n, we obtain the new model defined in the cloaking layer:

$$\nabla \cdot \big(\widehat{\boldsymbol{C}}(\boldsymbol{r}, \omega)\, \nabla u(\boldsymbol{r})\big) + k^2\, \tilde{n}(\boldsymbol{r}, \omega)\, u(\boldsymbol{r}) = 0, \tag{3.99}$$

where $\widehat{\boldsymbol{C}} = (\widehat{C}_{ij})_{1 \le i,j \le 2}$, and $k = \omega\sqrt{\epsilon_0\mu_0}$ as before.

Remark 3.6. *Observe from* (3.92) *that if* $\omega = \omega_c$, *then* $\beta_i = 1$ *and* $\lambda_i = \tilde{\lambda}_i$ *for* $i = 1, 2$. *Thus, in this case,* (3.99) *reduces to* (3.1) *and* $\widehat{\boldsymbol{C}}(\boldsymbol{r}, \omega_c)$ *is singular at the cloaking boundary* $r = R_1$. *However, if* $\omega \neq \omega_c$ *(so* $\beta_2 \neq 1$*), then* $\widehat{\boldsymbol{C}}(\boldsymbol{r}, \omega)$ *becomes regular at* $r = R_1$. *Indeed, by* (3.98),

$$\widehat{C}_{ij} = \frac{(r - R_1)\widetilde{C}_{ij}}{\beta_2(r - R_1) + (1 - \beta_2)(r - R_1)\lambda_1}.$$

In fact, one can verify that if $\beta_2 \neq 1$,

$$\lim_{r \to R_1} (r - R_1)\big\{\boldsymbol{C}, \lambda_1, \lambda_2\big\} \quad \textit{all exist.}$$

Thus, we can claim from (3.94) *and the above that* $\widehat{\boldsymbol{C}}(\boldsymbol{r}, \omega)$ *is well-defined at* $r = R_1$. *In view of this, the CBCs can not be applied. Here, we follow [107, 71] and impose a PMC shell instead.* □

In the computation, we take $\omega_c = k_c/\sqrt{\epsilon_0\mu_0}$ with $k_c = 40$, and $\gamma_i/\sqrt{\epsilon_0\mu_0} = 0.0001$ for $i = 2, 3$. In Figure 3.7 (e)-(f), we plot the electric field distributions with $k = 39$ and $k = 41$ illuminated by plane wave in (3.86) with incident angle $\theta_0 = 0$ and the cut-off number $M = 60$ and $N = 45$ in each element. In contrast with Figure 3.5 (c) (where perfect cloaking effect can be obtained for $k_c = 40$), we observe from Figure 3.7 that the electric field distributions are affected and distorted in both cases (i.e., $k = k_c \pm 1$), in particular, more severely when $k < k_c$. Indeed, similar to the phenomena observed in [71, 107] for circular and spherical cloaks, the incident wave with frequency slightly deviated below k_c, the field after the wave passes the cloak is dissipated and a large shadow appears in the forward scattering region. While for the incident wave with frequency slightly deviated above k_c, the field in most part of the cloaking layer does not change much, except for the part close to the cloaking boundary $r = R_1$, and the field behind the cloak is reinforced. This can be regarded as the frequency shift effect as in [71].

3.3 Accurate simulation of concentrators and rotators

In this section, we further apply the efficient spectral-element solver to accurately simulate the electromagnetic concentrators and rotators.

3.3.1 Polygonal concentrators

The electromagnetic concentrator aims at intensifying electromagnetic waves in a certain region, which play an important role in the harnessing of light in solar cells or similar devices, where high field intensities are needed.

Here, we are interested in the polygonal concentrator with a configuration similar to the polygonal cloak illustrated in Figure 3.8 (b), where EM waves are expected to be concentrated in the interior convex polygonal region Ω_-^p. It is accomplished by a coordinate transformation that maps the "polygonal annulus" in Figure 3.8 (a) to the "polygonal annulus" in Figure 3.8 (b), where the interior portion of the latter has larger area. More precisely, the polygonal concentrator is mapped from the same structure in Figure 3.8 (b) but with a different ratio (see Figure 3.8 (a)):

$$\breve{\rho} = \frac{OA_o}{OA} = \frac{OB_o}{OB} = \cdots, \quad 0 < \rho < \breve{\rho} < 1, \tag{3.100}$$

where ρ is defined in (3.45). Then the ratio $\rho/\breve{\rho}$ is known as the rate of concentration. For notational convenience, we define

$$\varrho := 1 - \frac{1-\rho}{1-\breve{\rho}}. \tag{3.101}$$

The corresponding coordinate transformation takes the form (see, e.g., [109]):

(i) In Ω_-,

$$\begin{cases} r = \dfrac{\rho}{\breve{\rho}}\,\breve{r}, & \breve{r} \in [0, \breve{R}_1], \;\; r \in [0, R_1], \\ r = (1-\varrho)\,\breve{r} + \varrho\, R_2, & \breve{r} \in [\breve{R}_1, R_2], \;\; r \in [R_1, R_2], \end{cases} \tag{3.102}$$

and $\theta = \breve{\theta} \in [0, 2\pi)$;

(ii) In $\Omega_+ = B_R \setminus \bar{\Omega}_-$, the transformation is identity: $r = \breve{r},\ \theta = \breve{\theta}$.

Here, $R_i,\ i = 1, 2$, are the same as in (3.47) and $\breve{R}_1 = \breve{\rho}/\rho R_1$.

Lemma 3.2. *Using* (1.6)*, we can derive the coefficients* $\boldsymbol{C}$ *and* n *as follows:*

(i)$_a$ *In* Ω_-^{p}*,*

$$\boldsymbol{C} = \boldsymbol{I}_2, \quad n = \breve{\rho}^2/\rho^2\,. \tag{3.103}$$

(i)$_b$ *In* Ω_-^{a}*,*

$$C_{11} = \chi\,\frac{x^2}{r^2} + \frac{\varrho}{r - \varrho R_2}\left(\frac{\varrho}{r}\frac{\mathrm{d}R_2}{\mathrm{d}\theta}\frac{x^2}{r^2} - \frac{2xy}{r^2}\right)\frac{\mathrm{d}R_2}{\mathrm{d}\theta} + \frac{1}{\chi}\,\frac{y^2}{r^2}, \tag{3.104}$$

$$C_{22} = \chi\,\frac{y^2}{r^2} + \frac{\varrho}{r - \varrho R_2}\left(\frac{\varrho}{r}\frac{\mathrm{d}R_2}{\mathrm{d}\theta}\frac{y^2}{r^2} + \frac{2xy}{r^2}\right)\frac{\mathrm{d}R_2}{\mathrm{d}\theta} + \frac{1}{\chi}\,\frac{x^2}{r^2}, \tag{3.105}$$

$$C_{12} = \left(\chi - \frac{1}{\chi}\right)\frac{xy}{r^2} + \frac{\varrho}{r - \varrho R_2}\left(\frac{x^2}{r^2} + \frac{\varrho}{r}\frac{\mathrm{d}R_2}{\mathrm{d}\theta}\frac{xy}{r^2} - \frac{y^2}{r^2}\right)\frac{\mathrm{d}R_2}{\mathrm{d}\theta}, \tag{3.106}$$

and

$$n = \frac{r - \varrho R_2}{r(1 - \varrho)^2}\,, \tag{3.107}$$

where $\chi = (r - \varrho R_2)/r$.

(ii) *In* Ω_+*, we have* $\boldsymbol{C} = \boldsymbol{I}_2$ *and* $n = 1$.

Proof. Similarly with the polygonal invisibility cloak, for the polygonal cylindrical concentrator, we obtain from the transformation (3.102) that in Ω_-^{a},

$$\breve{r} = \frac{1}{1 - \varrho}(r - \varrho R_2), \quad \breve{\theta} = \theta, \tag{3.108}$$

and

$$\tilde{\boldsymbol{J}} = \begin{bmatrix} 1 - \varrho & \varrho\partial_\theta R_2 \\ 0 & 1 \end{bmatrix}, \quad \det(\tilde{\boldsymbol{J}}) = 1 - \varrho\,. \tag{3.109}$$

Inserting (3.108) and (3.109) into (3.56)-(3.59), we obtain $\boldsymbol{C}$ and n in (3.104)-(3.107).

□

In summary, the governing equation for the polygonal concentrator reads

$$\nabla \cdot (\boldsymbol{C}(\boldsymbol{r})\,\nabla u(\boldsymbol{r})) + k^2 n(\boldsymbol{r}) u(\boldsymbol{r}) = 0 \quad \text{in } B_R, \tag{3.110}$$

$$[\![u]\!] = [\![\boldsymbol{C}\,\nabla u]\!] = 0 \quad \text{at } \Gamma^p \cup \Gamma^a, \tag{3.111}$$

$$\partial_r u - T_R[u] = h \quad \text{at } \partial B_R. \tag{3.112}$$

Note that in the interior polygon, (3.110) becomes the Helmholtz equation:

$$\Delta u + \frac{\breve{\rho}^2}{\rho^2} k^2 u = 0 \quad \text{in } \Omega_-^p, \tag{3.113}$$

where the ratio $\breve{\rho}^2/\rho^2 > 1$ is a constant. Therefore, the coordinate transformation enlarges the wavenumber k that produces the effect of concentration.

We can implement the spectral-element solver based on the partition of the computational domain as with the previous application. However, different from the previous case, the interior region is part of the computational domain, where a normal transmission condition is imposed along its boundary (see (3.111)). Below, we provide some numerical results with the setting: a square concentrator centred at the origin with length of each side 1.2 and the parameters: $\rho = 1/3,\ \breve{\rho} = 2/3$ in (3.45) and (3.100) and $R = 1.0$. We set the cut-off number $M = 60$ in the DtN operator. In Figure 3.9, we depict the electric field distributions and the associated time averaged Poynting vectors illuminated with different incident angles ((a)-(b): $\theta_0 = 0$ and (c)-(d): $\theta_0 = \pi/4$) with $k = 40$ and the grid $N = 50$ in each element. It can be seen that the electric field and energy flux are smoothly concentrated into the inner concentration region Ω_-^p, and the field outside is not affected regardless of the incident angle on the concentrator.

3.3.2 Circular rotators

In contrast with the invisibility cloak and concentrator, the electromagnetic rotator is based upon a coordinate transformation of the angular variable rather than the radial variable in (3.43).

As illustrated in Figure 3.8 (c), the domain Ω_- is a disk of radius $r = b$, which encloses a concentric disk of radius $r = a < b$. The waves are expected to rotate with a fixed angle θ_1 in the interior disk. This can be realised by the coordinate transformation (cf. [9]):

$$\begin{cases} r = \breve{r}, \quad \theta = \breve{\theta} + \theta_1, & 0 < \breve{r} < a, \ \ \breve{\theta},\, \theta \in [0, 2\pi), \\ r = \breve{r}, \quad \theta = \breve{\theta} + \dfrac{s(b) - s(\breve{r})}{s(b) - s(a)}\theta_1, & a < \breve{r} < b, \ \ \breve{\theta},\, \theta \in [0, 2\pi), \end{cases} \tag{3.114}$$

where s is any smooth function such that $s(b) \neq s(a)$. As before, the transformation is identity exterior to Ω_-.

Lemma 3.3. *Define*

$$\kappa = \frac{s'(r)}{s(b) - s(a)}\,\theta_1. \tag{3.115}$$

Working out the material parameters as before, we have

$$\boldsymbol{C} = \frac{1}{r^2}\begin{bmatrix} r^2 + 2\kappa xy + \kappa^2 y^2 & -\kappa x^2 - \kappa^2 xy + \kappa y^2 \\ -\kappa x^2 - \kappa^2 xy + \kappa y^2 & r^2 - 2\kappa xy + \kappa^2 x^2 \end{bmatrix}, \quad n = 1 \quad \text{for } \ a < r < b,$$

and

$$\boldsymbol{C} = \boldsymbol{I}_2, \quad n = 1 \quad \text{for } \ 0 < r < a, \ \ b < r < R.$$

Proof. For the circular rotators, we have from (3.114) that

$$\breve{r} = r, \quad \breve{\theta} = \theta - \frac{s(b) - s(r)}{s(b) - s(a)}\theta_1, \tag{3.116}$$

and

$$\begin{bmatrix} \partial_{\breve{r}} r & \partial_{\breve{\theta}} r \\ \partial_{\breve{r}} \theta & \partial_{\breve{\theta}} \theta \end{bmatrix} = \begin{bmatrix} 1 & 0 \\ -\kappa & 1 \end{bmatrix}, \tag{3.117}$$

where κ is defined in (3.115). Then we can compute the material parameters (3.115) in a similar fashion as the polygonal invisibility cloak. □

In Figure 3.8 (d), we illustrate a partition of the computational domain B_R. Together with the standard transmission conditions in (3.4), we can implement

the spectral-element scheme as the previous cases with a similar partition of the computational domain (see Figure 3.8 (d)). In the computation, we set $a = 0.3$, $b = 0.7$ and $s(r) = r$ in (3.114) and choose $R = 1.0$, $M = 60$ and $N = 40$ in each element. In Figure 3.10, we fix $k = 40$, and plot the electric field distribution (real part) and the corresponding time averaged Poynting vector with the same incident angle $\theta_0 = 0$ and different rotation angles ((a)-(b): $\theta_1 = \pi/4$, (c)-(d): $\theta_1 = 3\pi/4$). We find that the electric field distribution rotates its direction by $\pi/4$ in Figure 3.10 (a) and the power flux (b) flows with the same direction in the closed region $r < a$. It can be observed in Figure 3.10 (c)-(d) that even for a very sharp rotation angle $\theta_1 = 3\pi/4$, the field rotates exactly by $3\pi/4$ angle without introducing any scattering wave outside.

3.4 Extension to three-dimensional simulations

The methodology can shed light on three-dimensional simulations. Indeed, the semi-analytic approach for dealing with the nonlocal DtN boundary condition is extendable to the three-dimensional DtN boundary condition, though it is much more involved, and requires the use of special partition of the computational domain. Recall the three-dimensional DtN boundary condition (see, e.g., [56]):

$$T_R[U] = \sum_{l=1}^{\infty} \sum_{|m|=0}^{l} k \frac{h_l^{(1)'}(kR)}{h_l^{(1)}(kR)} \widehat{U}_l^m Y_l^m, \quad \text{with} \quad \widehat{U}_l^m = \int_S U\big|_{r=R} \overline{Y_l^m}\, dS,$$

where $\{Y_l^m(\theta, \phi)\}$ (with $(\theta, \phi) \in [0, \pi] \times [0, 2\pi)$) are spherical harmonics defined on the unit spherical surface S, and $\{h_l\}$ are the spherical Hankel functions. We show in [110] that given the nodal values of U on a longitude-latitude θ-ϕ partition of S, and using the trigonometric form of the associated Legendre functions $\{P_l^m(\cos\theta)\}$, we can evaluate the double integral on S (the counterpart of (3.23)) by products of two one-dimensional integrals, and notably, similar analytic formulas can be used. Note that such a partition of S can be seamlessly integrated with spectral elements (but with some non-standard elements near

two poles). Another approach is to partition the spherical surface by using the popular cubed-sphere transform. This allows to use standard hexahedral elements for the interior computational domain, but one has to adopt an element-wise interpolation between spectral-element grids and grids for the analytic approach in ϕ direction.

Below, we further discuss the extension of our approach to accurate simulation of polyhedral invisibility cloaks with an emphasis on the understanding of the singularity at the inner boundary induced by the singular coordinate transformation.

Similar to the polygonal cloak, the coordinate transformation for a polyhedral cloak blows up the origin O in the original $(\breve{x}, \breve{y}, \breve{z})$-coordinates to the polyhedral domain Ω_-^p, which forms the "cloaked region". Accordingly, the polyhedral domain Ω_- is compressed into the "polyhedral annulus" $\Omega_-^a = \Omega_- \setminus \bar{\Omega}_-^p$. In Figure 3.11, we illustrate the pyramid $OABCD$ (one subdomain of Ω_-) is compressed into the pyramidal frustum $A_pB_pC_pD_pABCD$ (the corresponding subdomain of Ω_-^a). To fix the idea, we consider the case with the base $ABCD$ being perpendicular to z-axis.

Like (3.43)-(3.44), the coordinate transformation for a polyhedral cloak is defined between two spherical coordinates:

$$r = (1-\rho)\,\breve{r} + R_1, \quad \breve{r} \in [0, R_2], \;\; r \in [R_1, R_2], \tag{3.118}$$

$\theta = \breve{\theta}$ and $\phi = \breve{\phi}$, where

$$\rho = \frac{OA_p}{OA} = \frac{OB_p}{OB} = \cdots, \quad 0 < \rho < 1,$$

and $(R_1(\theta,\phi),\theta,\phi)$ (resp. $(R_2(\theta,\phi),\theta,\phi)$) is the parametric form of the surface $A_pB_pC_pD_p$ (resp. $ABCD$).

Different from the 2D case, we work with the full Maxwell's equations (1.3), but we can still follow Subsection 3.2.1 to compute the material parameters $\boldsymbol{\epsilon}$ and $\boldsymbol{\mu}$. The parameters are singular at the inner surface of the polyhedral domain Ω_-^a (e.g., $A_pB_pC_pD_p$), but the singularity behaves quite differently, compared with the

2D case. In fact, the situation is akin to the difference between the singularities of the cylindrical cloak (cf. [105]) and the spherical cloak (cf. [65, 67]).

We next follow the argument in Proposition 3.3 to derive the essential cloaking boundary conditions for 3D case, which are critical for the accurate simulation. For simplicity, we consider the subdomain in Figure 3.11, where the surface $A_pB_pC_pD_p$ is perpendicular to z-axis defined by $z = z_0 \neq 0$.

Proposition 3.4. *Let $\boldsymbol{E} = (u_1, u_2, u_3)^t$, and denote the tangential and normal components of a vector field by the subscripts $_\parallel$ and $_\perp$, respectively, that is,*

$$\begin{aligned} &(\nabla \times \boldsymbol{E})_\parallel = (\partial_y u_3 - \partial_z u_2, \partial_z u_1 - \partial_x u_3)^t, \\ &(\boldsymbol{E})_\parallel = (u_1, u_2)^t, \quad (\nabla \times \boldsymbol{E})_\perp = \partial_x u_2 - \partial_y u_1. \end{aligned} \tag{3.119}$$

Under the assumption that the finite and well-behaved field $\boldsymbol{E}$ in $\breve{\boldsymbol{r}} = (\breve{x}, \breve{y}, \breve{z})$ still be finite in the new coordinates, the essential cloaking boundary conditions on the surface $A_pB_pC_pD_p : z = z_0$, take the form

$$\begin{aligned} &(\boldsymbol{E}^+)_\parallel = (\nabla \times \boldsymbol{E}^+)_\parallel = \boldsymbol{0}, \ \ \frac{1}{z - z_0}(\nabla \times \boldsymbol{E}^+)_\perp = 0, \ \ \text{at} \ \ \Gamma_+^p; \\ &(\nabla \times \boldsymbol{E}^-)_\parallel = \boldsymbol{0} \ \ \text{at} \ \ \Gamma_-^p, \end{aligned} \tag{3.120}$$

where $\boldsymbol{E}^+ = \boldsymbol{E}\,|_{\bar{\Omega}_-^a}$ and $\boldsymbol{E}^- = \boldsymbol{E}\,|_{\bar{\Omega}_-^p}$.

Proof. Like the case for polygonal invisibility cloaks, the derivation of CBCs for 3D polyhedral cloaks essentially relies on the decomposition the $\nabla\times$ operators and then carefully study the singularity.

Using (1.3), $\boldsymbol{J}^{-1} = \partial\breve{\boldsymbol{r}}/\partial\boldsymbol{r}$ and $z_0 = R_1 \cos\breve{\theta}$, we derive from some calculations that

$$\boldsymbol{\mu}^{-1} = \boldsymbol{\epsilon}^{-1} = (\boldsymbol{J}^{-1})^t \boldsymbol{J}^{-1}/\det(\boldsymbol{J}^{-1}) = \frac{1-\rho}{(z-z_0)^2} \begin{bmatrix} (z-z_0)^2 \boldsymbol{I}_{2\times 2} & (z-z_0)\boldsymbol{\delta} \\ (z-z_0)\boldsymbol{\delta}^t & \delta_0 \end{bmatrix},$$

where $\boldsymbol{I}_{2\times 2}$ is a two-by-two identity matrix, $\boldsymbol{\delta} = z_0 \tan\theta(\cos\phi, \sin\phi)^t$ and $\delta_0 = z^2 + z_0^2 \tan^2\theta$. Like (3.68)-(3.69), we derive $\boldsymbol{H}^+$ from (3.66) and obtain

$$\begin{aligned} \mathrm{i}\omega\mu_0 \boldsymbol{H}^+ = (1-\rho)\Big(&(\nabla \times \boldsymbol{E}^+)_\parallel + \frac{1}{z-z_0}\boldsymbol{\delta}(\nabla \times \boldsymbol{E}^+)_\perp, \\ &\frac{1}{z-z_0}\boldsymbol{\delta}^t(\nabla \times \boldsymbol{E}^+)_\parallel + \frac{1}{(z-z_0)^2}\delta_0(\nabla \times \boldsymbol{E}^+)_\perp \Big)^t. \end{aligned} \tag{3.121}$$

Since $\boldsymbol{\delta}$ and δ_0 are uniformly bounded in $\bar{\Omega}_-^a$ (note: $\tan\theta \to \infty$ implies $A_pB_pC_pD_p$ intersects with x-y plane, which is impossible as $z_0 \neq 0$), $\boldsymbol{H}^+$ is a finite field in $\bar{\Omega}_-^a$, if and only if the conditions at Γ_+^p in (3.120) holds.

Following [5], we set $\boldsymbol{\epsilon} = \boldsymbol{\mu} = \boldsymbol{I}_{3\times 3}$ in Ω_-^p. By (3.66),

$$\mathrm{i}\omega\mu_0\boldsymbol{H}^- = \big((\nabla\times\boldsymbol{E}^-)_\parallel, (\nabla\times\boldsymbol{E}^-)_\perp\big)^t. \tag{3.122}$$

Similar to (3.71), we obtain from (3.121)-(3.122) and (3.119) that

$$\boldsymbol{n}\times(\boldsymbol{H}^+-\boldsymbol{H}^-)|_{z=z_0} = \frac{1}{\mathrm{i}\omega\mu_0}\Big\{\boldsymbol{n}\times\Big((\nabla\times\boldsymbol{E}^+)_\parallel+\frac{1}{z-z_0}\boldsymbol{\delta}(\nabla\times\boldsymbol{E}^+)_\perp-(\nabla\times\boldsymbol{E}^-)_\parallel,0\Big)^t\Big|_{z=z_0}\Big\}.$$

Then by the first condition in (3.120), we derive

$$\boldsymbol{n}\times(\boldsymbol{H}^+-\boldsymbol{H}^-)|_{z=z_0} = -\frac{1}{\mathrm{i}\omega\mu_0}\boldsymbol{n}\times\big((\nabla\times\boldsymbol{E}^-)_\parallel,0\big)^t\big|_{z=z_0}.$$

Imposing the last condition in (3.120) to (3.122) and the above equation leads to

$$\boldsymbol{n}\times(\boldsymbol{H}^+-\boldsymbol{H}^-)|_{z=z_0} = \boldsymbol{n}\times\boldsymbol{H}^-|_{z=z_0} = \boldsymbol{0}, \tag{3.123}$$

which guarantees the continuity of the tangential component of $\boldsymbol{H}$ at the cloaking boundary. □

Remark 3.7. *In fact, in the polygonal case with one side of the cloaking boundary perpendicular to y-axis (i.e., $y = y_0$), $\boldsymbol{H}^+$ in* (3.68)-(3.69) *reduces to*

$$\begin{aligned}\mathrm{i}\omega\mu_0\boldsymbol{H}^+ =&\Big(\frac{y-y_0}{y}\nabla_{\boldsymbol{n}}u^+ + \frac{y_0x}{y^2}\nabla_{\boldsymbol{\tau}}u^+,\\ &\frac{y_0x}{y^2}\nabla_{\boldsymbol{n}}u^+ + \frac{1}{y-y_0}\Big(y+\frac{y_0^2x^2}{y^3}\Big)\nabla_{\boldsymbol{\tau}}u^+,0\Big)^t.\end{aligned} \tag{3.124}$$

Observe from (3.121) *that $\boldsymbol{H}^+$ has a stronger singularity $(z-z_0)^{-2}$ for the polyhedral cloak, while under the same setting, it only has a singularity $(y-y_0)^{-1}$ in* (3.124) *for the polygonal cloak. This is akin to the situation of spherical and cylindrical cloaks. Accordingly, we have different CBCs in Proposition 3.3 and Proposition 3.4 for the polygonal and polyhedral cloak, respectively. We point out that the CBCs in* (3.120) *can also lead to the decoupling of the inside and outside.*

In order to accurately simulate the three-dimensional polyhedral cloak, the CBCs (3.120) *need to be built in the spectral-element solution space. This can be accomplished by properly modifying the mixed order curl-comforming basis functions in e.g., [111].* □

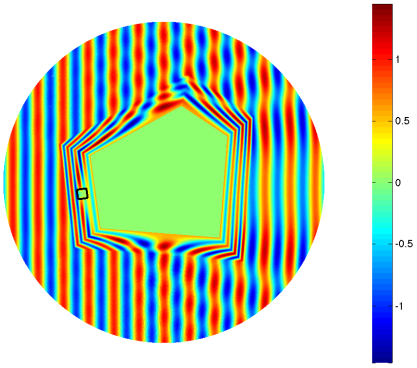

(a) Defect with $a = b = 0.06$

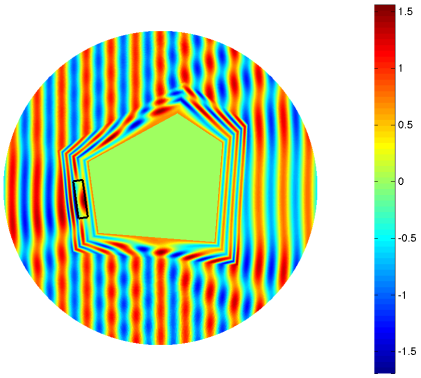

(b) Defect with $a = 0.24$, $b = 0.06$

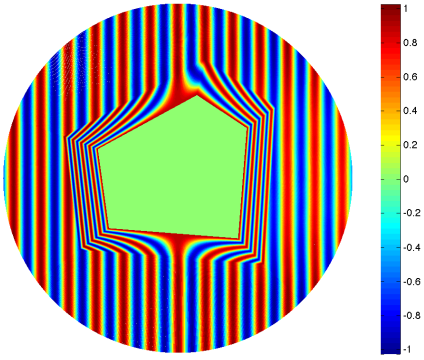

(c) Loss tangent $\tan\delta = 0.01$

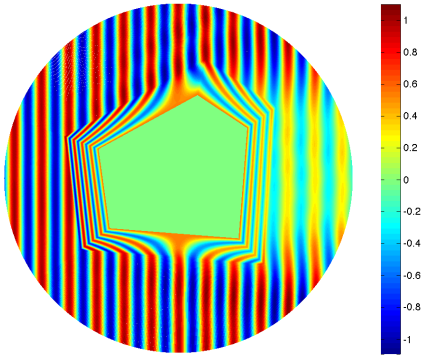

(d) Loss tangent $\tan\delta = 0.05$

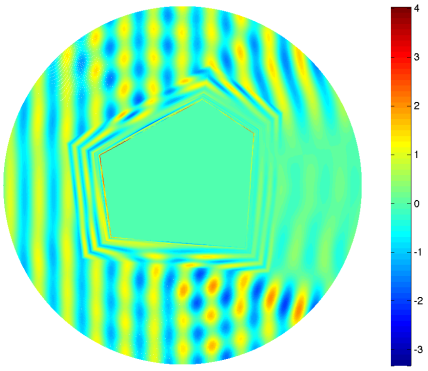

(e) Dispersion with $k = 39$

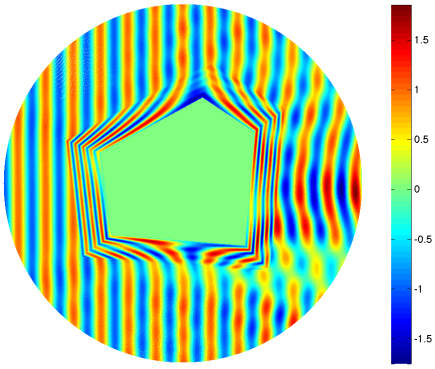

(f) Dispersion with $k = 41$

Figure 3.7: The effects of defects, loss and dispersion on the polygonal invisibility cloak.

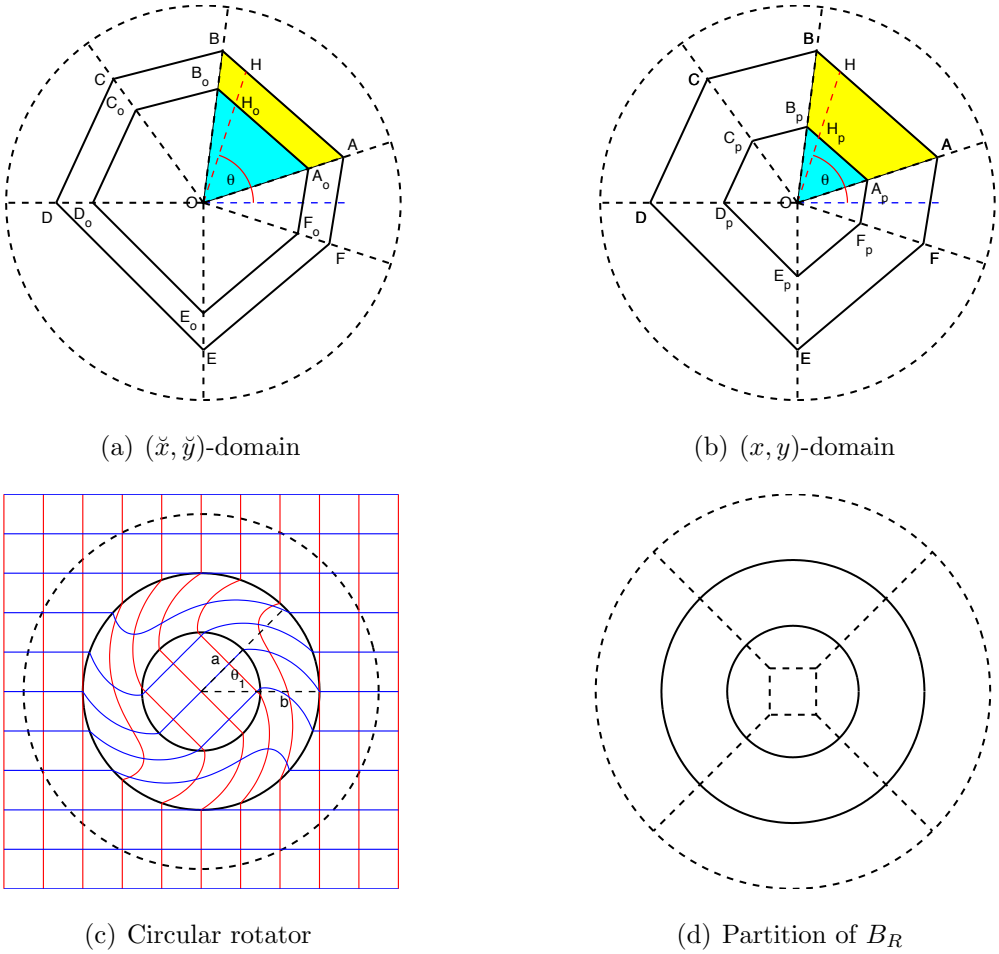

(a) $(\breve{x}, \breve{y})$-domain

(b) (x, y)-domain

(c) Circular rotator

(d) Partition of B_R

Figure 3.8: Schematic geometry of a polygonal concentrator and a circular rotator. (a) The polygonal domain in the original coordinates $(\breve{x}, \breve{y})$. (b) Through the coordinate transformation (3.102), the polygonal domain $\Omega_-^o = A_o B_o \cdots F_o$ is compressed into the polygonal domain Ω_-^p that forms the concentration region. Consequently, the original polygonal annulus domain $\Omega_- \setminus \bar{\Omega}_-^o$ in (a) is expanded into the polygonal annulus Ω_-^a. (c) Through the coordinate transformation (3.114), points in the circular annulus $a < r < b$ are rotated with a fixed angle θ_1. (d) The computational mesh for the circular rotator.

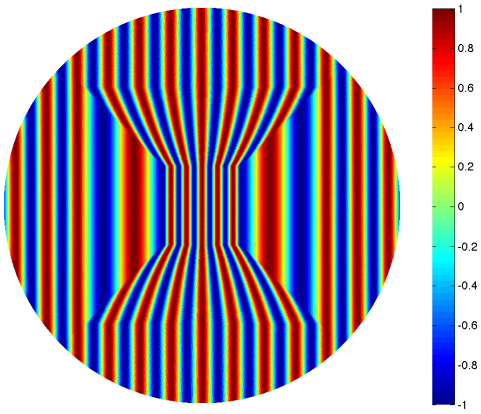

(a) Electric field with $\theta_0 = 0$

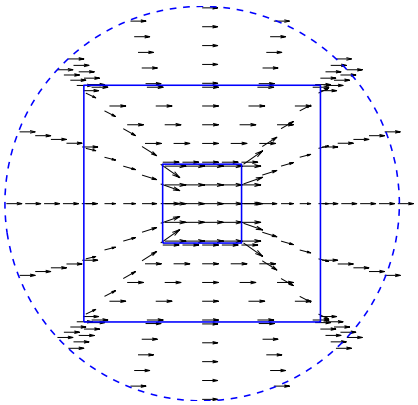

(b) Poynting vector

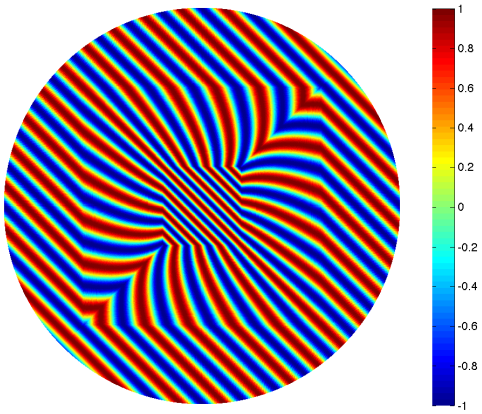

(c) Electric field with $\theta_0 = \pi/4$

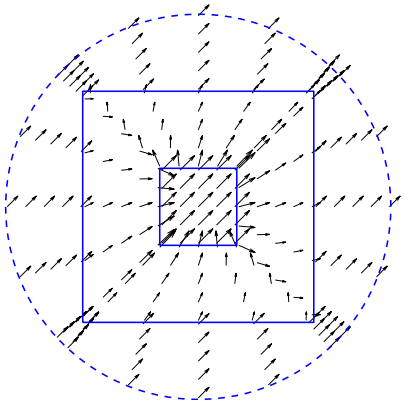

(d) Poynting vector

Figure 3.9: The real part of the electric field distributions and associated Poynting vectors for square concentrators with (a)-(b): $\theta_0 = 0$ and (c)-(d): $\theta_0 = \pi/4$, respectively.

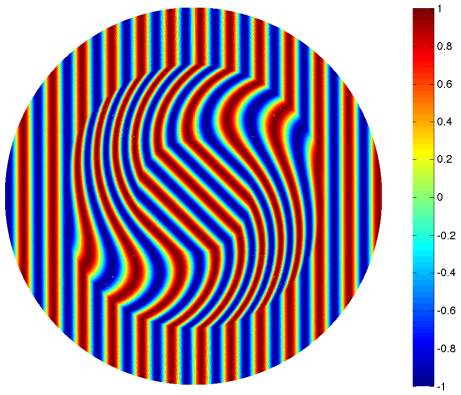

(a) Electric field with $\theta_1 = \pi/4$

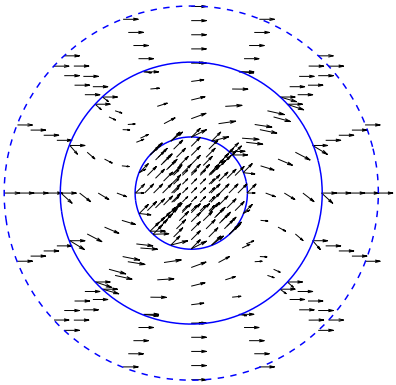

(b) Poynting vector

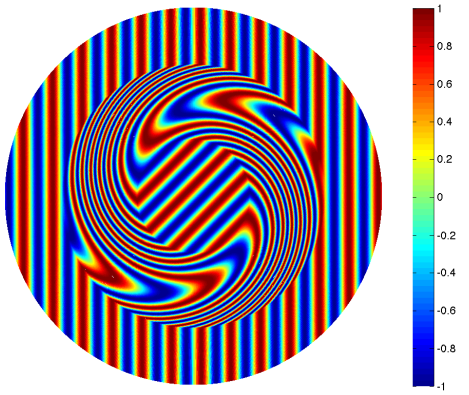

(c) Electric field with $\theta_1 = 3\pi/4$

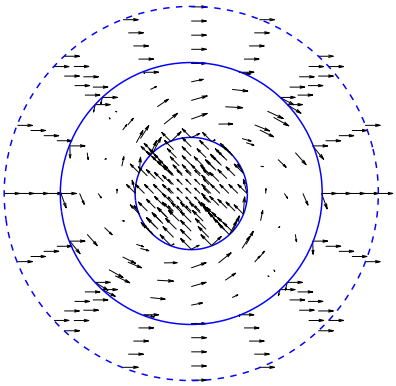

(d) Poynting vector

Figure 3.10: The real part of the electric field distributions and associated Poynting vectors for circular rotators with (a)-(b): $\theta_1 = \pi/4$ and (c)-(d): $\theta_1 = 3\pi/4$, respectively.

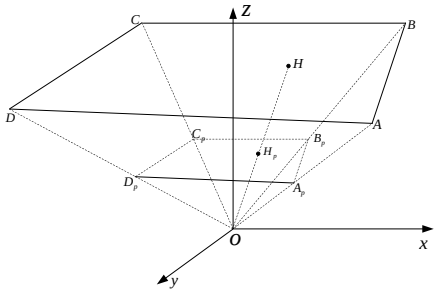

Figure 3.11: Sketch of the geometry of polyhedral cloaks

Chapter 4

Wavenumber Explicit Analysis for Time-Harmonic Maxwell's Equations

This chapter is devoted to the analysis and spectral-Galerkin approximation of the Maxwell's equations in an exterior domain , i.e.,

$$\begin{aligned} &-\mathrm{i}\omega\mu_0\boldsymbol{H}+\nabla\times\boldsymbol{E}=\boldsymbol{0}, \quad -\mathrm{i}\omega\epsilon_0\boldsymbol{E}-\nabla\times\boldsymbol{H}=\boldsymbol{F}, \quad \text{in} \quad \mathbb{R}^3\backslash\bar{D};\\ &\boldsymbol{E}\times\boldsymbol{n}|_{\partial D}=\boldsymbol{0}; \quad (\nabla\times\boldsymbol{E})\times\hat{\boldsymbol{x}}-\mathrm{i}k\boldsymbol{E}_T=o(r^{-1}), \end{aligned} \tag{4.1}$$

where D is a three-dimensional, simply connected, bounded, perfect conductor (or scatterer). As mentioned in Section 1.3, the system (4.1) is notoriously difficult to solve numerically. Some of the main challenges include: (i) the indefiniteness when ω is not sufficiently small; (ii) highly oscillatory solutions when ω is large; (iii) the incompressibility (i.e., $\operatorname{div}\boldsymbol{H}=\operatorname{div}\boldsymbol{E}=0$), which is implicitly implied by (4.1); and (iv) the unboundedness of the domain. On the one hand, one needs to construct approximation spaces such that the discrete problems are well posed and lead to good approximations for a wide range of wavenumbers. On the other hand, one needs to develop efficient algorithms for solving the indefinite linear system, particularly for large wavenumbers, resulted from a given discretization. We refer to [35] and the references therein, for various contributions with respect to numerical approximations of the time-harmonic Maxwell's equations.

Once again, we reduce the above Maxwell's equations in unbounded domain to a bounded one with a TBC characterized by the capacity operator $\mathscr{T}_b$ (see, e.g., [3]). As usual, we assume that the electric current density $\boldsymbol{F}$ is compactly supported in a ball B of radius b (that encloses the scatterer D), and solenoidal, i.e., $\operatorname{div} \boldsymbol{F} = 0$. After eliminating the magnetic field $\boldsymbol{H}$, we can reduce (4.1) to

$$\nabla \times \nabla \times \boldsymbol{E} - k^2 \boldsymbol{E} = \boldsymbol{F}, \quad \text{in } \Omega := B \backslash \bar{D}\,; \tag{4.2}$$

$$\boldsymbol{E} \times \boldsymbol{n} = \boldsymbol{0}, \quad \text{on } \partial D; \quad (\nabla \times \boldsymbol{E}) \times \boldsymbol{e}_r - \mathrm{i}k \mathscr{T}_b[\boldsymbol{E}_T] = \boldsymbol{h}, \quad \text{at } r = b, \tag{4.3}$$

where $\boldsymbol{e}_r = \hat{\boldsymbol{x}} = \boldsymbol{x}/r$, $\mathscr{T}_b$ is the capacity operator (cf. [3, (5.3.88)]), and the tangential field $\boldsymbol{E}_T = -\boldsymbol{E} \times \boldsymbol{e}_r \times \boldsymbol{e}_r$. Here, we add a boundary data function $\boldsymbol{h}$ in (4.3) to deal with potentially inhomogeneous boundary conditions.

We shall start with the special case where D is a ball of radius a:

$$\Omega = \big\{(r, \theta, \varphi) : a < r < b,\ \theta \in [0, \pi],\ \varphi \in [0, 2\pi)\big\}, \tag{4.4}$$

and the solution $\boldsymbol{E}$ can be represented in terms of vector spherical harmonics (VSH).

In [3] and other related works, the usual VSH (cf. Section 4.1) are used to represent $\boldsymbol{E}$. In particular, the system (4.2)-(4.3) can be reduced to a coupled system of two components of $\boldsymbol{E}$, while the other component satisfies the same equation reduced from the Helmholtz equation (cf. [112]):

$$-\Delta U - k^2 U = F, \qquad \text{in } \Omega := B \backslash \bar{D}\,, \tag{4.5}$$

$$U|_{\partial D} = 0; \quad \partial_r U - T_b[U] = H, \quad \text{at } r = b, \tag{4.6}$$

where T_b is the DtN operator [3] (see (4.19)). The wavenumber explicit analysis for the above Helmholtz equation has been carried out in [77], but the analysis for the coupled system of two other components appears very difficult. In fact, only the result on well-posedness of (4.2)-(4.3) was obtained in [112].

However, if we use divergence-free vector spherical harmonics [113], the Maxwell's system (4.2)-(4.3), in the case D is a sphere, can be reduced to two sequences

of one-dimensional problems, which are completely decoupled and the same as those obtained from the Helmholtz equations (4.5) (note: one sequence is with the boundary conditions (4.6), but the other is with a slightly different boundary condition at $r = a$). Therefore, we can carry out wavenumber explicit analysis for these decoupled problems, leading to wavenumber explicit estimates for the Maxwell's equations.

The main purposes of this chapter are to extend the analysis in [77] to the Maxwell's equations, and in the meantime, provide an essential improvement, which is critical to obtaining the desired estimate for the Maxwell's equations, to an estimate for the Helmholtz equation in [77]. We demonstrate that the spectral algorithm and analysis for the Maxwell's equations in the special domain Ω (4.4) are the major component for dealing with general scatterers using the transformed field expansion (TFE) approach [84].

The rest of the chapter is organized as follows. In Section 4.2, we have a delicate study of the DtN kernel in (4.20), and use the new estimates to derive the improved estimates for the Helmholtz equation (cf. Lemma 4.2 and Theorem 4.2), by removing the factor $k^{1/3}$ in [77, Thm. 3.1]. In Section 4.3, we first reduce the Maxwell's system (4.2)-(4.4) to two sequences of decoupled one-dimensional (in the radial direction) Helmholtz problems in a similar setting by using the divergence-free VSH expansions in angular directions. This step is essential for the subsequent analysis. By a delicate analysis of the decoupled one-dimensional problems (cf. Theorems 4.3 and 4.5), we derive the wavenumber explicit bounds (cf. Theorem 4.6). In Section 4.5, we study a spectral approximation of the reduced Maxwell's equations, and derive the corresponding wavenumber explicit error estimates for the one-dimensional problems (cf. Lemmas 4.3 and 4.5), which finally lead to the wavenumber explicit error estimates for the Maxwell's system (cf. Theorem 4.8). Then, in Section 4.6, we apply the transformed field expansion technique to deal with general scatterers, and using the general framework derived in [114], we obtain rigorous wavenumber explicit error estimates for the complete

algorithm.

4.1 Vector spherical harmonics

In what follows, we adopt the notation and normalization of SH in Nédélec [3]. The spherical coordinates (r, θ, φ) are related to the Cartesian coordinates $\boldsymbol{x} = (x_1, x_2, x_3)$ by

$$x_1 = r\sin\theta\cos\varphi, \quad x_2 = r\sin\theta\sin\varphi, \quad x_3 = r\cos\theta, \tag{4.7}$$

where $r \geq 0, \theta \in [0, \pi]$ and $\varphi \in [0, 2\pi)$, and the corresponding (right-handed) orthonormal coordinate basis consists of $\{\boldsymbol{e}_r, \boldsymbol{e}_\theta, \boldsymbol{e}_\varphi\}$ where

$$\boldsymbol{e}_r = \hat{\boldsymbol{x}} = \boldsymbol{x}/r, \;\; \boldsymbol{e}_\theta = (\cos\theta\cos\varphi,\; \cos\theta\sin\varphi, -\sin\theta), \;\; \boldsymbol{e}_\varphi = (-\sin\varphi,\; \cos\varphi, 0).$$

Let S be the unit spherical surface. Denote by ∇_S and Δ_S the tangent gradient operator and the Laplace-Beltrami operator on S, defined respectively by

$$\nabla_S u = \frac{\partial u}{\partial\theta}\boldsymbol{e}_\theta + \frac{1}{\sin\theta}\frac{\partial u}{\partial\varphi}\boldsymbol{e}_\varphi\,, \quad \Delta_S u = \frac{1}{\sin\theta}\frac{\partial}{\partial\theta}\Big(\sin\theta\frac{\partial u}{\partial\theta}\Big) + \frac{1}{\sin^2\theta}\frac{\partial^2 u}{\partial\varphi^2}. \tag{4.8}$$

We denote by $\{Y_l^m(\theta, \varphi)\}$ the (scalar) spherical harmonics which are eigenfunctions of Δ_S, namely,

$$\Delta_S Y_l^m = -\beta_l Y_l^m, \quad l \geq 0,\; |m| \leq l; \quad \beta_l := l(l+1) \tag{4.9}$$

and form an orthonormal basis of $L^2(S)$ with the inner product:

$$\langle u, v\rangle_S = \int_S u\,\bar{v}\,dS = \int_0^{2\pi}\!\!\int_0^{\pi} u\,\bar{v}\,\sin\theta\,d\theta d\varphi. \tag{4.10}$$

We use the family of VSH: $\big\{Y_l^m\boldsymbol{e}_r, \nabla_S Y_l^m, \boldsymbol{T}_l^m := \nabla_S Y_l^m \times \boldsymbol{e}_r\big\}$ in the SpherePack [117] (also see [4]). They are mutually orthogonal in $\boldsymbol{L}^2(S)$, with the inner product given by (4.10) (but for vector fields), and normalised such that

$$\big\langle \boldsymbol{T}_l^m, \boldsymbol{T}_l^m\big\rangle_S = \beta_l, \quad \big\langle \nabla_S Y_l^m, \nabla_S Y_l^m\big\rangle_S = \beta_l, \quad \big\langle Y_l^m\boldsymbol{e}_r, Y_l^m\boldsymbol{e}_r\big\rangle_S = 1. \tag{4.11}$$

We have

$$\boldsymbol{T}_l^m \times \boldsymbol{e}_r = -\nabla_S Y_l^m, \quad \nabla_S Y_l^m \times \boldsymbol{e}_r = \boldsymbol{T}_l^m, \quad Y_l^m \boldsymbol{e}_r \times \boldsymbol{e}_r = \boldsymbol{0}. \tag{4.12}$$

Define the differential operators:

$$d_l^{\pm} = \frac{d}{dr} \pm \frac{l}{r}, \quad \mathcal{L}_l = \frac{d^2}{dr^2} + \frac{2}{r}\frac{d}{dr} - \frac{l(l+1)}{r^2}, \quad \hat{\partial}_r = \frac{d}{dr} + \frac{1}{r}. \tag{4.13}$$

Let f be a scalar function of r. The following properties can be derived from [121]:

$$\mathrm{div}\big(f\boldsymbol{T}_l^m\big) = 0, \quad \Delta\big(f\boldsymbol{T}_l^m\big) = \mathcal{L}_l(f)\boldsymbol{T}_l^m, \tag{4.14}$$

$$\nabla \times \big(f\boldsymbol{T}_l^m\big) = \hat{\partial}_r f\, \nabla_S Y_l^m + l(l+1)\frac{f}{r} Y_l^m \boldsymbol{e}_r, \tag{4.15}$$

$$\nabla \times \big(f\nabla_S Y_l^m\big) = -\hat{\partial}_r f\, \boldsymbol{T}_l^m, \quad \nabla \times \big(f Y_l^m \boldsymbol{e}_r\big) = \frac{f}{r}\boldsymbol{T}_l^m. \tag{4.16}$$

Moreover, we have

$$\mathrm{div}\big(f\nabla_S Y_l^m\big) = \frac{l(l+1)}{2l+1}\big(d_{l-1}^- - d_{l+2}^+\big) f\, Y_l^m = -l(l+1)\frac{f}{r}\, Y_l^m\,, \tag{4.17}$$

$$\mathrm{div}\big(fY_l^m \boldsymbol{e}_r\big) = \frac{1}{2l+1}\big(l d_{l-1}^- + (l+1) d_{l+2}^+\big) f\, Y_l^m = \Big(\frac{d}{dr} + \frac{2}{r}\Big) f\, Y_l^m\,. \tag{4.18}$$

4.2 Improved estimates for the Helmholtz equation

In this section, we improve the *a prior* estimates for the Helmholtz equation (4.5)-(4.6) in [77, Thm. 3.1], where the DtN operator is defined by

$$T_b[U] = \sum_{l=1}^{\infty} \sum_{|m|=0}^{l} k \frac{h_l^{(1)'}(kb)}{h_l^{(1)}(kb)}\, \widehat{U}_l^m\, Y_l^m, \ \text{ where } \ \widehat{U}_l^m = \int_S U\big|_{r=b}\, \overline{Y_l^m}\, dS, \tag{4.19}$$

and $\{Y_l^m\}$ are spherical harmonics defined in (4.9).

4.2.1 Properties of the DtN kernel

The key to the improvement is through a delicate analysis of the real part of the DtN kernel:

$$\mathcal{T}_{l,\kappa} := \frac{h_l^{(1)'}(\kappa)}{h_l^{(1)}(\kappa)}, \quad l \geq 1, \ \ \kappa > 0. \tag{4.20}$$

Recall that (cf. [77, (2.16)])

$$\mathrm{Re}(\mathcal{T}_{l,\kappa}) = -\frac{1}{2\kappa} + \frac{J_\nu(\kappa)J'_\nu(\kappa) + Y_\nu(\kappa)Y'_\nu(\kappa)}{J_\nu^2(\kappa) + Y_\nu^2(\kappa)}, \tag{4.21a}$$

$$\mathrm{Im}(\mathcal{T}_{l,\kappa}) = \frac{2}{\pi\kappa}\frac{1}{J_\nu^2(\kappa) + Y_\nu^2(\kappa)}, \quad \nu := l + 1/2, \tag{4.21b}$$

where J_ν and Y_ν are Bessel functions of the first and second kinds, respectively, of order ν (cf. [87]). Alternatively, we can formulate

$$\mathrm{Re}(\mathcal{T}_{l,\kappa}) = \frac{l}{\kappa} - \frac{Y_{\nu+1}(\kappa)}{Y_\nu(\kappa)} - \mathrm{Im}(\mathcal{T}_{l,\kappa})\frac{J_\nu(\kappa)}{Y_\nu(\kappa)} = -\frac{1}{2\kappa} + \frac{Y'_\nu(\kappa)}{Y_\nu(\kappa)} - \mathrm{Im}(\mathcal{T}_{l,\kappa})\frac{J_\nu(\kappa)}{Y_\nu(\kappa)}, \tag{4.22}$$

which can be derived from (4.21) and the following properties of Bessel functions (cf. [87]):

$$J_{\nu+1}(\kappa)Y_\nu(\kappa) - J_\nu(\kappa)Y_{\nu+1}(\kappa) = \frac{2}{\pi\kappa}, \quad Y_{\nu+1}(\kappa) = \frac{\nu}{\kappa}Y_\nu(\kappa) - Y'_\nu(\kappa). \tag{4.23}$$

We collect some important properties of $\mathrm{Re}(\mathcal{T}_{l,\kappa})$ and $\mathrm{Im}(\mathcal{T}_{l,\kappa})$ (cf. [3]):

$$-\frac{l+1}{\kappa} \leq \mathrm{Re}(\mathcal{T}_{l,\kappa}) < -\frac{1}{\kappa}, \quad 0 < \mathrm{Im}(\mathcal{T}_{l,\kappa}) < 1, \ \ \text{for } \ l \geq 1. \tag{4.24}$$

For $\kappa > \kappa_0$, $\mathcal{E}^I_{l,\kappa}$ derived from asymptotic formulas of Bessel functions provides a good approximation to $\mathrm{Im}(\mathcal{T}_{l,\kappa})$ (cf. [77, (2.35)]):

$$\mathrm{Im}(\mathcal{T}_{l,\kappa}) \sim \mathcal{E}^I_{l,\kappa} = \begin{cases} \sqrt{1-\nu^2/\kappa^2}, & \text{if } \ \kappa > \nu \geq 1, \\ C_0\nu^{-1/3}, & \text{if } \ \kappa = \nu, \\ \dfrac{4\nu\tanh\alpha}{\kappa\big[\exp(2\nu(\tanh\alpha - \alpha)) + 4\exp(2\nu(\alpha - \tanh\alpha))\big]}, & \text{if } \ \kappa = \nu\mathrm{sech}\alpha, \end{cases} \tag{4.25}$$

where $C_0 \approx 0.7954$ and $\alpha > 0$. It is noteworthy that the approximation (4.25) played an important role in the analysis in [77].

As already mentioned, the improved *a priori* estimate essentially relies on deriving approximation to $\mathrm{Re}(\mathcal{T}_{l,\kappa})$, akin to (4.25). In what follows, let $0 < \theta_0 < 1$ be a prescribed constant, and let

$$\kappa_0 = \sqrt{\theta_0/2}\,(1-\theta_0)^{-3/2} \quad (\text{e.g., } \kappa_0 \approx 21.21, \text{ if } \theta_0 = 0.9). \tag{4.26}$$

Based upon asymptotic properties of Bessel functions, we shall carry out the analysis separately for four cases (note: in the course of the analysis, we shall show how these arise):

$$\rho := \frac{\nu}{\kappa} \in (0,\theta_0) \cup [\theta_0,\vartheta_1] \cup (\vartheta_1,\vartheta_2) \cup [\vartheta_2,\infty) \quad \text{for } \nu = l + 1/2, \;\; l \geq 1, \tag{4.27}$$

where $\kappa > \kappa_0$ is fixed, and

$$\begin{aligned} \vartheta_1 := \vartheta_1(\kappa) &= \frac{1}{2}\left(\sqrt[3]{1+\sqrt{1+\frac{2}{27\kappa^2}}} + \sqrt[3]{1-\sqrt{1+\frac{2}{27\kappa^2}}}\right)^3, \\ \vartheta_2 := \vartheta_2(\kappa) &= \frac{1}{2}\left(\sqrt[3]{1+\sqrt{1-\frac{2}{27\kappa^2}}} + \sqrt[3]{1-\sqrt{1-\frac{2}{27\kappa^2}}}\right)^3. \end{aligned} \tag{4.28}$$

Lemma 4.1. *Let $\theta_0, \kappa_0, \vartheta_1$ and ϑ_2 be the same as above. Then we have*

$$0 < \vartheta_1 < 1 < \vartheta_2, \quad \forall\, \kappa > \sqrt{2/27}, \tag{4.29}$$

and

$$\vartheta_1 = 1 - \frac{1}{\sqrt[3]{2}\,\kappa^{2/3}} + O(\kappa^{-4/3}), \quad \vartheta_2 = 1 + \frac{1}{\sqrt[3]{2}\,\kappa^{2/3}} + O(\kappa^{-4/3}). \tag{4.30}$$

Moreover, if $\kappa > \kappa_0$, then we have $\theta_0 < \vartheta_1$.

Proof. We examine the function:

$$f(t) := \sqrt[3]{1+t} + \sqrt[3]{1-t}, \quad t \geq 0,$$

and verify readily that $f'(t) < 0$ for all $t > 0, t \neq 1$. Thus, $f(t)$ is monotonically decreasing, and

$$\sqrt[3]{2\vartheta_1} = f\big(\sqrt{1+2/(27\kappa^2)}\big) < f(1) < f\big(\sqrt{1-2/(27\kappa^2)}\big) = \sqrt[3]{2\vartheta_2}, \tag{4.31}$$

which implies (4.29).

It is evident that

$$t_1 := \sqrt{1+\frac{2}{27\kappa^2}} = 1+\frac{1}{27\kappa^2}+O(\kappa^{-4}). \tag{4.32}$$

A direct calculation from (4.28) yields

$$\begin{aligned}
2\vartheta_1 &= 2+3\big\{(1+t_1)^{2/3}(1-t_1)^{1/3}+(1+t_1)^{1/3}(1-t_1)^{2/3}\big\}\\
&= 2-\frac{\sqrt[3]{2}}{\kappa^{2/3}}\big(\sqrt[3]{1+t_1}+\sqrt[3]{1-t_1}\,\big)\\
&= 2-\frac{\sqrt[3]{2}}{\kappa^{2/3}}\bigg(\sqrt[3]{2+\frac{1}{27\kappa^2}}-\frac{1}{3\kappa^{2/3}}\bigg)+O(\kappa^{-2})\\
&= 2-\frac{\sqrt[3]{2}}{\kappa^{2/3}}\Big(\sqrt[3]{2}-\frac{1}{3\kappa^{2/3}}+O(\kappa^{-2})\Big)+O(\kappa^{-2}),
\end{aligned}$$

which implies the asymptotic estimate of ϑ_1 in (4.30). Similarly, we can derive the estimate of ϑ_2.

We now prove $\theta_0<\vartheta_1$, for all $\kappa>\kappa_0$ with κ_0 given by (4.26). Observe from (4.31)-(4.32) that $\sqrt[3]{2\vartheta_1}=f(t_1)$, so it suffices to show $\sqrt[3]{2\vartheta_0}<\sqrt[3]{2\vartheta_1}=f(t_1)$. Using the monotonic decreasing property of f, we just require

$$f^{-1}(\sqrt[3]{2\theta_0})>t_1=\sqrt{1+2/(27\kappa^2)},$$

so working out the inverse of f, we can obtain

$$\kappa>\frac{\sqrt{\theta_0}}{\sqrt{2}(1-\theta_0)^{3/2}}:=\kappa_0. \tag{4.33}$$

With this, we end the proof. □

We have the following estimates of $\mathrm{Re}(\mathcal{T}_{l,\kappa})$, and also refined estimates of $\mathrm{Re}(\mathcal{T}_{l,\kappa})$ in (4.25).

In what follows, the expression "$A\lesssim B$" means that there exists a positive constant C, only depending on the domain (but independent of k, and the related unknowns or functions), such that $A\le CB$. As with [87], the notation "$A\sim B$" stands for $A(\nu)=B(\nu)+\mathrm{LH}(\nu)$ or $A(\nu)=B(\nu)(1+\mathrm{LH}(\nu))$, where for sufficiently small or large parameter ν, $\mathrm{LH}(\nu)$ is some insignificant lower-order or higher-order term to be dropped in the bound or estimate.

Theorem 4.1. *Let $\theta_0, \vartheta_1, \vartheta_2$ and κ_0 be defined as above. Denote $\nu = l + 1/2$ and $\rho = \nu/\kappa$. Then for any $\kappa > \kappa_0$, we have the approximation*

$$\mathrm{Re}(\mathcal{T}_{l,\kappa}) \sim E^R_{l,\kappa}, \quad \mathrm{Im}(\mathcal{T}_{l,\kappa}) \sim E^I_{l,\kappa}, \quad \forall\, l \geq 1, \ \text{ where} \tag{4.34}$$

(i) *for $\rho = \nu/\kappa \in (0, \theta_0)$,*

$$E^R_{l,\kappa} = -\frac{1}{2\kappa}\Big(1 + \frac{1}{1-\rho^2}\Big), \quad E^I_{l,\kappa} = \sqrt{1-\rho^2}\,; \tag{4.35}$$

(ii) *for $\rho = \nu/\kappa \in [\theta_0, \vartheta_1]$,*

$$E^R_{l,\kappa} = -\frac{1}{2\kappa}\Big(1 + \frac{1}{2(1-\rho)}\Big), \quad E^I_{l,\kappa} = \sqrt{2\rho(1-\rho)}\,; \tag{4.36}$$

(iii) *for $\rho = \nu/\kappa \in (\vartheta_1, \vartheta_2)$,*

$$\begin{aligned} E^R_{l,\kappa} &= -\frac{1}{c_1}\Big(\frac{2}{\nu}\Big)^{1/3}\big(1 + 2c_1 t + c_2 t^2\big) - \frac{1}{2\kappa}, \\ E^I_{l,\kappa} &= \sqrt{3}c_1\rho\big(1 - 2c_1 t\big)\Big(\frac{2}{\nu}\Big)^{1/3}, \end{aligned} \tag{4.37}$$

where $t = -\sqrt[3]{2}\,(\kappa - \nu)/\sqrt[3]{\nu}$ (note: $|t| < 1$), and

$$c_1 = \frac{3^{\frac{1}{3}}}{2}\frac{\Gamma(\frac{2}{3})}{\Gamma(\frac{1}{3})} \approx 0.3645, \quad c_2 = \frac{1 - 16c_1^3}{2c_1} \approx 0.3088; \tag{4.38}$$

(iv) *for $\rho = \nu/\kappa \in [\vartheta_2, \infty)$,*

$$E^R_{l,\kappa} = -\sqrt{\rho^2 - 1} - \frac{1}{2\kappa}\Big(1 - \frac{1}{\rho^2 - 1}\Big), \quad E^I_{l,\kappa} = \sqrt{\rho^2 - 1}\, e^{-2\nu\Psi}, \tag{4.39}$$

where

$$\Psi = \ln(\rho + \sqrt{\rho^2 - 1}) - \frac{\sqrt{\rho^2 - 1}}{\rho}, \quad \rho > 1. \tag{4.40}$$

Proof. **Case (i)** $\rho = \nu/\kappa \in (0, \theta_0)$. Set $\sec\beta = \kappa/\nu = \rho^{-1}$, i.e., $\cos\beta = \rho$ with $0 < \beta < \pi/2$. One verifies for $0 < \rho < \theta_0 < 1$

$$\sin\beta = \sqrt{1-\rho^2}, \quad \tan\beta = \frac{\sqrt{1-\rho^2}}{\rho}, \quad \cot\beta = \frac{\rho}{\sqrt{1-\rho^2}}. \tag{4.41}$$

Recall the formulas (cf. [87, (9.3.15-9.3.20)])

$$\begin{aligned}
J_\nu(\nu\sec\beta) &= \sqrt{\frac{2}{\pi\nu\tan\beta}}\big(L_1\cos\psi + M_1\sin\psi\big),\\
Y_\nu(\nu\sec\beta) &= \sqrt{\frac{2}{\pi\nu\tan\beta}}\big(L_1\sin\psi - M_1\cos\psi\big),\\
J'_\nu(\nu\sec\beta) &= -\sqrt{\frac{\sin 2\beta}{\pi\nu}}\big(L_2\sin\psi + M_2\cos\psi\big),\\
Y'_\nu(\nu\sec\beta) &= \sqrt{\frac{\sin 2\beta}{\pi\nu}}\big(L_2\cos\psi - M_2\sin\psi\big),
\end{aligned}$$

where $\psi = \nu(\tan\beta-\beta)-1/4$, and $L_i = L_i(\nu,\beta), M_i = M_i(\nu,\beta), i = 1,2$ are given in [87, P. 366-367]. Inserting them into (4.21) leads to

$$\mathrm{Re}(\mathcal{T}_{l,\kappa}) = -\frac{1}{2\kappa} - \sin\beta\,\frac{L_1M_2+L_2M_1}{L_1^2+M_1^2}, \quad \mathrm{Im}(\mathcal{T}_{l,\kappa}) = \frac{\rho\tan\beta}{L_1^2+M_1^2}. \tag{4.42}$$

We find it suffices to take the leading term of $L_i, M_i, i = 1,2$ in [87, P. 366-367], that is,

$$L_1\sim 1,\ \ L_2\sim 1,\ \ M_1\sim\frac{3\cot\beta+5\cot^3\beta}{24\nu},\ \ M_2\sim\frac{9\cot\beta+7\cot^3\beta}{24\nu}. \tag{4.43}$$

By a direct calculation and using (4.41), we obtain

$$\sin\beta\,\big(L_1M_2+L_2M_1\big)\sim\sin\beta\,\frac{\cot\beta+\cot^3\beta}{2\nu} = \frac{1}{2\kappa}\frac{1}{1-\rho^2}, \tag{4.44}$$

and

$$M_1^2\sim\frac{3+5\rho^2}{192(1-\rho^2)^2}\frac{1}{\kappa^2}, \quad \frac{1}{L_1^2+M_1^2}\sim 1-M_1^2 = 1+O(\kappa^{-2}). \tag{4.45}$$

Then we obtain (4.35) from (4.42) and the above.

Cases (ii)-(iii) $\rho = \nu/\kappa \in [\theta_0,\vartheta_1]\cup(\vartheta_1,\vartheta_2)$. We adopt the asymptotic formulas [87, (9.3.23-9.3.28)]:

$$\begin{aligned}
J_\nu(\nu+z\sqrt[3]{\nu}) &\sim \Big(\frac{2}{\nu}\Big)^{\frac{1}{3}}\mathrm{Ai}(-\sqrt[3]{2}z)+O(\nu^{-1}),\\
Y_\nu(\nu+z\sqrt[3]{\nu}) &\sim -\Big(\frac{2}{\nu}\Big)^{\frac{1}{3}}\mathrm{Bi}(-\sqrt[3]{2}z)+O(\nu^{-1}),\\
J'_\nu(\nu+z\sqrt[3]{\nu}) &\sim -\Big(\frac{2}{\nu}\Big)^{\frac{2}{3}}\mathrm{Ai}'(-\sqrt[3]{2}z)+O(\nu^{-\frac{4}{3}}),\\
Y'_\nu(\nu+z\sqrt[3]{\nu}) &\sim \Big(\frac{2}{\nu}\Big)^{\frac{2}{3}}\mathrm{Bi}'(-\sqrt[3]{2}z)+O(\nu^{-\frac{4}{3}}),
\end{aligned} \tag{4.46}$$

where $\mathrm{Ai}(t)$ and $\mathrm{Bi}(t)$ are Airy functions of the first and second kinds, respectively. Set

$$t := -\sqrt[3]{2}\, z, \quad \kappa = \nu + z\sqrt[3]{\nu} \ \ (\text{i.e.,} \ \ z = (\kappa - \nu)/\sqrt[3]{\nu}\,). \tag{4.47}$$

We obtain from (4.46) and (4.21) that

$$\mathrm{Re}(\mathcal{T}_{l,\kappa}) \sim -\frac{1}{2\kappa} - \Big(\frac{2}{\nu}\Big)^{1/3} T_R(t), \quad \mathrm{Im}(\mathcal{T}_{l,\kappa}) \sim \frac{2}{\pi\kappa}\Big(\frac{\nu}{2}\Big)^{2/3} T_I(t), \tag{4.48}$$

where

$$T_R(t) = \frac{\mathrm{Ai}(t)\mathrm{Ai}'(t) + \mathrm{Bi}(t)\mathrm{Bi}'(t)}{\mathrm{Ai}^2(t) + \mathrm{Bi}^2(t)}, \quad T_I(t) = \frac{1}{\mathrm{Ai}^2(t) + \mathrm{Bi}^2(t)}. \tag{4.49}$$

Note that the Airy functions have different asymptotic behaviours for $t \le -1$ and $-1 < t < 1$ (see, e.g., [87, 115]). We therefore solve the equations: $t = -\sqrt[3]{2}\, z = -\sqrt[3]{2}(\kappa - \nu)/\sqrt[3]{\nu} = \mp 1$, that is,

$$\nu + 2^{-\frac{1}{3}}\nu^{\frac{1}{3}} - \kappa = 0, \quad \nu - 2^{-\frac{1}{3}}\nu^{\frac{1}{3}} - \kappa = 0. \tag{4.50}$$

Both are cubic equations in $\nu^{\frac{1}{3}}$ with only one real root each. We find the real root of the first equation is $\kappa\,\vartheta_1$, while that of the second one is $\kappa\,\vartheta_2$, where ϑ_1 and ϑ_2 are given in (4.28).

(a) For $\rho \in [\theta_0, \vartheta_1]$ (note: $t = -\sqrt[3]{2}z \le -1$), we recall the asymptotic formulas (see [87, (10.4.60)])

$$\begin{aligned}
&\mathrm{Ai}(t) \sim \frac{1}{\sqrt[4]{-\pi^2 t}}\Big(\sin\xi - \frac{5}{72\eta}\cos\xi\Big), \quad \mathrm{Ai}'(t) \sim -\sqrt[4]{-\frac{t}{\pi^2}}\Big(\cos\xi - \frac{7}{72\eta}\sin\xi\Big),\\
&\mathrm{Bi}(t) \sim \frac{1}{\sqrt[4]{-\pi^2 t}}\Big(\cos\xi + \frac{5}{72\eta}\sin\xi\Big), \quad \mathrm{Bi}'(t) \sim \sqrt[4]{-\frac{t}{\pi^2}}\Big(\sin\xi + \frac{7}{72\eta}\cos\xi\Big),
\end{aligned}$$

where

$$\xi = \eta + \frac{\pi}{4}, \quad \eta = \frac{2}{3}(-t)^{3/2} = \frac{2}{3}\big(\sqrt[3]{2}z\big)^{3/2}.$$

Thus, a direct calculation leads to

$$\begin{aligned}
&\mathrm{Ai}(t)\mathrm{Ai}'(t) + \mathrm{Bi}(t)\mathrm{Bi}'(t) \sim \frac{1}{6\pi\eta} = \frac{1}{4\pi}(-t)^{-3/2},\\
&\mathrm{Ai}^2(t) + \mathrm{Bi}^2(t) \sim \frac{1}{\pi\sqrt{-t}}\Big(1 + \Big(\frac{5}{72\eta}\Big)^2\Big) = \frac{1}{\pi\sqrt{-t}} + O((-t)^{-7/2}).
\end{aligned} \tag{4.51}$$

Inserting them into (4.49), we obtain

$$T_R(t) \sim -\frac{1}{4t} = \frac{1}{4\sqrt[3]{2}}\frac{\sqrt[3]{\nu}}{\kappa-\nu}, \quad T_I(t) \sim \frac{\pi\sqrt{-t}}{1+O((-t)^{-3})} \sim 2^{1/6}\pi\Big(\frac{\kappa-\nu}{\nu^{1/3}}\Big)^{1/2}.$$

We derive from (4.48) that

$$\mathrm{Re}(\mathcal{T}_{l,\kappa}) \sim -\frac{1}{2\kappa} - \frac{1}{4(\kappa-\nu)}, \quad \mathrm{Im}(\mathcal{T}_{l,\kappa}) \sim \frac{\nu}{\kappa}\sqrt{2\Big(\frac{\kappa}{\nu}-1\Big)}. \tag{4.52}$$

This yields (4.36).

(b) For $\rho \in (\vartheta_1, \vartheta_2)$ (note: $|t| = \sqrt[3]{2}|z| < 1$), we approximate $T_R(t)$ and $T_I(t)$ in (4.49) by their Taylor expansions at $t = 0$, which requires to evaluate $\mathrm{Ai}^{(m)}(0)$ and $\mathrm{Bi}^{(m)}(0)$ for $m \geq 1$. Recall that the Airy functions satisfy the Airy equation: $w''(t) - tw(t) = 0$, $t \in \mathbb{R}$, and some special values are

$$\mathrm{Ai}(0) = \frac{1}{3^{\frac{2}{3}}\Gamma(\frac{2}{3})}, \ \mathrm{Ai}'(0) = -\frac{1}{3^{\frac{1}{3}}\Gamma(\frac{1}{3})}, \ \mathrm{Bi}(0) = \frac{1}{3^{\frac{1}{6}}\Gamma(\frac{2}{3})}, \ \mathrm{Bi}'(0) = \frac{3^{\frac{1}{6}}}{\Gamma(\frac{1}{3})}.$$

With these and some tedious calculation, we can obtain

$$T_R(t) = T_R(0)+T_R'(0)t+\frac{T_R''(0)}{2}t^2+O(t^3), \ T_I(t) = T_I(0)+T_I'(0)t+\frac{T_I''(0)}{2}t^2+O(t^3),$$

with

$$c_1 := T_R(0) = \frac{3^{\frac{1}{3}}}{2}\frac{\Gamma(\frac{2}{3})}{\Gamma(\frac{1}{3})} \approx 0.3645, \quad T_R'(0) = 2c_1^2, \quad T_R''(0) = 1-16c_1^3,$$
$$T_I(0) = \frac{3^{\frac{4}{3}}}{4}\Big(\Gamma\Big(\frac{2}{3}\Big)\Big)^2 = \sqrt{3}\pi c_1, \quad T_I'(0) = -2\sqrt{3}\pi c_1^2, \quad T_I''(0) = 0.$$

Noting that $t = -\sqrt[3]{2}(\kappa-\nu)/\sqrt[3]{\nu}$, Thus, we derive from (4.48)-(4.49) that

$$\mathrm{Re}(\mathcal{T}_{l,\kappa}) \sim -\sqrt[3]{\frac{2}{\nu}}\Big(c_1 + 2c_1^2 t + \frac{1}{2}\big(1-16c_1^3\big)t^2\Big) - \frac{1}{2\kappa}, \tag{4.53}$$
$$\mathrm{Im}(\mathcal{T}_{l,\kappa}) \sim 2^{\frac{1}{3}}\sqrt{3}c_1\frac{\nu^{2/3}}{\kappa}\big(1-2c_1 t\big), \quad \text{where } t = -\sqrt[3]{2}\,\frac{\kappa-\nu}{\sqrt[3]{\nu}}. \tag{4.54}$$

Hence, we obtain the desired estimates for this case.

Case (iv) $\rho = \nu/\kappa \in [\vartheta_2, \infty)$. Set $\mathrm{sech}\alpha = \rho^{-1}$, i.e., $\cosh\alpha = \rho$ with $\alpha > 0$. One verifies

$$\sinh\alpha = \sqrt{\rho^2-1}, \quad \tanh\alpha = \frac{\sqrt{\rho^2-1}}{\rho}, \quad \Psi := \alpha - \tanh\alpha > 0. \tag{4.55}$$

Recall the asymptotic formulas [87, (9.3.7-9.3.8)]:

$$\begin{aligned} J_\nu(\nu\mathrm{sech}\alpha) &\sim \frac{e^{-\nu\Psi}}{\sqrt{2\pi\nu\tanh\alpha}}\big\{1+O(\nu^{-1})\big\};\\ Y_\nu(\nu\mathrm{sech}\alpha) &\sim -\frac{e^{\nu\Psi}}{\sqrt{\pi/2\,\nu\tanh\alpha}}\big\{1+O(\nu^{-1})\big\}. \end{aligned} \tag{4.56}$$

Note that by (4.55),

$$\Psi(\rho) = \mathrm{arccosh}\,\rho - \sqrt{1-\rho^{-2}} = \ln(\rho+\sqrt{\rho^2-1}) - \frac{\sqrt{\rho^2-1}}{\rho}, \quad \rho > 1, \tag{4.57}$$

which is monotonically increasing with respect to ρ. By (4.30), we have

$$\begin{aligned} \Psi(\vartheta_2) &\sim \ln(1+\tau+\sqrt{2\tau+\tau^2}) - \frac{\sqrt{2\tau+\tau^2}}{1+\tau} \sim \tau + \sqrt{2\tau+\tau^2} - \frac{\sqrt{2\tau+\tau^2}}{1+\tau}\\ &= \tau + \tau\frac{\sqrt{2\tau+\tau^2}}{1+\tau} \sim \tau, \quad \text{where } \tau := \frac{1}{\sqrt[3]{2}\,\kappa^{2/3}}. \end{aligned} \tag{4.58}$$

Thus, we observe from (4.56) that in the range of interest, J_ν, J_ν' decay exponentially, while Y_ν, Y_ν' grow exponentially. By (4.21) and (4.56),

$$\mathrm{Im}(\mathcal{T}_{l,\kappa}) = \frac{2}{\pi\kappa}\frac{1}{J_\nu^2(\kappa)+Y_\nu^2(\kappa)} \sim \frac{4\nu}{\kappa}\tanh\alpha\,\frac{e^{-2\nu\Psi}}{4+e^{-4\nu\Psi}} \sim \sqrt{\rho^2-1}\,e^{-2\nu\Psi}, \tag{4.59}$$

which leads to the estimate of the imaginary part in (4.39). As $\mathrm{Im}(\mathcal{T}_{l,\kappa})$ decays exponentially with respect to l. We derive from (4.22) that

$$\mathrm{Re}(\mathcal{T}_{l,\kappa}) = \frac{l}{\kappa} - \frac{Y_{\nu+1}(\kappa)}{Y_\nu(\kappa)} - \mathrm{Im}(\mathcal{T}_{l,\kappa})\frac{J_\nu(\kappa)}{Y_\nu(\kappa)} \sim \frac{l}{\kappa} - \frac{Y_{\nu+1}(\kappa)}{Y_\nu(\kappa)}. \tag{4.60}$$

In order to obtain better estimate, we resort to the asymptotic approximation of the ratio (cf. [116]):

$$\frac{Y_{\nu+1}(\kappa)}{Y_\nu(\kappa)} = \frac{1+\sqrt{1-\rho^{-2}}}{\rho^{-1}}\Big\{1 - \frac{1-\sqrt{1-\rho^{-2}}}{2(1-\rho^{-2})}\frac{1}{\nu} + O\Big(\frac{1}{\nu^2}\Big)\Big\}, \tag{4.61}$$

which is valid for $\nu > \kappa$ and $\kappa \sim \nu$. In fact, as shown in [116], it is derived from the formula (4.56) with more terms. Inserting (4.61) into (4.60) leads to the estimate of the real part in (4.39).

□

In Figure 4.1, we depict in (a)-(b) $\mathrm{Re}(\mathcal{T}_{l,\kappa})$ and $\mathrm{Im}(\mathcal{T}_{l,\kappa})$ for various l and κ, and in (c)-(d), the exact value and approximations in Theorem 4.1 for various samples of κ.

4.2.2 Improved estimates

We first introduce some notation. Let $I := (a, b)$ and $\varpi = r^2$. The weighted Sobolev space $H^s_\omega(\Lambda)$ with $s \geq 0$ is defined as usual in Admas [1]. We denote by $L^2_\omega(I)$ a Hilbert space of real or complex functions with inner product and norm

$$(u, v)_\omega = \int_I u(r)\bar{v}(r)\omega(r)dr, \quad \|u\|_\omega = \sqrt{(u, u)_\omega},$$

where $\bar{v}$ is the complex conjugate of v. We also use the anisotropic Sobolev spaces, e.g., $H^{s'}_p(S; H^s_\omega(I))$ defined via the SPH expansion coefficients $\widehat{U}^m_l$ of U with the norm:

$$\|U\|_{H^{s'}_p(S;H^s_\omega(I))} = \Big(\sum_{l=1}^{\infty} \sum_{|m|=0}^{l} (1+l)^{2s'} \|\widehat{U}^m_l\|^2_{H^s_\omega(I)} \Big)^{1/2}, \tag{4.62}$$

where p indicates the 2π-periodicity in φ-direction. If $\omega \equiv 1$, we drop ω in the notation.

The weak form of (4.5)-(4.6) is to find $U \in H^1_p(S; {}_0H^1(I))$ such that (cf. [77, (3.9)]):

$$\begin{aligned} \mathbb{B}(U, V) &= (\partial_r U, \partial_r V)_{\varpi,\Omega} + (\nabla_S U, \nabla_S V)_\Omega - k^2 (U, V)_{\varpi,\Omega} - b^2 \langle \mathcal{T}_b U, V\rangle_S \\ &= (F, V)_{\varpi,\Omega} + \langle H, V\rangle_S, \quad \forall\, V \in H^1_p(S; {}_0H^1(I)), \end{aligned} \tag{4.63}$$

where ${}_0H^1(I) = \{v \in H^1(I) \,:\, v(a) = 0\}$. We expand U, F, H in SPH series as

$$\big\{U, F, H\big\} = \sum_{l=1}^{\infty} \sum_{|m|=0}^{l} \big\{\widehat{U}^m_l(r), \widehat{F}^m_l(r), \widehat{H}^m_l(r)\big\} Y^m_l(\theta, \varphi). \tag{4.64}$$

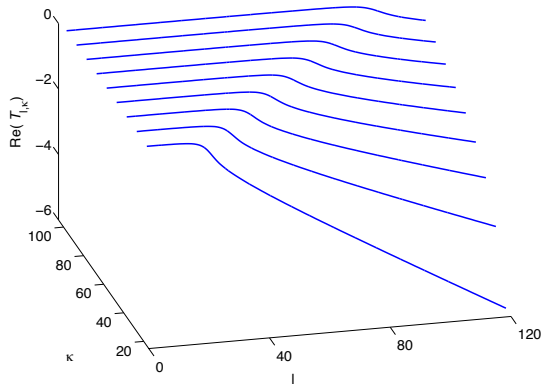

(a) $\mathrm{Re}(\mathcal{T}_{l,\kappa})$

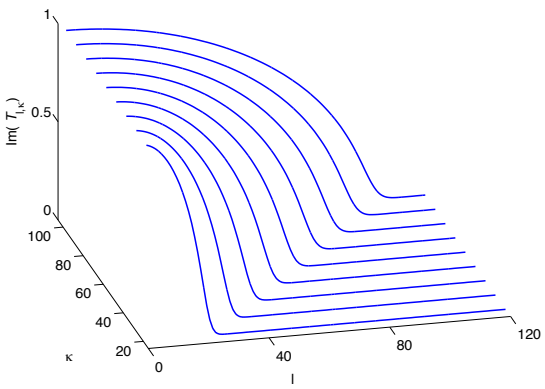

(b) $\mathrm{Im}(\mathcal{T}_{l,\kappa})$

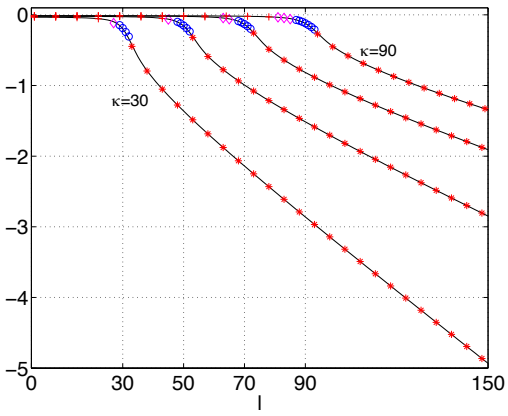

(c) $\mathrm{Re}(\mathcal{T}_{l,\kappa})$ versus $E^R_{l,\kappa}$

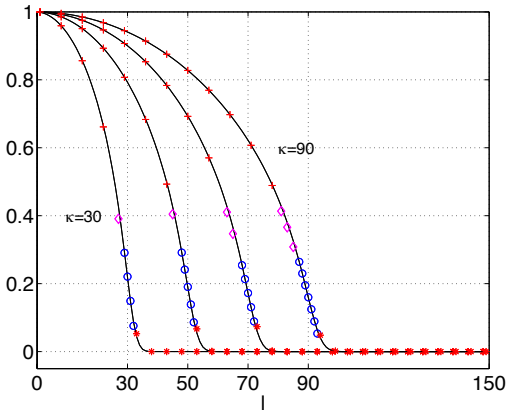

(d) $\mathrm{Im}(\mathcal{T}_{l,\kappa})$ versus $E^I_{l,\kappa}$

Figure 4.1: (a)-(b): Real and imaginary parts of $\mathcal{T}_{l,\kappa}$ with various samples $(l,\kappa) \in [0,120]\times[1,100]$. (c) $\mathrm{Re}(\mathcal{T}_{l,\kappa})$ (solid line) against $E^R_{l,\kappa}$; (d) $\mathrm{Im}(\mathcal{T}_{l,\kappa})$ (solid line) against $E^I_{l,\kappa}$ with $\kappa = 30, 50, 70, 90$ (note: in (c)-(d), "+" for $\rho = \nu/\kappa \in (0,\theta_0)$, "$\diamond$" for $\rho \in [\theta_0,\vartheta_1]$, "$\circ$" for $\rho \in (\vartheta_1,\vartheta_2)$ and "$*$" for $\rho \in [\vartheta_2,\infty)$).

Taking $V = \widehat{V}_{l'}^{m'}(r)Y_{l'}^{m'}$ in (4.63) and using the property of SPH (cf. Section 4.1), we obtain the corresponding weak form for each mode (l,m) : find $u := \widehat{U}_l^m \in {}_0H^1(I)$ such that

$$\begin{aligned}\mathbb{B}_l^m(u,v) &:= (u',v')_\varpi + \beta_l(u,v) - k^2(u,v)_\varpi - kb^2\mathcal{T}_{l,kb}u(b)\bar{v}(b)\\ &= (f,v)_\varpi + b^2h\bar{v}(b), \quad \forall v \in {}_0H^1(I),\end{aligned} \tag{4.65}$$

where $\beta_l = l(l+1)$, the weight function $\varpi = r^2$ appears naturally in the weak formulation and we denote $v := \widehat{V}_l^m$, $f := \widehat{F}_l^m$ and $h := \widehat{H}_l^m$. Here, we drop the weight function ϖ in the space ${}_0H^1(I)$ as it is uniformly bounded below away 0 on I.

One main result of this section is the following improved optimal estimate, which removes a factor of $k^{1/3}$ from the upper bound of [77, Lemma 3.1].

Lemma 4.2. *Let u be the solutions of (4.65). If $f \in L^2(I)$, then we have that for all $k \geq k_0 > 0$ (for some fixed constant k_0), and for $l \geq 1, 0 \leq |m| \leq l$,*

$$\|u'\|_\varpi^2 + \beta_l\|u\|^2 + k^2\|u\|_\varpi^2 \lesssim \|f\|_\varpi^2 + |h|^2. \tag{4.66}$$

Proof. Taking $v = u$ in (4.65), we obtain

$$\begin{aligned}&\|u'\|_\varpi^2 + \beta_l\|u\|^2 - k^2\|u\|_\varpi^2 - kb^2\,\mathrm{Re}(\mathcal{T}_{l,kb})|u(b)|^2\\ &= \mathrm{Re}(f,u)_\varpi + b^2\,\mathrm{Re}(h\bar{u}(b)),\end{aligned} \tag{4.67a}$$

$$-kb^2\,\mathrm{Im}(\mathcal{T}_{l,kb})|u(b)|^2 = \mathrm{Im}(f,u)_\varpi + b^2\,\mathrm{Im}(h\bar{u}(b)). \tag{4.67b}$$

Next taking $v = 2(r-a)u'$ in (4.65), and following the derivations in [77, (3.26)-(3.28)], we obtain

$$\begin{aligned}&b^2|I||u'(b)|^2 + \beta_l|I||u(b)|^2 + 2a\|\sqrt{r}u'\|^2 + k^2\int_a^b\Big(3-\frac{2a}{r}\Big)|u|^2r^2dr\\ &= \|u'\|_\varpi^2 + \beta_l\|u\|^2 + k^2b^2|I||u(b)|^2 + 2\,\mathrm{Re}(f,(r-a)u')_\varpi\\ &\quad + 2b^2|I|\,\mathrm{Re}\big(h\bar{u}'(b)\big) + 2kb^2|I|\,\mathrm{Re}\big\{\mathcal{T}_{l,kb}\,u(b)\bar{u}'(b)\big\},\end{aligned} \tag{4.68}$$

where $|I| = b - a$. Substituting $\|u'\|_\varpi^2 + \beta_l \|u\|^2$ in the identity (4.67a) into the above, and collecting the terms, we obtain

$$\begin{aligned} & b^2|I||u'(b)|^2 + \big\{\beta_l|I| - kb^2\,\mathrm{Re}(\mathcal{T}_{l,kb})\big\}|u(b)|^2 \\ & \quad + 2a\|\sqrt{r}u'\|^2 + 2k^2\int_a^b \Big(1 - \frac{a}{r}\Big)|u|^2 r^2 dr \\ & = k^2b^2|I||u(b)|^2 + 2kb^2|I|\,\mathrm{Re}\big\{\mathcal{T}_{l,kb}\,u(b)\,\bar{u}'(b)\big\} + 2b^2|I|\,\mathrm{Re}\big(h\bar{u}'(b)\big) \\ & \quad + 2\,\mathrm{Re}(f, (r-a)u')_\varpi + b^2\,\mathrm{Re}(h\bar{u}(b)) + \mathrm{Re}(f,u)_\varpi. \end{aligned} \tag{4.69}$$

Hereafter, let C and $\{C_i, \varepsilon_i\}$ be generic constants independent of k, l, m, and any function. Using the Cauchy-Schwarz inequality, we obtain

$$\begin{aligned} & 2kb^2|I|\,\Big|\mathrm{Re}\big\{\mathcal{T}_{l,kb}\,u(b)\,\bar{u}'(b)\big\}\Big| \le \varepsilon_1 b^2|I||u'(b)|^2 + \varepsilon_1^{-1}k^2b^2|I||\mathcal{T}_{l,kb}|^2|u(b)|^2; \\ & 2b^2|I|\,\Big|\mathrm{Re}\big(h\bar{u}'(b)\big)\Big| \le \varepsilon_2 b^2|I||u'(b)|^2 + \varepsilon_2^{-1}b^2|I||h|^2; \\ & b^2\,\Big|\mathrm{Re}(h\bar{u}(b))\Big| \le \varepsilon_3 kb^2\,|\mathrm{Re}(\mathcal{T}_{l,kb})||u(b)|^2 + \frac{b^2}{\varepsilon_3 k\,|\mathrm{Re}(\mathcal{T}_{l,kb})|}|h|^2; \\ & 2\,\Big|\mathrm{Re}(f,(r-a)u')_\varpi\Big| \le \varepsilon_4\|\sqrt{r}u'\|^2 + \varepsilon_4^{-1}b|I|^2\|f\|_\varpi^2; \\ & \Big|\mathrm{Re}(f,u)_\varpi\Big| \le \varepsilon_5\|u\|_\varpi^2 + (4\varepsilon_5)^{-1}\|f\|_\varpi^2. \end{aligned} \tag{4.70}$$

Thus, by choosing suitable $\{\varepsilon_i\}$, we obtain from (4.69)-(4.70) that

$$\begin{aligned} & C_1b^2|I||u'(b)|^2 + D_{l,k}|I||u(b)|^2 + C_2a\|\sqrt{r}u'\|^2 + C_3k^2\|u\|_\varpi^2 \\ & \lesssim \|f\|_\varpi^2 + \Big(1 + \frac{1}{k\,|\mathrm{Re}(\mathcal{T}_{l,kb})|}\Big)|h|^2, \end{aligned} \tag{4.71}$$

where $C_1 = 1 - (\varepsilon_1 + \varepsilon_2), C_2 = 2 - \varepsilon_4$, $C_3 = 2(1 - a/\xi) - \varepsilon_5/k^2$ with $\xi \in (a, b)$, and

$$D_{l,k} := \beta_l - (1 - \varepsilon_3)kb^2|I|^{-1}\,\mathrm{Re}(\mathcal{T}_{l,kb}) - k^2b^2\big(1 + \varepsilon_1^{-1}|\mathcal{T}_{l,kb}|^2\big). \tag{4.72}$$

It remains to estimate $D_{l,k}$, which is negative for e.g., small l. According to the estimates in Lemma 4.1, we conduct the analysis for four different cases as in (4.27).

(i) If $\rho = \frac{\nu}{kb} \in (0, \theta_0]$ for fixed $0 < \theta_0 < 1$, we obtain from (4.67b) that

$$\begin{aligned} k^2 b^2 \, |u(b)|^2 &\leq \frac{k}{|\mathrm{Im}(\mathcal{T}_{l,kb})|} \big\{ |\mathrm{Im}(f,u)_\varpi| + b^2 \, |\mathrm{Im}(h\overline{u(b)})| \big\} \\ &\leq \frac{\varepsilon_7}{2} k^2 \|u\|_\varpi^2 + \frac{\|f\|_\varpi^2}{2\varepsilon_7 |\mathrm{Im}(\mathcal{T}_{l,kb})|^2} + \frac{k^2 b^2}{2} |u(b)|^2 + \frac{|h|^2}{2|\mathrm{Im}(\mathcal{T}_{l,kb})|^2}. \end{aligned} \tag{4.73}$$

By (4.35), $\mathrm{Im}(\mathcal{T}_{l,kb})$ in this range behaves like a constant, so (4.73) implies

$$k^2 b^2 \, |u(b)|^2 \leq \varepsilon_7 k^2 \|u\|_\varpi^2 + C\big(\|f\|_\varpi^2 + |h|^2\big). \tag{4.74}$$

By (4.35), $|\mathcal{T}_{l,kb}|^2 \leq C$, so $D_{l,k} \leq -Ck^2 b^2$. Therefore, using (4.71) and (4.74) leads to

$$\|\sqrt{r} u'\|^2 + k^2 \|u\|_\varpi^2 + k^2 |u(b)|^2 \leq C\big(\|f\|_\varpi^2 + |h|^2\big). \tag{4.75}$$

Thus, we derive the desired estimate in this case from (4.67a) and (4.75).

(ii) For $\rho = \frac{\nu}{kb} \in (\theta_0, \vartheta_1]$, we first show that for any $\bar{c}_0 \in (1 - \theta_0, 1/\sqrt[3]{2})$ and $kb > 1$, there exists a unique $\gamma_0 \in [1/3, 1)$ such that

$$\rho = 1 - \bar{c}_0 (kb)^{\gamma_0 - 1}, \quad \text{i.e.,} \quad \gamma_0 = 1 + \frac{\ln((1-\rho)/\bar{c}_0)}{\ln(kb)}. \tag{4.76}$$

Apparently, γ_0 decreases with respect to ρ, so by (4.30),

$$\begin{aligned} &\frac{1}{3} - \frac{\ln(\sqrt[3]{2}\bar{c}_0)}{\ln(kb)} + \frac{\ln(1 + O((kb)^{-2/3})}{\ln(kb)} \\ &= 1 + \frac{\ln((1-\vartheta_1)/\bar{c}_0)}{\ln(kb)} \leq \gamma_0 < 1 + \frac{\ln((1-\theta_0)/\bar{c}_0)}{\ln(kb)}, \end{aligned} \tag{4.77}$$

Then one verifies readily that for $\bar{c}_0 \in (1 - \theta_0, 1/\sqrt[3]{2})$, we have $\gamma_0 \in [1/3, 1)$. In view of (4.76), we can write

$$\nu = kb - \bar{c}_0 (kb)^{\gamma_0}. \tag{4.78}$$

Thus, by (4.36),

$$\begin{aligned} &\mathrm{Re}(\mathcal{T}_{l,kb}) \sim -\frac{1}{2\bar{c}_0} (kb)^{-\gamma_0}, \quad \mathrm{Im}(\mathcal{T}_{l,kb}) \sim \sqrt{2\bar{c}_0} (kb)^{(\gamma_0 - 1)/2}, \\ &|\mathcal{T}_{l,kb}|^2 \sim 2\bar{c}_0 (kb)^{\gamma_0 - 1}, \end{aligned} \tag{4.79}$$

which implies

$$\begin{aligned} D_{l,k} \sim \nu^2 - \frac{1}{4} + (1-\varepsilon_3)\frac{b}{2|I|\bar{c}_0}(kb)^{1-\gamma_0} \\ - k^2b^2\big(1+\varepsilon_1^{-1}2\bar{c}_0(kb)^{\gamma_0-1}\big) \sim -2\bar{c}_0(1+\varepsilon_1^{-1})(kb)^{\gamma_0+1}. \end{aligned} \tag{4.80}$$

By (4.67b) and the Cauchy-Schwarz inequality,

$$\begin{aligned} &(kb)^{\gamma_0+1}\,|u(b)|^2 \le \frac{(kb)^{\gamma_0}}{|\mathrm{Im}(\mathcal{T}_{l,kb})|}\big\{|\mathrm{Im}(f,u)_\varpi| + b^2\,|\mathrm{Im}(h\bar{u}(b))|\big\} \\ &\le \frac{\varepsilon_7}{2}k^2\|u\|_\varpi^2 + \frac{(kb)^{2\gamma_0-2}}{2\varepsilon_7|\mathrm{Im}(\mathcal{T}_{l,kb})|^2}\|f\|_\varpi^2 + \frac{(kb)^{\gamma_0+1}}{2}|u(b)|^2 + \frac{(kb)^{\gamma_0-1}}{2|\mathrm{Im}(\mathcal{T}_{l,kb})|^2}|h|^2. \end{aligned} \tag{4.81}$$

Then by (4.79) and (4.81),

$$(kb)^{\gamma_0+1}\,|u(b)|^2 \le \varepsilon_7k^2\|u\|_\varpi^2 + C\big((kb)^{\gamma_0-1}\|f\|_\varpi^2 + |h|^2\big). \tag{4.82}$$

Thus, we derive from (4.71) that

$$\|\sqrt{r}u'\|^2 + k^2\|u\|_\varpi^2 + (kb)^{\gamma_0+1}|u(b)|^2 \le C\big(\|f\|_\varpi^2 + |h|^2\big). \tag{4.83}$$

Therefore, we obtain (4.66) from (4.67a) and (4.83).

(iii) If $\rho = \frac{\nu}{kb} \in (\vartheta_1, \vartheta_2]$, we find from (4.30) that

$$kb - \sqrt[3]{\frac{kb}{2}} + O(k^{-1/3}) < \nu \le kb + \sqrt[3]{\frac{kb}{2}} + O(k^{-1/3}). \tag{4.84}$$

By (4.37),

$$\mathrm{Re}(\mathcal{T}_{l,kb}) \sim -\bar{c}_1(kb)^{-1/3}, \quad \mathrm{Im}(\mathcal{T}_{l,kb}) \sim \bar{c}_2(kb)^{-1/3}, \quad |\mathcal{T}_{l,kb}|^2 \sim \bar{c}_3(kb)^{-2/3}, \tag{4.85}$$

where $\{\bar{c}_i\}$ are some positive constants independent of k, l. We can follow the same procedure as for Case (ii) (but with $\gamma_0 = 1/3$) to derive

$$\|\sqrt{r}u'\|^2 + k^2\|u\|_\varpi^2 + (kb)^{4/3}|u(b)|^2 \le C\big(\|f\|_\varpi^2 + |h|^2\big). \tag{4.86}$$

Similarly, (4.66) follows from (4.67a) and (4.86).

(iv) If $\rho = \frac{\nu}{kb} \in (\vartheta_2, \infty)$, we find from (4.39) that $\mathrm{Im}(\mathcal{T}_{l,kb})$ decays exponentially with respect to l, so we cannot get a useful bound of $|u(b)|$ from (4.67b). We therefore consider two cases:

$$\text{(a)}\ \ \nu = kb + \bar{c}_5(kb)^{\gamma_1}\ \ \text{with}\ \ 1/3 < \gamma_1 < 1; \quad \text{(b)}\ \ \nu \geq \eta\, kb, \tag{4.87}$$

for constant $\bar{c}_5 \in (\eta - 1, 1/\sqrt[3]{2})$ and $1 < \eta < 1 + 1/\sqrt[3]{2}$. Here, we show that Case (a) can cover $\rho \in (\vartheta_2, \eta)$. Indeed, similar to (4.76)-(4.77), we have $\rho = 1 + \bar{c}_5(kb)^{\gamma_1 - 1}$, and

$$\begin{aligned} &\frac{1}{3} - \frac{\ln(\sqrt[3]{2}\bar{c}_5)}{\ln(kb)} + \frac{\ln(1 + O((kb)^{-2/3})}{\ln(kb)} \\ &= 1 + \frac{\ln((\vartheta_2 - 1)/\bar{c}_5)}{\ln(kb)} < \gamma_1 < 1 + \frac{\ln((\eta - 1)/\bar{c}_5)}{\ln(kb)}. \end{aligned} \tag{4.88}$$

This implies if $\bar{c}_5 \in (\eta - 1, 1/\sqrt[3]{2})$ and $1 < \eta < 1 + 1/\sqrt[3]{2}$, then $1/3 < \gamma_1 < 1$ and we can write ν in the form of (a).

In the first case, we derive from (4.39) that

$$\begin{aligned} &\mathrm{Re}(\mathcal{T}_{l,kb}) \sim \sqrt{2\bar{c}_5}(kb)^{(\gamma_1 - 1)/2}, \quad |\mathcal{T}_{l,kb}|^2 \sim 2\bar{c}_5(kb)^{\gamma_1 - 1}, \\ &D_{l,k} \sim -2\bar{c}_5(\varepsilon_1^{-1} - 1)(kb)^{\gamma_1 + 1}, \end{aligned} \tag{4.89}$$

where we recall that $\varepsilon_1 < 1$. Noticing that

$$\beta_l \|u\|^2 - k^2\|u\|_\varpi^2 \geq (\beta_l - k^2 b^2)\|u\|^2 \geq 0, \tag{4.90}$$

and $\mathrm{Re}(\mathcal{T}_{l,kb}) < 0$, we deduce from (4.67a) that

$$-kb^2\,\mathrm{Re}(\mathcal{T}_{l,kb})|u(b)|^2 \leq |\mathrm{Re}(f, u)_\varpi| + b^2\,|\mathrm{Re}(h\bar{u}(b))|. \tag{4.91}$$

Using (4.89), (4.91) and following the derivation of (4.81), we can get

$$(kb)^{\gamma_1 + 1}\,|u(b)|^2 \leq \varepsilon_8 k^2\|u\|_\varpi^2 + C\big((kb)^{\gamma_1 - 1}\|f\|_\varpi^2 + |h|^2\big). \tag{4.92}$$

We then derive from (4.71) that

$$\|\sqrt{r}u'\|^2 + k^2\|u\|_\varpi^2 + (kb)^{\gamma_1 + 1}|u(b)|^2 \leq C\big(\|f\|_\varpi^2 + |h|^2\big). \tag{4.93}$$

Thus, we derive (4.66) for this case from (4.67a) and (4.93).

In the second case of (4.87), we observe from (4.39) that

$$\mathrm{Re}(\mathcal{T}_{l,kb}) \sim -\frac{\nu}{kb}, \quad |\mathcal{T}_{l,kb}|^2 \sim \frac{\nu^2}{k^2b^2}, \tag{4.94}$$

which implies

$$D_{l,k} \sim \nu^2 - \frac{1}{4} + (1-\varepsilon_3)\frac{b\nu}{|I|} - k^2b^2 - \varepsilon_1^{-1}\nu^2 \sim -\bar{c}_6\,\beta_l. \tag{4.95}$$

Then, by (4.94) and (4.91),

$$\beta_l|u(b)|^2 \le \varepsilon_8\beta_l\|u\|^2 + C\big(\|f\|_\varpi^2 + |h|^2\big). \tag{4.96}$$

We then derive from (4.71) that

$$\|\sqrt{r}u'\|^2 + k^2\|u\|_\varpi^2 + \beta_l|u(b)|^2 \le C\big(\|f\|_\varpi^2 + |h|^2\big). \tag{4.97}$$

Finally, we obtain (4.66) from (4.67a) and (4.97). □

Thanks to the above lemma and the orthogonality of SPH, one can easily derive the following improved result, where a factor of $k^{1/3}$ is removed from the upper bound of [77, Thm. 3.1].

Theorem 4.2. *Let U be the solution of* (4.63). *If $F \in L^2(\Omega)$ and $H \in L^2(S)$, then we have*

$$\|\nabla U\|_\Omega + k\|U\|_\Omega \lesssim \|F\|_\Omega + \|H\|_{L^2(S)}. \tag{4.98}$$

4.3 Estimates for Maxwell's equations

In this section, we perform the wavenumber explicit *a prior* estimates for the Maxwell's equations (4.2)-(4.3). The key is to employ a divergence-free vector harmonic expansion of the fields and reduce the problem of interest into two sequences of *decoupled one-dimensional* Helmholtz problems. This decoupling not only leads to a more efficient numerical algorithm, but also greatly simplifies its analysis.

4.3.1 Dimension reduction via divergence-free VSH expansions

Let $\{Y_l^m\}$ be the spherical harmonics, and $\big\{Y_l^m \boldsymbol{e}_r, \nabla_S Y_l^m, \boldsymbol{T}_l^m := \nabla_S Y_l^m \times \boldsymbol{e}_r\big\}$ (where S is a unit spherical surface) be the vector spherical harmonics (see Section 4.1). The divergence-free VSHs that we shall use are introduced in [113], but it appears that they are rarely discussed, if not at all, in mathematical literature.

Introduce the spaces

$$\mathbb{H}(\mathrm{div};\Omega) = \big\{\boldsymbol{E} \in \boldsymbol{L}^2(\Omega) : \mathrm{div}\boldsymbol{E} \in L^2(\Omega)\big\},$$
$$\mathbb{H}(\mathbf{curl};\Omega) = \big\{\boldsymbol{E} \in (L^2(\Omega))^3 : \nabla \times \boldsymbol{E} \in (L^2(\Omega))^3\big\},$$

equipped the graph norm defined as in [35, P. 52], and

$$\mathbb{H}_0(\mathrm{div};\Omega) = \big\{\boldsymbol{E} \in \mathbb{H}(\mathrm{div};\Omega) : \mathrm{div}\boldsymbol{E} = 0\big\},$$
$$\mathbb{H}_0(\mathbf{curl};\Omega) = \big\{\boldsymbol{v} \in \mathbb{H}(\mathbf{curl};\Omega) : \boldsymbol{v} \times \boldsymbol{e}_r|_{r=a} = \boldsymbol{0}\big\}.$$

We have following important properties of solenoidal (or divergence-free) fields.

Proposition 4.1. *For any $\boldsymbol{E} \in (L^2(\Omega))^3$, we expand it as*

$$\boldsymbol{E} = v_{2,0}^0\, Y_0^0 \boldsymbol{e}_r + \sum_{l=1}^{\infty} \sum_{|m|=0}^{l} \Big\{ v_{1,l}^m\, \boldsymbol{T}_l^m + v_{2,l}^m\, Y_l^m \boldsymbol{e}_r + v_{3,l}^m\, \nabla_S Y_l^m \Big\}, \tag{4.99}$$

where we recall $\beta_l = l(l+1)$ and

$$v_{1,l}^m = \beta_l^{-1} \langle \boldsymbol{E}, \boldsymbol{T}_l^m \rangle_S, \quad v_{2,l}^m = \langle \boldsymbol{E}, Y_l^m \boldsymbol{e}_r \rangle_S, \quad v_{3,l}^m = \beta_l^{-1} \langle \boldsymbol{E}, \nabla_S Y_l^m \rangle_S. \tag{4.100}$$

If $\boldsymbol{E} \in \mathbb{H}(\mathrm{div}^0;\Omega)$, then we have

$$\Big(\frac{d}{dr} + \frac{2}{r}\Big) v_{2,0}^0 = 0, \quad \frac{r}{\beta_l}\Big(\frac{d}{dr} + \frac{2}{r}\Big) v_{2,l}^m = v_{3,l}^m, \tag{4.101}$$

and we can write

$$\boldsymbol{E} = u_0^0\, Y_0^0 \boldsymbol{e}_r + \sum_{l=1}^{\infty} \sum_{|m|=0}^{l} \Big\{ u_{1,l}^m\, \boldsymbol{T}_l^m + \nabla \times \big(u_{2,l}^m\, \boldsymbol{T}_l^m \big) \Big\}, \tag{4.102}$$

where

$$u_0^0 = v_{2,0}^0 = \frac{c}{r^2}, \quad u_{1,l}^m = v_{1,l}^m, \quad u_{2,l}^m = \beta_l^{-1} r v_{2,l}^m, \tag{4.103}$$

with c being an arbitrary constant.

Proof. Since $\mathrm{div}(v_{1,l}^m \boldsymbol{T}_l^m) = 0$ (cf. (4.15)), we obtain from (4.196) and (4.17)-(4.18) that

$$\mathrm{div}\, \boldsymbol{E} = \Big(\frac{d}{dr} + \frac{2}{r}\Big) v_{2,0}^0 + \sum_{l=1}^{\infty} \sum_{|m|=0}^{l} \Big\{ \Big(\frac{d}{dr} + \frac{2}{r}\Big) v_{2,l}^m - \frac{\beta_l}{r} v_{3,l}^m \Big\} Y_l^m. \tag{4.104}$$

Then the identities in (4.101) follow from $\mathrm{div}\, \boldsymbol{E} = 0$ immediately.

Note that the equation of $v_{2,0}^0$ in (4.101) has the general solution: $v_{2,0}^0 = c/r^2$. To derive (4.102) under (4.103), it suffices to show that

$$\beta_l^{-1} \nabla \times \big(r v_{2,l}^m \boldsymbol{T}_l^m \big) = v_{2,l}^m Y_l^m \boldsymbol{e}_r + v_{3,l}^m \nabla_S Y_l^m \,. \tag{4.105}$$

It follows from a direct calculation using (4.15), that is,

$$\begin{aligned} \beta_l^{-1} \nabla \times \big(r v_{2,l}^m \boldsymbol{T}_l^m \big) &= v_{2,l}^m Y_l^m \boldsymbol{e}_r + \beta_l^{-1} \hat{\partial}_r (r v_{2,l}^m) \nabla_S Y_l^m \\ &= v_{2,l}^m Y_l^m \boldsymbol{e}_r + \frac{r}{\beta_l} \Big(\frac{d}{dr} + \frac{2}{r} \Big) v_{2,l}^m \nabla_S Y_l^m \,. \end{aligned} \tag{4.106}$$

Therefore, the expansion (4.102) is a direct consequence of (4.99), (4.101) and (4.103). □

Remark 4.1. *Equivalently, we can reformulate* (4.102) *as*

$$\boldsymbol{E} = u_0^0 Y_0^0 \boldsymbol{e}_r + \sum_{l=1}^{\infty} \sum_{|m|=0}^{l} \Big\{ u_{1,l}^m \boldsymbol{T}_l^m + \hat{\partial}_r u_{2,l}^m \nabla_S Y_l^m + \frac{\beta_l}{r} u_{2,l}^m Y_l^m \boldsymbol{e}_r \Big\}, \tag{4.107}$$

which allows for exact imposition of the divergence-free condition. Such a VSH expansion turns out to be a very useful analytic and numerical tool for e.g., Maxwell equations and Navier-Stokes equations in spherical geometry (cf. [4, 113, 3, 35]). □

Recall that the capacity operator in (4.3) is defined by (cf. [3, (5.3.88)]):

$$\mathscr{T}_b[\boldsymbol{\Phi}] := \sum_{l=1}^{\infty}\sum_{|m|=0}^{l}\Big\{-\mathrm{i}\frac{\hat{\partial}_r h_l^{(1)}(kb)}{h_l^{(1)}(kb)}\,\phi_{T,l}^m\,\boldsymbol{T}_l^m + \mathrm{i}\frac{h_l^{(1)}(kb)}{\hat{\partial}_r h_l^{(1)}(kb)}\,\phi_{Y,l}^m\,\nabla_S Y_l^m\Big\}, \tag{4.108}$$

where $h_l^{(1)}$ is the spherical Bessel function of the first kind (cf. [87]), and

$$\hat{\partial}_r h_l^{(1)}(kb) = \Big(\frac{d}{dr}+\frac{1}{r}\Big)h_l^{(1)}(r)\Big|_{r=kb}. \tag{4.109}$$

The expansion coefficients $\{\phi_{T,l}^m, \phi_{Y,l}^m\}$ are associated with the expansion:

$$\boldsymbol{\Phi} := \boldsymbol{E}_S|_{r=b} = \sum_{l=1}^{\infty}\sum_{|m|=0}^{l}\big\{\phi_{T,l}^m\,\boldsymbol{T}_l^m + \phi_{Y,l}^m\nabla_S Y_l^m\big\}, \tag{4.110}$$

and given by

$$\phi_{T,l}^m = \beta_l^{-1}\big\langle\boldsymbol{\Phi},\boldsymbol{T}_l^m\big\rangle_S,\quad \phi_{Y,l}^m = \beta_l^{-1}\big\langle\boldsymbol{\Phi},\nabla_S Y_l^m\big\rangle_S. \tag{4.111}$$

As $\boldsymbol{F}$ in (4.5) is a solenoidal field, we can expand it as (4.102) with the coefficients f_0^0 and $\{f_{1,l}^m, f_{2,l}^m\}$. We also expand the data $\boldsymbol{h}\in\boldsymbol{L}_T^2(S)$ in (4.6) (the space of tangential components) as

$$\boldsymbol{h} = \sum_{l=1}^{\infty}\sum_{|m|=0}^{l}\big\{h_{T,l}^m\,\boldsymbol{T}_l^m + h_{Y,l}^m\,\nabla_S Y_l^m\big\}, \tag{4.112}$$

where the expansion coefficients are given by (4.111) with $\boldsymbol{h}$ in place of $\boldsymbol{\Phi}$.

Proposition 4.2. *Denote*

$$\begin{aligned} &u_1 = u_{1,l}^m,\quad u_2 = u_{2,l}^m,\quad f_1 = f_{1,l}^m,\quad f_2 = f_{2,l}^m,\\ &h_1 = h_{T,l}^m,\quad h_2 = k^{-1}\big(\mathcal{T}_{l,kb}+(kb)^{-1}\big)h_{Y,l}^m, \end{aligned} \tag{4.113}$$

for $l\ge 1$. Then the Maxwell's equations (4.2)-(4.3) *reduce to $-k^2u_0^0 = f_0^0$, and the following two sequences of one-dimensional problems:*

$$\begin{aligned} &-\frac{1}{r^2}(r^2u_i')' + \frac{\beta_l}{r^2}u_i - k^2u_i = f_i,\quad r\in I := (a,b),\\ &u_i'(b) - k\,\mathcal{T}_{l,kb}\,u_i(b) = h_i,\quad i=1,2, \end{aligned} \tag{4.114}$$

but with different boundary conditions at $r=a$:

$$u_1(a) = 0,\quad u_2'(a) + a^{-1}u_2(a) = 0. \tag{4.115}$$

Proof. We first consider (4.2). Recall that if $\operatorname{div} \boldsymbol{u} = 0$, then we have

$$\nabla \times \nabla \times \boldsymbol{u} = -\Delta \boldsymbol{u}. \tag{4.116}$$

Using (4.14) and $\operatorname{div}\big(\nabla \times (f\boldsymbol{T}_l^m)\big) = 0$, we derive from (4.102), (4.116) and (4.15)-(4.16) that

$$\begin{aligned} &\nabla \times \nabla \times \big(u_{1,l}^m \boldsymbol{T}_l^m\big) = -\Delta\big(u_{1,l}^m \boldsymbol{T}_l^m\big) = -\mathcal{L}_l\big(u_{1,l}^m\big)\boldsymbol{T}_l^m, \\ &\nabla \times \nabla \times \nabla \times \big(u_{2,l}^m \boldsymbol{T}_l^m\big) = -\nabla \times \big(\Delta\big(u_{2,l}^m \boldsymbol{T}_l^m\big)\big) = -\nabla \times \big(\mathcal{L}_l\big(u_{2,l}^m\big)\boldsymbol{T}_l^m\big), \end{aligned} \tag{4.117}$$

where

$$\mathcal{L}_l = \frac{d^2}{dr^2} + \frac{2}{r}\frac{d}{dr} - \frac{l(l+1)}{r^2}. \tag{4.118}$$

Therefore, by using the expansions (4.102), we can reduce (4.2) to:

$$-(\mathcal{L}_l + k^2)w(r) = f(r) \quad \text{for } \{w, f\} = \{u_{1,l}^m, f_{1,l}^m\} \text{ or } \{u_{2,l}^m, f_{2,l}^m\}, \tag{4.119}$$

for $l \geq 1$ and $r \in I$. In addition, we have

$$-k^2 u_0^0 = f_0^0, \quad \text{as } \nabla \times (u_0^0\, Y_0^0 \boldsymbol{e}_r) = \nabla \times (f_0^0\, Y_0^0 \boldsymbol{e}_r) = \boldsymbol{0}, \tag{4.120}$$

since $\boldsymbol{E}$ and $\boldsymbol{F}$ are solenoidal. This leads to the mode u_0^0, so we only consider the modes with $l \geq 1$ and $0 \leq |m| \leq l$. A direct calculation using (4.12)-(4.13) and (4.15)-(4.16) leads to the reduction of the first boundary condition in (4.3):

$$u_{1,l}^m(a) = 0\,, \quad \hat{\partial}_r u_{2,l}^m(a) = 0, \quad \text{where } \hat{\partial}_r := \frac{d}{dr} + \frac{1}{r}\,. \tag{4.121}$$

We now turn to the DtN boundary condition (4.3). By (4.102) and (4.117),

$$\nabla \times \boldsymbol{E} = \sum_{l=1}^{\infty} \sum_{|m|=0}^{l} \Big\{\nabla \times \big(u_{1,l}^m \boldsymbol{T}_l^m\big) - \mathcal{L}_l(u_{2,l}^m)\boldsymbol{T}_l^m\Big\}. \tag{4.122}$$

Again from (4.12)-(4.13) and (4.15)-(4.16), we derive

$$\begin{aligned} &\big(\nabla \times \boldsymbol{E}\big) \times \boldsymbol{e}_r\Big|_{r=b} = \sum_{l=1}^{\infty} \sum_{|m|=0}^{l} \Big\{\big(\hat{\partial}_r u_{1,l}^m\big)\boldsymbol{T}_l^m + \mathcal{L}_l(u_{2,l}^m)\nabla_S Y_l^m\Big\}\Big|_{r=b}, \\ &\boldsymbol{E}_S\Big|_{r=b} = \sum_{l=1}^{\infty} \sum_{|m|=0}^{l} \Big\{u_{1,l}^m \boldsymbol{T}_l^m + \hat{\partial}_r u_{2,l}^m\, \nabla_S Y_l^m\Big\}\Big|_{r=b}. \end{aligned} \tag{4.123}$$

Then, by (4.108) and (4.123),

$$-\mathrm{i}k\mathscr{T}_b[\boldsymbol{E}_S] = \sum_{l=1}^{\infty}\sum_{|m|=0}^{l}\Big\{ -k\frac{\hat{\partial}_r h_l^{(1)}(kb)}{h_l^{(1)}(kb)}\, u_{1,l}^m(b)\,\boldsymbol{T}_l^m + k\frac{h_l^{(1)}(kb)}{\hat{\partial}_r h_l^{(1)}(kb)}\,\hat{\partial}_r u_{2,l}^m(b)\,\nabla_S Y_l^m\Big\}. \tag{4.124}$$

Consequently, by (4.112) and (4.123), the DtN boundary condition (4.3) reduces to

$$\hat{\partial}_r u_{1,l}^m(b) - k\frac{\hat{\partial}_r h_l^{(1)}(kb)}{h_l^{(1)}(kb)}\, u_{1,l}^m(b) = h_{T,l}^m, \tag{4.125}$$

$$\mathcal{L}_l(u_{2,l}^m)(b) + k\frac{h_l^{(1)}(kb)}{\hat{\partial}_r h_l^{(1)}(kb)}\,\hat{\partial}_r u_{2,l}^m(b) = h_{Y,l}^m. \tag{4.126}$$

By the equation (4.119) (note: $f_{2,l}^m(b) = 0$ as the source field is assumed to be compact supported), we have $\mathcal{L}_l(u_{2,l}^m)(b) = -k^2 u_{2,l}^m(b)$, so we can simplify (4.126) as

$$\hat{\partial}_r u_{2,l}^m(b) - k\frac{\hat{\partial}_r h_l^{(1)}(kb)}{h_l^{(1)}(kb)}\, u_{2,l}^m(b) = \frac{1}{k}\frac{\hat{\partial}_r h_l^{(1)}(kb)}{h_l^{(1)}(kb)}\, h_{Y,l}^m. \tag{4.127}$$

This ends the derivation. □

4.3.2 A priori estimates for $\{u_{1,l}^m, u_{2,l}^m\}$

The weak form of (4.114)-(4.115) with $i = 1$ is to find $u_1 \in {}_0H^1(I)$ such that

$$\mathbb{B}_l^m(u_1, w) = (f_1, w)_\varpi + b^2 h_1 \bar{w}(b)\,, \quad \forall\, w \in {}_0H^1(I), \tag{4.128}$$

and the weak form of (4.114)-(4.115) with $i = 2$ is to find $v \in H^1(I)$ such that

$$\mathbb{B}_l^m(u_2, w) - a u_2(a)\bar{w}(a) = (f_2, w)_\varpi + b^2 h_2 \bar{w}(b), \quad \forall\, w \in H^1(I), \tag{4.129}$$

where the bilinear form $\mathbb{B}_l^m(\cdot,\cdot)$ is defined in (4.65).

Observe that the weak form for u_1 is the same as that of the Helmholtz equation in (4.65), while (4.129) differ from (4.128) an extra term: $-a u_2(a)\bar{w}(a)$. As a result, we can obtain the *a priori* estimates like Lemma 4.2 by using the same argument.

Theorem 4.3. *Let u_1 and u_2 be solutions of* (4.128) *and* (4.129)*, respectively. If $f_1, f_2 \in L^2(\Lambda)$, then for all $k \geq k_0 > 0$ (for some fixed constant k_0), and $l \geq 1, 0 \leq |m| \leq l$, we have*

$$\|u_i'\|_\varpi^2 + \beta_l \|u_i\|^2 + k^2 \|u_i\|_\varpi^2 \lesssim \|f_i\|_\varpi^2 + |h_i|^2, \quad i = 1, 2. \tag{4.130}$$

Proof. The estimates in Lemma 4.2 carry over to u_1, so it suffices to consider u_2 and deal with the extra term herein. Following the proof of Lemma 4.2, we take two test functions: $w = u_2$ and $w = 2(r-a)u_2$, and note that the term "$-au_2(a)\bar{w}(a)$" vanishes for the second test function. Thus, we only need to deal with the contribution from this extra term as follows:

$$\|u_2'\|_\varpi^2 + \beta_l \|u_2\| + k^2 \|u_2\|_\varpi^2 - a|u_2(a)|^2 \lesssim \|f_2\|_\varpi + |h_2|. \tag{4.131}$$

Using the Sobolev inequality (see, e.g., [47, (B.33)]), we obtain

$$\begin{aligned} a|u_2(a)|^2 &\leq a\Big(2 + \frac{1}{b-a}\Big)\|u_2\|\|u_2\|_1 \leq a\Big(2 + \frac{1}{b-a}\Big)\big(\|u_2\|^2 + \|u_2\|\|u_2'\|\big) \\ &\leq a^{-3}\Big(2 + \frac{1}{b-a}\Big)\big(\|u_2\|_\varpi^2 + \|u_2\|_\varpi \|u_2'\|_\varpi\big). \end{aligned} \tag{4.132}$$

where we used the simple inequality: $\sqrt{A^2 + B^2} \leq |A| + |B|$, and the fact $\varpi/a^2 \geq 1$. Thus,

$$a|u_2(a)|^2 \leq \frac{1}{2}\|u_2'\|_\varpi^2 + C\|u_2\|_\varpi^2. \tag{4.133}$$

Thus, by (4.131) and (4.133),

$$\frac{1}{2}\|u_2'\|_\varpi^2 + \beta_l \|u_2\|^2 + k^2\big(1 - Ck^{-1}\big)\|u_2\|_\varpi^2 \lesssim \|f_2\|_\varpi^2 + |h_2|^2. \tag{4.134}$$

This leads to the desired estimate. □

It is important to point out that as the expansion in (4.107) involves $\{\hat{\partial}_r u_{2,l}^m\}$, the direct use of Theorem 4.3 and the orthogonality of VSH only leads to an overly pessimistic estimate: $\|\boldsymbol{E}\|_\Omega = O(1)$. However, the expected optimal estimate should be $\|\boldsymbol{E}\|_\Omega = O(k^{-1})$. In view of this, we next derive an "auxiliary" equation of $\hat{\partial}_r u_{2,l}^m$ and apply the analysis similar to that for $\{u_{1,l}^m, u_{2,l}^m\}$ in the previous subsection.

4.3.3 A priori estimates for $\hat{\partial}_r u_{2,l}^m$

Equation of $\hat{\partial}_r u_{2,l}^m$

Denote

$$\begin{aligned} &v_2 := \beta_l u_{2,l}^m/r = \beta_l u_2/r, \quad v_3 := \hat{\partial}_r u_{2,l}^m = \hat{\partial}_r u_2, \quad h_Y := -k\mathcal{S}_{l,kb} h_2 = h_{Y,l}^m, \\ &g_2 := \beta_l f_{2,l}^m/r = \beta_l f_2/r, \quad g_3 := \hat{\partial}_r f_{2,l}^m = \hat{\partial}_r f_2, \end{aligned} \tag{4.135}$$

where the DtN kernel pertinent to (4.108) is defined by

$$\mathcal{S}_{l,\kappa} := -\frac{h_l^{(1)}(\kappa)}{\hat{\partial}_r h_l^{(1)}(\kappa)} = -\frac{h_l^{(1)}(\kappa)}{h_l^{(1)\prime}(\kappa) + \kappa^{-1} h_l^{(1)}(\kappa)} = -\frac{1}{\mathcal{T}_{l,\kappa} + \kappa^{-1}}, \tag{4.136}$$

for $l \geq 1$, $\kappa > 0$. Recall that $\mathcal{T}_{l,\kappa}$ is defined in (4.20).

From the equation of u_2 in Proposition 4.2, we can derive the following "auxiliary" equation.

Proposition 4.3. *Let $v_3 = \hat{\partial}_r u_2$. Then we have*

$$\begin{aligned} &-\frac{1}{r^2}(r^2 v_3')' + \frac{\beta_l}{r^2} v_3 - k^2 v_3 - \frac{2}{r^2} v_2 = g_3, \quad r \in I, \\ &v_3(a) = 0, \quad v_3'(b) - k\big(\mathcal{S}_{l,kb} - (kb)^{-1}\big) v_3(b) - b^{-1} v_2(b) = h_Y. \end{aligned} \tag{4.137}$$

Alternatively, we can replace the boundary condition at $r = b$ in (4.137) by

$$v_3'(b) - \frac{\sigma_{l,kb}}{b} v_2(b) = \frac{h_Y}{kb\,\mathcal{S}_{l,kb}} = -\frac{h_2}{b}, \tag{4.138}$$

where

$$\sigma_{l,kb} := 1 - \frac{k^2 b^2}{\beta_l}\Big(1 - \frac{1}{kb\mathcal{S}_{l,kb}}\Big) = 1 - \frac{k^2 b^2}{\beta_l}\Big(1 + \frac{\mathcal{T}_{l,kb}}{kb} + \frac{1}{k^2 b^2}\Big). \tag{4.139}$$

Proof. One verifies readily that

$$\hat{\partial}_r v_3 = \hat{\partial}_r(\hat{\partial}_r u_2) = r^{-2}(r^2 u_2')',$$

so by (4.114),

$$-\hat{\partial}_r v_3 + \frac{\beta_l}{r^2} u_2 - k^2 u_2 = f_2, \quad r \in I. \tag{4.140}$$

Acting $\hat{\partial}_r$ on both sides of the above equation, we obtain the first equation in (4.137) by a direct calculation. Since $v_3(a) = \hat{\partial}_r u_2(a)$, the boundary condition $v_3(a) = 0$ is a direct consequence of (4.115). Noting that $u_2'(b) = v_3(b) - u_2(b)/b$, we obtain from (4.136) and the boundary condition in (4.114) that

$$u_2(b) + \frac{\mathcal{S}_{l,kb}}{k} v_3(b) = \frac{\mathcal{S}_{l,kb}}{k} h_2 = -\frac{h_Y}{k^2}. \tag{4.141}$$

Taking $r = b$ in (4.140) (note: $f_2(b) = 0$), we obtain

$$u_2(b) = -k^{-2}\big(v_3'(b) + b^{-1}v_3(b) - b^{-1}v_2(b)\big). \tag{4.142}$$

Inserting (4.142) into (4.141) yields the boundary condition at $r = b$ in (4.137).

The alternative boundary condition (4.138) can be obtained by eliminating $v_3(b)$ in (4.137). More precisely, solving out $v_3(b)$ from (4.141), and using the fact $u_2(b) = bv_2(b)/\beta_l$, we can obtain (4.138)-(4.139) from (4.137). □

Properties of the DtN kernel $\mathcal{S}_{l,\kappa}$

By (4.136), we have that for integer $l \geq 1$ and real $\kappa > 0$,

$$\mathrm{Re}(\mathcal{S}_{l,\kappa}) = -\frac{\mathrm{Re}(\mathcal{T}_{l,\kappa}) + \kappa^{-1}}{(\mathrm{Re}(\mathcal{T}_{l,\kappa}) + \kappa^{-1})^2 + (\mathrm{Im}(\mathcal{T}_{l,\kappa}))^2}, \tag{4.143a}$$

$$\mathrm{Im}(\mathcal{S}_{l,\kappa}) = \frac{\mathrm{Im}(\mathcal{T}_{l,\kappa})}{(\mathrm{Re}(\mathcal{T}_{l,\kappa}) + \kappa^{-1})^2 + (\mathrm{Im}(\mathcal{T}_{l,\kappa}))^2}, \tag{4.143b}$$

which, together with (4.24), implies

$$\mathrm{Re}(\mathcal{S}_{l,\kappa}) > 0, \quad \mathrm{Im}(\mathcal{S}_{l,\kappa}) > 0, \quad \text{for } l \geq 1, \ \kappa > 0. \tag{4.144}$$

In Figure 4.2, we depict the graphs of $\mathrm{Re}(\mathcal{S}_{l,\kappa})$ and $\mathrm{Im}(\mathcal{S}_{l,\kappa})$ for various samples $(l, \kappa) \in [0, 120] \times [1, 100]$, which shows a quite different behaviour, compared with that of $\mathcal{T}_{l,\kappa}$ in Figure 4.1.

Thanks to (4.143) and the estimates in Theorem 4.1, we can analyze the behaviour of $\mathcal{S}_{l,\kappa}$.

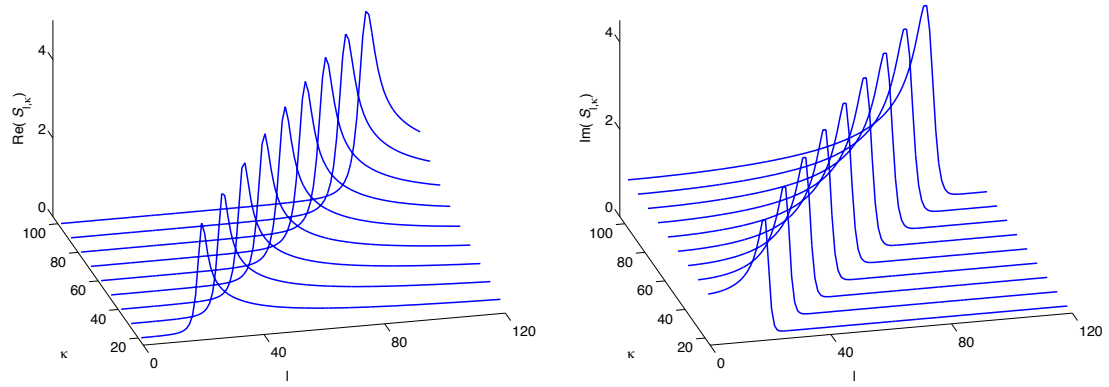

(a) $\mathrm{Re}(\mathcal{S}_{l,\kappa})$ (b) $\mathrm{Im}(\mathcal{S}_{l,\kappa})$

Figure 4.2: Graphs of real and imaginary parts of $\mathcal{S}_{l,\kappa}$ for various $(l,\kappa) \in [0,120] \times [1,100]$.

Theorem 4.4. *Let $\theta_0, \vartheta_1, \vartheta_2$ and κ_0 be defined as before. Denote $\nu = l + 1/2$ and $\rho = \nu/\kappa$. Then for any $\kappa > \kappa_0$,*

$$\mathrm{Re}(\mathcal{S}_{l,\kappa}) \sim S^R_{l,\kappa}, \quad \mathrm{Im}(\mathcal{S}_{l,\kappa}) \sim S^I_{l,\kappa}, \quad \forall\, l \geq 1, \tag{4.145}$$

where

(i) *for $\rho = \nu/\kappa \in (0, \theta_0)$,*

$$S^R_{l,k} = \frac{1}{2\kappa}\Big(\frac{\rho}{1-\rho^2}\Big)^2, \quad S^I_{l,k} = \frac{1}{\sqrt{1-\rho^2}}\,; \tag{4.146}$$

(ii) *for $\rho = \nu/\kappa \in [\theta_0, \vartheta_1]$,*

$$S^R_{l,\kappa} = \frac{1}{4\rho(1-\rho)\kappa}\Big(1 + \frac{1}{2(1-\rho)}\Big), \quad S^I_{l,\kappa} = \frac{1}{\sqrt{2\rho(1-\rho)}}; \tag{4.147}$$

(iii) *for $\rho = \nu/\kappa \in (\vartheta_1, \vartheta_2)$,*

$$S^R_{l,\kappa} = \frac{1}{4c_1}\Big(\frac{\nu}{2}\Big)^{1/3} H^R(t), \quad S^I_{l,\kappa} = \frac{\sqrt{3}}{4c_1}\Big(\frac{\nu}{2}\Big)^{1/3} H^I(t), \tag{4.148}$$

where $t = -\sqrt[3]{2}\,(\kappa-\nu)/\sqrt[3]{\nu}$ *(note:* $|t|<1$*), and*

$$\begin{aligned} H^R(t) &:= \frac{1+2c_1t+c_2t^2}{1-2c_1t+(4c_1^2+c_2/2)t^2+c_1c_2t^3+c_2^2t^4/4},\\ H^I(t) &:= \frac{1-2c_1t}{1-2c_1t+(4c_1^2+c_2/2)t^2+c_1c_2t^3+c_2^2t^4/4}, \end{aligned} \tag{4.149}$$

with c_1, c_2 *given by* (4.38)*;*

(iv) *for* $\rho=\nu/\kappa\in[\vartheta_2,\infty)$,

$$S^R_{l,\kappa} = \frac{1}{\sqrt{\rho^2-1}}\Big(1+\frac{1}{2\kappa\sqrt{\rho^2-1}}\Big(1+\frac{1}{\rho^2-1}\Big)\Big), \tag{4.150}$$

$$S^I_{l,\kappa} = \frac{e^{-2\nu\Psi}}{\sqrt{\rho^2-1}}\Big(1+\frac{1}{\kappa\sqrt{\rho^2-1}}\Big(1+\frac{1}{\rho^2-1}\Big)\Big), \tag{4.151}$$

where Ψ *is defined in* (4.40)*.*

Proof. **Case (i)** $\rho=\nu/\kappa\in(0,\theta_0)$. By (4.143) and (4.35),

$$\begin{aligned} \mathrm{Re}(\mathcal{S}_{l,\kappa}) &\sim \frac{\rho^2}{2\kappa}\frac{1-\rho^2}{(1-\rho^2)^3+\kappa^{-2}\rho^4} \sim \frac{\rho^2}{2\kappa}\frac{1}{(1-\rho^2)^2},\\ \mathrm{Im}(\mathcal{S}_{l,\kappa}) &\sim \frac{(1-\rho^2)^2\sqrt{1-\rho^2}}{(1-\rho^2)^3+4\kappa^{-2}\rho^4} \sim \frac{1}{\sqrt{1-\rho^2}}. \end{aligned}$$

This leads to (4.146).

Case (ii) $\rho=\nu/\kappa\in[\theta_0,\vartheta_1]$. By (4.143) and (4.36),

$$\begin{aligned} \mathrm{Re}(\mathcal{S}_{l,\kappa}) &\sim \frac{1}{2\kappa}\Big(1+\frac{1}{2(1-\rho)}\Big)\Big(\frac{1}{4\kappa^2}(1+\frac{1}{2(1-\rho)})^2+2\rho(1-\rho)\Big)^{-1}\\ &\sim \frac{1}{4\rho(1-\rho)\kappa}\Big(1+\frac{1}{2(1-\rho)}\Big), \end{aligned}$$

and

$$\mathrm{Im}(\mathcal{S}_{l,\kappa}) \sim \frac{\sqrt{2\rho(1-\rho)}}{\frac{1}{4\kappa^2}(1+\frac{1}{2(1-\rho)})^2+2\rho(1-\rho)} \sim \frac{1}{\sqrt{2\rho(1-\rho)}},$$

so (4.147) follows.

Case (iii) $\rho = \nu/\kappa \in (\vartheta_1, \vartheta_2)$. By (4.143) and (4.37),

$$\begin{aligned}
\mathrm{Re}(\mathcal{S}_{l,\kappa}) &\sim \frac{\sqrt[3]{2/\nu}\big(c_1 + 2c_1^2 t + \frac{1}{2}\big(1 - 16c_1^3\big)t^2\big) - 1/(2\kappa)}{\big(\sqrt[3]{2/\nu}\big(c_1 + 2c_1^2 t + \frac{1}{2}\big(1 - 16c_1^3\big)t^2\big) - 1/(2\kappa)\big)^2 + \big(\sqrt[3]{2/\nu}\sqrt{3}c_1\rho(1 - 2c_1 t)\big)^2} \\
&\sim \frac{1}{c_1}\Big(\frac{\nu}{2}\Big)^{1/3} \frac{1 + 2c_1 t + c_2 t^2}{(1 + 2c_1 t + c_2 t^2)^2 + 3\rho^2(1 - 2c_1 t)^2} \\
&\sim \frac{1}{c_1}\Big(\frac{\nu}{2}\Big)^{1/3} \frac{1 + 2c_1 t + c_2 t^2}{(1 + 2c_1 t + c_2 t^2)^2 + 3(1 - 2c_1 t)^2} \\
&= \frac{1}{4c_1}\Big(\frac{\nu}{2}\Big)^{1/3} \frac{1 + 2c_1 t + c_2 t^2}{1 - 2c_1 t + (4c_1^2 + c_2/2)t^2 + c_1 c_2 t^3 + c_2^2 t^4/4}.
\end{aligned}$$

where $c_2 = (1 - 16c_1^3)/(2c_1) \approx 0.3088$. In the above derivation, we dropped the term $-1/(2\kappa)$, and used the factor $\rho \approx 1$.

Similarly, we can derive

$$\mathrm{Im}(\mathcal{S}_{l,\kappa}) \sim \frac{\sqrt{3}}{4c_1}\Big(\frac{\nu}{2}\Big)^{1/3} \frac{1 - 2c_1 t}{1 - 2c_1 t + (4c_1^2 + c_2/2)t^2 + c_1 c_2 t^3 + c_2^2 t^4/4}.$$

Thus, we obtain (4.148).

Case (iv) $\rho = \nu/\kappa \in [\vartheta_2, \infty)$. Noticing from (4.39) that $\mathrm{Im}(\mathcal{T}_{l,\kappa})$ is exponentially small in this range, we obtain from (4.143) and (4.39) that

$$\begin{aligned}
\mathrm{Re}(\mathcal{S}_{l,\kappa}) &\sim \Big(\sqrt{\rho^2 - 1} - \frac{1}{2\kappa}\Big(1 + \frac{1}{\rho^2 - 1}\Big)\Big)^{-1} \\
&= \frac{1}{\sqrt{\rho^2 - 1}}\Big(1 - \frac{1}{2\kappa\sqrt{\rho^2 - 1}}\Big(1 + \frac{1}{\rho^2 - 1}\Big)\Big)^{-1} \\
&\sim \frac{1}{\sqrt{\rho^2 - 1}}\Big(1 + \frac{1}{2\kappa\sqrt{\rho^2 - 1}}\Big(1 + \frac{1}{\rho^2 - 1}\Big)\Big),
\end{aligned}$$

and

$$\begin{aligned}
\mathrm{Im}(\mathcal{S}_{l,\kappa}) &\sim \frac{e^{-2\nu\Psi}}{\sqrt{\rho^2 - 1}}\Big(1 - \frac{1}{2\kappa\sqrt{\rho^2 - 1}}\Big(1 + \frac{1}{\rho^2 - 1}\Big)\Big)^{-2} \\
&\sim \frac{e^{-2\nu\Psi}}{\sqrt{\rho^2 - 1}}\Big(1 + \frac{1}{\kappa\sqrt{\rho^2 - 1}}\Big(1 + \frac{1}{\rho^2 - 1}\Big)\Big),
\end{aligned}$$

where we used $(1 - y)^{-1} \sim 1 + y$, $(1 - y)^{-2} \sim 1 + 2y$ for $y \sim 0$. This ends the proof. □

Remark 4.2. *We plot in Figure 4.3 the graphs of two functions (solid lines) and their first-order derivatives (dashed line) in* (4.149)*. In fact, a direct calculation leads to*

$$\frac{d}{dt}H^R(t) = -\frac{8(4c_1+c_2t)(-2+4c_1t+4c_1^2t^2+2c_2t^2+c_1c_2t^3+c_2^2t^4)}{(4-8c_1t+16c_1^2t^2+2c_2t^2+4c_1c_2t^3+c_2^2t^4)^2},$$
$$\frac{d}{dt}H^I(t) = \frac{8t(-16c_1^2-2c_2+16c_1^3t-4c_1c_2t+8c_1^2c_2t^2-2c_2^2t^2+3c_1c_2^2t^3)}{(4-8c_1t+16c_1^2t^2+2c_2t^2+4c_1c_2t^3+c_2^2t^4)^2}.$$

One verifies that

$$\min\{H^R(t)\} = H^R(t=-1) \approx 0.2493, \quad \max\{H^R(t)\} = H^R(t \approx 0.8004) \approx 1.9291,$$
$$\min\{H^I(t)\} = H^I(t=1) \approx 0.2479, \quad \max\{H^I(t)\} = H^I(t=0) = 1.$$

Thus, we roughly have $0.2493 \le H^R(t) \le 1.9291$ *and* $0.2479 \le H^I(t) \le 1$. □

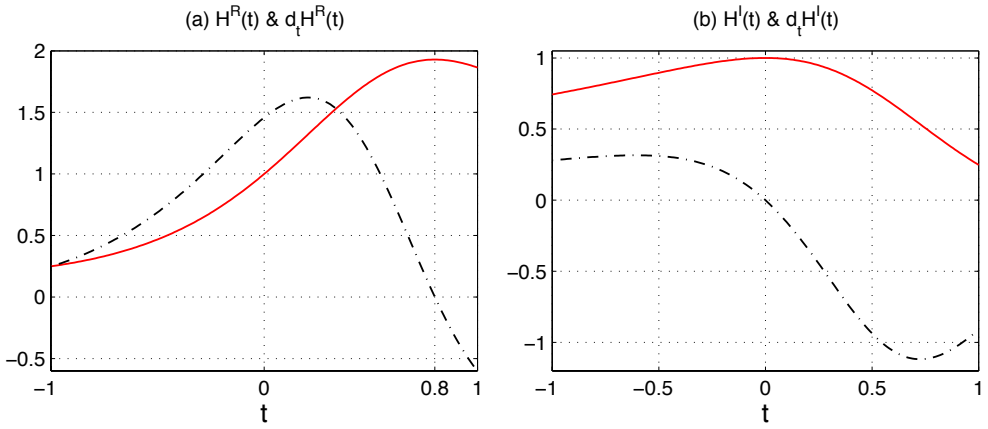

Figure 4.3: Graphs of (a) $H^R(t)$ and $\frac{d}{dt}H^R(t)$ (dashed line), and (b) $H^I(t)$ and $\frac{d}{dt}H^I(t)$ (dashed line) for $|t| < 1$.

A weak form of (4.137) is to find $v_3 \in {}_0H^1(\Lambda)$ such that

$$\begin{aligned}\widehat{\mathbb{B}}_l^m(v_3,w) &:= (v_3',w')_\varpi + \beta_l(v_3,w) - k^2(v_3,w)_\varpi \\ &= b\,v_2(b)\bar{w}(b) + 2(v_2,w) + b^2h_Y\bar{w}(b) + (g_3,w)_\varpi \\ &+ kb^2\big(\mathcal{S}_{l,kb} - (kb)^{-1}\big)\,v_3(b)\bar{w}(b), \quad \forall\, w \in {}_0H^1(\Lambda),\end{aligned} \tag{4.152}$$

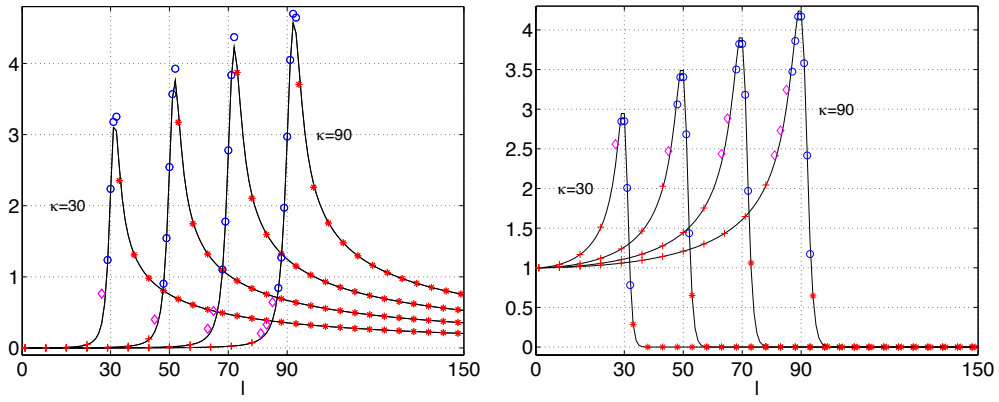

(a) $\mathrm{Re}(\mathcal{S}_{l,\kappa})$ vs $S^R_{l,\kappa}$ (b) $\mathrm{Im}(\mathcal{S}_{l,\kappa})$ vs $S^I_{l,\kappa}$

Figure 4.4: (a) $\mathrm{Re}(\mathcal{S}_{l,\kappa})$ (solid line) against $S^R_{l,\kappa}$; (b) $\mathrm{Im}(\mathcal{S}_{l,\kappa})$ (solid line) against $S^I_{l,\kappa}$ with $\kappa = 30, 50, 70, 90$ (note: "+" for $\rho = \nu/\kappa \in (0, \theta_0)$, "$\diamond$" for $\rho \in [\theta_0, \vartheta_1]$, "$\circ$" for $\rho \in (\vartheta_1, \vartheta_2)$ and "$*$" for $\rho \in [\vartheta_2, \infty)$).

where $\varpi = r^2$. Alternatively, we can use the equivalent boundary condition (4.138)-(4.139), and modify (4.152) as: find $v_3 \in {}_0H^1(\Lambda)$ such that

$$\begin{aligned}\widehat{\mathbb{B}}^m_l(v_3, w) := (v_3', w')_\varpi + \beta_l(v_3, w) - k^2(v_3, w)_\varpi = b\,\sigma_{l,kb} v_2(b)\bar{w}(b) \\ + 2(v_2, w) + (g_3, w)_\varpi + b^2 \frac{h_Y}{k\,\mathcal{S}_{l,kb}}\bar{w}(b), \quad \forall\, w \in {}_0H^1(\Lambda).\end{aligned} \tag{4.153}$$

Theorem 4.5. *Let θ_0 and $\{\vartheta_i\}_{i=1}^2$ be the same as in (4.27)-(4.28). If $g_2, g_3 \in L^2(\Lambda)$, then we have that for all $k \geq k_0 > 0$ (for some fixed constant k_0), and $l \geq 1, 0 \leq |m| \leq l$,*

$$\|v_3'\|^2_\varpi + \beta_l\|v_3\|^2 + k^2\|v_3\|^2_\varpi \leq C_{l,k}\Big(\frac{1}{\beta_l}\|g_2\|^2_\varpi + \|g_3\|^2_\varpi\Big) + C\Big(1 + \frac{\beta_l^2}{k^4}\Big)|h_Y|^2, \tag{4.154}$$

where C is a generic positive constant independent of k, l, m and v_3, and

$$C_{l,k} = C\begin{cases} 1, & \text{if } \rho = \nu/(kb) \in (0, \theta_0] \cup (\vartheta_2, \infty), \\ (kb)^{1-\gamma}, & \text{if } \rho = \nu/(kb) \in (\theta_0, \vartheta_2]. \end{cases} \tag{4.155}$$

Note that for $\rho \in (\theta_0, \vartheta_2]$, we have $\rho = 1 + \xi(kb)^{-\gamma}$ or $\nu = l + 1/2 = kb + \xi(kb)^{\gamma-1}$, for $1/3 \leq \gamma < 1$, and some constant ξ.

Proof. Taking $w = v_3$ in (4.152), we obtain

$$\begin{aligned}
&\|v_3'\|_\varpi^2 + \beta_l\|v_3\|^2 - k^2\|v_3\|_\varpi^2 - kb^2\,\mathrm{Re}(\mathcal{S}_{l,kb})|v_3(b)|^2 + b|v_3(b)|^2 \\
&\qquad = b\,\mathrm{Re}(v_2(b)\bar v_3(b)) + 2\mathrm{Re}(v_2, v_3) + b^2\,\mathrm{Re}(h_Y\bar v_3(b)) + \mathrm{Re}(g_3, v_3)_\varpi,
\end{aligned} \tag{4.156a}$$

$$\begin{aligned}
-kb^2\,\mathrm{Im}(\mathcal{S}_{l,kb})|v_3(b)|^2 =& b\,\mathrm{Im}(v_2(b)\bar v_3(b)) + 2\mathrm{Im}(v_2, v_3) \\
&+ b^2\,\mathrm{Im}(h_Y\bar v_3(b)) + \mathrm{Im}(g_3, v_3)_\varpi.
\end{aligned} \tag{4.156b}$$

Next taking $w = 2(r-a)v_3'$ in (4.152), and following the derivation of (4.68)-(4.69), we can obtain

$$\begin{aligned}
&b^2|I||v_3'(b)|^2 + (\beta_l|I| + b)|v_3(b)|^2 + 2a\|\sqrt{r}v_3'\|^2 + 2k^2\int_a^b\Big[1 - \frac{a}{r}\Big]|v_3|^2 r^2 dr \\
&= \big(k^2b^2|I| + kb^2\,\mathrm{Re}(\mathcal{S}_{l,kb})\big)|v_3(b)|^2 + 2\mathrm{Re}(v_2, v_3) + \mathrm{Re}(g_3, v_3)_\varpi \\
&\quad + b\,\mathrm{Re}(v_2(b)\bar v_3(b)) + b^2\,\mathrm{Re}(h_Y\bar v_3(b)) + 2b|I|\,\mathrm{Re}\big(v_2(b)\bar v_3'(b)\big) \\
&\quad + 2b^2|I|\,\mathrm{Re}\big(h_Y\bar v_3'(b)\big) + 4\,\mathrm{Re}(v_2, (r-a)v_3') + 2\,\mathrm{Re}(g_3, (r-a)v_3')_\varpi \\
&\quad + 2kb^2|I|\mathrm{Re}\big\{(\mathcal{S}_{l,kb} - (kb)^{-1})v_3(v)\bar v_3'(b)\big\}.
\end{aligned} \tag{4.157}$$

Then we can derive the estimate similar to (4.71) (by noting that $\mathcal{S}_{l,kb} - (kb)^{-1}$ should be in place of $\mathcal{T}_{l,kb}$ and the term of the left endpoint $r = a$ is not involved):

$$\begin{aligned}
&b^2|I||v_3'(b)|^2 + \mathcal{D}_{l,k}|I||v_3(b)|^2 + a\|\sqrt{r}v_3'\|^2 + k^2\|v_3\|_\varpi^2 \\
&\qquad \le C\big(\|v_2\|_\varpi^2 + |v_2(b)|^2 + \|g_3\|_\varpi^2 + |h_Y|^2\big),
\end{aligned} \tag{4.158}$$

where

$$\mathcal{D}_{l,\kappa} := \beta_l - (1-\varepsilon_3)|I|^{-1}\,kb^2\,\mathrm{Re}(\mathcal{S}_{l,kb}) - k^2b^2\big(1 + \varepsilon_1^{-1}\big|\mathcal{S}_{l,kb} - (kb)^{-1}\big|^2\big). \tag{4.159}$$

Thus, it remains to bound the term $\mathcal{D}_{l,\kappa}|I||v_3(b)|^2$ (note: it is negative for some range of l), and to estimate the terms of v_2 by using that of u_2 in Theorem 4.3 and its proof. Following the proof of Theorem 4.3, we proceed with several cases.

(i) If $\rho = \frac{\nu}{kb} \in (0, \theta_0)$ for fixed $0 < \theta_0 < 1$, we find from (4.146) that both $kb\mathrm{Re}(\mathcal{S}_{l,kb})$ and $\mathrm{Im}(\mathcal{S}_{l,kb})$ behave like constants. Thus, from (4.156b), we can obtain the bound like (4.74):

$$k^2b^2\,|v_3(b)|^2 \le \varepsilon k^2\|v_3\|_\varpi^2 + C\big(\|v_2\|_\varpi^2 + |v_2(b)|^2 + \|g_3\|_\varpi^2 + |h_Y|^2\big). \tag{4.160}$$

Noting from (4.146) and (4.159) that

$$\mathcal{D}_{l,\kappa} \sim \beta_l - Ck^2b^2, \tag{4.161}$$

we infer from (4.158) that

$$\begin{aligned} &b^2|I||v_3'(b)|^2 + \beta_l|I||v_3(b)|^2 + a\|\sqrt{r}v_3'\|^2 + k^2\|v_3\|_\varpi^2 \\ &\le C\big(\|v_2\|_\varpi^2 + |v_2(b)|^2 + \|g_3\|_\varpi^2 + |h_Y|^2\big). \end{aligned} \tag{4.162}$$

Recall from (4.135) that $h_2 = -h_Y/(k\,\mathcal{S}_{l,kb}), u_2 = r\beta_l^{-1}v_2$ and $f_2 = r\beta_l^{-1}g_2$. Then by (4.75),

$$\|v_2\|_\varpi^2 + |v_2(b)|^2 \le C\Big(\frac{1}{k^2}\|g_2\|_\varpi^2 + \frac{\beta_l^2}{k^4}|h_Y|^2\Big) \le C\Big(\frac{1}{\beta_l}\|g_2\|_\varpi^2 + \frac{\beta_l^2}{k^4}|h_Y|^2\Big). \tag{4.163}$$

Thus, using (4.156a), (4.160), (4.162), (4.163) and the Cauchy-Schwarz inequality, we can obtain the desired estimate (4.154).

(ii) If $\rho = \frac{\nu}{kb} \in [\theta_0, \vartheta_1]$, we start with (4.78), and find from (4.147) that

$$\mathrm{Re}(\mathcal{S}_{l,kb} - (kb)^{-1}) \sim \frac{1}{8\bar{c}_0^2}(kb)^{1-2\gamma_0}, \quad \mathrm{Im}(\mathcal{S}_{l,kb}) \sim \frac{1}{\sqrt{2\bar{c}_0}}(kb)^{(1-\gamma_0)/2}, \tag{4.164}$$

where $1/3 \le \gamma_0 < 1$. Thus, we have from (4.161)-(4.164) implies

$$\mathcal{D}_{l,k} \sim -C(kb)^{3-\gamma_0}. \tag{4.165}$$

As with (4.80)-(4.82), we can derive

$$(kb)^{3-\gamma_0}\,|v_3(b)|^2 \le \varepsilon k^2\|v_3\|_\varpi^2 + C\Big((kb)^{1-\gamma_0}(\|v_2\|_\varpi^2 + \|g_3\|_\varpi^2) + |v_2(b)|^2 + |h_Y|^2\Big).$$

Therefore, we have

$$\begin{aligned} &\|\sqrt{r}v_3'\|^2 + k^2\|v_3\|_\varpi^2 + (kb)^{3-\gamma_0}|v_3(b)|^2 \\ &\le C\Big((kb)^{1-\gamma_0}(\|v_2\|_\varpi^2 + \|g_3\|_\varpi^2) + |v_2(b)|^2 + |h_Y|^2\Big). \end{aligned} \tag{4.166}$$

Like (4.163), we derive from (4.83) (note: $h_2 = -h_Y/(k\,\mathcal{S}_{l,kb}), u_2 = r\beta_l^{-1}v_2$ and $f_2 = r\beta_l^{-1}g_2$) and (4.164) that

$$\begin{aligned} k^{1-\gamma_0}\|v_2\|_\varpi^2 + |v_2(b)|^2 &\le C\Big(\frac{1}{k^{1+\gamma_0}}\|g_2\|_\varpi^2 + \frac{\beta_l^2}{k^4}|h_Y|^2\Big) \\ &\le C\Big(\frac{k^{1-\gamma_0}}{\beta_l}\|g_2\|_\varpi^2 + \frac{\beta_l^2}{k^4}|h_Y|^2\Big). \end{aligned} \tag{4.167}$$

Thus, as with the previous case, we can obtain the desired estimate.

(iii) If $\rho = \frac{\nu}{kb} \in (\vartheta_1, \vartheta_2)$, we have the range of (4.84). Using (4.148)-(4.149), we can actually show that in this range the bound is the same as (4.93) with $\gamma_0 = 1/3$:

$$\begin{aligned} &\|\sqrt{r}v_3'\|^2 + k^2\|v_3\|_\varpi^2 + (kb)^{8/3}|v_3(b)|^2 \\ &\le C\Big((kb)^{2/3}(\|v_2\|_\varpi^2 + \|g_3\|_\varpi^2) + |v_2(b)|^2 + |h_Y|^2\Big). \end{aligned} \tag{4.168}$$

Similarly, we can bound the terms involving v_2 by (4.167) with $\gamma_0 = 1/3$.

(iv) If $\rho = \frac{\nu}{kb} \in [\vartheta_2, \infty)$, we find from (4.151) that $\mathrm{Im}(\mathcal{S}_{l,kb})$ decays exponentially with respect to l. However, since $\mathrm{Re}(\mathcal{S}_{l,kb} - (kb)^{-1}) > 0$, we do not have (4.91) to bound the term $\mathcal{D}_{l,k}|I||v_3(b)|^2$ (note: $\mathcal{D}_{l,k} < 0$), as opposite to the estimate of u_2 in Theorem 4.3. For this purpose, we use the equivalent boundary condition (4.138)-(4.139). Correspondingly, we modify the weak form (4.152) as

$$\begin{aligned} (v_3', w')_\varpi + \beta_l(v_3, w) - k^2(v_3, w)_\varpi &= b\sigma_{l,kb}v_2(b)\bar{w}(b) + 2(v_2, w) \\ &+ (g_3, w)_\varpi + b^2\frac{h_Y}{k\,\mathcal{S}_{l,kb}}\bar{w}(b)\,, \quad \forall\, w \in {}_0H^1(\Lambda). \end{aligned} \tag{4.169}$$

Taking $w = v_3$ in (4.169),

$$\begin{aligned} \|v_3'\|_\varpi^2 + \beta_l\|v_3\|^2 - k^2\|v_3\|_\varpi^2 &= b\,\mathrm{Re}(\sigma_{l,kb}\,v_2(b)\bar{v}_3(b)) \\ &+ \mathrm{Re}(g_3, v_3)_\varpi + 2\mathrm{Re}(v_2, v_3) + b^2\mathrm{Re}\Big(\frac{h_Y}{k\,\mathcal{S}_{l,kb}}\bar{v}_3(b)\Big), \end{aligned} \tag{4.170}$$

Next taking $w = 2(r-a)v_3'$ and following the same procedure in deriving (4.68)-(4.69), we have

$$\begin{aligned} &b^2|I||v_3'(b)|^2 + (\beta_l - k^2b^2)|I||v_3(b)|^2 + 2a\|\sqrt{r}v_3'\|^2 \\ &+ 2k^2\int_a^b\Big(1 - \frac{a}{r}\Big)|v_3|^2r^2dr = 2b|I|\mathrm{Re}\{\sigma_{l,kb}\,v_2(b)\bar{v}_3'(b)\} + 2\mathrm{Re}(v_2, v_3) \\ &+ 4\,\mathrm{Re}(v_2, (r-a)v_3') + b\mathrm{Re}\{\sigma_{l,kb}v_2(b)\bar{v}_3(b)\} + 2\mathrm{Re}(g_3, (r-a)v_3')_\varpi \\ &+ \mathrm{Re}(g_3, v_3)_\varpi + 2b^2|I|\mathrm{Re}\Big(\frac{h_Y}{k\,\mathcal{S}_{l,kb}}\bar{v}_3'(b)\Big) + b^2\mathrm{Re}\Big(\frac{h_Y}{k\,\mathcal{S}_{l,kb}}\bar{v}_3(b)\Big). \end{aligned} \tag{4.171}$$

Using the Cauchy-Schwarz inequality, we can derive

$$\begin{aligned}|v_3'(b)|^2 + (\beta_l - k^2b^2)|v_3(b)|^2 + \|\sqrt{r}v_3'\|^2 + k^2\|v_3\|_\varpi^2 \\ \le C\Big\{|\sigma_{l,kb}|^2\big(1 + (\beta_l - k^2b^2)^{-1}\big)|v_2(b)|^2 + \|v_2\|_\varpi^2 + \|g_3\|_\varpi^2 \\ + \frac{1}{(kb)^2\,|\mathcal{S}_{l,kb}|^2}\big(1 + (\beta_l - k^2b^2)^{-1}\big)|h_Y|^2\Big\}.\end{aligned} \tag{4.172}$$

We first consider the range (a) in (4.87), i.e., $\nu \sim kb + \bar{c}_5(kb)^{\gamma_1}$ for $1/3 \le \gamma_1 < 1$ and some constant $\bar{c}_5 > 0$. From (4.139) and (4.150), one verifies

$$\begin{aligned}&\beta_l - k^2b^2 \sim 2\bar{c}_5(kb)^{1+\gamma_1}, \quad |\sigma_{l,kb}| \sim 2\bar{c}_5(kb)^{\gamma_1 - 1} \\ &|\mathcal{S}_{l,kb}| \sim |\mathrm{Re}(\mathcal{S}_{l,kb})| \sim \frac{1}{\sqrt{2\bar{c}_5(kb)^{\gamma_1-1}}}.\end{aligned} \tag{4.173}$$

Then we obtain from (4.172)-(4.173) that

$$k^2\|v_3\|_\varpi^2 \le C\Big((kb)^{2(\gamma_1-1)}|v_2(b)|^2 + \|v_2\|_\varpi^2 + \|g_3\|_\varpi^2 + (kb)^{-(1+\gamma_1)}|h_Y|^2\Big). \tag{4.174}$$

Recalling that $h_2 = -h_Y/(k\,\mathcal{S}_{l,kb})$, $u_2 = r\beta_l^{-1}v_2$ and $f_2 = r\beta_l^{-1}g_2$, we have from (4.93) and (4.173) that

$$\|v_2\|_\varpi^2 + (kb)^{2(\gamma_1-1)}|v_2(b)|^2 \le C\Big(\frac{1}{\beta_l}\|g_2\|_\varpi^2 + \frac{\beta_l^2}{k^4}|h_Y|^2\Big). \tag{4.175}$$

As $v_3 \in {}_0H^1(I)$, one verifies readily that

$$|v_3(b)| \le \int_a^b |v_3'(r)|dr \le C\|v_3'\|_\varpi. \tag{4.176}$$

Thus, using (4.170) and the Cauchy-Schwarz inequality, we can obtain the same upper bound as (4.174) for $\|v_3'\|_\varpi^2 + \beta_l\|v_3\|^2$. This leads to the desired estimate for this case.

We then consider the range (b) in (4.87), i.e., $\nu > \eta\,kb$ with $\eta > 1$. Once again, from (4.139) and (4.150), we get

$$|\mathcal{S}_{l,kb}| \sim |\mathrm{Re}(\mathcal{S}_{l,kb})| \sim \frac{kb}{\nu\sqrt{1-\eta^{-2}}}, \quad |\sigma_{l,kb}| \sim 1 - \eta^{-2}. \tag{4.177}$$

It is evident that

$$\beta_l\|v_3\|^2 - k^2\|v_3\|_\varpi^2 \ge (\beta_l - k^2b^2)\|v_3\|^2 \ge \beta_l(1-\eta^{-2})\|v_3\|^2. \tag{4.178}$$

Using the Cauchy-Schwarz inequality, and (4.176)-(4.178), we have from (4.170) that

$$\|v_3'\|_\varpi^2 + \beta_l\|v_3\|^2 \le C\Big(|v_2(b)|^2 + \beta_l^{-1}\|v_2\| + \beta_l^{-1}\|g_3\|_\varpi^2 + \frac{\beta_l}{k^4}|h_Y|^2\Big). \tag{4.179}$$

Then by (4.66), (4.97) and the fact that $h_2 = -h_Y/(k\,\mathcal{S}_{l,kb}), u_2 = r\beta_l^{-1}v_2$ and $f_2 = r\beta_l^{-1}g_2$,

$$|v_2(b)|^2 + \beta_l^{-1}\|v_2\|^2 \le C\Big(\frac{1}{\beta_l}\|g_2\|_\varpi^2 + \frac{\beta_l^2}{k^4}|h_Y|^2\Big). \tag{4.180}$$

Then we can derive the desired estimates. □

Remark 4.3. *It is seen from* (4.130) *that* $\|u_2'\|_\varpi = O(1)$, *while by* (4.154), $\|u_2'\|_\varpi = O(k^{-1}\sqrt{C_{l,k}})$ *by noting that* $v_3 = \hat{\partial}_r u_2$. □

4.4 Main result on a priori estimates of $\boldsymbol{E}$

Now, we are in a position to derive *a prior* estimates for the Maxwell's equations. A weak form of (4.2)-(4.3) is to find $\boldsymbol{E} \in V := \mathbb{H}_0(\mathbf{curl};\Omega)\cap\mathbb{H}_0(\mathrm{div};\Omega)$ such that

$$\begin{aligned}\mathcal{B}(\boldsymbol{E},\boldsymbol{\Psi}) &:= \big(\nabla\times\boldsymbol{E},\nabla\times\boldsymbol{\Psi}\big)_\Omega - k^2\big(\boldsymbol{E},\boldsymbol{\Psi}\big)_\Omega - \mathrm{i}kb^2\big\langle\mathscr{T}_b\boldsymbol{E}_S,\boldsymbol{\Psi}_S\big\rangle_S \\ &= \big(\boldsymbol{F},\boldsymbol{\Psi}\big)_\Omega + b^2\big\langle\boldsymbol{h},\boldsymbol{\Psi}_S\big\rangle_S, \quad \forall\,\boldsymbol{\Psi}\in V.\end{aligned} \tag{4.181}$$

Its well-posedness can be established using the property: $\mathrm{Re}\langle\mathscr{T}_b\boldsymbol{E}_S,\boldsymbol{E}_S\rangle_S > 0$ (see, e.g., Nédélec [3, Chapter 5] and Monk [35, Chapter 10]).

By [3, (5.3.47)], the surface divergence of $\boldsymbol{h}$ (with the expansion (4.112)) can be expressed as

$$\mathrm{div}_S\,\boldsymbol{h} = -\sum_{l=1}^{\infty}\sum_{|m|=0}^{l}\beta_l\,h_{Y,l}^m\,Y_l^m, \quad \text{so} \quad \|\mathrm{div}_S\,\boldsymbol{h}\|_{L^2(S)}^2 = \sum_{l=1}^{\infty}\sum_{|m|=0}^{l}\beta_l^2\big|h_{Y,l}^m\big|^2. \tag{4.182}$$

Theorem 4.6. *Let* $\boldsymbol{E}$ *be the solution to* (4.181). *If* $\boldsymbol{F}\in\boldsymbol{L}^2(\Omega)$, $\boldsymbol{h}\in\boldsymbol{L}_T^2(S)$ *and* $\mathrm{div}_S\,\boldsymbol{h}\in L^2(S)$, *then we have* $\boldsymbol{E}\in\mathbb{H}_0(\mathbf{curl};\Omega)$ *and*

$$\|\nabla\times\boldsymbol{E}\|_\Omega + k\|\boldsymbol{E}\|_\Omega \le C\big(k^{1/3}\|\boldsymbol{F}\|_\Omega + \|\boldsymbol{h}\|_{\boldsymbol{L}_T^2(S)} + k^{-2}\|\mathrm{div}_S\boldsymbol{h}\|_{L^2(S)}\big), \tag{4.183}$$

for all $k\ge k_0 > 0$ (k_0 *is some positive constant*), *and* C *is a positive constant independent of* k *and any function.*

Proof. With the notation in (4.135), we can rewrite the field $\boldsymbol{E}$ in (4.107) as

$$\boldsymbol{E} = u_0^0 Y_0^0 \boldsymbol{e}_r + \sum_{l=1}^{\infty}\sum_{|m|=0}^{l} \{u_{1,l}^m \boldsymbol{T}_l^m + v_{2,l}^m Y_l^m \boldsymbol{e}_r + v_{3,l}^m \nabla_S Y_l^m\}, \tag{4.184}$$

where we recall (cf. Proposition 4.2): $-k^2 u_0^0 = f_0^0$. Thus, by the orthogonality and (4.11),

$$\|\boldsymbol{E}\|_\Omega^2 = \|u_0^0\|_\varpi^2 + \sum_{l=1}^{\infty}\sum_{|m|=0}^{l} \beta_l \Big\{\|u_{1,l}^m\|_\varpi^2 + \beta_l^{-1}\|v_{2,l}^m\|_\varpi^2 + \|v_{3,l}^m\|_\varpi^2\Big\}. \tag{4.185}$$

Working out $\nabla\times\boldsymbol{E}$ via (4.184) and (4.15)-(4.16), we obtain from (4.11) that

$$\|\nabla\times\boldsymbol{E}\|_\Omega^2 = \sum_{l=1}^{\infty}\sum_{|m|=0}^{l} \beta_l \Big\{\|\hat\partial_r u_{1,l}^m\|_\varpi^2 + \beta_l\|u_{1,l}^m\|^2 + \big\|v_{2,l}^m/r - \hat\partial_r v_{3,l}^m\big\|^2\Big\}, \tag{4.186}$$

Noting that $\beta_l + 2 \le 2\beta_l$ (as $\beta_l \ge 2$), and

$$\|\hat\partial_r u_{1,l}^m\|_\varpi^2 \le 2\big(\big\|(u_{1,l}^m)'\big\|_\varpi^2 + \|u_{1,l}^m\|^2\big),$$

we obtain from (4.185)-(4.186) that

$$\begin{aligned}\|\nabla\times\boldsymbol{E}\|_\Omega^2 + k^2\|\boldsymbol{E}\|_\Omega^2 \le{}& \|u_0^0\|_\varpi^2 + \sum_{l=1}^{\infty}\sum_{|m|=0}^{l} \beta_l\Big\{2\big(\|(u_{1,l}^m)'\|_\varpi^2 + \beta_l\|u_{1,l}^m\|^2\big) + k^2\|u_{1,l}^m\|_\varpi^2\Big\}\\ &+ \sum_{l=1}^{\infty}\sum_{|m|=0}^{l} \beta_l\Big\{2\|v_{2,l}^m\|^2 + k^2\beta_l^{-1}\|v_{2,l}^m\|_\varpi^2\Big\}\\ &+ \sum_{l=1}^{\infty}\sum_{|m|=0}^{l} \beta_l\Big\{4\big(\|(v_{3,l}^m)'\|_\varpi^2 + \|v_{3,l}^m\|^2\big) + k^2\|v_{3,l}^m\|_\varpi^2\Big\}.\end{aligned}$$

Similarly, using the orthogonality of VSH, we have

$$\begin{aligned}\|\boldsymbol{F}\|_\Omega^2 &= \|f_0^0\|_\varpi^2 + \sum_{l=1}^{\infty}\sum_{|m|=0}^{l} \beta_l\Big\{\|f_{1,l}^m\|_\varpi^2 + \beta_l^{-1}\|g_{2,l}^m\|_\varpi^2 + \|g_{3,l}^m\|_\varpi^2\Big\},\\ \|\boldsymbol{h}\|_{\boldsymbol{L}_T^2(S)}^2 &= \sum_{l=1}^{\infty}\sum_{|m|=0}^{l} \beta_l\big\{\big|h_{T,l}^m\big|^2 + \big|h_{Y,l}^m\big|^2\big\}.\end{aligned} \tag{4.187}$$

Recall from (4.135) that $h_{2,l}^m = -h_{Y,l}^m/(k\,\mathcal{S}_{l,kb})$, $u_{2,l}^m = r\beta_l^{-1}v_{2,l}^m$ and $f_{2,l}^m = r\beta_l^{-1}g_{2,l}^m$. Then by Theorem 4.3 with $i=2$,

$$\|v_{2,l}^m\|^2 + k^2\beta_l^{-1}\|v_{2,l}^m\|_\varpi^2 \le C\big\{\beta_l^{-1}\|g_{2,l}^m\|_\varpi^2 + k^{-4}\beta_l^2|h_{Y,l}^m|^2\big\}, \tag{4.188}$$

where we use the fact $|\mathcal{S}_{l,kb}|^{-2} \leq C\beta_l/k^2$ for all the ranges of l, k in the proof of Theorem 4.5. We further derive from Theorems 4.3-4.5 and (4.188) that

$$\begin{aligned}\|\nabla\times\boldsymbol{E}\|_\Omega^2 + k^2\|\boldsymbol{E}\|_\Omega^2 \leq k^{-2}\|f_0^0\|_\varpi^2 &+ C\sum_{l=1}^{\infty}\sum_{|m|=0}^{l}\beta_l\Big\{\|f_{1,l}^m\|_\varpi^2 + \Big|h_{T,l}^m\Big|^2\Big\}\\ &+ C\sum_{l=1}^{\infty}\sum_{|m|=0}^{l}\beta_l\Big\{\beta_l^{-1}\|g_2\|_\varpi^2 + k^{-4}\beta_l^2|h_{Y,l}^m|^2\Big\}\\ &+ \sum_{l=1}^{\infty}\sum_{|m|=0}^{l}\beta_l\Big\{C_{l,k}\big(\beta_l^{-1}\|g_2\|_\varpi^2 + \|g_3\|_\varpi^2\big) + C\big(1+k^{-4}\beta_l^2\big)|h_{Y,l}^m|^2\Big\}.\end{aligned}$$

Finally, the desired estimate follows from (4.182), (4.187) and the above. □

4.5 Spectral-Galerkin approximation

In this section, we consider the analysis of spectral-Galerkin approximation to (4.181). We look for the approximation of $\boldsymbol{E}$ in the form

$$\boldsymbol{E}_N^L = -k^{-2}f_0^0\,Y_0^0\boldsymbol{e}_r + \sum_{l=1}^{L}\sum_{|m|=0}^{l}\big\{u_{1,l}^{N,m}\boldsymbol{T}_l^m + \nabla\times\big(u_{2,l}^{N,m}\boldsymbol{T}_l^m\big)\big\}, \tag{4.189}$$

where $u_{1,l}^{N,m} := u_1^N$ and $u_{2,l}^{N,m} := u_2^N$ are respectively the solutions of the spectral-Galerkin schemes:

(i) Find $u_1^N \in {}_0\mathcal{P}_N := {}_0H^1(I)\cap\mathcal{P}_N$ (where $\mathcal{P}_N$ is the space of polynomials of degree at most N) such that

$$\mathbb{B}_l^m(u_1^N,\phi) = (f_1,\phi)_\varpi + b^2h_1\bar{\phi}(b), \quad \forall\,\phi\in{}_0\mathcal{P}_N, \tag{4.190}$$

(ii) Find $u_2^N \in \mathcal{P}_N$ such that

$$\mathbb{B}_l^m(u_2^N,\psi) - au_2^N(a)\bar{\psi}(a) = (f_2,\psi)_\varpi + b^2h_2\bar{\psi}(b), \quad \forall\,\psi\in\mathcal{P}_N. \tag{4.191}$$

Here, the bilinear forms $\mathbb{B}_l^m$ is defined in (4.65). It is evident that by Proposition 4.1, the expansion in (4.189) preserves the divergence-free property of the continuous field.

Theorem 4.7. *Theorem* 4.3 *hold when* u_1^N, u_2^N *are in place of* u_1, u_2 *in* (4.130)*, respectively.*

Remark 4.4. *The algorithm in the recent work [112] was based on VSH expansion in [3], so the divergence-free condition could only be fulfilled approximately. Moreover, one had to deal three components where two were coupled. In a nutshell, the above algorithm is much more efficient.* □

4.5.1 Error estimates

As before, we start with the schemes (4.190)-(4.191) in one dimension. To describe the errors more precisely, we introduce the weighted Sobolev space

$$\mathbb{X}^s(I) := \Big\{ u \in L^2(I) \ : \ [(r-a)(b-r)]^{\frac{l-1}{2}} u^{(l)} \in L^2(I),\ 1 \le l \le s \Big\}, \quad s \in \mathbb{N},$$

with the norm and semi-norm

$$\|u\|_{\mathbb{X}^s(I)} = \Big(\|u\|^2 + \sum_{l=1}^{s} \big\| [(r-a)(b-r)]^{\frac{l-1}{2}} u^{(l)} \big\|^2 \Big)^{1/2},$$
$$|u|_{\mathbb{X}^s(I)} = \big\| [(r-a)(b-r)]^{\frac{s-1}{2}} u^{(s)} \big\|.$$

Following the proof of [77, Thm 4.2] (but using the improved estimates in Theorem 4.3), we have the following error estimate for the scheme (4.190).

Lemma 4.3. *Let* u_1 *and* u_1^N *be the solution of* (4.128) *and* (4.190)*, respectively, and define* $e_N^{u_1} = u_1 - u_1^N$*. If* $u_1 \in {}_0H^1(I) \cap \mathbb{X}^s(I)$ *with integer* $s \ge 1$*, then for all* $k \ge k_0$ (*where* k_0 *is a certain constant*)*, we have*

$$\big\| (e_N^{u_1})' \big\|_{\varpi} + \sqrt{\beta_l} \|e_N^{u_1}\| + k \|e_N^{u_1}\|_{\varpi} \lesssim \big(\sqrt{\beta_l} + k^2 N^{-1} \big) N^{1-s} |u_1|_{\mathbb{X}^s(I)}, \tag{4.192}$$

where $\beta_l = l(l+1)$ *and* $\varpi = r^2$ *as before.*

Now, we turn to (4.191). Consider the orthogonal projection $\pi_N^1 : H^1(I) \to \mathcal{P}_N$ defined by

$$\big((\pi_N^1 v - v)', \phi' \big)_{\varpi} + \big(\pi_N^1 v - v, \phi \big)_{\varpi} = 0, \quad \forall\, \phi \in \mathcal{P}_N. \tag{4.193}$$

Noting that the weight function ϖ is uniformly bounded below and above, we follow the argument in [47, Ch. 3], and derive the following estimate.

Lemma 4.4. *For any $v \in \mathbb{X}^s(I)$ with $s \in \mathbb{N}$, we have*

$$\|(\pi_N^1 v - v)'\|_\varpi + N\|\pi_N^1 v - v\|_\varpi \lesssim N^{1-s}|v|_{\mathbb{X}^s(I)}. \tag{4.194}$$

Lemma 4.5. *Let u_2 and u_2^N be the solution of* (4.129) *and* (4.191)*, respectively, and define $e_N^{u_2} = u_2 - u_2^N$. If $u_2 \in \mathbb{X}^s(\Lambda)$ with $s \in \mathbb{N}$, then for all $k \geq k_0$ (where k_0 is a certain constant), then the estimate* (4.192) *holds when u_2 and $e_N^{u_2}$ are in place of u_1 and $e_N^{u_1}$, respectively.*

Proof. Let $\hat{e}_N = u_2^N - \pi_N^1 u_2$ and $\tilde{e}_N = u_2 - \pi_N^1 u_2$. Then $e_N^{u_2} = \tilde{e}_N - \hat{e}_N$. By (4.129) and (4.191),

$$\begin{aligned}&\mathbb{B}_l^m(e_N^{u_2}, \psi) - a e_N^{u_2}(a)\bar{\psi}(a) = 0\\ =&\mathbb{B}_l^m(\tilde{e}_N, \psi) - a\tilde{e}_N(a)\bar{\psi}(a) - \mathbb{B}_l^m(\hat{e}_N, \psi) + a\hat{e}_N(a)\bar{\psi}(a),\ \forall\, \psi \in \mathcal{P}_N.\end{aligned}$$

Thus, by (4.193),

$$\begin{aligned}&\mathbb{B}_l^m(\hat{e}_N, \psi) - a\hat{e}_N(a)\bar{\psi}(a) = \mathbb{B}_l^m(\tilde{e}_N, \psi) - a\tilde{e}_N(a)\bar{\psi}(a)\\ &= \beta_l(\tilde{e}_N, \psi) - (k^2+1)(\tilde{e}_N, \psi)_\varpi - a\,\tilde{e}_N(a)\bar{\psi}(a)\\ &- kb^2\mathcal{T}_{l,kb}\tilde{e}_N(b)\bar{\psi}(b),\ \ \forall\, \psi \in \mathcal{P}_N.\end{aligned} \tag{4.195}$$

Compared with the analysis for (4.190), the only difference is the presence of the extra term "$-a\,\tilde{e}_N(a)\bar{\psi}(a)$", which is akin to the situation in the proof of Theorem 4.3. We omit the details, as one can refer to the proofs of [77, Thm 4.2] and Theorem 4.3. □

We now estimate the error between the electric field and its spectral approximation in (4.189)-(4.191). We first introduce suitable functional spaces to characterize the regularity of the electric field. For any $\boldsymbol{E} \in \boldsymbol{L}^2(\Omega)$, we write

$$\boldsymbol{E} = v_{2,0}^0(r)\, Y_0^0 \boldsymbol{e}_r + \sum_{l=1}^{\infty}\sum_{|m|=0}^{l}\big\{v_{1,l}^m(r)\,\boldsymbol{T}_l^m + v_{2,l}^m(r)\,Y_l^m\boldsymbol{e}_r + v_{3,l}^m(r)\,\nabla_S Y_l^m\big\}. \tag{4.196}$$

We introduce the anisotropic Sobolev space $\boldsymbol{H}^t(S;H^s_\varpi(I))$ for $t\geq 0$ and integer $s\geq 0$, equipped with the norm:

$$\begin{aligned}\|\boldsymbol{E}\|_{\boldsymbol{H}^t(S;H^s_\varpi(I))}=\bigg(\|v^0_{2,0}\|^2_{H^s_\varpi(I)}+\sum_{l=1}^{\infty}\sum_{|m|=0}^{l}\beta_l^{1+t}\Big\{\|v^m_{1,l}\|^2_{H^s_\varpi(I)}\\ +\beta_l^{-1}\big\|v^m_{2,l}\big\|^2_{H^s_\varpi(I)}+\|v^m_{3,l}\|^2_{H^s_\varpi(I)}\Big\}\bigg)^{\frac12}.\end{aligned}\tag{4.197}$$

Note that $\boldsymbol{H}^0(S;H^0_\varpi(I))=\boldsymbol{L}^2(\Omega)$. Here, we are interested in the divergence-free fields. In this case, like Proposition 4.1, we can rewrite $\boldsymbol{E}\in\mathbb{H}_0(\mathbf{curl};\Omega)$ in the divergence-free form:

$$\boldsymbol{E}=\frac{c}{r^2}Y_0^0\boldsymbol{e}_r+\sum_{l=1}^{\infty}\sum_{|m|=0}^{l}\big\{u^m_{1,l}(r)\,\boldsymbol{T}^m_l+\nabla\times\big(u^m_{2,l}(r)\,\boldsymbol{T}^m_l\big)\big\},\tag{4.198}$$

where c is an arbitrary constant, and for $l\geq 1$,

$$v^m_{1,l}(r)=u^m_{1,l}(r),\quad v^m_{2,l}(r)=\frac{\beta_l}{r}u^m_{2,l}(r),\quad v^m_{3,l}(r)=\Big(\frac{d}{dr}+\frac{1}{r}\Big)u^m_{2,l}(r)\,.\tag{4.199}$$

Note that we can substitute (4.199) into (4.197) to express the norm in (4.197) in terms of $\{u^m_{1,l},u^m_{2,l}\}$.

Theorem 4.8. *If $\boldsymbol{E}\in\mathbb{H}_0(\mathbf{curl};\Omega)\cap\boldsymbol{L}^2(S;H^s_\varpi(I))\cap\boldsymbol{H}^s(S;L^2_\varpi(I))$ with $s\in\mathbb{N}$, then*

$$\begin{aligned}\|\boldsymbol{E}-\boldsymbol{E}_N^L\|_\Omega\lesssim(1+k^{-1}N)(L+k^2N^{-1})N^{-s}\big\|\boldsymbol{E}\big\|_{\boldsymbol{L}^2(S;H^s_\varpi(I))}\\ +L^{-s}\big\|\boldsymbol{E}\big\|_{\boldsymbol{H}^s(S;L^2_\varpi(I))},\end{aligned}\tag{4.200}$$

for all $k\geq k_0$ with k_0 being a positive constant.

Proof. By (4.102) and (4.189),

$$\begin{aligned}\boldsymbol{E}-\boldsymbol{E}_N^L=\sum_{l=1}^{L}\sum_{|m|=0}^{l}\big\{(u^m_{1,l}-u^{N,m}_{1,l})\,\boldsymbol{T}^m_l+\nabla\times\big((u^m_{2,l}-u^{N,m}_{2,l})\,\boldsymbol{T}^m_l\big)\big\}\\ +\sum_{l=L+1}^{\infty}\sum_{|m|=0}^{l}\big\{u^m_{1,l}\,\boldsymbol{T}^m_l+\nabla\times\big(u^m_{2,l}\,\boldsymbol{T}^m_l\big)\big\}:=\boldsymbol{S}_1+\boldsymbol{S}_2,\end{aligned}\tag{4.201}$$

where $\boldsymbol{S}_2$ counts the error from truncating the VSH series. It is clear that by the orthogonality of VSH, (4.197) and (4.199),

$$\begin{aligned}\|\boldsymbol{S}_2\|_\Omega^2 &= \sum_{l=L+1}^{\infty}\sum_{|m|=0}^{l}\beta_l\big\{\|u_{1,l}^m\|_\varpi^2+\big\|\hat{\partial}_r u_{2,l}^m\big\|_\varpi^2+\beta_l\|u_{2,l}^m\|^2\big\}\\ &\le L^{-2s}\big\|\boldsymbol{E}\big\|_{\boldsymbol{H}^s(S;L^2_\varpi(I))}^2.\end{aligned}\tag{4.202}$$

Next, by (4.185), Lemma 4.3, Lemma 4.5 and (4.199),

$$\begin{aligned}\|\boldsymbol{S}_1\|_\Omega^2 &\lesssim \sum_{l=1}^{L}\sum_{|m|=0}^{l}\beta_l\Big\{\|u_{1,l}^m-u_{1,l}^{N,m}\|_\varpi^2\\ &\quad+\big\|(u_{2,l}^m-u_{2,l}^{N,m})'\big\|_\varpi^2+\beta_l\big\|u_{2,l}^m-u_{2,l}^{N,m}\big\|^2\Big\}\\ &\lesssim \sum_{l=1}^{L}\sum_{|m|=0}^{l}\beta_l\big(\sqrt{\beta_l}+k^2N^{-1}\big)^2k^{-2}N^{2-2s}|u_{1,l}^m|_{\mathbb{X}^s(I)}^2\\ &\quad+\sum_{l=1}^{L}\sum_{|m|=0}^{l}\beta_l\big(\sqrt{\beta_l}+k^2N^{-1}\big)^2N^{-2s}|u_{2,l}^m|_{\mathbb{X}^{s+1}(I)}^2.\end{aligned}\tag{4.203}$$

By (4.199) and a direct calculation,

$$\begin{aligned}|u_{2,l}^m|_{\mathbb{X}^{s+1}(I)}^2 &\lesssim \|\partial_r^{s+1}u_{2,l}^m\|_{L^2(I)}^2=\|\partial_r^s(\hat{\partial}_r u_{2,l}^m)-\partial_r^s(u_{2,l}^m/r)\|_{L^2(I)}^2\\ &\lesssim \|\partial_r^s(\hat{\partial}_r u_{2,l}^m)\|_{L^2(I)}^2+\|\partial_r^s(u_{2,l}^m/r)\|_{L^2(I)}^2\\ &= \|\partial_r^s v_{3,l}^m\|_{L^2(I)}^2+\beta_l^{-2}\|\partial_r^s v_{2,l}^m\|_{L^2(I)}^2.\end{aligned}\tag{4.204}$$

As the weight ϖ is uniformly bounded below and above for $r\in(a,b)$, we derive from (4.197), (4.199) and (4.203)-(4.204) that

$$\|\boldsymbol{S}_1\|_\Omega\lesssim(1+k^{-1}N)(L+k^2N^{-1})N^{-s}\big\|\boldsymbol{E}\big\|_{\boldsymbol{L}^2(S;H^s_\varpi(I))}.\tag{4.205}$$

A combination of (4.202) and (4.205) leads to the desired estimate. □

Remark 4.5. *Note that the estimate in* (4.200) *is in the L^2-norm, not in the usual energy norm. For the continuous problem, we were able to obtain the bound for the energy norm through a further estimate of $\hat{\partial}_r u_{2,l}^m$ in Subsection 4.3.3. However, this approach does not carry over to the discrete problem, as the second test function does not belong to the finite dimensional space for the spectral-Galerkin*

approximation of (4.152). *We shall derive below a sub-optimal error estimate in the energy norm through a different approach.* □

In what follows, we will derive a bound for the error $\nabla\times(\boldsymbol{E}-\boldsymbol{E}_N^L)$.

Theorem 4.9. *If* $\boldsymbol{E}\in\boldsymbol{L}^2(S;H^s_\varpi(I))\cap\boldsymbol{H}^{s-1}(S;H^1_\varpi(I))\cap\boldsymbol{H}^s(S;L^2_\varpi(I))$ *with* $s\geq 3$, *then*

$$\begin{aligned}\big\|\nabla\times(\boldsymbol{E}-\boldsymbol{E}_N^L)\big\|_{w,\Omega}&\lesssim L^{1-s}\big\{\|\boldsymbol{E}\|_{\boldsymbol{H}^{s-1}(S;H^1_\varpi(I))}+\|\boldsymbol{E}\|_{\boldsymbol{H}^s(S;L^2_\varpi(I))}\big\}\\&+\big(N+(1+kN^{-1})(L+k^2N^{-1})\big)N^{1-s}\big\|\boldsymbol{E}\big\|_{\boldsymbol{L}^2(S;H^s_\varpi(I))},\end{aligned}\tag{4.206}$$

for all $k\geq k_0$ *with* k_0 *being a positive constant, where* $w=(b-r)(r-a)$.

Proof. For notational convenience, let $e_{lm}^{u_i}=u_{i,l}^m-u_{i,l}^{N,m}(i=1,2)$. By (4.201), (4.11) and (4.16)-(4.15),

$$\begin{aligned}&\big\|\nabla\times(\boldsymbol{E}-\boldsymbol{E}_N^L)\big\|_{w,\Omega}^2\\&\lesssim\sum_{l=1}^{L}\sum_{|m|=0}^{l}\beta_l\big\{\|r\hat\partial_r e_{lm}^{u_1}\|_w^2+\beta_l\|e_{lm}^{u_1}\|_w^2+\|r\mathcal{L}_l(e_{lm}^{u_2})\|_w^2\big\}\\&\quad+\sum_{l=L+1}^{\infty}\sum_{|m|=0}^{l}\beta_l\big\{\|r\hat\partial_r u_{1,l}^m\|_w^2+\beta_l\|u_{1,l}^m\|_w^2+\|r\mathcal{L}_l(u_{2,l}^m)\|_w^2\big\}:=T_1+T_2.\end{aligned}\tag{4.207}$$

We first estimate T_2. It is clear that by (4.197) and (4.199),

$$\begin{aligned}&\|r\hat\partial_r u_{1,l}^m\|_w^2+\beta_l\|u_{1,l}^m\|_w^2\lesssim\|v_{1,l}^m\|_{H^1_\varpi(I)}^2+\beta_l\|v_{1,l}^m\|_{L^2_\varpi(I)}^2,\\&\|r\mathcal{L}_l(u_{2,l}^m)\|_w^2=\|r\hat\partial_r^2u_{2,l}^m-\beta_l r^{-1}u_{2,l}^m\|_w^2=\|r\hat\partial_r^2u_{2,l}^m-\beta_l r^{-1}u_{2,l}^m\|_w^2\\&\qquad=\|r\hat\partial_r v_{3,l}^m-v_{2,l}^m\|_w^2\lesssim\|v_{3,l}^m\|_{H^1_\varpi(I)}^2+\|v_{2,l}^m\|_{L^2_\varpi(I)}^2,\end{aligned}\tag{4.208}$$

so we have

$$\begin{aligned}T_2&\leq\sum_{l=L+1}^{\infty}\sum_{|m|=0}^{l}\beta_l\big\{\|v_{1,l}^m\|_{H^1_\varpi(I)}^2+\|v_{2,l}^m\|_{L^2_\varpi(I)}^2+\|v_{3,l}^m\|_{H^1_\varpi(I)}^2\big\}\\&\quad+\sum_{l=L+1}^{\infty}\sum_{|m|=0}^{l}\beta_l^2\|v_{1,l}^m\|_{L^2_\varpi(I)}^2\\&\lesssim\beta_{L+1}^{1-s}\big\{\|\boldsymbol{E}\|^2_{\boldsymbol{H}^{s-1}(S;H^1_\varpi(I))}+\|\boldsymbol{E}\|^2_{\boldsymbol{H}^s(S;L^2_\varpi(I))}\big\}.\end{aligned}\tag{4.209}$$

We next turn to estimating T_1. We see that it is necessary to obtain H^2-estimate of $e_{lm}^{u_2}$. To simplify the notation, we will drop l, m from the notations if no confusion may arise. Taking $v = w(r)\hat{e}_N''(\in \mathcal{P}_N)$ with $w(r) = (r-a)(b-r)$ in (4.195), and using integration by parts, we obtain

$$\begin{aligned}\mathbb{B}_l^m(\hat{e}_N, w\hat{e}_N'') &= -((r^2\hat{e}_N')', w\hat{e}_N'') + \beta_l(\hat{e}_N, w\hat{e}_N'') - k^2(r^2\hat{e}_N, w\hat{e}_N'') \\ &= \beta_l(\tilde{e}_N, w\hat{e}_N'') - (k^2+1)(r^2\tilde{e}_N, w\hat{e}_N'').\end{aligned} \tag{4.210}$$

Using integration by parts again, we derive from a direct calculation that

$$\begin{aligned}-\operatorname{Re}\big((r^2\hat{e}_N')', w\hat{e}_N''\big) &= -\|r\hat{e}_N''\|_w^2 - 2\operatorname{Re}\big(r\hat{e}_N', w\hat{e}_N''\big) \\ &= -\|r\hat{e}_N''\|_w^2 + \int_a^b |\hat{e}_N'|^2(rw)'dr; \\ \operatorname{Re}(\hat{e}_N, w\hat{e}_N'') &= -\|\hat{e}_N'\|_w^2 - \operatorname{Re}\int_a^b \hat{e}_N\overline{\hat{e}_N'}w'dr \\ &= -\|\hat{e}_N'\|_w^2 - \frac{1}{2}|\hat{e}_N|^2w'\Big|_a^b + \frac{1}{2}\int_a^b |\hat{e}_N|^2w''dr \\ &= -\|\hat{e}_N'\|_w^2 + \frac{b-a}{2}\big(|\hat{e}_N(a)|^2 + |\hat{e}_N(b)|^2\big) - \|\hat{e}_N\|^2; \\ -\operatorname{Re}(r^2\hat{e}_N, w\hat{e}_N'') &= \|r\hat{e}_N'\|_w^2 + \frac{1}{2}|\hat{e}_N|^2(r^2w)'\Big|_a^b - \frac{1}{2}\int_a^b |\hat{e}_N|^2(r^2w)''dr \\ &= \|r\hat{e}_N'\|_w^2 - \frac{b-a}{2}\big(a^2|\hat{e}_N(a)|^2 + b^2|\hat{e}_N(b)|^2\big) - \frac{1}{2}\int_a^b |\hat{e}_N|^2(r^2w)''dr,\end{aligned}$$

and further by the Cauchy-Schwartz inequality,

$$\begin{aligned}|(\tilde{e}_N, w\hat{e}_N'')| &\le \int_a^b |(w\tilde{e}_N)'||\hat{e}_N'|dr \le \frac{1}{2}\|\hat{e}_N'\|^2 + \frac{1}{2}\|(w\tilde{e}_N)'\|^2 \\ &\le \frac{1}{2}\|\hat{e}_N'\|^2 + c\big(\|\tilde{e}_N\|^2 + \|\tilde{e}_N'\|^2\big); \\ |(r^2\tilde{e}_N, w\hat{e}_N'')| &\le \int_a^b |(r^2w\tilde{e}_N)'||\hat{e}_N'|dr \le \frac{1}{2}\|\hat{e}_N'\|^2 + \frac{1}{2}\|(r^2w\tilde{e}_N)'\|^2 \\ &\le \frac{1}{2}\|\hat{e}_N'\|^2 + c\big(\|\tilde{e}_N\|^2 + \|\tilde{e}_N'\|^2\big).\end{aligned}$$

Thus, we obtain from (4.210) and the above estimates that

$$\|r\hat{e}_N''\|_w^2 \lesssim (\beta_l + k^2)\big(\|\hat{e}_N\|_{H^1(I)}^2 + \|\tilde{e}_N\|_{H^1(I)}^2\big). \tag{4.211}$$

Recall that $\hat{e}_N = u_2^N - \pi_N^1 u_2$, $\tilde{e}_N = u_2 - \pi_N^1 u_2$ and $e_N^{u_2} = \tilde{e}_N - \hat{e}_N$, so we derive from Lemma 4.3 and Lemma 4.5 that

$$\begin{aligned} \|r(e_N^{u_2})''\|_w^2 &\lesssim \|r(\tilde{e}_N)''\|_w^2 + (\beta_l + k^2)\big(\|e_N^{u_2}\|_{H^1(I)}^2 + \|\tilde{e}_N\|_{H^1(I)}^2\big) \\ &\lesssim \|(u_2 - \pi_N^1 u_2)''\|^2 + (\beta_l + k^2)(\sqrt{\beta_l} + k^2 N^{-1})^2 N^{-2s} |u_2|_{\mathbb{X}^{s+1}(I)}^2. \end{aligned} \tag{4.212}$$

In order to estimate $\|(u_2 - \pi_N^1 u_2)''\|^2$, we need to use the orthogonal projection $\pi_N^2 : H^2(I) \to \mathcal{P}_N$, and recall its approximation result (cf. [47, Ch. 4]): for any $v \in \mathbb{X}^s(I)$,

$$\|\pi_N^2 v - v\|_{H^\mu(I)} \lesssim N^{\mu - s} |v|_{\mathbb{X}^s(I)}, \quad \mu = 0, 1, 2, \quad s \geq 2. \tag{4.213}$$

Applying the inverse inequality (cf. [47, Thm 3.33]) and the above approximation result , we obtain

$$\|(\pi_N^1 v - \pi_N^2 v)''\| \lesssim N^2 \|(\pi_N^1 v - \pi_N^2 v)'\| \lesssim N^{3-s} |v|_{\mathbb{X}^s(I)}, \quad s \geq 2.$$

Therefore, we have

$$\|(\pi_N^1 v - v)''\| \leq \|(\pi_N^1 v - \pi_N^2 v)''\| + \|(v - \pi_N^2 v)''\| \lesssim N^{3-s} |v|_{\mathbb{X}^s(I)}. \tag{4.214}$$

From (4.212) and (4.214), we have

$$\|(e_N^{u_2})''\|_w^2 \lesssim \big\{N^4 + (\beta_l + k^2)(\sqrt{\beta_l} + k^2 N^{-1})^2\big\} N^{-2s} |u_2|_{\mathbb{X}^{s+1}(I)}^2. \tag{4.215}$$

Now, we are ready to estimate T_1 in (4.207). Using Lemma 4.5, we obtain

$$\begin{aligned} \|r\mathcal{L}_l(e_{lm}^{u_2})\|_w^2 &\lesssim \|(e_{lm}^{u_2})''\|_w^2 + \beta_l^2 \|e_{lm}^{u_2}\|^2 \\ &\lesssim \big\{N^4 + (\beta_l + k^2)(\sqrt{\beta_l} + k^2 N^{-1})^2\big\} N^{-2s} |u_{2,l}^m|_{\mathbb{X}^{s+1}(I)}^2. \end{aligned} \tag{4.216}$$

Therefore, we derive from Lemma 4.3, (4.216) and (4.204),

$$\begin{aligned} T_1 \lesssim & \sum_{l=1}^{L} \sum_{|m|=0}^{l} \beta_l \big(\sqrt{\beta_l} + k^2 N^{-1}\big)^2 N^{2-2s} |u_{1,l}^m|_{\mathbb{X}^s(I)}^2 \\ & + \sum_{l=1}^{L} \sum_{|m|=0}^{l} \big\{N^4 + (\beta_l + k^2)(\sqrt{\beta_l} + k^2 N^{-1})^2\big\} N^{-2s} |u_{2,l}^m|_{\mathbb{X}^{s+1}(I)}^2 \\ & \lesssim \big\{N^2 + (1 + k^2 N^{-2})(L + k^2 N^{-1})^2\big\} N^{2-2s} \big\|\boldsymbol{E}\big\|_{\boldsymbol{L}^2(S; H_\varpi^s(I))}^2. \end{aligned} \tag{4.217}$$

A combination of (4.207), (4.209) and (4.217) leads to the desired estimate. □

4.6 General scatterers through transformed field expansion

We consider now a general scatterer enclosed by

$$D = \big\{(r,\theta,\phi) \,:\, 0 < r < a + g(\theta,\phi),\ \theta \in [0,\pi],\ \phi \in [0,2\pi)\big\},$$

for some $a > 0$ and given g. Let us choose the radius b of the artificial spherical boundary such that $b > \max_{\theta,\phi}\{a+g(\theta,\phi)\}$, and consider the Maxwell's equations (4.2)-(4.3) in the domain $\hat{\Omega} = \{a+g(\theta,\phi) < r < b\}$. An effective approach to deal with scattering problems in general domains with moderately large wave numbers is the so-called transformed field expansion [84]. It has been successfully applied to various situations, including in particular acoustic scattering problems in 2-D [118] and 3-D [119].

In our recent work [112], we applied the TFE approch to the Maxwell's equation (4.2)-(4.3) in $\hat{\Omega}$. We outline below the essential steps of this approach, and refer to [112] for more details.

- The first step is to transform the general domain $\hat{\Omega} = \{a + g < r < b\}$ to the spherical shell $\Omega = \{a < r' < b\}$ in (4.4) with the change of variables:

$$r' = \frac{(b-a)r - b\,g(\theta,\phi)}{b - a - g(\theta,\phi)}, \quad \theta' = \theta, \quad \phi' = \phi. \tag{4.218}$$

  With this change of variable, the Maxwell's equation (4.2)-(4.3) in $\hat{\Omega}$ is transformed to a Maxwell's equation in Ω which can still be written in the form (4.2)-(4.3) with the understanding that all new terms (induced by the transform) are included in $\boldsymbol{F}$ and $\boldsymbol{h}$ (cf. [112, (3.6)]). With a slight abuse of notation, we shall still use r to denote r' and the same notations to denote the transformed functions.

- The second step is to assume $g(\theta,\phi) = \epsilon f(\theta,\phi)$ and expand the solution $\boldsymbol{E}$ in ϵ:

$$\boldsymbol{E}(r,\theta,\phi) = \sum_{n=0}^{\infty} \boldsymbol{E}_n(r,\theta,\phi)\epsilon^n. \tag{4.219}$$

Similarly, we can expand $\boldsymbol{F}$ (the original source function) and $\boldsymbol{h}$ as

$$\boldsymbol{F}(r,\theta,\phi)=\sum_{n=0}^{\infty}\boldsymbol{F}_n(r,\theta,\phi)\epsilon^n,\quad \boldsymbol{h}(\theta,\phi)=\sum_{n=0}^{\infty}\boldsymbol{h}_n(\theta,\phi)\epsilon^n. \tag{4.220}$$

One can then derive a recursion formula for $\boldsymbol{E}_n$ (for $n\geq 0$):

$$\nabla\times\nabla\times\boldsymbol{E}_n-k^2\boldsymbol{E}_n=\boldsymbol{F}_n+\boldsymbol{G}_n,\quad \text{in } \Omega; \tag{4.221}$$

$$\boldsymbol{E}_n\times\boldsymbol{e}_r=\boldsymbol{0},\quad \text{at } r=a; \tag{4.222}$$

$$(\nabla\times\boldsymbol{E}_n)\times\boldsymbol{e}_r-\mathrm{i}k\mathscr{T}_b\big[(\boldsymbol{E}_n)_S\big]=\boldsymbol{h}_n,\quad \text{at } r=b, \tag{4.223}$$

where $\boldsymbol{G}_n$ and $\boldsymbol{h}_n$ are given by explicit recurrence formulae in [112, Appendix B].

- The third step is to obtain approximation $\boldsymbol{E}_{n,N}^L$ (in the form of (4.189)) to $\boldsymbol{E}_n$ (for $0\leq n\leq M$) by solving the above Maxwell's equations (4.221)-(4.223) in the spherical shell Ω using the decoupled method presented in Section 4.5. Then, we define our approximation to $\boldsymbol{E}$ by

$$\boldsymbol{E}_N^{L,M}(r,\theta,\phi)=\sum_{n=0}^{M}\boldsymbol{E}_{n,N}^L(r,\theta,\phi)\,\epsilon^n. \tag{4.224}$$

Next, we shall use the general convergence theory developed in [114] to give an error estimate for $\boldsymbol{E}-\boldsymbol{E}_N^{L,M}$. Using essentially the same argument as in the proof of [114, Thm 5.5] for the Helmholtz equation, we can prove the following bounds.

Proposition 4.4. *Let $\boldsymbol{F}\in(H^{s-2}(\Omega))^3$, $f\in H^s(S)$ and $\boldsymbol{h}\in(H^{s-3/2}(S))^2$ for an integer $s\geq 2$. Then, the expansion* (4.219) *converges strongly, i.e., there exists $C_1,C_2>0$ such that*

$$\|\boldsymbol{E}_n\|_{(H^s(\Omega))^3}\leq C_1\big(\|\boldsymbol{F}\|_{(H^{s-2}(\Omega))^3}+\|\boldsymbol{h}\|_{(H^{s-3/2}(S))^2}\big)B^n, \tag{4.225}$$

for some $B>C_2\|f\|_{H^s(S)}$.

On the other hand, it can be shown that the space with the norm in (4.197) satisfies $\boldsymbol{H}^t(S; H^s_\varpi(I)) \subseteq (H^{s+t}(\Omega))^3$. Therefore, with the above result and Theorems 4.8-4.9 at our disposal, we can then apply Theorem 2.1 in [114] to obtain the following:

Theorem 4.10. *Let $\boldsymbol{E}$ be the solution of the Maxwell's equations in $\hat{\Omega}$ and $\boldsymbol{E}_N^{L,M}$ be its approximation defined in* (4.224)*. Then, under the condition of Proposition 4.4 and Theorems 4.8-4.9, we have*

$$\begin{aligned}\|\boldsymbol{E} - \boldsymbol{E}_N^{L,M}\|_{\hat{\Omega}} &\lesssim (B\epsilon)^{M+1} \\ &+ \big\{(1+k^{-1}N)(L+k^2N^{-1})N^{-s} + L^{-s}\big\}(\|\boldsymbol{F}\|_{(H^{s-2}(\hat{\Omega}))^3} + \|\boldsymbol{h}\|_{(H^s(S))^2}),\end{aligned}$$

and

$$\begin{aligned}\|\nabla\times(\boldsymbol{E} - \boldsymbol{E}_N^{L,M})\|_{w,\hat{\Omega}} &\lesssim (B\epsilon)^{M+1} + \big\{\big(N + (1+kN^{-1})(L+k^2N^{-1})\big)N^{1-s} \\ &\quad + L^{1-s}\big\}\big(\|\boldsymbol{F}\|_{(H^{s-2}(\hat{\Omega}))^3} + \|\boldsymbol{h}\|_{(H^s(S))^2}\big),\end{aligned}$$

for any $B > C_2\|f\|_{H^s(S)}$, where C_2 is the constant in Proposition 4.4.

4.7 Numerical results

We first provide some numerical results to demonstrate the high accuracy of the proposed method. We use the exact multiple solution of (4.2)-(4.3) (cf. [3]) as the reference solution. For example, we can take

$$\boldsymbol{E} = \sum_{l=1}^{M_0}\sum_{|m|=0}^{l}\Big\{h_l^{(1)}(kr)\boldsymbol{T}_l^m(\theta,\varphi) + \nabla\times\big(h_l^{(1)}(kr)\boldsymbol{T}_l^m(\theta,\varphi)\big)\Big\}, \tag{4.226}$$

which is formed by a linear combination of the transverse electric and magnetic multipole solutions. We then approximate the exact field by the spectral-Galerkin approximation:

$$\boldsymbol{E}_N^{M_0}(r,\theta,\varphi) = \sum_{l=1}^{M_0}\sum_{|m|=0}^{l}\Big[u_{l,N}^m(r)\boldsymbol{T}_l^m(\theta,\varphi) + \nabla\times\big(v_{l,N}^m(r)\boldsymbol{T}_l^m(\theta,\varphi)\big)\Big], \tag{4.227}$$

where $\{u_{l,N}^m, v_{l,N}^m\}$ are computed from (4.190)-(4.191).

In the computation, we take $a = 2, b = 4$ and $M_0 = 10$. In Figure 4.5 (left), we plot the relative discrete L^2-error: $\left\|\boldsymbol{E}-\boldsymbol{E}_N^{M_0}\right\|_{l^2(\Omega)}/\|\boldsymbol{E}\|_{l^2(\Omega)}$, against various N for $k = 10, 40, 80, 200$ from left to right. Observe that the error decays exponentially, as soon as N enters the asymptotic range, which is for this case roughly $N > k$. Nevertheless, the round-off errors become severe for very large N and dominate the convergence rate.

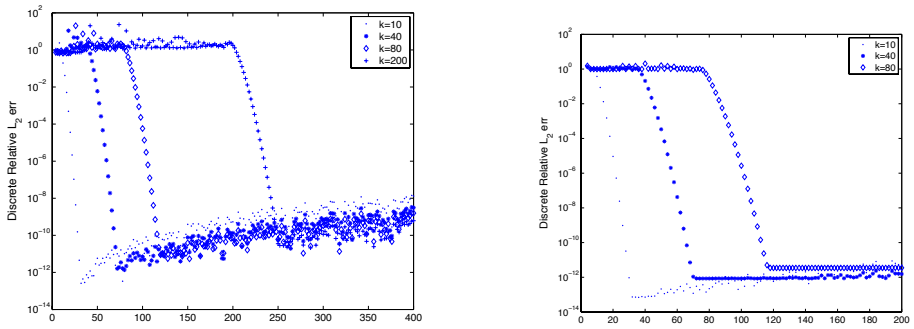

Figure 4.5: Left: Relative discrete l^2-errors against N for $k = 10, 40, 80, 200$. Right: Relative discrete l^2-errors against N for $k = 10, 40, 80$.

We next consider an exact solution generated by $\boldsymbol{g}$ at $r = a$. To be more pricise, the electric field $\boldsymbol{E}$ takes the form

$$\boldsymbol{E} = \sum_{l=1}^{M_1} \sum_{|m|=0}^{l} \left\{ g_{1,l}^m h_l^{(1)}(kr) \boldsymbol{T}_l^m(\theta,\varphi) + g_{2,l}^m \nabla\times\big(h_l^{(1)}(kr)\boldsymbol{T}_l^m(\theta,\varphi)\big)\right\},$$

where

$$g_{1,l}^m = -\frac{1}{l(l+1)h_l^{(1)}(ka)} \int_S (\boldsymbol{g}\cdot\overline{\nabla_S Y_l^m})\, dS,$$
$$g_{2,l}^m = \frac{a}{l(l+1)h_l^{(1)}(ka)(\rho_l(ka)+1)} \int_S (\boldsymbol{g}\cdot\overline{\boldsymbol{T}_l^m})\, dS.$$

Note that we can compute $g_{1,l}^m$ and $g_{2,l}^m$ using Spherepack [117]. In the computation, we take a plane incident wave: $\boldsymbol{g} = e^{\mathrm{i}k\boldsymbol{x}}$. In order to have good approximation using Spherepack, we choose $M_1 = 60$. We plot in Figure 4.5 (right), the discrete relative L^2-errors against N for $k = 10, 40, 80$, which indicates a very similar exponential convergence as with the first example.

Chapter 5

Conclusion and Future Works

In this chapter, we give a summary of the works done in this thesis and explore some relevant topics for further investigation.

5.1 Conclusion

(i) In Chapter 2, we proposed from a new perspective, the CBCs for the ideal circular and elliptic cylindrical cloaks, which, together with an accurate spectral-element solver, demonstrated that the cloaks can achieve perfect concealment of incoming incident waves with very mild conditions on the incident frequency. We also illustrated the perfect cloaking effect, when the incoming wave is generated by a source exterior to the cloaking device.

(ii) In Chapter 3, we presented an accurate and efficient spectral-element solver for time-harmonic Helmholtz equations in general inhomogeneous media. We focused on several applications arisen from transformation electromagnetics which included the polygonal invisibility cloaks and concentrators, and circular rotators. We introduced new ideas of how to seamlessly integrate local elements and global DtN boundary condition. We proposed

new cloaking boundary conditions for accurate simulation of perfect polygonal invisibility cloaks. The proposed method also provided a reliable tool to study the interesting phenomena when defects and other media were embedded or placed in a perfect cloak.

(iii) In Chapter 4, we are devoted to wavenumber explicit analysis of three-dimensional time-harmonic Maxwell's equations in an exterior domain.

First, we considered the special case with the scatterer being a sphere:

(a) We reduced the Maxwell's system into two sequences of decoupled one-dimensional problems by using divergence-free vector spherical harmonics. This reduction not only led to a more efficient spectral-Galerkin algorithm, but also greatly simplified its analysis.

(b) We derived wavenumber explicit bounds for the (continuous) Maxwell's system with (exact) transparent boundary conditions, and wavenumber explicit error estimates for its spectral-Galerkin approximation.

(c) We derived optimal wavenumber explicit *a priori* bounds and error estimates for the Helmholtz equation, which improved the results in [77].

Then, we applied the transformed field expansion (TFE) approach[84] to deal with general scatterers. By using the general framework developed in [114], we derived rigorous wavenumber explicit error estimates for the complete algorithm for general scatterers. To the best of our knowledge, these are the first such estimates for Maxwell's system with transparent boundary conditions. Note that the scattering problems with transparent boundary conditions at an artificial boundary can not be dealt with the usual approach in [81, 76, 78, 82, 80], for the underlying domain is not of star shape, the method presented here provides a viable approach to deal with an important class of scattering problems with transparent boundary conditions at an artificial boundary.

5.2 Future works

We explore some relevant topics for further investigation in this section.

(i) In Chapter 3, we introduced new ideas of how to seamlessly integrate local spectral elements and global DtN boundary condition and proposed new cloaking boundary conditions for accurate simulation of perfect polygonal invisibility cloaks. One of the future works is to extend these ideas to three-dimensional polyhedral cloaks simulations. In fact, we provide some insights in Section 3.4 on how to integrate the spectral-element solver with three-dimensional DtN boundary condition involving global spherical harmonic coefficients.

(ii) In Chapters 2-3, we conducted both rigorous mathematical study and numerical experiments for invisibility cloaks of various types. These could shed light on the study of simulation of inside-out (or inverse) cloaks for electromagnetic waves proposed by Zharova et al. [120]. The challenges resides in (a) the material parameters are singular; (b) the wave oscillates infinitely inside the inverse cloak. Moreover, the underlying coordinate transformation induces absorbing non-reflecting media as a matching layer for numerical simulations of wave problems. These could be explored as well in the future.

(iii) In Chapter 4, we reduced the time-harmonic Maxwell's equations into two sequences of decoupled Helmholtz equations using divergence-free vector spherical harmonics and proposed efficient spectral-Garlerkin solvers. These could be extended to the simulation of spherical dispersive invisibility cloaks and the time-domain Maxwell's equations will be reduced to two sequences of 1-D wave equations with convolution terms.

Bibliography

[1] R.A. Adams and J.J. Fournier. *Sobolev Spaces*, volume 140. Academic press, 2003.

[2] G.N. Watson. *A Treatise of the Theory of Bessel Functions (second edition)*. Cambridge University Press, Cambridge, UK, 1966.

[3] J.C. Nédélec. *Acoustic and Electromagnetic Equations*, volume 144 of *Applied Mathematical Sciences*. Springer-Verlag, New York, 2001. Integral representations for harmonic problems.

[4] P.M. Morse and H. Feshbach. *Methods of Theoretical Physics*. McGraw-Hill Book Co., Inc., New York, 1953.

[5] J.B. Pendry, D. Schurig, and D.R. Smith. Controlling electromagnetic fields. *Science*, 312(5781):1780–1782, 2006.

[6] U. Leonhardt. Optical conformal mapping. *Science*, 312(5781):1777–1780, 2006.

[7] M. Yan, W. Yan, and M. Qiu. Cylindrical superlens by a coordinate transformation. *Phys. Rev. B*, 78(12):125113, 2008.

[8] M. Rahm, D. Schurig, D.A. Roberts, S.A. Cummer, D.R. Smith, and J.B. Pendry. Design of electromagnetic cloaks and concentrators using form-invariant coordinate transformations of Maxwells equations. *Phot. Nano. Fund. Appl.*, 6(1):87–95, 2008.

[9] H.Y. Chen and C.T. Chan. Transformation media that rotate electromagnetic fields. *Appl. Phys. Lett.*, 90(24):241105, 2007.

[10] H.Y. Chen, X.D. Luo, H.R. Ma, and C.T. Chan. The anti-cloak. *Opt. Express*, 16(19):14603–14608, 2008.

[11] T. Yang, H.Y. Chen, X.D. Luo, and H.R. Ma. Superscatterer: enhancement of scattering with complementary media. *Opt. Express*, 16(22):18545–18550, 2008.

[12] M. Rahm, D.A. Roberts, J.B. Pendry, and D.R. Smith. Transformation-optical design of adaptive beam bends and beam expanders. *Opt. Express*, 16(15):11555–11567, 2008.

[13] D.H. Werner and D.H. Kwon. *Transformation Electromagnetics and Metamaterials*. Springer, 2013.

[14] E.J. Post. *Formal Structure of Electromagnetics: General Covariance and Electromagnetics*. Courier Corporation, 1997.

[15] H.Y. Chen. Transformation optics in orthogonal coordinates. *J. Opt. A: Pure Appl. Opt.*, 11(7):75–102, 2009.

[16] H.Y. Chen, C.T. Chan, and P. Sheng. Transformation optics and metamaterials. *Nature Materials*, 9(5):387–396, 2010.

[17] A. Greenleaf, M. Lassas, and G. Uhlmann. On nonuniqueness for Calderon's inverse problem. *Math. Res. Lett.*, 10(5/6):685–694, 2003.

[18] A. Greenleaf, Y. Kurylev, M. Lassas, and G. Uhlmann. Cloaking devices, electromagnetic wormholes, and transformation optics. *SIAM Rev.*, 51(1):3–33, 2009.

[19] E. Cojocaru. Exact analytical approaches for elliptic cylindrical invisibility cloaks. *J. Opt. Soc. Am. B.*, 26(5):1119–1128, 2009.

[20] W.X. Jiang, T.J. Cui, G.X. Yu, X.Q. Lin, Q. Cheng, and J.Y. Chin. Arbitrarily elliptical–cylindrical invisible cloaking. *J. Phys. D: Appl. Phys.*, 41(8):085504, 2008.

[21] D.H. Kwon and D.H. Werner. Two-dimensional eccentric elliptic electromagnetic cloaks. *Appl. Phys. Lett*, 92(1):013505, 2008.

[22] R. Liu, C. Ji, J.J. Mock, J.Y. Chin, T.J. Cui, and D.R. Smith. Broadband ground-plane cloak. *Science*, 5912(323):366–369, 2009.

[23] H.F. Ma and T.J. Cui. Three-dimensional broadband ground-plane cloak made of metamaterials. *Nature communications*, 1:21, 2010.

[24] M. Gharghi, C. Gladden, T. Zentgraf, Y.M. Liu, X.B. Yin, J. Valentine, and X. Zhang. A carpet cloak for visible light. *Nano Lett.*, 11(7):2825–2828, 2011.

[25] S. Xi, H.S. Chen, B.I. Wu, and J.A. Kong. One-directional perfect cloak created with homogeneous material. *IEEE Microw. Wirel. Compon. Lett.*, 19(3):131–133, 2009.

[26] Y. Luo, L.X. He, S.Z. Zhu, and Y. Wang. Arbitrary polygonal cloaks with multiple invisible regions. *J. Modern Opt.*, 58(1):14–20, 2011.

[27] Q. Wu, K. Zhang, F.Y. Meng, and L.W. Li. Material parameters characterization for arbitrary N-sided regular polygonal invisible cloak. *J. Phys. D: Appl. Phys.*, 42(3):035408, 2009.

[28] S.J. Orfanidis. *Electromagnetic Waves and Antennas*. Rutgers University, 2002.

[29] A. Taflove and S.C. Hagness. *Computational Electrodynamics: the Finite-Difference Time-Domain Method*. Third edition. Artech house Inc., Boston, MA, 2005.

[30] Y. Hao and R. Mittra. *FDTD Modeling of Metamaterials: Theory and Applications*. Artech House, 2008.

[31] Y. Zhao, C. Argyropoulos, and Y. Hao. Full-wave finite-difference time-domain simulation of electromagnetic cloaking structures. *Opt. Express*, 16:6717–6730, 2008.

[32] W.S. Li, D. Liang, and Y.P. Lin. A new energy-conserved S-FDTD scheme for Maxwells equations in metamaterials. *Int. J. Numer. Anal. Model.*, 10:775–794, 2013.

[33] P.G. Ciarlet. *The Finite Element Method for Elliptic Problems*. North-Holland, 1978.

[34] J.M. Jin. *The Finite Element Method in Electromagnetics.* John Wiley & Sons, 2014.

[35] P. Monk. *Finite Element Methods for Maxwell's Equations.* Numerical Mathematics and Scientific Computation. Oxford University Press, New York, 2003.

[36] J.C. Li and Y.Q. Huang. *Time-Domain Finite Element Methods for Maxwell's Equations in Metamaterials*, volume 43. Springer, 2012.

[37] S. Cummer, B. Popa, D. Schurig, D. Smith, and J.B. Pendry. Full-wave simulations of electromagnetic cloaking structures. *Phys. Rev. E*, 74(3):036621, 2006.

[38] J.C. Li and Y.Q. Huang. Mathematical simulation of cloaking metamaterial structures. *Adv. Appl. Math. Mech.*, 4(01):93–101, 2012.

[39] J.C. Li, Y.Q. Huang, W. Yang, and A.H. Wood. Mathematical analysis and time-domain finite element simulation of carpet cloak. *SIAM J. Appl. Math.*, 74(4):1136–1151, 2014.

[40] J.C. Li, Y.Q. Huang, and W. Yang. Developing a time-domain finite-element method for modeling of electromagnetic cylindrical cloaks. *J. Comput. Phys.*, 231(7):2880–2891, 2012.

[41] J.C. Li, Y.Q. Huang, and W. Yang. Well-posedness study and finite element simulation of time-domain cylindrical and elliptical cloaks. *Math. Comp.*, 84:543–562, 2014.

[42] F. Ihlenburg and I. Babuška. Finite element solution of the Helmholtz equation with high wave number, part I: the h-version of FEM. *Comput. Math. Appl.*, 30:9–37, 1995.

[43] I. Babuška and S.A. Sauter. Is the pollution effect of the FEM avoidable for the Helmholtze equation considering high wave number. *SIAM Rev.*, 42:451–484, 2000.

[44] J. Shen and L.L. Wang. Spectral approximation of the Helmholtz equation with high wave numbers. *SIAM J. Numer. Anal.*, 43(2):623–644, 2005.

[45] D. Gottlieb and S.A. Orszag. *Numerical Analysis of Spectral Methods: Theory and Applications.* SIAM-CBMS, Philadelphia, 1977.

[46] C. Canuto, M.Y. Hussaini, A. Quarteroni, and T.A. Zang. *Spectral Methods: Evolution to Complex Geometries and Applications to Fluid Dynamics*. Springer, 2007.

[47] J. Shen, T. Tang, and L.L. Wang. *Spectral Methods: Algorithms, Analysis and Applications*, volume 41 of *Springer Series in Computational Mathematics*. Springer-Verlag, Berlin, Heidelberg, 2011.

[48] Y. Maday. Spectral element multigrid II. *J. Sci. Comput.*, 3:323–353, 1988.

[49] Q.H. Liu. The PSTD algorithm: A time-domain method requiring only two cells per wavelength. *Microw. Opt. Techn. Lett.*, 15(3):158–165, 1997.

[50] J.S. Hesthaven and T. Warburton. *Nodal Discontinuous Galerkin Methods: Algorithms, Analysis, and Applications*, volume 54. Springer, 2007.

[51] J.P. Berenger. A perfectly matched layer for the absorption of electromagetic waves. *J. Comput. Phys.*, 114:185–200, 1994.

[52] J.M. Jin, J.L. Volakis, and J.D. Collins. A finite element-boundary integral method for scattering and radiation by two-and three-dimensional structures. *IEEE Antennas. Propag. Mag.*, 33(3):22–32, 1991.

[53] Y. Lin, J.H. Lee, J.G. Liu, M. Chai, J.A. Mix, and Q.H. Liu. A hybrid SIM-SEM method for 3-D electromagnetic scattering problems. *IEEE Trans. Antennas. Propag.*, 57(11):3655–3663, 2009.

[54] T. Hagstrom. Radiation boundary conditions for the numerical simulation of waves. In *Acta numerica, 1999*, volume 8 of *Acta Numer.*, pages 47–106. Cambridge Univ. Press, Cambridge, 1999.

[55] B. Engquist and A. Majda. Absorbing boundary conditions for the numerical simulation of waves. *Math. Comp.*, 31(139):629–651, 1977.

[56] M.J. Grote and J.B. Keller. On non-reflecting boundary conditions. *J. Comput. Phys.*, 122:231–243, 1995.

[57] A. Fournier. Exact calculation of fourier series in nonconforming spectral-element methods. *J. Comput. Phys.*, 215:1–5, 2006.

[58] Y. He, M. Min, and D.P. Nicholls. A spectral element method with transparent boundary condition for periodic layered media scattering. *J. Sci. Comput.*, 68(2):772–802, 2016.

[59] H. Ma, S.B. Qu, Z. Xu, J.Q. Zhang, B.W. Chen, and J.F. Wang. Material parameter equation for elliptical cylindrical cloaks. *Phys. Rev. A*, 77(1):013825, 2008.

[60] Z. Ruan, M. Yan, C.W. Neff, and M. Qiu. Ideal cylindrical cloak: perfect but sensitive to tiny perturbations. *Phys. Rev. Lett.*, 99(11):113903, 2007.

[61] B.L. Zhang, H.S. Chen, B. Wu, Y. Luo, L. Ran, and J.A. Kong. Response of a cylindrical invisibility cloak to electromagnetic waves. *Phys. Rev. B*, 76(12):121101, 2007.

[62] B.L. Zhang. Electrodynamics of transformation-based invisibility cloaking. *Light: Science & Applications*, 1(10):e32, 2012.

[63] J.C. Li and Y.Q. Huang. Mathematical simulation of cloaking metamaterial structures. *Adv. Appl. Math. Mech*, 4:93–101, 2012.

[64] J.C. Nédélec. Mixed finite elements in $\mathbf{R}^3$. *Numer. Math.*, 35(3):315–341, 1980.

[65] R. Weder. The boundary conditions for point transformed electromagnetic invisibility cloaks. *J. Phys. A: Math. Theor.*, 41(41):415401, 2008.

[66] M. Lassas and T. Zhou. Two dimensional invisibility cloaking for Helmholtz equation and non-local boundary conditions. *Math. Res. Lett.*, 18(3):473–488, 2011.

[67] M. Lassas and T. Zhou. Singular partial differential operators and pseudo-differential boundary conditions in invisibility cloaking. In *Fourier Analysis, Trends in Mathematics*, pages 263–284, 2014. Springer, Switzerland.

[68] J.F. Lee and Z. Sacks. Whitney elements time domain (WETD) methods. *IEEE Trans. Magn.*, 31(3):1325–1329, 1995.

[69] K.S. Yee. Numerical solution of initial boundary value problems involving Maxwells equations in isotropic media. *IEEE Trans. Antennas Propag.*, 14(3):302–307, 1966.

[70] N. Okada and J.B. Cole. FDTD modeling of a cloak with a nondiagonal permittivity tensor. *ISRN. Opt.*, 2012:063903, 2012.

[71] B.L. Zhang, B.I. Wu, H.S. Chen, and J.A. Kong. Rainbow and blueshift effect of a dispersive spherical invisibility cloak impinged on by a nonmonochromatic plane wave. *Phys. Rev. Lett.*, 101(6):063902, 2008.

[72] J. Douglas, J.E. Santos, D. Sheen, and L.S. Bennethum. Frequency domain treatment of one-dimensional scalar waves. *Math. Mod. Meth. Appl. Sci.*, 3:171–194, 1993.

[73] F. Ihlenburg. *Finite Element Analysis of Acoustic Scattering*, volume 132 of *Applied Mathematical Sciences*. Springer-Verlag, New York, 1998.

[74] L. Demkowicz and F. Ihlenburg. Analysis of a coupled finite-infinite element method for exterior Helmholtz equations. *Numer. Math.*, 88:43–73, 2001.

[75] M. Ainsworth. Discrete dispersion relation for hp-version finite element approximation at high wave number. *SIAM J. Numer. Anal.*, 42(2):553–575, 2004.

[76] P. Cummings and X.B. Feng. Sharp regularity coefficient estimates for complex-valued acoustic and elastic Helmholtz equations. *Math. Mod. Meth. Appl. Sci.*, 16(1):139–160, 2006.

[77] J. Shen and L.L. Wang. Analysis of a spectral-Galerkin approximation to the Helmholtz equation in exterior domains. *SIAM J. Numer. Anal.*, 45:1954–1978, 2007.

[78] U. Hetmaniuk. Stability estimates for a class of Helmholtz problems. *Commun. Math. Sci.*, 5(3):665–678, 2007.

[79] S.N. Chandler-Wilde and P. Monk. Wave-number-explicit bounds in time-harmonic scattering. *SIAM J. Math. Anal.*, 39(5):1428–1455, 2008.

[80] J.M. Melenk and S. Sauter. Wavenumber explicit convergence analysis for Galerkin discretizations of the Helmholtz equation. *SIAM J. Numer. Anal.*, 49(3):1210–1243, 2011.

[81] J.M. Melenk. *On Generalized Finite Element Methods.* PhD thesis, University of Maryland, College Park, 1995.

[82] R. Hiptmair, A. Moiola, and I. Perugia. Stability results for the time-harmonic Maxwell equations with impendance boundary conditions. *Math. Mod. Meth. Appl. Sci.*, 21(11), 2011.

[83] X.B. Feng. Wave number-dependent a priori estimates for the time-harmonic Maxwell equations. *Private Communication*, 2011.

[84] P.N. David and R. Fernando. Shape deformations in rough surface scattering: improved algorithms. *J. Opt. Soc. Am. A*, 21(4):606–621, 2004.

[85] Jie Shen. Efficient spectral-Galerkin methods III. polar and cylindrical geometries. *SIAM J. Sci. Comput.*, 18:1583–1604, 1997.

[86] J.P. Boyd. *Chebyshev and Fourier Spectral Methods*. Dover Publications, second edition, 2001.

[87] M. Abramowitz and I. Stegun. *Handbook of Mathematical Functions*. Dover, New York, 1964.

[88] J. Shen, L.L. Wang, and H.Y. Li. A triangular spectral element method using fully tensorial rational basis functions. *SIAM J. Numer. Anal.*, 47(3):1619–1650, 2009.

[89] R. Courant and D. Hilbert. *Methods of Mathematical Physics, volume 1*. Interscience Publishers, Inc., New York, 1953.

[90] M.A. Al-Gwaiz. *Sturm-Liouville Theory and Its Applications*. Springer Undergraduate Mathematics Series. Springer-Verlag London, Ltd., London, 2008.

[91] Y.Y. Ji, H. Wu, H.P. Ma, and B.Y. Guo. Multidomain pseudospectral methods for nonlinear convection-diffusion equations. *Appl. Math. Mech.*, 32(10):1255–1268, 2011.

[92] E.T. Whittaker and G.N. Watson. *A Course of Modern Analysis*. Cambridge University Press, 4th edition, 1927.

[93] N.W. McLachlan. *Theory and Application of Mathieu Functions*, volume 4. Dover New York, 1964.

[94] Q. Fang, J. Shen, and L.L. Wang. An efficient and accurate spectral method for acoustic scattering in elliptic domains. *Numer. Math.: Theory, Methods Appl.*, 2:258–274, 2009.

[95] F.P. Mechel. *Formulas of Acoustics*, volume 2. Springer, 2002.

[96] I. Harari and T. Hughes. Analysis of continuous formulations underlying the computation of time-harmonic acoustics in exterior domains. *Comput. Methods. Appl. Mech. Engrg.*, 97:103–124, 1992.

[97] G.C. Hsiao, N. Nigam, J.E. Pasciak, and L.W. Xu. Error analysis of the DtN-FEM for the scattering problem in acoustics via Fourier analysis. *J. Comput. Appl. Math*, 235:4949–4965, 2011.

[98] W.J. Gordon and C.A. Hall. Transfinite element methods: blending-function interpolation over arbitrary curved element domains. *Numer. Math.*, 21(2):109–129, 1973.

[99] M.O. Deville, P.F. Fischer, and E.H. Mund. *High-Order Methods for Incompressible Fluid Flow*, volume 9. Cambridge University Press, 2002.

[100] C. Ronchi, R. Lacono, and P.S. Paolucci. The cubed sphere: a new method for the solution of partial differential equations in spherical geometry. *J. Comput. Phys.*, 124(1):93–114, 1996.

[101] J. Zhang, L.L. Wang, and Z.J. Rong. A prolate-element method for nonlinear PDEs on the sphere. *J. Sci. Comput.*, 47(1):73–92, 2011.

[102] G. Karniadakis and S. Sherwin. *Spectral/hp Element Methods for Computational Fluid Dynamics*. Oxford University Press, 2005.

[103] G.B. Arfken and H.J. Weber. *Mathematical Methods for Physicists*. Harcourt/Academic press, 2001.

[104] J.J. Zhang, Y. Luo, H.S. Chen, and B.I. Wu. Cloak of arbitrary shape. *J. Opt. Soc. Am. B*, 25(11):1776–1779, 2008.

[105] Z.G. Yang and L.L. Wang. Accurate simulation of ideal circular and elliptic cylindrical invisibility cloaks. *Commun. Comput. Phys.*, 17(03):822–849, 2015.

[106] H.S. Chen, B.I. Wu, B.L. Zhang, and J.A. Kong. Electromagnetic wave interactions with a metamaterial cloak. *Phys. Rev. Lett.*, 99:063903, 2007.

[107] C. Argyropoulos, E. Kallos, and Y. Hao. Dispersive cylindrical cloaks under nonmonochromatic illumination. *Phys. Rev. E*, 81(1):016611, 2010.

[108] H.Y. Chen, Z.X. Liang, P.J. Yao, X.Y. Jiang, H.R. Ma, and C.T. Chan. Extending the bandwidth of electromagnetic cloaks. *Phys. Rev. B.*, 76(24):241104, 2007.

[109] W.X. Jiang, T.J. Cui, Q. Cheng, J.Y. Chin, X.M. Yang, R.P. Liu, and D.R. Smith. Design of arbitrarily shaped concentrators based on conformally optical transformation of nonuniform rational b-spline surfaces. *Appl. Phys. Lett.*, 92(26):264101, 2008.

[110] B. Wang, L.L. Wang, and Z.Q. Xie. Accurate calculation of spherical and vector spherical harmonics expansions via spectral element grids. *arxiv.org*, 2015.

[111] J.F. Chen and Q.H. Liu. A non-spurious vector spectral element method for Maxwell's equations. *Prog. Electro. Res.*, 96:205–215, 2009.

[112] L.N. Ma, J. Shen, and L.L. Wang. Spectral approximation of time-harmonic Maxwell equations in three-dimensional exterior domains. *Int. J. Numer. Anal. Model.*, 12(2):366–383, 2015.

[113] E. Bullard and H. Gellman. Homogeneous dynamos and terrestrial magnetism. *Philosophical Transactions of the Royal Society of London A: Mathematical, Physical and Engineering Sciences*, 247(928):213–278, 1954.

[114] D.P. Nicholls and J. Shen. A rigorous numerical analysis of the transformed field expansion method. *SIAM J. Numer. Anal.*, 47(4):2708–2734, 2009.

[115] S.J. Zhang and J.M. Jin. *Computation of Special Functions.* Wiley-Interscience, 1996.

[116] J.E. Kiefer and G.H. Weiss. Some asymptotic bessel function ratios. *Isr. J. Math.*, 12:46–48, 1972.

[117] P.N. Swarztrauber and W.F. Spotz. Generalized discrete spherical harmonic transforms. *J. Comput. Phys.*, 159(2):213–230, 2000.

[118] D. Nicholls and J. Shen. A stable, high–order method for two–dimensional bounded–obstacle scattering. *SIAM J. Sci. Comput.*, 28:1398–1419, 2006.

[119] Q. Fang, D.P. Nicholls, and J. Shen. A stable, high–order method for two–dimensional bounded–obstacle scattering. *J. Comput. Phys.*, 224:1145–1169, 2007.

[120] N.A. Zharova, L.V. Shadrivov, and Y.S. Kivshar. Inside-out electromagnetic cloaking. *Opt. Express*, 16(7):4615–4620, 2008.

[121] E.L. Hill. The theory of vector spherical harmonics. *Amer. J. Phys.*, 22:211–214, 1954.

List of Publications

Papers published in referred Journals

(i) Z.G. Yang and L.L. Wang. Accurate simulation of ideal circular and elliptic cylindrical invisibility cloaks. *Commun. Comput. Phys.*, 17(03): 822–849, 2015.

(ii) Z.G. Yang, L.L. Wang, Z.J. Rong, B. Wang and B.L. Zhang. Seamless Integration of global Dirichlet-to-Neumann boundary condition and spectral elements for transformation electromagnetics. *Comput. Methods Appl. Mech. Engrg.*, 301: 137-163, 2016.

Paper in review

(i) L.N. Ma, J. Shen, L.L. Wang and Z.G. Yang. Wavenumber explicit analysis of spectral-Galerkin methods for time-harmonic Maxwell equations in exterior domains, *submitted to IMA J. Numer. Anal., 2016 (in revision).*